

Alma Mater Studiorum – Università di Bologna

DOTTORATO DI RICERCA IN

CHIMICA

Ciclo XXXI

**Settore Concorsuale: 03/A1**

**Settore Scientifico Disciplinare: CHIM/01**

**Synthesis and Characterization of Prussian Blue  
Analogue Materials for Li-ion and post-Li Batteries**

**Presentata da:** Angelo Mullaliu

**Coordinatore Dottorato**

**Prof. Aldo Roda**

**Supervisore**

**Prof. Marco Giorgetti**

**Esame finale anno 2019**

*Synthesis and Characterization of Prussian Blue  
Analogue Materials for Li-ion and post-Li Batteries*

A DISSERTATION PRESENTED

BY

ANGELO MULLALIU

TO

THE DEPARTMENT OF INDUSTRIAL CHEMISTRY "TOSO MONTANARI"

IN PARTIAL FULFILLMENT OF THE REQUIREMENTS

FOR THE DEGREE OF

DOCTOR OF PHILOSOPHY

IN THE SUBJECT OF

CHEMISTRY

UNIVERSITY OF BOLOGNA

BOLOGNA, ITALY

APRIL 2019

## *Synthesis and Characterization of Prussian Blue Analogue Materials for Li-ion and post-Li Batteries*

### ABSTRACT

The global challenge responding to the need of efficient electrical energy storage is answered by rechargeable batteries, which are based on high-rate intercalation reaction of lithium ions into nano- and micro-structured porous materials. A class of insertion-type materials is represented by Prussian blue analogues (PBAs), characterized by porous open 3D-frameworks which allow for a facile insertion/ extraction of ions with negligible lattice strain. The electroactivity of the metals constituting the lattice forms the basis for a series of properties, which have been studying in several fields. Due to their high electrochemical efficiency, low-cost, affordable price, and versatility towards a wide selection of ions, they have been investigating as electrode materials in Li-ion batteries, as well as Na-ion batteries and aqueous systems in the perspective of a post-lithium strategy, intended to provide for alternatives to the use of lithium in current technologies. The performance of such hosts derives from a combination of structural and electronic properties and their reversible evolution along cycling, therefore the investigation of such features and the comprehension of limiting or irreversible steps are of great technological importance to better design advanced materials.

The complexity of a battery, which consists of different components and various contributions to the overall redox process, could be untangled by using a combined multi-technique approach that probes different aspects of the same system. A blend of complementary and independent techniques has been demonstrated to have a wide potentiality in retrieving the local structural dynamics of selected absorbing species. To this purpose, we have combined X-ray diffraction (XRD) and X-ray absorption fine structure (XAFS) to investigate the long- and short-range order and electronic evolution, recording time-resolved snapshots of the system under study through *operando* measurements. The large datasets have been analyzed through chemometric techniques to reveal the occurrence of complex multicomponent reactions, allowing a quick and efficient data interpretation which would be otherwise time consuming. In addition, the support of theoretical studies permitted the validation of our hypotheses and gave further insight into reaction mechanisms.

In the present work we focused on the synthesis and characterization of PBAs in Li-ion and post-Li battery systems, their redox activity, electronic and structural reversibility while cycling. All synthesized materials exhibit good structural stability and negligible lattice strain during (de)insertion of ions and redox processes ascribable to one or more redox species. For instance, copper hexacyanoferrate features two redox sites, copper and iron, contrarily to what reported in the literature, while copper nitroprusside has been demonstrated to possess three redox centres, including the two metals, as well as the *non innocent* nitrosyl ligand as third site. Electrosynthesized copper hexacyanoferrate results extremely versatile towards a wide selection of ions in aqueous solution, ranging from monovalent to multivalent ions, while titanium hexacyanoferrate may reach a capacity equal to 55 mAh/g in potassium nitrate aqueous solution. This led to the conclusion that a H<sub>2</sub>O-based system would be feasible for the studied materials, and more in general for this class of compounds. Although they do not feature high specific capacities, they are characterized by good cycling ability and efficiency, as well as ion-versatility which can be favorable to a post-lithium strategy. The investigation of their reaction mechanism has led to the deep understanding of limiting steps, whereby it is possible to tailor new promising materials that could result competitive in the next future.

TO MY PARENTS, SHEFQET AND MIMOZA

# Acknowledgments

SOMETIMES I FIND THE ACKNOWLEDGEMENTS SECTION HARD TO WRITE. I could acknowledge several people who supported/ helped/ cheered me during these last three beautiful years. Yeah, beautiful. Perhaps the best period of my life: I traveled, I met different people, I spoke different languages, I always was in a good environment. The real reason I had such a happy and beautiful time is because I met my thesis advisor. He gave me all these possibilities and taught me basically how to do science. Therefore, as in all other acknowledgements I have read, I would like to thank first my supervisor, Marco, for the passion he puts in his work, which is contagious. Besides, I would like to thank my parents, Shefqet and Mimoza, who are always there for me. Sometimes I still try to explain them what I do (spectroscopy included), and they never get bored.

# Thesis Review

I would like to thank the reviewers for their useful help and comments:

- Prof. Dr. Robert Dominko, National Institute of Chemistry, Ljubljana, Slovenia
- Prof. Dr. Francesco Nobili, University of Camerino - School of Science and Technology, Camerino, Italy

# List of publications

1. The electrochemical activity of the nitrosyl ligand in copper nitroprusside: a new possible redox mechanism for lithium battery electrode materials? Angelo Mullaliu, Moulay-Tahar Sougrati, Nicolas Louvain, Giuliana Aquilanti, Marie-Liesse Doublet, Lorenzo Stievano, Marco Giorgetti. *Electrochimica Acta* 2017, 257, 364-371
2. Copper Electroactivity in Prussian Blue-Based Cathode Disclosed by Operando XAS. Angelo Mullaliu, Giuliana Aquilanti, Paolo Conti, Jasper R. Plaisier, Marcus Fehse, Lorenzo Stievano, Marco Giorgetti. *Journal of Physical Chemistry C* 2018, 122, 28, 15868-15877
3. Thin layer films of copper hexacyanoferrate: Structure identification and analytical applications. Michele Ventura, Angelo Mullaliu, Diana Elena Ciurduc, Sergio Zappoli, Gabriele Giuli, Dino Tonti, Eduardo Enciso, Marco Giorgetti. *Journal of Electroanalytical Chemistry*, 2018, 827, 10-20
4. Operando XAFS and XRD study of a Prussian Blue Analogue cathode material: Iron Hexacyanocobaltate. Angelo Mullaliu, Paolo Conti, Giuliana Aquilanti, Jasper Rikkert Plaisier, Lorenzo Stievano, and Marco Giorgetti. *Condensed Matter* 2018, 3, 36
5. Metal hexacyanoferrates: ion insertion (or exchange) capabilities. Angelo Mullaliu, Marco Giorgetti. Book chapter in "Applications of Ion exchange Materials", Editor: Inamuddin, Mohd. Imran Ahamed, Abdullah M. Asiri, Springer, UK, 2018. *In press*

6. The peculiar redox mechanism of copper nitroprusside disclosed by a multi-technique approach. Angelo Mullaliu, Lorenzo Stievano, Giuliana Aquilanti, Jasper Plaisier, Sylvain Cristol and Marco Giorgetti. *Radiation Physics and Chemistry. Submitted*
7. XAFS studies on battery materials: data analysis supported by a chemometric approach. Marco Giorgetti, Angelo Mullaliu, Paolo Conti. *Radiation Physics and Chemistry. Submitted*
8. Battery Dynamics Revealed by Operando XRD and XAFS and by Theoretical Approach. Angelo Mullaliu, Giuliana Aquilanti, Lorenzo Stievano, Paolo Conti, Jasper R. Plaisier, Sylvain Cristol and Marco Giorgetti. *Submitted*
9. Newly developed electrochemical synthesis of Co-based Layered Double Hydroxides: toward noble metal-free electro-catalysis. Elisa Musella, Isacco Gualandi, Erika Scavetta, Arianna Rivalta, Elisabetta Venuti, Meganne Christian, Vittorio Morandi, Angelo Mullaliu, Marco Giorgetti, Domenica Tonelli. *Submitted*

# List of contributions to conferences

1. The uncommon electrochemistry of copper nitroprusside disclosed by spectroscopic and diffraction techniques.

Angelo Mullaliu, Elisa Musella, Reinhard Denecke, Marco Giorgetti.

Abstract accepted as oral presentation in XXVII Congresso della Divisione di Chimica Analitica in Bologna (Italy)

2. The peculiar redox mechanism of copper nitroprusside disclosed by a multi-technique approach.

Angelo Mullaliu, Elisa Musella, Lorenzo Stievano, Giuliana Aquilanti, Jasper Plaisier, Sylvain Cristol, Reinhard Denecke, Marco Giorgetti.

Abstract accepted as oral presentation in the 69<sup>th</sup> Annual Meeting of the International Society of Electrochemistry in Bologna (Italy)

3. Soft x-ray microscopy of lithium-rich layered-oxide cathode materials.

A. Sorrentino, L. Simonelli, N. Laszczynski, A. Birrozzi, A. Mullaliu, E. Pereiro, M. Giorgetti, S. Passerini and D. Tonti.

Abstract accepted as poster in the 69<sup>th</sup> Annual Meeting of the International Society of Electrochemistry in Bologna (Italy)

4. The peculiar redox mechanism of copper nitroprusside disclosed by a multi-technique approach.

Angelo Mullaliu, Lorenzo Stievano, Giuliana Aquilanti, Jasper Plaisier, Sylvain Cristol, and Marco Giorgetti.

Abstract accepted as oral presentation in XAFS17 2018 congress in Cracow (Poland)

5. XAFS studies on battery materials: data analysis supported by a chemometric approach.

Marco Giorgetti, Angelo Mullaliu, Paolo Conti.

Abstract accepted as poster in XAFS17 2018 congress in Cracow (Poland)

6. Operando characterization of batteries using X-ray absorption and X-ray diffraction.

Marco Giorgetti, Angelo Mullaliu.

Abstract accepted as oral presentation in the 6<sup>th</sup> World Congress and Expo on Nanotechnology and Materials Science in Valencia (Spain)

7. Electronic Structure Investigation of a Layered-Oxide Cathode Material by a Multi-technique Approach.

L. Simonelli, A. Sorrentino, S. Passerini, M. Giorgetti, A. Mullaliu, A. Birrozzi, N. Laszczynski, W. Olszewski, C. Marini, N. Ramanan, D. Heinis, D. Tonti.

Abstract accepted as oral presentation in VIII AUSE CONGRESS in Barcelona (Spain).

8. Operando characterization of a battery material: the case of copper nitroprusside.

Angelo Mullaliu, Lorenzo Stievano, Giuliana Aquilanti, Jasper Plaisier, Sylvain Cristol, Marco Giorgetti.

Abstract accepted as poster in FisMat2017 congress in Trieste (Italy)

9. Participation to the ASC Winter School 2017 in Rimini (Italy) as part of the local organizing committee

# Contents

<b>1</b>	<b>INTRODUCTION</b>	<b>1</b>
1.1	Energy demand and energy storage . . . . .	1
1.2	Prussian blue analogues . . . . .	6
1.3	PBAs as battery materials - A brief overview . . . . .	11
	Motivation . . . . .	16
<b>2</b>	<b>BACKGROUND</b>	<b>18</b>
2.1	Battery electrochemistry . . . . .	18
	Cyclic Voltammetry . . . . .	19
	Galvanostatic cycling with potential limitation . . . . .	21
2.2	X-rays and X-ray techniques . . . . .	23
	X-ray Diffraction . . . . .	28
	X-ray Absorption Fine Structure . . . . .	30
2.3	Multivariate Curve Resolution with Alternate Least Squares . . . . .	34
<b>3</b>	<b>METHODOLOGY</b>	<b>36</b>
3.1	Synthesis . . . . .	36
3.2	Material Characterization . . . . .	37
3.3	Electrode preparation and cell set-up . . . . .	39
3.4	Electrochemical characterization . . . . .	41
3.5	<i>Operando</i> Characterization . . . . .	43

3.6	DFT calculations . . . . .	45
3.7	XANES calculations . . . . .	46
4	RESULTS AND DISCUSSION	47
4.1	Potassium iron hexacyanocobaltate . . . . .	48
4.2	Copper hexacyanoferrate . . . . .	58
4.3	Copper nitroprusside . . . . .	70
4.4	Copper hexacyanoferrate - Electrodeposition of thin layer films . . . . .	94
4.5	Titanium hexacyanoferrate . . . . .	112
5	FINALS REMARKS AND PERSPECTIVES	121
	REFERENCES	143

## List of figures

1.1.1	Battery market. Source: Avicenne Energy, 2016 . . . . .	3
1.1.2	Cobalt production . . . . .	4
1.1.3	Lithium reserves and resources. Reprinted from Supply and Demand of Lithium and Gallium. ©Cui Rongguo, 2016 . . . . .	5
1.2.1	Van Gogh's Starry Night. Van Gogh probably used the Prussian Blue pigment. Available at Wikimedia Commons free repository . . . . .	6
1.2.2	Crystal structure of PB. Fe <sup>II</sup> labeled as red, Fe <sup>III</sup> as blue, C as brown, and N as light blue . . . . .	7
1.3.1	Electrochemical characterizations of the FeFe(CN) <sub>6</sub> electrode: (a) CV curves measured at a scan rate of 1 mV/s, (b) charge and discharge profiles at a current density of 250 mA/g, (c) rate performance and (d) long-term cycling stability 10C rate. (1C= 125 mA/g). Reuse from Low-defect Prussian blue nanocubes as high capacity and long life cathodes for aqueous Na-ion batteries. Nano Energy, 13, 117–123, 2015. Copyright 2015, with permission from Elsevier . . . . .	13
1.3.2	The charge–discharge curves of Prussian blue analogues KMF <sub>2</sub> (CN) <sub>6</sub> –Na cells at the third cycle with a current of C/20. Insets show their corresponding chronoamperograms. Republished with permission of The Royal Society of Chemistry, from Prussian blue: a new framework of electrode materials for sodium batteries, Yuhao Lu, Long Wang, Jinguang Cheng and John B. Goodenough, Chem. Commun., 2012, 48, 6544–6546, 2012 Copyright; permission conveyed through Copyright Clearance Center, Inc. . . . .	15

1.3.3 Galvanostatic initial charge and discharge profiles of air-dried (left) and vacuum-dried (right) $\text{Na}_{2-\delta}\text{MnHCF}$ at a current of 0.1 C (15 mA/g) in the voltage range of 2.0 – 4.0 V vs. $\text{Na}^+/\text{Na}$ . Reproduced with permission from J. Am. Chem. Soc. 2015, 137, 2658–2664 Copyright 2015 American Chemical Society . . . . .	15
2.1.1 Li-ion insertion mechanism. Reprinted with permission from Chem. Rev., 2004, 104 (10), 4303–4418. DOI: 10.1021/cr030203g. Copyright 2004 American Chemical Society . . . . .	20
2.1.2 Variation in time of the potential in a typical cyclic voltammetry measurement . . . . .	21
2.1.3 GCPL measurement on a battery system . . . . .	22
2.2.1 X-ray emission spectrum from a conventional source. ©Copyright 2018, PhysicsOpen-Lab. All Rights Reserved . . . . .	25
2.2.2 Crab Nebula. Credits: NASA, ESA, J. Hester and A. Loll (Arizona State University) . . . . .	26
2.2.3 Schematic view of a synchrotron facility. ©Copyright 2018, ANSTO. The Australian Synchrotron . . . . .	27
2.2.4 Spectra of bending magnets and insertion devices. Reprinted from High Throughput Software for Powder Diffraction and its Application to Heterogeneous Catalysis, Taha Sochi. All rights reserved to Dr. Taha Sochi 2010 . . . . .	28
2.2.5 Schematic representation of constructive and totally destructive interference in Bragg’s law. By Cdang at English Wikipedia . . . . .	30
2.2.6 Transmission through an uniform sample of thickness $x$ . . . . .	31
2.2.7 XAFS spectrum of an isolated atom (red dot-line) and the corresponding coordinated species (black line) . . . . .	32
2.2.8 XAFS edges. By Atenderholt at English Wikipedia . . . . .	34
2.3.1 MCR-ALS analysis scheme . . . . .	35
4.1.1 On the left side, the Rietveld refinement on FeCo powder is presented. The most relevant Miller planes are indexed in brackets. On the right side, the <i>operando</i> XRD electrochemical profile (blue line) and concomitant lattice parameter evolution (red scatter) are shown . . . . .	49

4.1.2	Rietveld refinement on the 60 <sup>th</sup> XRD pattern: (a) 8c position not refined and (b) refined. Note the fit improvement at (220) plane . . . . .	50
4.1.3	XAFS K-edge evolution for both iron (left) and cobalt (right). In the bottom layer, pristine, charged and discharged states spectra are compared and presented for each metal site. The figure has been adapted from reference [1] . . . . .	50
4.1.4	MCR-ALS analysis results: (a) Concentration profile; (b) Pure spectral components. In panel (c), the electrochemical potential profile is reported, while the linear combination fit on the pristine sample is illustrated in panel (d). The MCR-ALS results have been adapted from reference [2] . . . . .	52
4.1.5	Pre-edge data analysis for the pristine, partially charged, fully charged, partially discharged, fully discharged states, and their comparison . . . . .	53
4.1.6	MS contributions and best fit for the pristine, partially charged, fully charged, partially discharged, fully discharged states at Fe (first layer) and Co (second layer) K-edge . . . . .	54
4.1.7	Relevant EXAFS fitting results: (a) First shell distances behavior: Fe-N and Cu-N; (b) EXAFS Debye-Waller factors; (c) Variation in Fe-N-C-Co chains degeneracy during lithiation; (d) Variation in the coordination number of the 8c interstitial cation . . . . .	55
4.2.1	XRD pattern of synthesized CuHCF. In the figure experimental, calculated and residual lines are illustrated. Miller indexes for the main reflections are also shown . . . . .	59
4.2.2	Fe and Cu K-edges. Fit on $k^2$ -extracted EXAFS signal and corresponding Fourier Transforms (FTs) . . . . .	61
4.2.3	Single edge fitting of the pristine sample (formulated). Fe K-edge . . . . .	62
4.2.4	Graphic representation and comparison of iron K-edge and copper K-edge during electrochemical cycling . . . . .	63
4.2.5	Pre-edge map for both iron and copper metals during cycling . . . . .	64
4.2.6	Comparison between pristine, charged, and discharged states at both Fe and Cu K-edge. Insets show the magnification of the pre-edge region . . . . .	64
4.2.7	Magnification of Fe pre-edge. Comparison between pristine, charged and discharged states . . . . .	65

4.2.8	Concentration profile $C_{S,F}$ and obtained pure spectral components $A_{W,F}$ of the normalized XANES data taken at the Cu K-edge of CuHCF material . . . . .	65
4.2.9	Best fit plots of the $k^2$ -extracted EXAFS signal of the pristine (spectrum #1) and charged samples (spectrum #33) analyzed at both Fe and Cu K-edges . . . . .	67
4.2.10	Graphical representation of the main EXAFS parameters trend during cycling. (a) Fe-C and Cu-N bond lengths and (b) Debye Waller factors variation. (c) Copper coordination number to N, or rather number of the Cu-N-C-Fe linear chains. (d) Coordination number to $8c$ interstitial positions . . . . .	68
4.2.11	Electrochemical curve recorded during the <i>operando</i> XAFS experiment . . . . .	69
4.3.1	TG Analysis of the synthesized batches . . . . .	71
4.3.2	Profile matching refinement of CuNP . . . . .	72
4.3.3	XRD patterns of AM <sub>1</sub> , AM <sub>2</sub> , AM <sub>3</sub> . The inset displays the magnification of the region around $19.6^\circ$ . . . . .	73
4.3.4	Cyclic voltammetry at $0.1 \text{ mV s}^{-1}$ scan rate of CuNP in the $1.5 < E < 4.0 \text{ V}$ vs. $\text{Li}^+/\text{Li}$ potential window . . . . .	74
4.3.5	Evolution of specific capacity and coulombic efficiency of CuNP upon cycling by imposing a C/5 rate in the $1.5 < E < 4.0 \text{ V}$ vs. $\text{Li}^+/\text{Li}$ potential window . . . . .	74
4.3.6	Electrochemical profile upon cycling by imposing a C/5 rate in the $1.5 < E < 4.0 \text{ V}$ vs. $\text{Li}^+/\text{Li}$ potential window. The 1 <sup>st</sup> , 20 <sup>th</sup> , 50 <sup>th</sup> and 90 <sup>th</sup> cycles are highlighted . . . . .	75
4.3.7	Voltammograms recorded at the 1 <sup>st</sup> , 20 <sup>th</sup> , 50 <sup>th</sup> and 90 <sup>th</sup> cycles. CVs have been recorded in the $1.5 < E < 4.0 \text{ V}$ vs. $\text{Li}^+/\text{Li}$ potential range at a $0.1 \text{ mV s}^{-1}$ scan rate . . . . .	76
4.3.8	C-rate test in the $1.5 < E < 4.0 \text{ V}$ vs. $\text{Li}^+/\text{Li}$ window at C/40, C/20, C/10, C/5 and C/2.5 . . . . .	76
4.3.9	Discharge process at C/40 rate to 1.5 V after charging at 4.0 V vs. $\text{Li}^+/\text{Li}$ . . . . .	77
4.3.10	Evolution of specific capacity and coulombic efficiency of CuNP upon cycling by imposing a C/5 rate in the $1.8 < E < 4.0 \text{ V}$ vs. $\text{Na}^+/\text{Na}$ potential window . . . . .	78
4.3.11	(a) Rietveld refinement of pristine CuNP electrode. (b) (002) and (110) Miller planes at different lithiation steps (pristine, 0.4, 0.9 and 0.72 Li-inserted) . . . . .	78

4.3.12	Evolution of the lattice parameters during discharge (left) and graphical representation of the lithiation process (Fe: light- brown; Cu: blue; C: brown; N: light blue; O: red, Li: green) . . . . .	80
4.3.13	Selected <i>operando</i> XAFS spectra at Fe and Cu K-edge during discharge. Pristine and discharged states (0.4 and 0.9 Li-inserted) are shown . . . . .	81
4.3.14	(a) Pre-edge data analysis at the Cu K-edge: evolution of normalized area of three different features (A, B, C) during lithiation. Inset displays the fit performed for the pristine material. (b) Centroid shift for peak B during lithiation. (c) MCR-ALS analysis at the Cu K-edge: concentration profile plot and (d) pure components spectra . . . . .	82
4.3.15	Comparison between pure spectral components and CuNP pristine and discharged states . . . . .	83
4.3.16	Details of the EXAFS fitting for the pristine electrode: single EXAFS contributions for (a) Fe and (b) Cu K-edge, comparing in the bottom part the theoretical and experimental EXAFS signals; Fourier transforms at (c) Fe and (d) Cu K-edge. Relevant EXAFS fitting results: (e) First shell distances: Fe-C, C-N and Cu-N; (f) Pair EXAFS Debye-Waller factors; (g) Variation in Cu-N-C-Fe chains degeneracy during lithiation . . . . .	85
4.3.17	Electrochemical curve during discharge and corresponding IR spectra . . . . .	86
4.3.18	Electrochemical curve during charge and corresponding IR spectra . . . . .	86
4.3.19	FTIR spectra associated with pristine, discharged, and charged states . . . . .	87
4.3.20	DFT-optimized geometries for pristine and lithiated structures up to 4 Li per unit cell . . . . .	90
4.3.21	DFT-computed vibrational frequencies and an example of derived geometries. Note that one lattice cell is made of two formula units . . . . .	91
4.3.22	Comparison between experimental XANES and calculated spectra at Fe K-edge . . . . .	91
4.3.23	Comparison between experimental XANES and calculated spectra at Cu K-edge . . . . .	92
4.3.24	Simulated XANES spectra at Fe K-edge (left) and Cu K-edge (right) during lithiation . . . . .	92
4.4.1	XRD patterns of CuHCF-A and CuHCF-B in the upper panel, compared to PB (4343748-ICSD) and CuHCF's (419454-ICSD) patterns in the bottom panel. Peaks marked with a star match with the aluminium sample holder . . . . .	96

4.4.2	XAFS spectra of CuHCF-A and CuHCF-B. (a) Cu K-edge. (b) Fe K-edge. Here the PB reference at Fe K-edge is also reported . . . . .	96
4.4.3	SEM images for electrodeposited CuHCF-A and CuHCF-B on graphite sheet (a), (b), and carbon cloth (c), (d), respectively . . . . .	97
4.4.4	CuHCF – Method A. Characterization via cyclic voltammetry of the as-synthesized copper hexacyanoferrate. $-0.2 < E < 1.05$ V vs. SCE potential window, $20 \text{ mVs}^{-1}$ scan rate, $0.1 \text{ M KNO}_3$ aqueous solution . . . . .	99
4.4.5	CuHCF – Method B. Characterization via cyclic voltammetry of the as-synthesized copper hexacyanoferrate. $-0.2 < E < 1.05$ V vs. SCE potential window, $20 \text{ mVs}^{-1}$ scan rate, $0.1 \text{ M KNO}_3$ aqueous solution . . . . .	101
4.4.6	Cyclic voltammeteries of electrosynthesized copper hexacyanoferrate in $0.1 \text{ M KNO}_3$ aqueous solution at $20 \text{ mV s}^{-1}$ scan rate. Method A on glassy carbon (a), graphite sheet (c), and carbon cloth (e). Method B on glassy carbon (b), graphite sheet (d), and carbon cloth (f). . . . .	102
4.4.7	Cyclic voltammeteries in aqueous $0.1 \text{ KNO}_3$ solution at different concentrations ( $0.01$ , $0.1$ , $1 \text{ M}$ ) at $50 \text{ mVs}^{-1}$ of electrosynthesized copper hexacyanoferrate: Method A (a), Method B (b). Cyclic voltammeteries in aqueous $0.1 \text{ KNO}_3$ solution at different scan rates ( $500$ , $200$ , $50$ , $20$ , $5 \text{ mV s}^{-1}$ ) of electrosynthesized copper hexacyanoferrate: Method A (c), Method B (d). Insets show curves recorded at a $5 \text{ mV s}^{-1}$ scan rate . . . . .	104
4.4.8	Cyclic voltammeteries of the electrosynthesized CuHCF in the $-0.2 < E < 1.05$ V vs. SCE potential range at a $20 \text{ mVs}^{-1}$ scan rate. Electrochemical signatures in $0.1 \text{ M KNO}_3$ solution, $0.1 \text{ M M}^{n+}(\text{NO}_3)_n$ solution, and again $0.1 \text{ M KNO}_3$ solution after the insertion of $\text{M}^{n+}$ . (a), (b): $0.1 \text{ M NaNO}_{3(\text{aq})}$ ; (c), (d): $0.1 \text{ M Mg}(\text{NO}_3)_{2(\text{aq})}$ ; (e), (f): $0.1 \text{ M Al}(\text{NO}_3)_{3(\text{aq})}$ ; (g), (f): $0.1 \text{ M CsNO}_{3(\text{aq})}$ . Panels (a), (c), (e), (g) refer to CuHCF-A, while panels (b), (d), (f), (h) refer to CuHCF-B . . . . .	107
4.4.9	Cs-insertion (a) and de-insertion (b) in CuHCF-A and CuHCF-B (c,d) . . . . .	109
4.4.10	(a) Chronoamperometry on synthesized CuHCF-A (red line) and CuHCF-B (black line). (b) Calibration curve for both methods . . . . .	110
4.5.1	XRD pattern of TiHCF and its profile matching refinement . . . . .	113

4.5.2	A section of the XRD profile for pristine TiHCF, as well as the cycled electrodes in the reduced and oxidized states . . . . .	114
4.5.3	TG analysis on TiHCF . . . . .	114
4.5.4	Cyclic voltammograms comparing different electrolyte solutions at a constant scan rate of $1 \text{ mV s}^{-1}$ and at a concentration of $0.1 \text{ M}$ . . . . .	115
4.5.5	Voltammograms taken at varying electrolyte concentration for $\text{KNO}_3$ (left) and $\text{NaNO}_3$ (right) . . . . .	116
4.5.6	Voltammograms taken at varying potential window for $\text{KNO}_3$ (left) and $\text{NaNO}_3$ (right)	117
5.0.1	Electrochemical tests on CoNP. CV (left) recorded in the $0.2 < E < 2.5 \text{ V}$ vs. $\text{Li}^+/\text{Li}$ at $0.1 \text{ mV/s}$ scan rate; and GCPL (right) recorded in the same potential window at different current rates ( $2\text{C}$ , $5\text{C}$ , $10\text{C}$ , $20\text{C}$ ) . . . . .	123
5.0.2	GCPL on MnHCF at $\text{C}/10$ rate in the $2.0 < E < 4.0 \text{ V}$ vs. $\text{Na}^+/\text{Na}$ potential window (top panel), and Mn K-edge evolution during the first charge (bottom panel) . . . . .	124

## List of Tables

3.3.1	Summary of the two-steps methods used for the electrodeposition of CuHCF . . . . .	40
3.5.1	Working parameters for <i>operando</i> experiments . . . . .	44
4.1.1	Correspondence between collected spectrum number and extracted/inserted ion equivalents . . . . .	53
4.2.1	Correspondence between extracted/ inserted ion equivalents and spectrum number in case of <i>operando</i> XAFS . . . . .	63
4.3.1	List of samples, Yield, TGA features, and chemical analysis by XRF and CHN . . . . .	71
4.3.2	Results of the profile matching on the synthesized batches. The water content is added as last column . . . . .	73
4.3.3	Wyckoff positions, site symmetries and multiplicity of atoms in the CuNP unit cell . . . . .	79
4.3.4	Fit goodness relative to the XRD data treatment . . . . .	80
4.3.5	Correspondence between the number of lithium per unit cell ( $Z=2$ ), electrochemically reacted lithium per CuNP formula unit, and number of unpaired electrons per cell . . . . .	89
4.4.1	EDX Analysis. Cu:Fe ratios for different CuHCF deposited on graphite sheet and carbon cloth . . . . .	98
4.4.2	CuHCF. Methods A, B. Differences in anodic ( $\Delta I_a$ ) and cathodic ( $\Delta I_c$ ) peak intensity in 0.1 M $KNO_3$ solution between prior and after insertion of $M^{n+}$ salt . . . . .	108
4.4.3	Sensitivity and linearity range for hydrogen peroxide detection. L.O.D. stands for limit of detection, while L.O.L. stands for limit of linearity . . . . .	110

4.5.1	Conditions pertaining to the pristine, oxidized, and reduced states of the XRD analyte.	
	Potentials were selected with help from completed cyclic voltammograms in $\text{KNO}_3$	113
4.5.2	Results of the EXAFS fitting procedure on FeCo	118
4.5.3	Results of the EXAFS fitting procedure on CuHCF	119
4.5.4	Results of the EXAFS fitting procedure on CuNP	120

# Abbreviations

<b>AM</b> Active material	<b>MCR</b> Multivariate curve resolution
<b>ALS</b> Alternating least square	<b>MHCF</b> Metal hexacyanoferrate
<b>ATR</b> Attenuated total reflection	<b>MHCM</b> Metal hexacyanometalate
<b>CB</b> Carbon black	<b>MnHCF</b> Manganese hexacyanoferrate
<b>CE</b> Counter electrode	<b>NMP</b> N-methylpyrrolidone
<b>CoNP</b> Cobalt nitroprusside	<b>PB</b> Prussian blue
<b>CuNP</b> Copper nitroprusside	<b>PBA</b> Prussian blue analogue
<b>CuHCF</b> Copper hexacyanoferrate	<b>PC</b> Propylene carbonate
<b>CV</b> Cyclic voltammetry	<b>PTFE</b> Polytetrafluoroethylene
<b>DFT</b> Density functional theory	<b>PVDF</b> Polyvinylidene fluoride
<b>DMC</b> Dimethyl carbonate	<b>RE</b> Reference electrode
<b>EC</b> Ethylene carbonate	<b>SEM</b> Scanning electron microscopy
<b>EDX</b> Energy dispersive X-ray spectroscopy	<b>TiHCF</b> Titanium hexacyanoferrate
<b>EV</b> Electric vehicle	<b>VGCF-H</b> Vapour grown carbon fibers-high density
<b>EXAFS</b> Extended X-ray absorption fine structure	<b>WE</b> Working electrode
<b>FeCo</b> Potassium iron hexacyanocobaltate	<b>XAFS</b> X-ray absorption fine structure
<b>FTIR</b> Fourier transform infrared spectroscopy	<b>XANES</b> X-ray absorption near edge spectroscopy
<b>GCPL</b> Galvanostatic cycling with potential limitation	<b>XRD</b> X-ray diffraction

*When wireless is perfectly applied the whole earth will be converted into a huge brain, which in fact it is, all things being particles of a real and rhythmic whole. We shall be able to communicate with one another instantly, irrespective of distance. Not only this, but through television and telephony we shall see and hear one another as perfectly as though we were face to face, despite intervening distances of thousands of miles; and the instruments through which we shall be able to do this will be amazingly simple compared with our present telephone. A man will be able to carry one in his vest pocket.*

Nikola Tesla

# 1

## Introduction

### 1.1 ENERGY DEMAND AND ENERGY STORAGE

THERE'S SOMETHING IN COMMON among all technological devices in our daily life, such as laptops, tablets, smartphones, instruments, flashlights, watches, other wearable devices, *e.g.* heart rate monitors and implanted medical devices, and so on. A device called battery.

Despite the given examples, a battery is not thought only for hand-held and portable devices, but also for stationary applications, *i.e.*, emergency power, local energy storage, remote relay stations, communication base stations, as well as electric vehicles (EVs).

Batteries are generally seen as black boxes of different sizes, which can be toxic, flammable, and hazardous. What this black box contains determines the application and the performance of the battery device. A battery is formed by several stacked cells, connected in a precise fashion in order to deliver

an appropriate voltage and/or current. These cells can be either *primary* or *secondary* in case the device should be disposed after the first discharge or can perform many discharge/charge cycles, respectively. The latter kind is commonly called rechargeable, and is nowadays of great research and industrial interest. Within this framework, Li-ion batteries have gained considerable attention due to the high performance and affordable costs, experiencing a tremendous growth in the battery market, which in total was \$65 billion worth in 2015. Additionally, the major part of the investments is addressed to the research of Li-ion batteries [3].

A battery is a device that converts chemical energy into electrical energy during discharge, viceversa electrical energy should be applied in the charge step to restore the initial chemical system. The design of a rechargeable battery is the compromise of different specifications and requirements, and the balance between several parameters, making this research a multi-disciplinary subject.

Three different classes of parameters can be identified: **sustainability** (*i.e.*, cost, availability, safety, recycle), **reaction dynamics** (*i.e.*, rate and cycle capabilities, power density), and **energy density** (specific capacity and working potential window). The research on battery systems is focused in all these three areas, while their interconnection is needed for the development of a good rechargeable battery.

**Sustainability** plays a key role in the development of a device that has to supply the growing demand of technologies. In 2016 2 billion of smartphones (+500% compared to 2000), 195 million of tablets, 165 million of portable PCs have been sold. Thanks to the optimization of the industrial processes and the costs abatement, the price of lithium, hence of portable devices, has dropped from 2.6\$/Wh in 2000 to 0.15\$/Wh in 2006 [3], while Li-ion batteries market has experienced a dramatic increase of 500% since year 2000.

EVs sales have also experienced a huge growth, 2 million of vehicles being sold in 2016 (+60% than 2015) [4]. In this context, the costs and availability of all the components constituting the battery is fundamental to meet the requirements of sustainability. In a typical lithium-ion battery (Section 2.1), lithium and cobalt are critical materials for different reasons.

As stated in the EU Critical Raw Materials Factsheets [5]:

*Cobalt is predominantly extracted as a by- or co-product of nickel or copper mining. The Cobalt Development Institute states that approximately 50% of global supplies of cobalt come from the nickel mining industry, whilst 44% is sourced from copper mining and only 6% from mining operations where cobalt is the primary objective.*

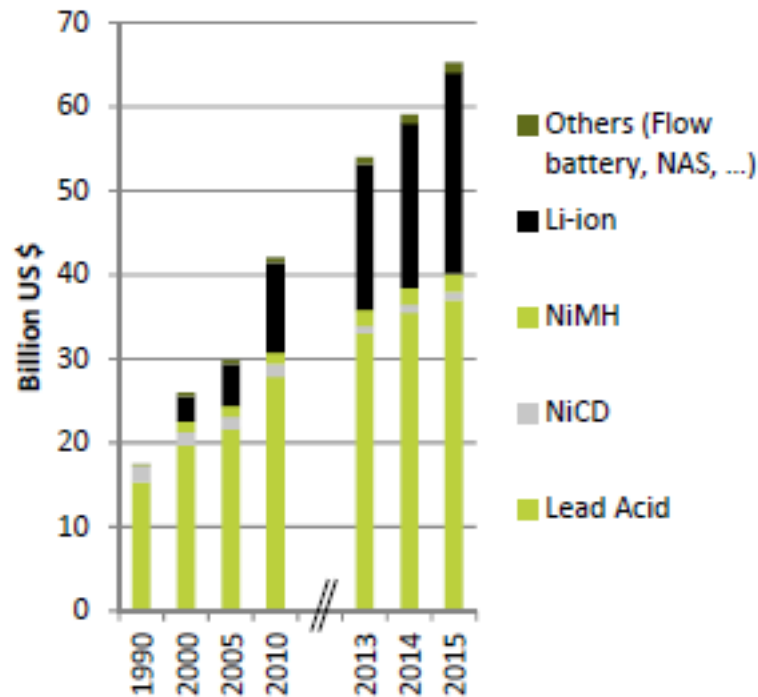


**Figure 1.1.1:** Battery market. Source: Avicenne Energy, 2016

Globally, cobalt is mined in 19 countries, as shown in Figure 1.1.2, with the largest producers being the Democratic Republic of Congo (with 64% of the global total, based on a five-year average over 2010-2014), China (6%) and Canada (5%). The world mine production of cobalt is about 135.5 thousand tonnes in average over the period 2010-2014 (BGS, 2016). Within the EU, cobalt is mined in New Caledonia (France) and Finland (respectively 2% and 1% of the global total). Additionally: There is no single source of comprehensive evaluations for resources and reserves that apply the same criteria to deposits of cobalt in different geographic areas of the EU or globally.

On the other side, lithium can be found mainly in pegmatite type deposit and brine deposit. Statistics reported in reference [6] shows that in 2014 the worldwide lithium reserves amounted to a total of 13.5 million tons which would allow the global lithium production to last for more than 360 years with an annual lithium output of 37000 tons. Around 59% of lithium is located in the "lithium triangle" (Chile, Bolivia and Argentina). Concerning lithium reserves (Figure 1.1.3), Chile is at first position with a reserve volume of 7.5 million tons, accounting for almost one third of the global volume. Bolivia, making up 24% of the total, comes next, followed by China with 3.5 million tons of lithium reserves. Argentina ranks as fourth, providing for 1.5 million tons thanks to the saline lakes. In recent years, an increasing demand of lithium has led to the discovery of lithium deposits and to an increase of lithium

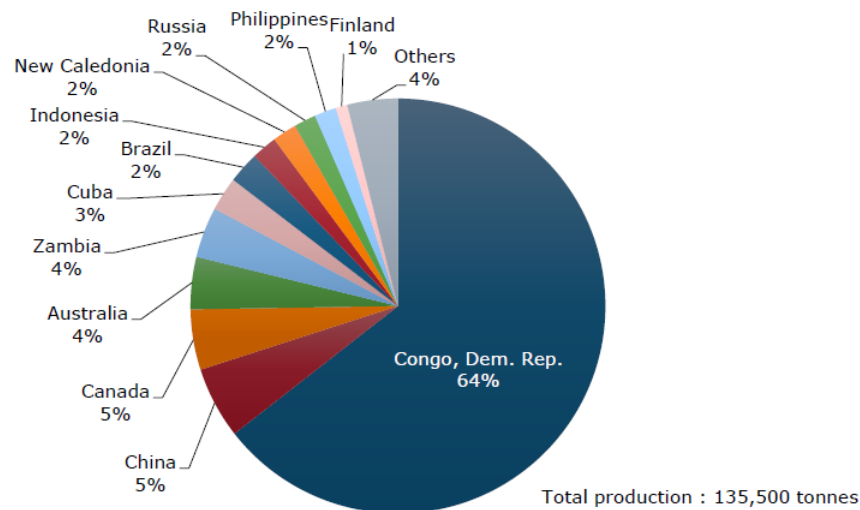


**Figure 1.1.2:** Global cobalt mine production, figures are percentage of global total, based on average production during 2010–2014 (Data from BGS World Mineral Statistics database; BGS, 2016). Other countries include (in order of production size) Morocco, South Africa, Madagascar, Papua New Guinea, Uganda, Botswana and Zimbabwe. Reprinted from Study on the review of the list of critical raw materials. ©European Union, 2017

reserves and resources, making it appear in the last EU survey for non critical raw materials [5], where its criticality was stated in the previous report.

However, lithium has safety issues regarding its reactivity towards oxidizing agents, besides dendrites formation. Being lithium an alkali metal, and specifically the most electropositive metal, the tendency to oxidize to  $\text{Li}^+$  is high. In such a situation, and in case of a closed system such as in a battery, the heat deriving from the exothermic reaction and the gases released are the causes of a potential explosion. New alternative strategies involving the replacement of lithium are currently studied and evaluated. Within this framework, other alkaline metals are being investigated for battery use (primarily sodium) as well as aqueous systems, which would cut down the safety hazard regarding Li-ion batteries. These alternative solutions aimed to replace lithium in current technologies belong to the so-called post-lithium strategy. Besides the availability concern, climate change is a global issue as pointed out in the 2015 Paris Climate Agreement. The global challenge responding to the need of lowering greenhouse gases (GHGs) emissions might be focusing on carbon emissions in the transportation and electricity generating sectors [7, 8]. In March 2012 the U.S. President Obama launched the EV Everywhere Grand Challenge [9] with the visionary intent to be the first nation in the world to produce plug-in electric vehicles that are as affordable for the average American family as gasoline-powered vehicles within the next 10 years, being an effort to recruit and inspire America's best and brightest individuals to join in this challenge.

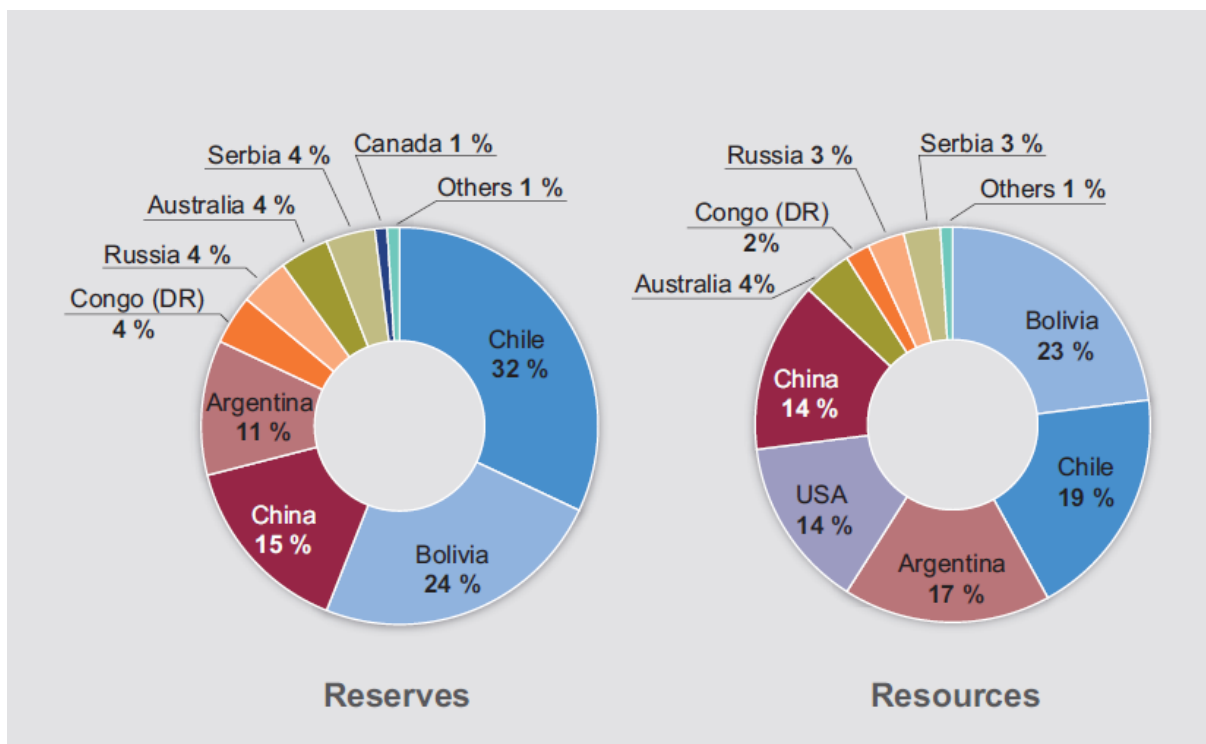


**Figure 1.1.3:** Lithium reserves and resources. Reprinted from Supply and Demand of Lithium and Gallium. ©Cui Rongguo, 2016

In this context, worldwide efforts towards fast charging have been doing together with the development and the financial support of a commensurate power grid. According to the International Energy Agency (IEA), Norway provides electric vehicle supply equipment (EVSE) public funding for fast-charging stations every 50 km (on average) on main roads [10]. In September 2018 the U.S. Department of Energy (DOE) announced the selection of 42 projects totaling \$80 million, where \$31.9 million were destined to develop technologies to recharge multiple electric vehicles quickly and at very high “extreme” power levels [11]. From the funding, it appears clear that fast charging and fast **reaction dynamics** offer room for improvement, however, the scientific efforts are headed to the right direction.

The **energy density** of a battery is mainly determined by the specific capacity of both positive and negative electrodes, as well as their operating potentials. For this reason, the research based on the improvement of energy density has been predominantly carried out on active materials. Solvent, electrolyte, additives, separator, and binder have in this sense a smaller contribution to the development of a high energy battery device.

A class of active materials is represented by Prussian blue analogues (Section 1.2), main focus of the present work.

## 1.2 PRUSSIAN BLUE ANALOGUES

Prussian blue (PB), named also ferric ferrocyanide, iron(III) hexacyanoferrate(II), and Milori Blue, was first synthesized accidentally in 1704 by Heinrich Diesbach of Berlin, assuming originally the name of *Berliner Blau*. The involuntarily finding arose from the preparation of crimson lake color and was based on the contamination of potash (potassium carbonate) by the “animal oil” elixir of the alchemist Johann Konrad Dippel, which was the source for the cyanide building block in PB. PB is the first synthetic coordination compound which has replaced as blue pigment the much more expensive *lapis lazuli* [12]. After its discovery, it was extensively used in painting, wallpaper, flags, postage stamps, tea colorant, and became the official uniform color of the Prussian Army [13]. Even Van Gogh probably used it in his masterpiece *Starry Night* (Figure 1.2.1).



**Figure 1.2.1:** Van Gogh's *Starry Night*. Van Gogh probably used the Prussian Blue pigment. Available at Wikimedia Commons free repository

The crystal structure of this compound (Figure 1.2.2) has been first investigated in 1936 through X-ray diffraction by Keggin and Miles [14]. They reported:

[..] The iron atoms are arranged, ferrous and ferric alternately, at the corners of a cubic lattice of 5.1 Å edge, and the CN groups lie in the edges of these small cubes. The alkali atoms occur at the centres of alternate small cubes. [..]

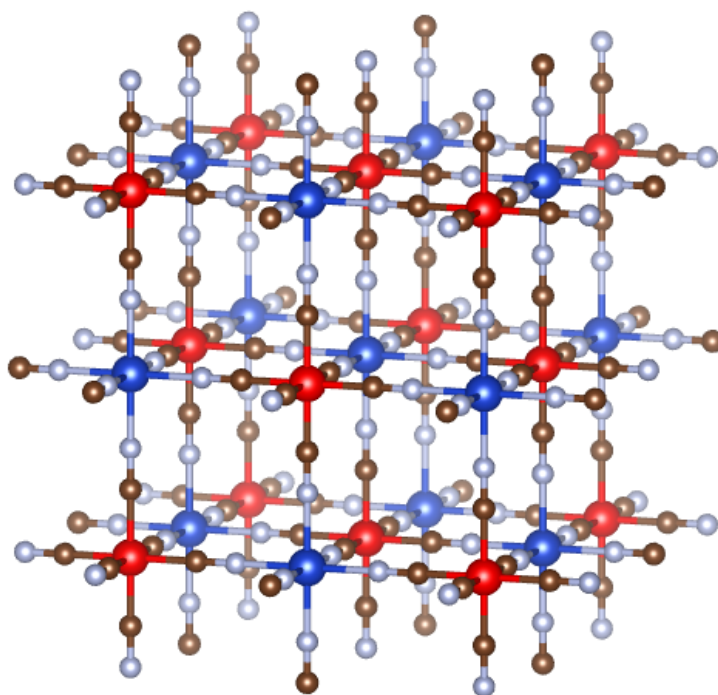


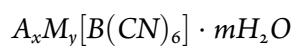
**Figure 1.2.2:** Crystal structure of PB. Fe<sup>II</sup> labeled as red, Fe<sup>III</sup> as blue, C as brown, and N as light blue

Buser *et al.* [15] further investigated this peculiar compound which revealed a cubic elementary cell (cell length of about 10 Å) and an exceptionally low density (roughly 1.8 g cm<sup>-3</sup>) compared to other iron salts (>3 g cm<sup>-3</sup>). This is due to the fashion iron atoms are linked together and to the presence of cavities, tunnels and vacancies throughout the 3D-dimensional lattice.

PB can exist in two different forms, namely “soluble” and “insoluble”, characterized by the general formula  $KFeFe(CN)_6$  and  $Fe_4[Fe(CN)_6]_3$ , respectively. Despite their names, both forms are insoluble in water, deriving these appellatives from the tendency to form colloidal suspension. Structurally speaking, the soluble PB, *i.e.*, the one originally proposed by Keggin and Miles, presents a highly ordered structure with alternating iron species in octahedral environment connected through cyanide bridges in an ideally infinite 3D crystal lattice. Contrarily, the insoluble form is distinguished by the absence of

$[Fe(CN)_6]^{4-}$  units and their replacement by water molecules and alkali cations, which explains also the dissimilarity in stoichiometry compared to the soluble form. Concerning the insoluble PB, the vacant sites can be either randomly or systematically distributed, the casual vacancies leading to a face centred cubic crystal shape (Space group  $225 Fm-3m$ ), while the non-random distribution to a cubic primitive or lower symmetry lattice (Space group  $221 Pm-3m$ ) [15, 16]. In other words, the casual allocation of vacant sites increases the apparent symmetry of the lattice shape. The crystal space group has been found to be influenced by synthesis conditions and post-synthesis treatments, given that a slow crystallization led to a non-statistical arrangement of the vacancies, and that this ordering can be partially destroyed by dehydrating and heating the sample [15].

The typical interatomic distances in PB are  $Fe^{II}-C = 2.00(4)$  Å,  $Fe^{III}-N = 1.98(4)$  Å, and  $C-N = 1.10(5)$  Å [15], being the iron species  $Fe^{II}-Fe^{III}$  distance roughly  $5.1$  Å, as Keggin and Miles reported. The cubic cell is, however, constituted by four of such cubes, resulting in a lattice length of about  $10.2$  Å, which corresponds to the distance of two consecutive  $Fe^{II}-Fe^{II}$ . The atoms arrangement guarantees enough space to accommodate water molecules and ions inside the zeolitic channels of approximately  $3$  Å, as well as in the cavities of about  $5$  Å arising from  $[Fe(CN)_6]^{4-}$  vacancies. Hence, the cubic open framework is formed by  $-CN-Fe^{III}-N-C-Fe^{II}-$  units, being the  $Fe^{II}$  in the  $4a$  (or  $1a$ ) Wyckoff position, the  $Fe^{III}$  in  $4b$  (or  $1b$ ), the C and N in  $24e$  (or  $6e$ ), and the alkali metals at the cube centre in  $8c$  (or  $8g$ ), if a  $Fm-3m$  (or  $Pm-3m$ ) symmetry is considered. Moreover, neutron diffraction [17] revealed the presence of two crystallographically and chemically distinct (deuterated) water molecules within the structure, where the first is part of the  $Fe^{III}$  coordination shell and fills empty nitrogen sites of the  $[Fe(CN)_6]^{4-}$  vacancies, while the second kind occupies interstitial positions as alkali ions and represents uncoordinated water. Metal hexacyanometallates (MHCMs) or Prussian blue analogues (PBAs) have general formula:



where M and B are transition metals, A is an alkali ion, x and y are stoichiometric coefficients and depend on the presence of vacancies, while m is the number of water molecules in the structure. In case of metal hexacyanoferrates (MHCFs), B is represented by iron. Transition metals M and B are linked through cyanides in a precise fashion, the M metal bound to the N-end, whilst the B metal to the C-end, constituting the repeating  $-CN-M-NC-B-$  unit. The orthogonal and almost linear  $-CN-M-NC-B-$

atomic chains, coupled to a high degeneration and short intermetallic distance, make PBAs a prototype for the study of highly ordered electron scattering contributions [18, 19]. As in the case of PB, the lattice shape is generally cubic with few exceptions [20, 21], while the lattice length is commonly around 10 Å and depends on structural metals' size, their oxidation states and moisture degree. Therefore, the –CN–M–NC–B– fragment can be finely tuned by changing for instance metallic species to define and modulate a series of physico-chemical properties that are herein briefly introduced.

PBAs are classified as mixed-valence compounds [22] for the metal-to-metal charge transfer that occurs, which is the cause for instance of the blue color of PB. By tuning the oxidation state of the iron species in PB, Everitt's salt (white colored) or Berlin green can be obtained, the iron species being both divalent or trivalent, respectively. Generally, the modulation of oxidation states can be achieved through the synthesis. Synthesis of MHCFs is commonly based on bulk co-precipitation methods in aqueous medium, where  $[\text{Fe}(\text{CN})_6]^{3-/4-}$  and  $\text{M}^{n+}$  salts are simultaneously mixed under constant stirring to yield a precipitate, easily recovered by filtration [23–25]. Although the synthesis might appear "easy", the critical point is the reproducibility. The number of vacancies and incorporated alkali ions, hence the stoichiometry, may vary even if repeated with the same starting reagents. Only the optimization and control of all parameters contributing to the synthesis can lead to a reproducible product.

An alternative synthetic procedure is based on electrochemical routes [26–30], whose advantage consists in the functionalization of a conductive substrate with a thin film, characterized by an extended active area per surface and further modifiable through polarization of either a current or potential. Also in this case, the product reproducibility is a difficult achievement.

PBAs have been widely synthesized for several applications, for instance analyte sensors [31], magnetic devices [32], electrochromism [33], charge storage [34], and ion-exchange sieves [35], and even antibacterial agents against *Escherichia coli* and *Staphylococcus aureus* [36]. The employment in the cited technological applications are related to the structure of PBAs and the activity of the constituting metals.

The peculiar zeolitic structure of MHCFs which allows for the flux of different ions into the channels of the tri-dimensional network, coupled to the redox activity of the metals, such as Cu and Fe in copper hexacyanoferrate (CuHCF), permits the use of MHCFs in electrocatalysis toward the oxidation of several organic analytes, and therefore the fabrication of amperometric sensors has been proposed for instance

for ascorbic acid [37], cysteine [38] and dopamine [39]. PB films were found to be excellent catalysts for hydrogen peroxide reduction in the presence of O<sub>2</sub>, with selectivity and activity close to those of peroxidase modified electrodes [40, 41], while a review on PB-based sensors and biosensors has been recently reported [42]. Among MHCs the copper analogue has been widely studied and its electrocatalytic properties have been investigated by many research groups. De Mattos *et al.* [43] described a hydrogen peroxide sensor by using a CuHCF-modified carbon paste electrode. Baioni *et al.* studied the electrocatalytic properties of CuHCF nanoparticles deposited by electrostatic layer-by-layer technique [44]. Brett *et al.* underlined the role of the H<sub>2</sub>O<sub>2</sub> determination in the development of biosensors, as it is a by-product of the reaction catalyzed by oxidase enzymes [45]. Photoinduced magnetization was first observed by Sato *et al.* [32] in cobalt hexacyanoferrate (CoHCF), where magnetization was controlled via photoirradiation, causing the variation in oxidation number of the transition metal ions through an internal photochemical redox reaction. The starting hexacyanoferrate was constituted by the Co<sup>III</sup>-NC-Fe<sup>II</sup> fragment, characterized by low spin Co(III) ( $t_{2g}^6$ , S = 0) and low spin Fe(II) ( $t_{2g}^6$ , S = 0). The irradiation through red light was responsible for the change in spin states, hence in magnetization value, inducing the system to change into Co<sup>II</sup>-NC-Fe<sup>III</sup>, characterized by high spin Co(II) ( $t_{2g}^5 e_g^2$ , S = 3/2) and low spin Fe(III) ( $t_{2g}^5$ , S = 1/2). The process could be partially inverted by illuminating the system with an incident blue light. Besides, spin transition at the Co site can be induced not only by photoirradiation, but also by an anatase-driven stimulus, as reported by Giorgetti *et al.* [46].

Berrettoni *et al.* adopted a new notation for the Fe–Co system in CoHCF, suggesting the use of the (FeCo)<sup>ox number</sup> notation for the oxidation state, which represents the actual situation where Co<sup>II/III</sup> and Fe<sup>II/III</sup> metal ions coexist at different ratios [46, 47].

Electrochromism is the property of certain materials to change color when placed in an electric field. This is stimulated by redox reactions and forms the basis for electrochromic devices, such as electrochromic displays. Neff *et al.* [48] studied in 1981 the electrochromic properties of a thin film of PB in the form of KFeFe(CN)<sub>6</sub> deposited on a conductive substrate. During reduction they observed the formation of Everitt's salt (K<sub>2</sub>FeFe(CN)<sub>6</sub>), while during oxidation the shift to Berlin green (K<sub>x</sub>FeFe<sup>III-x</sup>(CN)<sub>6</sub>; x < 1) by adopting KCl or K<sub>2</sub>SO<sub>4</sub> aqueous solutions. Furthermore, they noticed that potassium ion migration into or out of the film was associated with the redox reactions, being the potassium inserted during reduction, and extracted in the oxidative step. Electrochromism is a common feature in PBA materials,

such as ruthenium purple (iron hexacyanoruthenate) [49], vanadium hexacyanoferrate [50], CuHCF [51], palladium hexacyanoferrate [52], and it is always accompanied with redox reactions of the transition metals and migration of ions to achieve charge neutrality.

The migration of ions occurring together with the change in oxidation state can have several applications, like wastewater treatment, desalination, and building energy storage devices. PBAs are able to host monovalent, divalent and trivalent ions (for instance  $Rb^+$ ,  $Pb^{2+}$ ,  $Al^{3+}$ ,  $Y^{3+}$ ) with a good cycle stability and fast kinetics [53], thanks to the presence of vacancies and water molecules within the structure, which allow for the reversible exchange/insertion of multivalent ions.

PBAs, and in particular MHCFs, have gained considerable attention among insertion materials due to the ease of preparation and separation, effectiveness as electrode materials, and wide versatility towards several ions, ranging from monovalent ions such as lithium [54], sodium [55, 56], potassium [57, 58], to divalent and trivalent ions, for instance calcium [59], magnesium [60] and aluminum [61].

### 1.3 PBAS AS BATTERY MATERIALS - A BRIEF OVERVIEW

The redox and structural properties of PBAs responsible for exchange/insertion processes make this class of materials suitable to be employed as electrode materials in batteries. Several studies have been developing PBA-based electrodes in both organic and aqueous media, by using a wide range of ions as intercalating agents. This section does not aim to be an exhaustive review of the works employing PBAs as battery materials, instead, the purpose is to give a concise overview of the state of art.

The safety, environmental and cost issues of carbonate based solvents in Li-ion batteries could be overcome with the use of aqueous alternatives, as mentioned in Section 1.1. On the other side, such options are characterized by a limited and narrow electrochemical stability window (1.23 Volts at pH = 0). However, this window might be potentially expanded by using the so-called water-in-salt solutions, *i.e.*, highly concentrated aqueous electrolytes. Suo *et al.* [62] reported in *Science*, for instance, a full lithium-ion battery of 2.3 Volts using such an aqueous electrolyte. Similarly, Nakamoto *et al.* [63] employed a 17M  $NaClO_4$  aqueous solution, adopting  $Na_2MnFe(CN)_6$  hexacyanoferrate as cathode and  $NaTi_2(PO_4)_3$  as anode, extending the potential stability window to roughly 2.8 Volts, hence reaching extreme potentials at which additional redox reactions may take place.

Low-defect Prussian blue has been recently proposed as high performant cathode material in aqueous Na-ion batteries [64]. Figure 1.3.1 reports the highlights of the electrochemical characterization of the formulated electrode based on  $\text{FeFe}(\text{CN})_6$  material. The electrochemical measurements have been performed in 1 M  $\text{Na}_2\text{SO}_4$  aqueous solution, by adopting Ag/AgCl as reference electrode and a large piece of activated carbon as counter electrode. Panel a shows the cyclic voltammogram recorded on the studied material, featuring a couple of well-separated redox processes, attributed to the distinct iron sites in the structure. The respective charge/discharge profile (cf. panel b) clearly shows a correspondence between the insertion/extraction plateaux and the voltammetric peaks, evidencing two distinguishable insertion/extraction processes at +0.8/ +1.0 V and +0.10/ +0.15 V. The resulting reversible capacity reaches 125 mAh/g, to which corresponds roughly 1.4 Na/ formula unit. The rate performance and long-term cycle life are reported in panels c and d, respectively. The high efficiency and rate capability of the electrode (102 mAh/g delivered at 20C rate) are coupled to a good cyclability, even if performed at high rates (10C rate in this case) with a 83% retention of the initial capacity (108 mAh/g  $\rightarrow$  89 mAh/g). Another system here presented is an aqueous-based full cell where both electrodes are metal hexacyanometallates [65]. In this work published on *Nature Communications*, the authors adopted copper hexacyanoferrate as positive electrode, manganese hexacyanomanganate as negative electrode, and 10 M  $\text{NaClO}_4$  as electrolyte. The positive electrode was operating between  $0.85 < E < 1.15$  V vs. SHE (standard hydrogen electrode), while the negative electrode between  $-0.2 < E < 0.2$  V vs. SHE, resulting in a full cell working in the 0.65-1.35 V with a mid-discharge potential at 0.95 V. The striking feature about this cell was not the delivered specific capacity (roughly 27 mAh/g at 1C), instead, the high power density and long-cycle life, featuring 693 W/kg as specific power and 84.2% of energy efficiency when cycled at 50C current rate. The coulombic efficiency at 10C rate was 99.8%, while cycling at these conditions did not produce any capacity loss, which was stable at roughly 23 mAh/g.

Although the performance of this system appears interesting under some aspects, the cost of the reagents are prohibitive for an affordable device. Even though the authors declared the reagents are low-cost, potassium hexacyanomanganate is >400 times more expensive (Santa Cruz Biotechnology database) than potassium hexacyanoferrate (Sigma-Aldrich database), being only the latter economically affordable. Further issues concerning the safety and transport make hexacyanomanganate anion an undesirable building block for energy storage devices. To the best of our knowledge, this is in fact one of the few

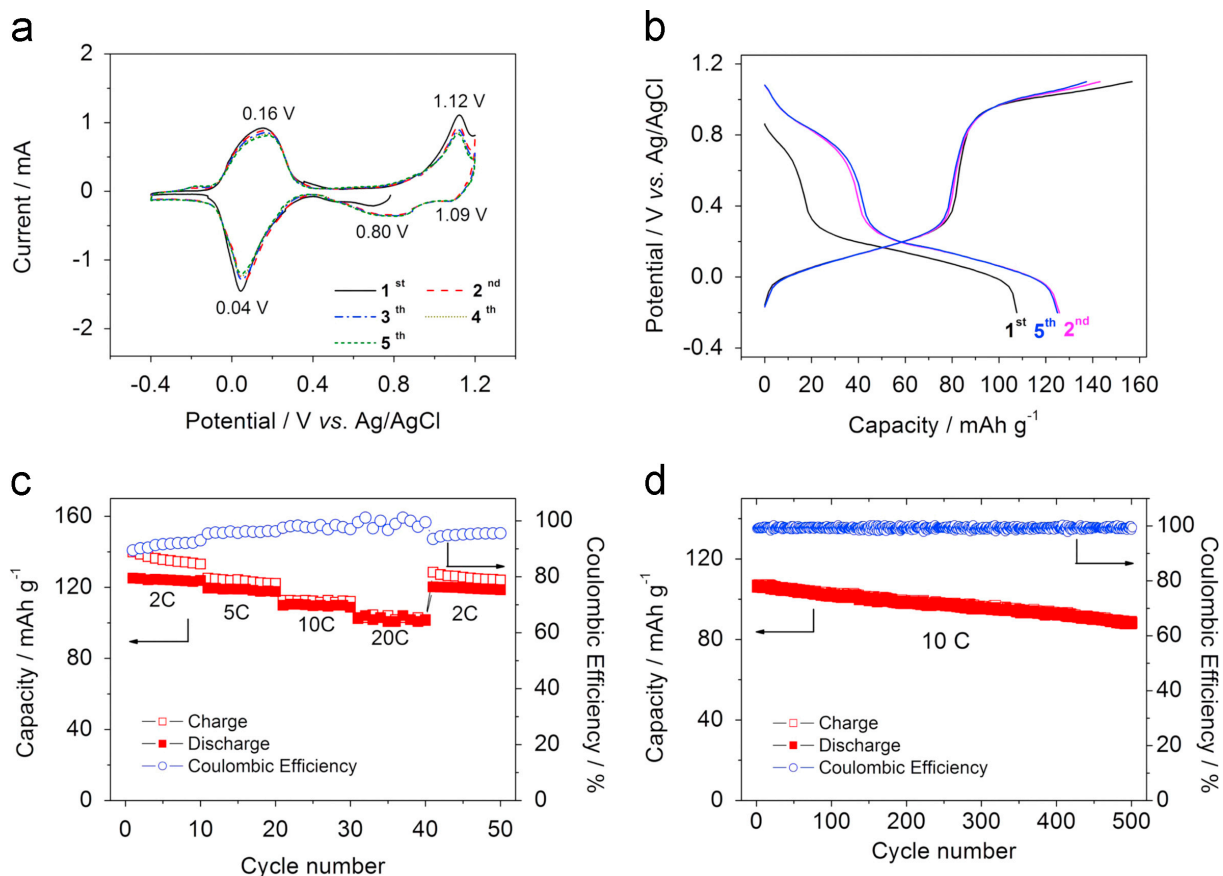


**Figure 1.3.1:** Electrochemical characterizations of the FeFe(CN)<sub>6</sub> electrode: (a) CV curves measured at a scan rate of 1 mV/s, (b) charge and discharge profiles at a current density of 250 mA/g, (c) rate performance and (d) long-term cycling stability 10C rate. (1C= 125 mA/g). Reuse from Low-defect Prussian blue nanocubes as high capacity and long life cathodes for aqueous Na-ion batteries. *Nano Energy*, 13, 117–123, 2015. Copyright 2015, with permission from Elsevier

studies proposing hexacyanomanganate as battery material. Another example is reported by the same research group in *Nature Communications* [66].

Contrarily, copper hexacyanoferrate is constituting by low-cost building blocks and has attracted much attention because of its electrochemical performance. A study adopting it as working electrode in a flooded three-electrode cell [67], containing 1M KNO<sub>3</sub> at pH = 2, Ag/AgCl as reference electrode and a mass in excess of partially reduced copper hexacyanoferrate or Prussian blue, evidenced an excellent long-term cycling (40k cycles) at 17C rate, retaining 83% of its initial capacity (roughly 40 mAh/g at the end of cycling) with a 99.7% coulombic efficiency. Moreover, the capacity retention at high current densities is exceptional compared to other commonly used materials, being able to sustain a 83C rate and delivering about 40 mAh/g (67% of the initial capacity, that is 59 mAh/g). The electrochemical process is accompanied by negligible lattice strain, since the cubic lattice parameter varies less than 1%

upon cycling.

Copper hexacyanoferrate has been employed in several electrolytes, for instance aqueous  $\text{NaNO}_3$  solution [25],  $\text{Na}_2\text{SO}_4$  solution [68],  $\text{Al}_2(\text{SO}_4)_3$  solution [61],  $\text{ZnSO}_4$  solution [69, 70], as well as organic electrolytes containing Li-ion [71, 72], Na-ion [73, 74], Ca-ion [75], Mg-ion [76].

In similar manner, nickel hexacyanoferrate has been proposed as cathode material in both aqueous [57, 77–79] and organic [24, 60, 72, 80] media.

A remarkable work has been carried out by Goodenough's research group, who studied several MHCs as Na-ion hosts in organic medium, by varying the metal M ( $M = \text{Mn}, \text{Co}, \text{Ni}, \text{Cu}, \text{Zn}$ ) [56, 73]. By considering the generic formula  $\text{KMFe}(\text{CN})_6$  and after studying the magnetic susceptibility of the compounds,  $\text{Fe}^{\text{III}}$  was found in its low-spin state ( $t_{2g}^5 e_g^0, S = 1/2$ ), while  $M = \text{Mn}, \text{Co}, \text{Ni}, \text{Cu}, \text{Zn}$  metals have, respectively spins  $S = 5/2$  (high-spin configuration),  $3/2$  (high-spin configuration),  $1, 1/2, 0$ . Figure 1.3.2 shows the electrochemical behavior of  $\text{KMFe}(\text{CN})_6\text{-Na}$  cells at the third cycle with a current of  $C/20$  in the range 2.0 to 4.0 V vs.  $\text{Na}^+ / \text{Na}$ . The reversible (de)insertion of Na has been appreciated in all analogue materials, being some  $\text{K}^+$  ions removed as well as  $\text{Na}^+$  ions during charge. For this reason, the charge capacity overcomes the one recorded during discharge. The reversible capacity ranges from roughly 35 mAh/g when  $M = \text{Zn}$ , while it increases to >50 mAh/g if  $M = \text{Mn}, \text{Co}, \text{Ni}, \text{Cu}$ , reaching a maximum of roughly 100 mAh/g for  $M = \text{Fe}$ .

Further research on sodium-rich manganese hexacyanoferrate led to specific capacity improvements in Na-ion organic electrolyte. Moritomo's team [81] reported the electrochemical performance of a sodium manganese ferrocyanide film, characterized by a fast and reversible ion (de)insertion with good long-term cycling stability and high efficiency, while another study featured the electronic/ structural properties of mixed Mn-Co hexacyanoferrates [82]. The cathode materials displayed in both studies a double-plateau, one ascribed to the  $\text{Fe}^{\text{III}}/\text{Fe}^{\text{II}}$  couple, the other to the  $\text{Mn}^{\text{III}}/\text{Mn}^{\text{II}}$  or  $\text{Co}^{\text{III}}/\text{Co}^{\text{II}}$  redox couples. Figure 1.3.3 reports another work of Goodenough's group, showing the difference in electrochemical profiles between the air-dried (left) and vacuum-dried (right) hexacyanoferrate. The first case well agrees with the previous reports (two plateaux are visible and the obtained capacity is roughly the same), while the latter led to the efficient removal of interstitial water and superior capabilities as cathode material. Vacuum-dried  $\text{Na}_{2.8}\text{MnHCF}$  exhibits an extremely narrow potential range where the redox takes place, and very reversible exchange abilities ( $E_{\text{charge}} = 3.53 \text{ V}$ ;  $E_{\text{discharge}} = 3.44 \text{ V}$ ). Besides,

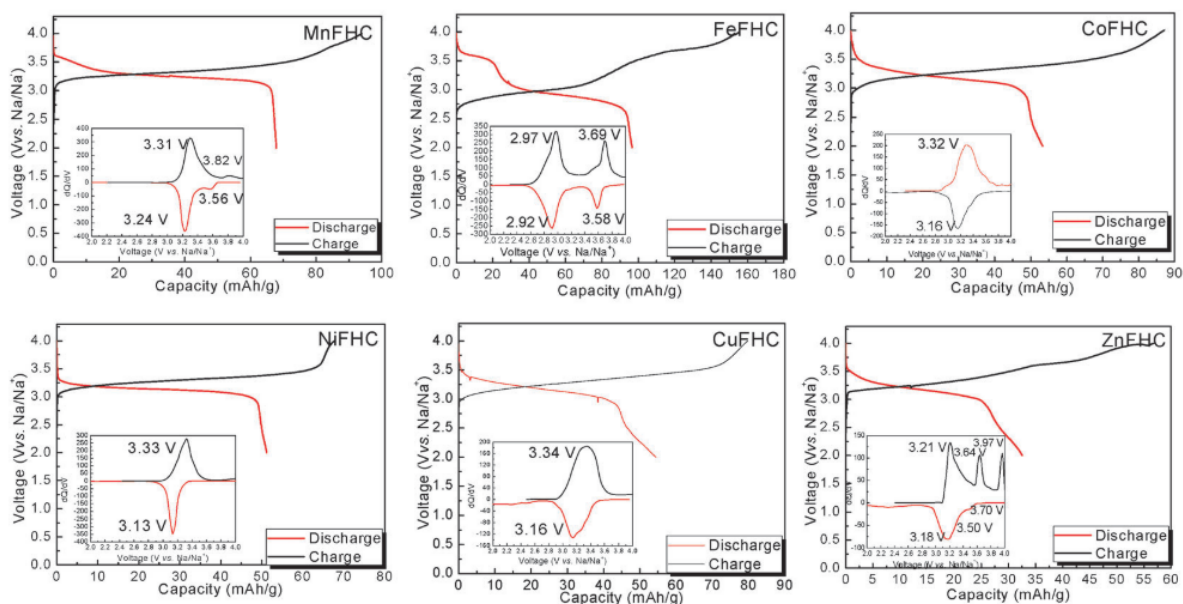


**Figure 1.3.2:** The charge–discharge curves of Prussian blue analogues  $\text{KMFe}(\text{CN})_6\text{--Na}$  cells at the third cycle with a current of  $C/20$ . Insets show their corresponding chronoamperograms. Republished with permission of The Royal Society of Chemistry, from Prussian blue: a new framework of electrode materials for sodium batteries, Yuhao Lu, Long Wang, Jinguang Cheng and John B. Goodenough, *Chem. Commun.*, 2012, 48, 6544–6546, 2012 Copyright; permission conveyed through Copyright Clearance Center, Inc.

the reversible capacity reaches about 150 mAh/g.

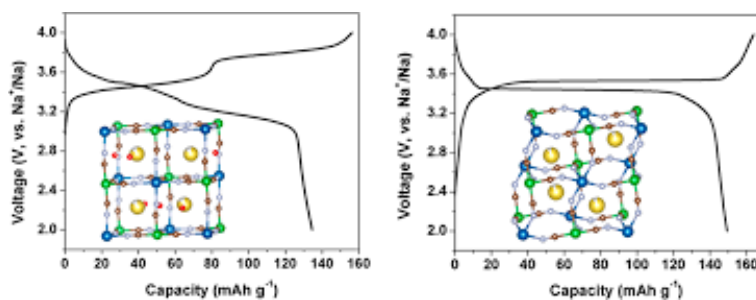


**Figure 1.3.3:** Galvanostatic initial charge and discharge profiles of air-dried (left) and vacuum-dried (right)  $\text{Na}_{2-\delta}\text{MnHCF}$  at a current of  $0.1 C$  ( $15 \text{ mA/g}$ ) in the voltage range of  $2.0 - 4.0 \text{ V vs. Na}^+/\text{Na}$ . Reproduced with permission from *J. Am. Chem. Soc.* 2015, 137, 2658–2664 Copyright 2015 American Chemical Society

Other examples in the literature regard mainly zinc hexacyanoferrate [83–86], cobalt hexacyanoferrate [87–89], and titanium hexacyanoferrate [90–92].

# Motivation

The development of sustainable energy sources and the storage of electrical energy is a worldwide concern, as pointed out in Section 1.1 [7]. The call for an efficient electrochemical energy storage is answered by rechargeable batteries, which are based on high rate intercalation reaction of lithium ions into nano- and micro- structured porous materials [93]. The performance of such hosts derives from a combination of structural and electronic properties and their reversible evolution along cycling, therefore the investigation of such features and the comprehension of limiting or irreversible steps are of great technological importance to better design advanced tailored materials [94]. However, the understanding of the redox and structural principles ruling the reaction mechanism is a difficult achievement, and sometimes erroneously taken for granted. The complexity of a battery, which consists of different components and various contributions to the overall redox process, could be untangled by using a combined multi-technique approach that probes different aspects of the same system.

X-ray diffraction (XRD) is commonly used to recover structural properties, as it is suitable to determine structural phases, and any separation or transitions [95–97]. X-ray absorption fine structure (XAFS) is the technique of choice for retrieving electronic and structural information [98, 99], by analyzing both X-ray absorption near edge structure (XANES) and extended X-ray absorption fine structure (EXAFS) portions, due to the presence of transition metals in most electrodes. Moreover, *operando* measurements allow for a continuous monitoring of the system dynamics [100], setting the stage for time resolved snapshots of a potential complex mechanism; however, the acquired large datasets make necessary an advanced analysis, often supported by chemometric techniques, such as multivariate curve resolution refined by alternating least squares (MCR-ALS) [101].

The present work focuses on the synthesis and thorough characterization of battery materials to untangle the reaction mechanism, the redox activity, the electronic and structural reversibility of the systems under study. The materials under investigation were PBAs, due to their low-cost and effectiveness as electrode materials. Even though they don't feature high specific capacities, they are characterized by a good cycling ability and efficiency, as well as ion-versatility which can be favorable to a post-lithium strategy. The reproducible synthesis of such materials derives from an expertise belonging to my research group, which was carried on during my PhD period and here discussed.

*Die Liebe zum Wunderbaren gehört eigentlich dem Poeten  
und die Lust Schwierigkeiten zu überwinden dem Mathe-  
matiker.*

Johann Wolfgang von Goethe

# 2

## Background

### 2.1 BATTERY ELECTROCHEMISTRY

The battery capacity is the total charge stored,  $Q$ , defined as:

$$\int_0^{\Delta t} I dt = \int_0^Q dq \quad (2.1)$$

where the output current during discharge at a voltage  $V$  in the time span  $\Delta t$  is  $I = dq/dt$ , which corresponds to a stored energy:

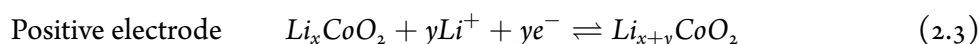
$$\int_0^{\Delta t} IV(t) dt = \int_0^Q V(q) dq \quad (2.2)$$

In rechargeable batteries the discharge is followed by a charge, where the input current can be described as in Eq. 2.2. The cycle efficiency and reversibility of the system is defined in the *coulombic efficiency*

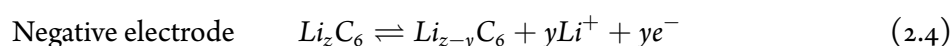
value, *i.e.*,  $Q_{charge}/Q_{discharge}$ .

For technological applications, the capacity is generally expressed as *specific capacity*, *i.e.*, normalized by the mass or volume, giving respectively the gravimetric (Wh/kg or mAh/g) or volumetric specific capacity (Wh/L).

Lithium-ion batteries have been introduced on the market in the 90's by Sony, and are based by the first investigation of Mizushima, Jones, Wiseman and Goodenough published in 1981 [102]. A cell is a two-electrode system constituted by a positive and negative electrode, kept away by an electrolyte-soaked separator. The electrolyte is generally an organic solution containing a soluble lithium salt, such as lithium hexafluorophosphate  $LiPF_6$ , in the presence or absence of additives. The positive electrode material is commercially a lithium rich cobalt oxide,  $Li_xCoO_2$ , while  $Li$  metal had first been adopted as negative electrode, being later replaced by  $Li$ -intercalated graphite,  $Li_zC_6$ , for safety reasons. The reactions that take place at the electrodes in a battery system are listed below:



where  $x \geq 0.067$  and  $x+y \leq 1$



where  $z \leq 1$

During the discharge process (see Figure 2.1.1) the intercalation of  $Li$ -ions is forced in the cobalt oxide insertion material ( $LiMO_2$  layer structure), causing the reduction of the cobalt species, while the reverse occurs in the charge process, being the  $Li$ -ions released in the electrolyte solution and the cobalt species oxidized to the original oxidation state. At the negative electrode the specular redox reactions take place, being the lithium de-intercalated and re-inserted in the graphite layers, respectively.

### 2.1.1 ELECTROCHEMICAL METHODS

#### CYCLIC VOLTAMMETRY

The term voltammetry indicates a class of electroanalytical methods where the information regarding the analyte is acquired by measuring the current flowing in a working electrochemical cell as a function

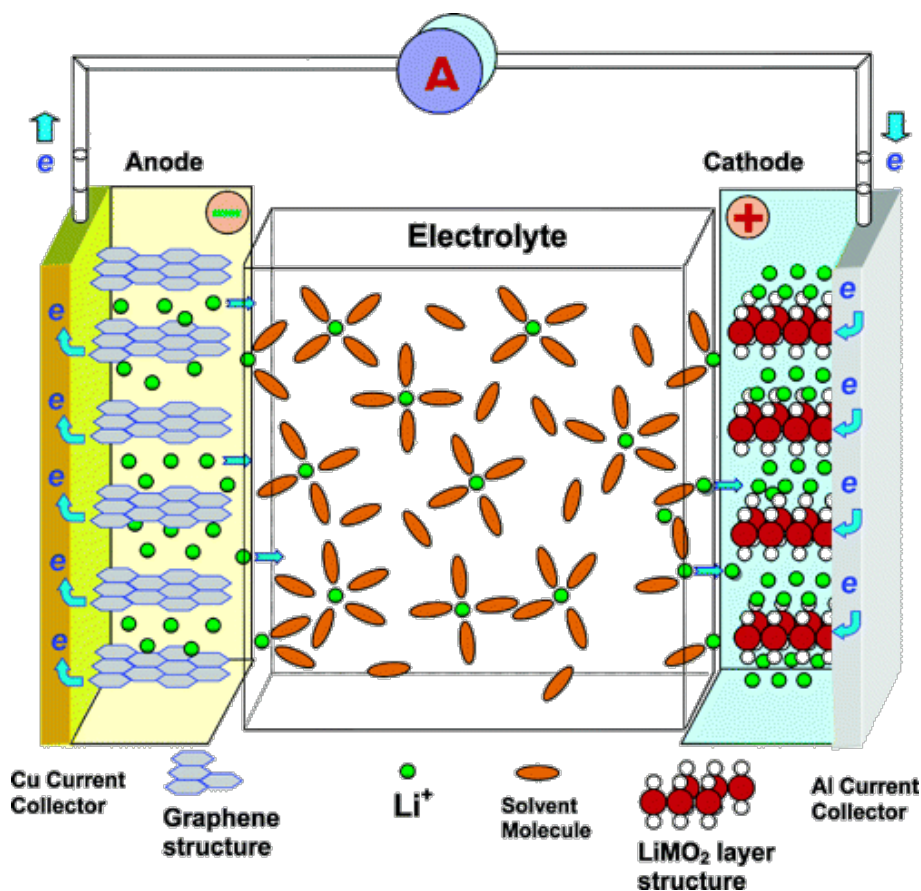


**Figure 2.1.1:** Li-ion insertion mechanism. Reprinted with permission from Chem. Rev., 2004, 104 (10), 4303–4418. DOI: 10.1021/cr030203g. Copyright 2004 American Chemical Society

of the applied potential. In particular, the signal is analyzed under precise conditions that favour the polarization of the working electrode, where polarization is commonly ascribed as the difference in Volts between the observed value and the theoretical value according to the Nernst equation.

During a voltammetric measurement, the potential of the working electrode (WE) is varied systematically by using a reference electrode (RE) while the current output is recorded against a counter electrode (CE). The produced current is characteristic of the studied WE. In cyclic voltammetry (CV), the potential applied to the cell varies during time at a defined scan rate (expressed in V/s) and assumes a typical triangular shape, as illustrated in Figure 2.1.2. The inversion of polarization induces alternately the oxidation and the reduction of the working electrode, which could be evidenced by the appearance of one or more peaks at precise potential values, characteristic of the WE electroactive material.

Together with the mentioned three electrodes, an excess of conducting electrolyte solution has to be employed to increase the ion mass transport in the bulk solution and decrease its ohmic resistance. Moreover, in case of CV measurements on intercalation-type battery materials, the electrolyte acts

also as intercalating agent, more precisely the cations/anions constituting the electrolyte salt are inserted/released in the studied material, which is in this case employed as WE.

Adapted voltammetric experiments have been carried out in this work. For more details, refer to Section 3.4.

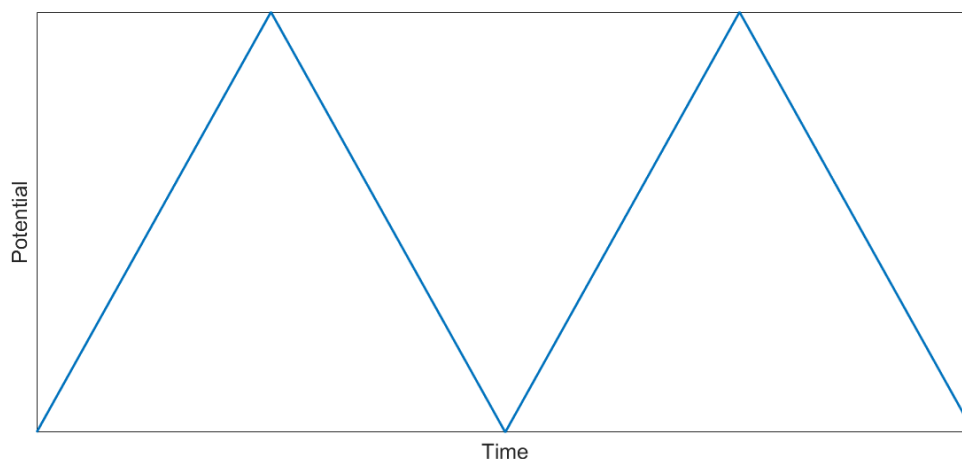


**Figure 2.1.2:** Variation in time of the potential in a typical cyclic voltammetry measurement

#### GALVANOSTATIC CYCLING WITH POTENTIAL LIMITATION

Galvanostatic cycling with potential limitation (GCPL) is a standard protocol used to investigate battery systems. As stated in the name, GCPL operates in galvanostatic mode, *i.e.*, a positive/negative constant current is imposed to induce the oxidation/reduction of the studied material, while the potential is recorded as a function of time. By inverting the current polarity, several cycles of charge/discharge are acquired in a defined and optimized potential window, as displayed in Figure 2.1.3.

In a typical experiment, the studied electrode has positive polarity, while a large piece of metallic lithium serves as negative electrode, if a two-electrode Li-ion half-cell is considered. A Swagelok T-cell may be used for a better accuracy on the potential reading. Indeed, the potential in intercalation compounds, where ions are inserted (released) in discharge (charge) processes while the positive electrode is reduced (oxidized), is thermodynamically related to the system composition. Moreover, the charge passed through a certain lapse of time is directly related to the inserted (extracted) ions, hence the reduction (oxidation) degree of the host.

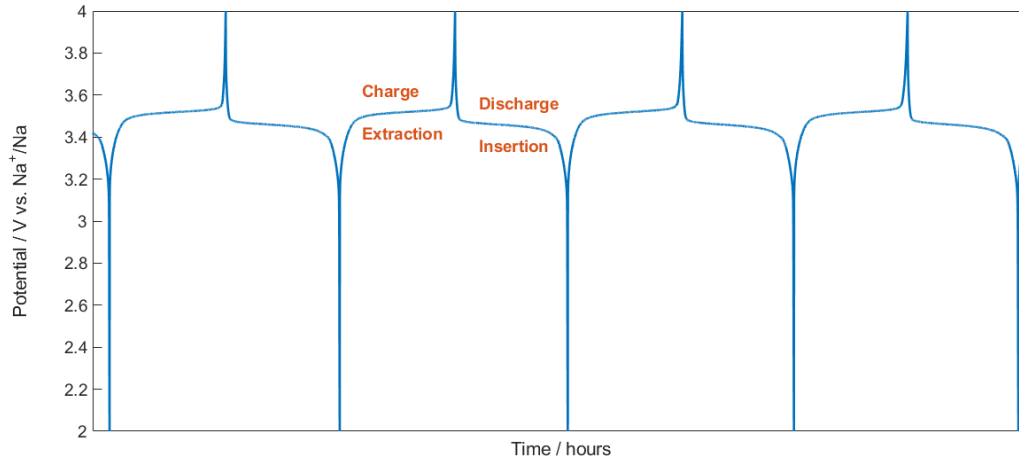


**Figure 2.1.3:** GCPL measurement on a battery system

The value of input current is usually expressed in mA; however, a common used physical quantity is the current rate ( $C/\tau$ ), being  $C$  the charge corresponding to the total expected reduction/oxidation of that electrode and  $\tau$  the number of hours at which the nominal charge of the battery will be passed through. If the specific capacity (mAh/g) of an intercalation-type electrode is considered, the current rate can be expressed per active material mass, that is in mA/g. In practice, the charge/discharge current rate is therefore calculated starting from the theoretical value of specific capacity (Equation 2.5) and dividing it by a value in hours corresponding to the half-cycle time (Equation 2.6) as it follows:

$$C^{\text{theoretical}} = F \cdot n / FW \quad (2.5)$$

where  $C^{\text{theoretical}}$  is the theoretical specific capacity (C/g),  $F$  is the Faraday constant (C/mol),  $n$  (mol) is the moles of ions able to be inserted/extracted per formula unit of active material,  $FW$  is the formula weight of the active material (g/mol);

$$C_{\text{rate}} = C^{\text{theoretical}} / \tau \quad (2.6)$$

where  $C_{\text{rate}}$  is the calculated current rate per active material mass (C/hg),  $\tau$  (h) is the number of hours at which the nominal charge of the battery will be passed through;

and by considering the following relation:

$$1C = 3.6mAh$$

## 2.2 X-RAYS AND X-RAY TECHNIQUES [103–107]

Electromagnetic (EM) waves are created as a result of vibrations between an electric field and a magnetic fields, and allow transmission of energy through vacuum or using no medium.

According to the Maxwell equations, the wave equations for the electric  $\hat{E}$  and magnetic  $\hat{H}$  fields can be expressed as:

$$\nabla^2 \hat{E} - \epsilon_0 \mu_0 \frac{\partial^2 \hat{E}}{\partial t^2} = 0 \quad (2.7)$$

$$\nabla^2 \hat{B} - \epsilon_0 \mu_0 \frac{\partial^2 \hat{B}}{\partial t^2} = 0 \quad (2.8)$$

where  $\epsilon_0$  and  $\mu_0$  are the dielectric constant and magnetic permeability in vacuum, respectively.

As a result of the Maxwell equations, the electric and magnetic fields propagate with a speed  $c = 1/\sqrt{\epsilon_0 \mu_0} \approx 3 \cdot 10^8 \text{ ms}^{-1}$ , while the vectors describing the electric and magnetic field are not independent, being orthogonal, oscillating in phase and having their amplitudes a defined ratio, that is the value  $c$ , the so called speed of light. In case of planes waves, we can re-write the Equations 2.7 and 2.8 as:

$$\hat{E} = \hat{E}_0 e^{j(\hat{k}r - \omega t)} \quad (2.9)$$

$$\hat{B} = \hat{B}_0 e^{j(\hat{k}r - \omega t)} \quad (2.10)$$

where (i) the vectors  $\hat{E}_0$  and  $\hat{B}_0$  give the direction of the oscillating electric and magnetic fields, respectively, while their modulus provide for the amplitudes of the oscillations; (ii) the vector  $\hat{k}$  is the wave vector, whose direction is the direction of the propagation of the plane wave, while its modulus is related to the wavelength  $\lambda$  of the radiation,  $k = 2\pi/\lambda$ ; (iii)  $\omega$  is the angular frequency,  $\omega = 2\pi\nu$ , and  $\nu$  is the frequency of the radiation.

The relation between the wavelength and the frequency is inversely proportional and determined by the following expression:

$$c = \nu\lambda \quad (2.11)$$

X-rays are electromagnetic radiations characterized by a wavelength in the  $10^{-2} < \lambda < 10^2 \text{ \AA}$  range, which is commensurate with both the atomic sizes and shortest interatomic distances. For this reason, they can be used to investigate systems at atomic scales, and are currently used in different spectroscopic, diffraction and imaging techniques. The energy related to such radiations varies from hundreds of electronvolts (eV) to thousands of eV, where 1 eV is defined as the energy to accelerate a particle carrying a unit electronic charge across an electric potential of 1 Volt.

In this Section, we are going to focus on two bulk techniques, namely X-ray absorption fine structure (XAFS) and X-ray diffraction (XRD). To this purpose, it is noteworthy to introduce first the interaction of X-rays with matter and the available sources of X-rays that can be used.

First of all, the interaction of X-rays with matter can be divided into three main processes:

1. Coherent (or elastic) scattering: it occurs when the energy of the X-ray photon ( $\propto \nu$ ) is small compared to the ionization energy of the atom. A change of direction (scatter) of the photon occurs, while  $\nu_{IN} = \nu_{OUT}$ ;
2. Incoherent (or Compton) scattering: it differs from coherent scattering, since the photon energy deriving from the primary beam is partially lost in collisions with core electrons, thus  $\nu_{IN} > \nu_{OUT}$ ;
3. Photoelectric effect: ejection of a core electron (photo electron) as a consequence of energy absorption. The difference between the energy of the incident beam ( $E_{IN}$ ) and the energy of the core electron ( $E_o$ ) determines the kinetic energy the photo electron possesses in the continuum:

$$E_{IN} = E_o + \frac{mv^2}{2} \quad (2.12)$$

where the last term is equivalent to the kinetic energy  $E_K$

Coherent scattering is the main event occurring in XRD, while XAFS is based on the photoelectric effect.

Concerning X-ray sources, X-rays are usually generated using two different methods.

Conventional X-ray sources are called X-ray tubes, and can be easily found in laboratories. The working principle is based on the generation of electromagnetic waves from impacts with a metal target (or anode) of high-energy electrons accelerated in an electric potential of 30-60 keV from a cathode (generally an electrically heated tungsten filament). The emitted radiation is collected after passing through

a transparent window of beryllium. These sources usually have low efficiency (<1%) and their brightness is limited by the thermal properties of the target material, which must be continuously cooled to avoid that the kinetic energy of the accelerated electrons is converted into heat after the collision with the target itself.

The X-ray spectrum generated in a conventional source consists of intense peaks, called characteristic spectral lines (precisely, they are characteristic of the target material), and a continuous background, known as the white radiation, which is generated by electrons decelerating and it is not related to the nature of the anode material. White radiation is also known as *Bremsstrahlung*, literally braking radiation (cf. Figure 2.2.1).

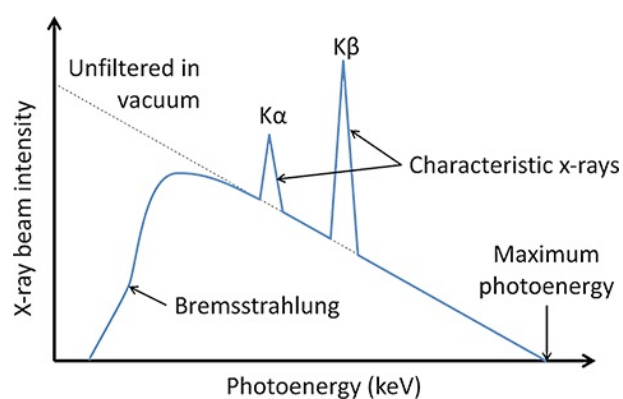


**Figure 2.2.1:** X-ray emission spectrum from a conventional source. ©Copyright 2018, PhysicsOpenLab. All Rights Reserved

In Figure 2.2.1, two characteristic lines are reported, adopting a notation which is recurring in X-ray techniques. The transitions from L and M shells to the K shell are designated as  $K\alpha$  and  $K\beta$  radiations, respectively, where K corresponds to the shell with principal quantum number  $n = 1$ , L to  $n = 2$  and M to  $n = 3$ . Moreover, the  $K\alpha$  transition consists of two characteristic wavelengths denominated  $K\alpha_1$  and  $K\alpha_2$ , corresponding to  $2p_{1/2} \rightarrow 1s_{1/2}$  and  $2p_{3/2} \rightarrow 1s_{1/2}$ , respectively, where the subscripts indicate the total angular momentum quantum number,  $j$ . The intensity of  $K\alpha_1$  exceeds that of  $K\alpha_2$  by a factor of two. Conventional X-ray sources for XRD adopt target materials that produce characteristic wavelengths between  $0.5 \text{ \AA}$  and  $2.3 \text{ \AA}$ . Some of these employ Fe, Cr, Co, however, only Cu and Mo are commonly used for powder and single crystal diffractometry, respectively ( $K\alpha_1(\text{Cu}) = 1.5405929(5) \text{ \AA}$ ,  $K\alpha_2(\text{Cu}) = 1.54441(2) \text{ \AA}$ ;  $K\alpha_1(\text{Mo}) = 0.7093171(4) \text{ \AA}$ ,  $K\alpha_2(\text{Mo}) = 0.71361(1) \text{ \AA}$ ). Nevertheless, other anode materials (such as Ag:  $K\alpha = 0.5594218 \text{ \AA}$ ) with shorter wavelength may be used to increase the resolution

of the atomic structure; on the other hand, Bragg peaks are observed closer and the resolution of the diffraction pattern may decrease excessively. A compromise should also take into account the sample to be measured to avoid that a higher energetic beam might deteriorate the sample itself, or pass through it more easily ( $\mu \propto E^{-3}$ , cf. Section 2.2.2).

Another source of X-rays is the so called synchrotron radiation. In 1054 Chinese astronomers observed a supernova explosion, which gave rise to the Crab Nebula (Figure 2.2.2). As stated by the National Aeronautics and Space Administration (NASA) [108]:

*A rapidly spinning neutron star (the ultra-dense core of the exploded star) is embedded in the center of the Crab Nebula. Electrons whirling at nearly the speed of light around the star's magnetic field lines produce the eerie blue light in the interior of the nebula. The neutron star, like a lighthouse, ejects twin beams of radiation that make it appear to pulse 30 times per second as it rotates.*

In other words, this is an example of natural synchrotron radiation.

When electrons travelling at relativistic speeds, *i.e.*, close to the speed of light, are forced to follow curved trajectories by applying magnetic fields, an amount of their energy is converted into radiation, namely the synchrotron radiation, which propagates in the direction of their motion, tangential to the orbit. Synchrotron radiation covers a large portion of the spectrum, extending from infrared to hard X-rays.

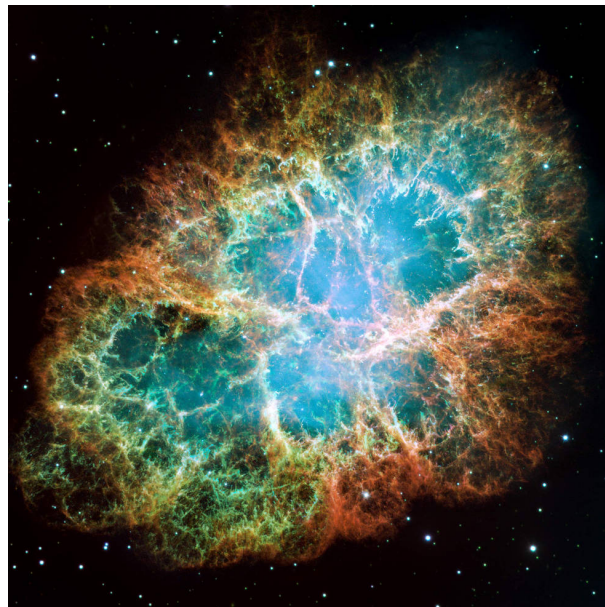


**Figure 2.2.2:** Crab Nebula. Credits: NASA, ESA, J. Hester and A. Loll (Arizona State University)

A synchrotron facility is made of circular evacuated pipes (ultrahigh vacuum is needed) where electrons

flow at relativistic speeds, diverged from linear trajectories by using magnets, such as bending magnets, wigglers or undulators. Figure 2.2.3 illustrates a schematic planar view of the Australian Synchrotron facility. The electrons are first accelerated in the linear accelerator (Linac) until their energy reaches several MeV, then the Booster further increases their energy to GeV, before they enter in the storage ring. Every time the electrons are deviated in correspondence of a magnet, the emitted radiation is converged to the beam line hutch, where experiments take place, while the energy lost by the electrons as synchrotron radiation is restored by the radio frequency electric fields, which accelerate the electrons along the liner sections.

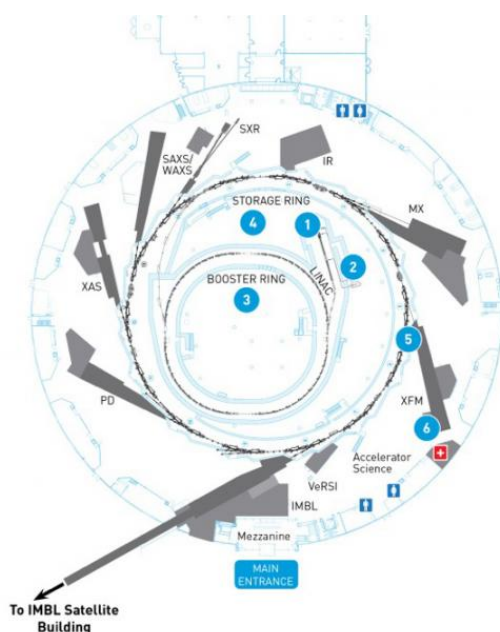


**Figure 2.2.3:** Schematic view of a synchrotron facility. ©Copyright 2018, ANSTO. The Australian Synchrotron

The spectrum originating from synchrotron radiation is depicted in Figure 2.2.4. Few considerations that can be done by considering a bending magnet are here summarized:

1. The beam is highly intense;
2. The spectrum is broad and continuous, ranging from infrared to hard X-rays;
3. The beam is polarized and is characterized by a natural narrow angular collimation;
4. The beam is highly brilliant, where the brilliance is defined as the photon flux per unit area per unit dihedral angle.

Only to have an idea about the synchrotron radiation, if the brightness (or intensity) of a light bulb is  $10^6$  units, the respective value for the sun would be  $10^{10}$ , while for the synchrotron radiation would be  $10^{16}$ . Moreover, the vertical half-opening angle is expressed as:

$$\psi \approx mc^2/E \quad (2.13)$$

so that for an electron in a storage ring of 2.0 GeV (such as in Elettra Sincrotrone, Basovizza, Italy), the angle would be  $\psi \approx 0.25$  mrad, that is  $< 0.015^\circ$ . The resulting beam is considerably collimated, and the intensity per unit area is extremely high also at tens of meters away from the storage ring.

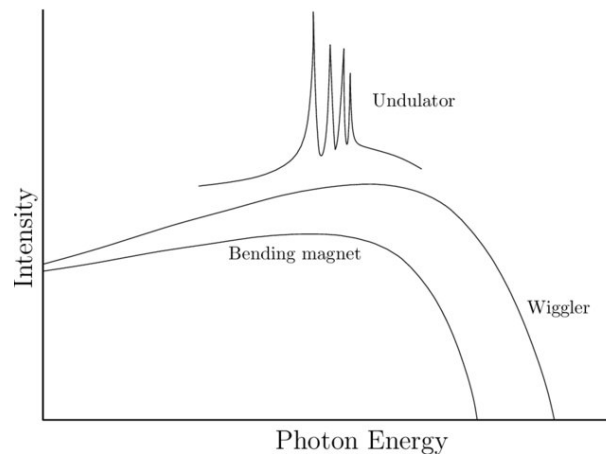


**Figure 2.2.4:** Spectra of bending magnets and insertion devices. Reprinted from High Throughput Software for Powder Diffraction and its Application to Heterogeneous Catalysis, Taha Sochi. All rights reserved to Dr. Taha Sochi 2010

### 2.2.1 X-RAY DIFFRACTION

In XRD experiments, the relationships between the directions of the incident and diffracted beams are given by the Laue equations:

$$a(\cos\psi_1 - \cos\varphi_1) = h\lambda \quad (2.14)$$

$$b(\cos\psi_2 - \cos\varphi_2) = k\lambda \quad (2.15)$$

$$c(\cos\psi_3 - \cos\varphi_3) = l\lambda \quad (2.16)$$

where  $a$ ,  $b$ ,  $c$  are the lattice parameters; angles  $\psi$  and  $\varphi$  are the incident and diffracted beams angles, respectively, in three independent directions;  $h$ ,  $k$ ,  $l$  are called the Miller indices and define in a unique way the peaks in the reciprocal space (the set  $(hkl)$  identifies Miller planes);  $\lambda$  is the adopted wavelength. Laue equations indicate that, in case of a periodic lattice, diffraction maxima are located at specific angles, defined by both the lattice ( $a$ ,  $b$ ,  $c$ ) and the used wavelength ( $\lambda$ ). Laue equations are generally used to describe the geometry of diffraction from a single crystal.

Regarding powder diffraction, the Bragg law is commonly used. Each plane in a set  $(hkl)$  may be considered as a separate scattering object. The set is periodic in the direction orthogonal to the planes, which are separated by a certain interplanar distance  $d_{hkl}$ . Constructive interference from a set of equally spaced objects is only possible at specific angles, established from Bragg's law:

$$n\lambda = 2d_{hkl}\sin\theta_{hkl} \quad (2.17)$$

If one considers an incident front of waves with parallel propagation vectors (cf. Figure 2.2.5), forming an angle  $\theta$  with the planes  $(hkl)$ , this can be reflected by the planes (exactly, by the electrons here present, since the highest electronic density is here located), originating a new front of waves with parallel propagation vectors, forming the same angle  $\theta$  with the planes. The path difference ( $\Delta$ ) between a parallel pair of waves depends on the interplanar distance and on the incident angle, precisely  $\Delta = d_{hkl}\sin\theta_{hkl}$ . The total path difference is  $2\Delta$ , and the constructive interference is observed only when  $2\Delta = n\lambda$ , where  $n$  is an integer, called order of reflection, and  $\lambda$  is the wavelength of the incident wave front.

The value of  $n$  is usually taken as 1, since orders higher than one ( $n > 1$ ) can always be represented by first order reflections ( $n = 1$ ) from a set of different crystallographic planes with indices that are multiples of  $n$ :

$$d_{hkl} = nd_{nh,nk,nl} \quad (2.18)$$

X-ray diffraction is a non-destructive analytical technique which can yield the unique fingerprint of

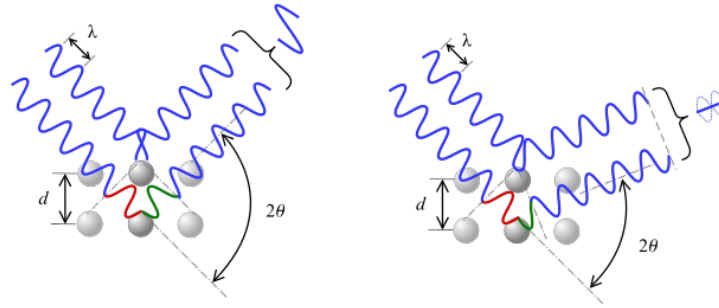


**Figure 2.2.5:** Schematic representation of constructive and totally destructive interference in Bragg's law. By Cdang at English Wikipedia

Bragg reflections associated with a crystal structure. It is used for phase identification of a crystalline material, can provide information on unit cell dimensions and determine crystal structures using Rietveld refinement.

### 2.2.2 X-RAY ABSORPTION FINE STRUCTURE

X-ray absorption fine structure (XAFS) is a quantum mechanical phenomenon based on the photoelectric effect: when an X-ray photon of appropriate energy is absorbed by an atom, an inner shell electron is freed into the continuum above the Fermi level and a core hole is left behind.

XAFS technique can be applied to all states of matter, to both crystalline and amorphous materials, making XAFS a powerful tool for several scientific fields. XAFS is element selective, as specific transitions take place at precise values of energies, and element tunable, since absorption edges of consecutive elements are sufficiently spaced in energy.

XAFS experiment measures the absorption coefficient  $\mu$  as a function of energy  $E$ : as  $E$  increases,  $\mu$  generally decreases ( $\mu \propto E^{-3}$ ), in other words matter becomes more transparent while X-rays more penetrating, except for some discontinuities at certain energies, the so-called absorption edges, characteristic of the material, where the energy of the primary beam exactly matches the core electron binding energy.

The measured quantity,  $\mu$  ( $\text{cm}^{-1}$ ), is the linear absorption coefficient, and is defined as the fraction of absorbed beam per unit thickness of absorbing matter, as described by the Bouguer-Lambert-Beer law (cf. Equation 2.19 and Figure 2.21). Normalization to the density of the material is usually done, obtaining

the mass absorption coefficient  $\mu_m$  ( $\text{cm}^2/\text{g}$ ) (Equation 2.20).

$$\mu x = \ln \frac{I_0}{I} \quad (2.19)$$

$$(\mu/\rho)\rho x = \mu_m \rho x = \ln \frac{I_0}{I} \quad (2.20)$$

where  $x$  is the sample length (cm),  $I_0$  is the incident beam,  $I_1$  the transmitted beam,  $\rho$  the density ( $\text{g}/\text{cm}^3$ ).

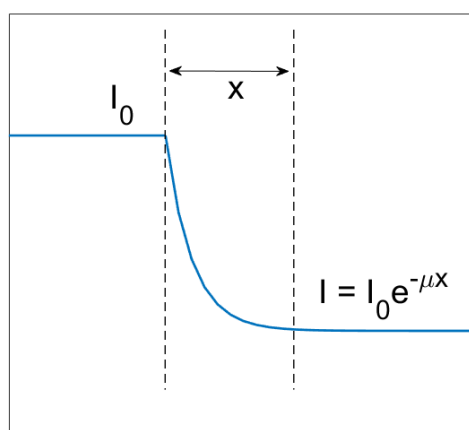


**Figure 2.2.6:** Transmission through a uniform sample of thickness  $x$

X-ray radiation is ionizing, since the absorbing atom turns to an excited ion after the electron ejection. Relaxation may occur along two different pathways: (i) the core hole may be filled by a higher-energy electron and the energy difference is released as a second photon, whose energy is smaller compared to that of the primary absorption, for an inner transition occurs; (ii) an Auger secondary electron may be freed, after having absorbed the second photon.

For energies lower than the absorption edge, an inner transition from an inner shell to a partially occupied or unoccupied state may occur, while more energetic radiations transfer to the photo electron enough kinetic energy, allowing it propagating like a spherical wave from the absorber atom and interacting with the potential of neighbouring atoms, giving rise to scattering events. More precisely, the incoming and scattered waves may interfere: for constructive interference, the probability to find the photo electron outside of the absorber is increased compared to the case of an isolated atom, while it is

decreased for destructive interference (cf. Figure 2.2.7).

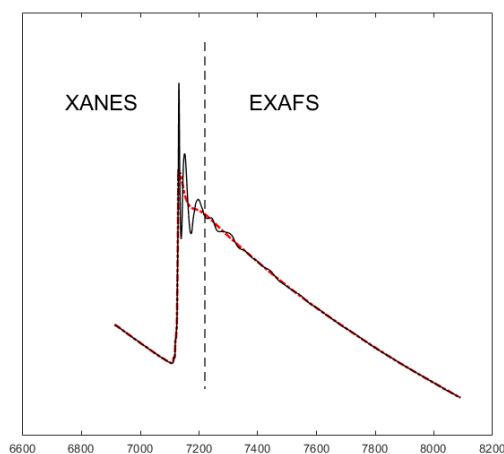


**Figure 2.2.7:** XAFS spectrum of an isolated atom (red dot-line) and the corresponding coordinated species (black line)

The XAFS spectrum can be divided into two main regions, *i.e.*, the X-ray absorption near edge structure (XANES) and the extended X-ray absorption fine structure (EXAFS) (cf. Figure 2.2.7).

The XANES region is sensitive to the element type and to other factors, such as the oxidation state, the electronic configuration, the spin configuration, and the local geometry around the photo absorber. For instance,  $\text{Fe}^{\text{III}}$  atom features a greater effective positive charge than  $\text{Fe}^{\text{II}}$ , hence a shift in binding energy ( $E_0$ ) to higher energies for a core shell electron is expected. Moreover, in case of a  $d^6$  electronic configuration (*e.g.*  $\text{Fe}^{\text{II}}$ ) in an octahedral geometry,  $d$  orbitals are split in 3  $t_{2g}$  orbitals and 2  $e_g$  orbitals (higher in energy). In case of a low spin state, only one transition from the core shell to the  $d$  orbitals is allowed, while for a high spin state, two different transitions may take place, the first one to the partially occupied  $t_{2g}$ , the second one to a likewise partially occupied  $e_g$  orbital.

Conversely, EXAFS region offers insight into structural domain, determining the environment of an atom and retrieving interatomic distances and angles, as well as structural/thermal disorder. The EXAFS signal is commonly described by a wave with a given amplitude and phase, which in first approximation depends on coordination number and type of atoms, and on distances, respectively, as it follows:

$$\chi(k) = \sum_j^{\text{shells}} A(R_j, k) \cdot \sin[2kR_j + \varphi(k)] \quad (2.2.1)$$

The overall signal is expressed as the sum of several sinusoidal contributions, where each atom at distance  $R_j$  accounts to the signal. The signal is in terms of the photo electron wavenumber,  $k$ , for which the following expression is valid:

$$k = \sqrt{\frac{2m(E - E_o)}{\hbar^2}} \quad (2.22)$$

According to Lytle, Sayers, and Stern, in case of the plane wave approximation, K threshold and only single scattering phenomena, the EXAFS equation can be written as:

$$\chi(k) = \sum_j^{\text{shells}} \frac{N_j}{kR_j^2} \cdot F_j(k) \cdot S_o^2 \cdot e^{-2R_j/\lambda(k)} \cdot e^{-2\sigma_j^2 k^2} \cdot \sin[2kR_j + \varphi(k)] \quad (2.23)$$

where  $N_j$  is the number of  $j$ -atom neighbors,  $R_j$  the distance,  $F_j(k)$  the backscattering amplitude,  $\varphi_j(k)$  the phase shift due to the absorber and scatterer atoms,  $\sigma_j$  the Debye-Waller like factor (structural and thermal disorder),  $\lambda(k)$  the photoelectron mean free path.

The EXAFS signal can also be written as energy dependent oscillations in  $\mu(E)$ :

$$\chi(E) = \frac{\mu(E) - \mu_o(E)}{\Delta\mu_o(E)} \quad (2.24)$$

where  $\chi(E)$  is the EXAFS signal,  $\mu(E)$  is the sample absorption,  $\mu_o(E)$  is the absorption of the "bare" atom, *i.e.*, without any coordinating atoms, and  $\Delta\mu_o(E)$  is the edge jump.

In other words, the signal of the investigated photo absorber is compared to the bare atom and normalized to a single absorption event.

Investigation through XAFS may occur at different absorption edges, namely K, L, M edges, as reported in Figure 2.2.8. Comparing the soft X-ray  $2p \rightarrow 3d$  transitions of the L-edge to the hard X-ray  $1s \rightarrow 3d$  transitions of the K pre-edge, energy resolution is gained as both the lifetime of the  $2p$  core hole is longer than the  $1s$  core hole and instrument monochromator energy resolution is higher at lower energy [109].

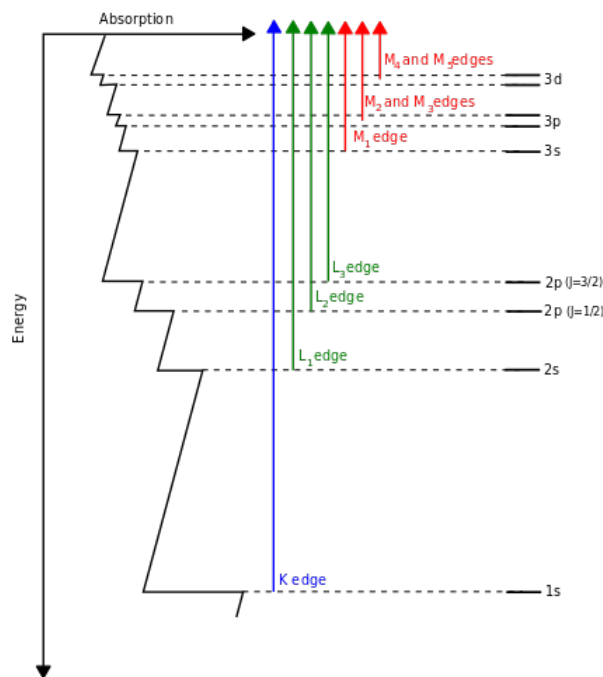


Figure 2.2.8: XAFS edges. By Atenderholt at English Wikipedia

### 2.3 MULTIVARIATE CURVE RESOLUTION WITH ALTERNATE LEAST SQUARES<sup>1</sup>

The large amount of data collected during a typical *operando* XAFS experiment and the interest to thoroughly investigate and comprehend a redox process occurring in a Li-ion battery need an advanced data analysis approach. By recording the electrochemical response relatively slowly compared to the spectral data collection, it is possible to build an experimental data matrix ( $X_{S,W}$ ) where each row is a XAFS spectrum in a very narrow potential range. Multivariate curve resolution refined by alternating least squares (MCR-ALS) provides an additive bilinear model of pure contributions without any preexisting model or *a priori* information on the system, decomposing the experimental matrix in a product of two matrices to which chemical meaning can be attributed [101, 110], as it follows:

$$X_{S,W} = C_{S,F} \cdot A_{F,W} \quad (2.25)$$

where  $C_{S,F}$  is the column matrix of the concentration profile, and  $A_{F,W}$  is the row matrix of the XANES spectra of pure species. A tentative initial value, as close as possible to the final solution, of one of the matrices must be provided for initializing the ALS refinement. Principal component analysis (PCA)

<sup>1</sup>Reprinted from XAFS studies on battery materials: data analysis supported by a chemometric approach, Marco Giorgetti, Angelo Mullaliu, Paolo Conti, Radiation Physics and Chemistry, *submitted*, Copyright 2018, with permission from Elsevier

has been replaced by evolving factor analysis (EFA) and fixed size window EFA (FSWEFA) methods to initialize the refinement, assessing not only the number of species but also their evolution along the row index [101]. Moreover, to obtain a unique and meaningful solution, constraints such as the closure condition and non-negativity (of concentration and/or of pure response) must be applied. A logical tree diagram 2.3.1 is reported to visualize the steps involved in the MCR-ALS analysis.

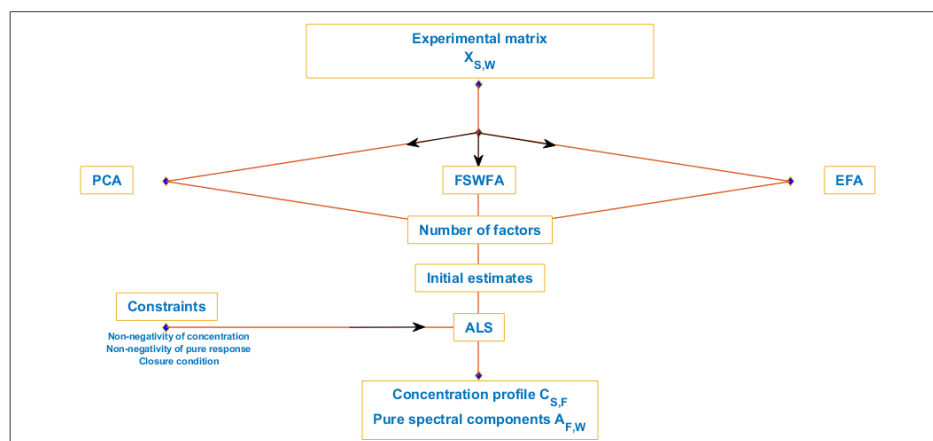


**Figure 2.3.1:** MCR-ALS analysis scheme

The call for an advanced data treatment is answered by a joint XAFS-MCR approach, able to unveil the local structural dynamics of the selected species, providing a quick and efficient data interpretation.

*Njeriu në jetë ka nevojë për 1 filxhan shkencë, 1 shishe kujdes,  
dhe 1 oqean durim.*

Ismail Kadare

# 3

## Methodology

### 3.1 SYNTHESIS

Potassium iron hexacyanocobaltate (FeCo) had been previously synthesized, hence the synthesis is here not reported. Please refer to reference [19].

Following a reported synthesis [54] and adapting it slightly, copper hexacyanoferrate (CuHCF) was synthesized by co-precipitation at 40 ° C, by mixing 250 mL of a 0.04 M aqueous solution of  $\text{CuSO}_4 \cdot 5\text{H}_2\text{O}$  and 250 mL of aqueous 0.02 M  $\text{K}_4[\text{Fe}(\text{CN}_6)]$ . Both solutions were prepared using double-distilled water ( $\text{ddH}_2\text{O}$ ) and previously thermostated at 40°C. Chemicals were purchased from Carlo Erba and used without further purification. The batch was aged for two days in the dark at room temperature. The red precipitate was separated by filtration on a Whatman 42 paper filter, washed twice with  $\text{ddH}_2\text{O}$  and dried at 40 ° C under vacuum. The obtained solid (2.98 g) was finally ground in an agate mortar.

The synthesis of copper nitroprusside (CuNP) was based on a bulk mixing co-precipitation method from 1000 mL of a solution containing 20 mM  $CuSO_4 \cdot 5H_2O$  and 1000 mL of a solution with 20 mM  $Na_2[Fe(CN)_5(NO)] \cdot 2H_2O$ . Both reagents were used as purchased from Sigma Aldrich. The two solutions were poured together in a large becher in 90 seconds at 40 °C under constant stirring, which was stopped 60 sec after ending the addition. The solution was aged for two days, then the precipitate was collected after centrifugation at 4000 revolutions per minute for 5 minutes using test tubes containing about 5 mL of suspension. After removing the supernatant, the precipitate was washed three times with roughly 2 mL distilled water per test tube, then air dried at 130°C for 6 hours.

Electrosynthesis of CuHCF is later described in detail in Section 3.3.2.

The synthesis of titanium hexacyanoferrate (TiHCF) was carried out via a solution precipitation method. 50 mL of a 0.1 M tetrabutyl titanate ethanol solution was slowly added to 100 mL of a 0.1 M  $Na_4Fe(CN)_6$  aqueous solution containing 1.5 M HCl. The  $Na_4Fe(CN)_6$ -HCl solution was kept in a heat bath at 40 °C and placed under continuous stirring set at 10 revolutions per second to generate a precipitate. The tetrabutyl titanate solution was added dropwise over the course of one hour, and done so under inert atmosphere ( $N_2$ ) in order to avoid the spontaneous ignition of the solution, as its flashpoint is at 50 °C. Following dropwise addition, the solution was heated under  $N_2$  with stirring for another 12 hours to ensure the completion of reaction. The resulting solution was dark in color, resembling black, however after centrifuging for 2 days a precipitate was collected on the walls of the round bottom flask. This precipitate was found to demonstrate a hint of dark blue color. The product was washed and centrifuged multiple times with water and acetone, and then dried at 70 °C for another 12 hours.

### 3.2 MATERIAL CHARACTERIZATION

Thermogravimetric analysis (TGA) was performed in air from 25°C to 500°C with a heating rate of 5 K/min, and rapid cooling.

X-ray fluorescence (XRF) analysis was performed by means of a PANalytical Axio<sup>mAX</sup> spectrometer on boric acid pellets with a 26 % concentration of the active material.

Inductively coupled plasma atomic emission spectroscopy (ICP-AES) was carried out by means of a Varian Vista Pro instrument. A charge coupled device (CCD) covering a broad spectral range (from 167 to 765 nm) was used as a detector.

ElementarVario Micro Cube was used for CHN analysis to acquire information on carbon, hydrogen and nitrogen content. The catalytic combustion of the sample occurred in the first oven set at 1150°C, while the reduction in the second one set at 850°C. Separation of the gas mixture took place in a temperature programmable column, while detection was achieved via thermal conductivity detector (TCD). Each sample was analyzed three times.

Powder X-ray diffraction (XRD) of battery materials was performed either on a X'pert PANalytical diffractometer in the range  $10^\circ < 2\theta < 70^\circ$  using Cu K-alpha radiation ( $\lambda = 1.5418 \text{ \AA}$ ) or at Elettra Sincrotrone in Basovizza (Italy) at the MCX [111] beam line.

In the latter case, the storage ring operated at 2.0 GeV in top up mode with a typical current of 300 mA, and the patterns were recorded in a capillary geometry, setting the spinner at 300 revolutions per minute, and acquiring the diffractogram consecutively in the  $5^\circ < 2\theta < 70^\circ$  range, with steps of  $0.01^\circ$  and an acquisition time of 1 s per step.

Electrosynthesized CuHCF (cf. Section 3.3.2) was deposited several times on an ITO (indium tin oxide) electrode, and the deposit was scraped by means of a blade after each synthesis. The powder was analysed by means of XRD on a Bruker-AXS diffractometer, Model D8 Advance, equipped with a Cu K-alpha source, in the  $10\text{-}90^\circ$   $2\theta$  range.

Scanning electron microscopy (SEM) was performed on a Quanta 650 FEG Instrument. The potential of the electron beam was set to 20 keV, while the reach magnification within 6kX and 10kX. Altogether with SEM analysis, energy dispersive X-ray spectroscopy (EDX) was carried out by incorporating an X-Ray detector Inca 250 SSD XMax20 with Peltier cooling, and with a detection area of 20 mm<sup>2</sup> and 129 eV resolution. SEM-EDX was carried out for both graphite sheet and carbon cloth supported CuHCF films.

XAFS characterization was carried out under the same working conditions as later discussed in Section 3.5 on electrosynthesized and already characterized CuHCF, deposited on a graphite sheet substrate. After the electrosynthesis, films were electrochemical characterized in 0.1 M KNO<sub>3</sub> solution via cyclic voltammetry, which ended after 15 scans at cathodic potentials (-0.2 V vs. SCE).

### 3.3 ELECTRODE PREPARATION AND CELL SET-UP

#### 3.3.1 ORGANIC MEDIUM

Electrodes for electrochemical measurements were obtained either by tape casting a slurry containing the 80% of pure active material (AM), 10% polyvinylidene fluoride (PVDF) and 10% carbon black (CB) in N-methylpyrrolidone (NMP) on a flat polytetrafluoroethylene (PTFE) surface (case of *operando* XAFS on FeCo), or by thoroughly mixing the pure AM (70%), 10% CB, and 10% vapour grown carbon fibers-high density (VGCF-H) in an agate mortar; 10% PTFE was finally added to the latter formulation and mixing continued until a homogeneous paste was obtained (all remaining cases). Obtained mass loadings were about 6-8 mg/cm<sup>2</sup> of AM.

A suitable electrochemical cell for *operando* experiments, described in detail elsewhere [112], was used during both XRD and XAFS measurements. The cell consisted of a large piece of lithium metal foil, adopted as negative electrode, while processed PBA was used as positive electrode. 1 M LiPF<sub>6</sub> in an ethylene carbonate, propylene carbonate, dimethyl carbonate 1:1:3 volumetric mixture (EC:PC:3DMC) served as electrolyte solution. Positive electrode, Celgard separator soaked in the electrolyte, and negative electrode were stacked and assembled under inert atmosphere in an Ar-filled glove-box.

#### 3.3.2 AQUEOUS MEDIUM

The set-up consisted in a three-electrode glass cell. A Pt wire was employed as counter electrode, a saturated calomel electrode (SCE) as reference, while the working electrode was either the PTFE-based electrode, prepared as described in the previous Section 3.3.1, or a functionalized conductive substrate, *i.e.*, glassy carbon, graphite sheet and carbon cloth. The 3-mm diameter glassy carbon (GC) electrode was provided by Basi, the graphite sheet by Cixi Weilite Sealing Material Co., Ltd, Zhejiang, China, while the carbon cloth by Quintech. In the first case, the PTFE-electrode was wrapped in an Al-mesh, pressed by means of a clamp, and used as WE. In the second case, the glassy carbon surface was polished prior to modification with alumina slurry on a wet polishing cloth until a mirror finish was obtained. Then, the electrode was thoroughly rinsed with water and cycled several times in 0.1 M H<sub>2</sub>SO<sub>4</sub> at 50 mV s<sup>-1</sup>, between -0.20 and +1.05 V vs. SCE, until superimposable voltammograms were recorded. Regarding both graphite sheet and carbon cloth, it has been evidenced from different tests that abrasion with

alumina on a polishing cloth and treatment in acidic medium did not produce benefits to the electrodeposition, hence the conductive materials were used as purchased. A defined and measured area ((5x5) mm<sup>2</sup>) delimited by parafilm was exposed and soaked in the electrolyte solution.

The procedures used for the electrodeposition of CuHCF were basically based on two steps, involving in the first one the electrodeposition of a thin film of metallic copper on the substrate, and its anodization and consequent formation of CuHCF on the electrode surface during the second step. The two used methods are labelled as Method A and Method B for convenience, and the main parameters are reported in Table 3.3.1.

		Applied potential (V vs. SCE)	Application time (s)
Method A	Step 1	-0.80	20
	Step 2	+0.60	300
Method B	Step 1	-1.00	4
	Step 2	+1.00	15

**Table 3.3.1:** Summary of the two-steps methods used for the electrodeposition of CuHCF

Method A is denoted by mild applied potentials and long run times: (i) in the first step, the electrode is immersed in a 0.05 M CuSO<sub>4</sub> and 0.05 M K<sub>2</sub>SO<sub>4</sub> solution, and copper deposition was carried out through chronoamperometry by applying a potential of -0.80 V vs. SCE for 20 seconds; (ii) in the second step, after having rinsed the electrode with distilled water, it is immersed in a 1 mM K<sub>3</sub>Fe(CN)<sub>6</sub> and 0.25 M K<sub>2</sub>SO<sub>4</sub> solution, and the formation of copper hexacyanoferrate is induced by applying a potential of +0.60 V vs. SCE for 300 seconds.

On the other side, Method B is distinguished by rather severe potential conditions and short run times: (i) in the first step, the electrode is immersed in a 0.05 M CuSO<sub>4</sub> and 0.05 M K<sub>2</sub>SO<sub>4</sub> solution, and copper deposition was carried out through chronoamperometry by applying a potential of -1.00 V vs. SCE for 4 seconds; (ii) in the second step, after having rinsed the electrode with distilled water, it is immersed in a 1 mM K<sub>3</sub>Fe(CN)<sub>6</sub> and 0.25 M K<sub>2</sub>SO<sub>4</sub> solution, and the formation of copper hexacyanoferrate is induced by applying a potential of +1.00 V vs. SCE for 15 seconds.

## 3.4 ELECTROCHEMICAL CHARACTERIZATION

### 3.4.1 ORGANIC MEDIUM

Cyclic voltammetry (CV) was performed by means of CHInstruments Model 660, while a MTI-Battery Analyzer was employed for galvanostatic cycling with potential limitation (GCPL), both by using a coin cell geometry, and short-cutting reference and counter electrode cables in case of cyclic voltammetry. The active material was used as either positive or working electrode for GCPL and CV, respectively. A large piece of lithium/ sodium metal foil was adopted as negative electrode in case of galvanostatic cycling, and for both counter and reference electrode in cyclic voltammetry. 1 M LiPF<sub>6</sub> in an ethylene carbonate : propylene carbonate : 3 dimethyl carbonate volumetric mixture (EC:PC:3DMC) without additives was used as electrolyte in Li half-cells, while 1 M NaPF<sub>6</sub> in EC:DMC volumetric mixture without additives served as electrolyte in Na half-cells.

Positive electrode, Whatman separator soaked in the electrolyte, and negative electrode were stacked and assembled in a 2036 stainless steel coin cell under inert atmosphere in an Ar-filled glove-box.

Cyclic voltammetry was conducted for copper nitroprusside in the 1.5 < E < 4.0 V vs Li<sup>+</sup>/Li potential range at a 0.1 mV s<sup>-1</sup> scan rate, starting from the open circuit potential (OCP) with a negative polarization.

GCPL was conducted for copper nitroprusside in the 1.5 < E < 4.0 V vs. Li<sup>+</sup>/Li potential window in Li half-cells, and in the 1.8 < E < 4.0 V vs. Na<sup>+</sup>/Na potential window in Na half-cells. 1C rate was considered equal to the current needed to insert one equivalent of Li-ion per active species in one hour, hence a theoretical specific capacity of 114 mAh/g. Cycling starting after a rest time at OCP conditions with a negative imposed current.

### 3.4.2 AQUEOUS MEDIUM

The electrochemical experiments were performed on a CHInstrument Model 660 potentiostat, connected to a personal computer via CH Instruments software.

PTFE-based TiHCF electrodes were characterized by means of cyclic voltammetry (CV) in different electrolytes. The working electrode was immersed in 0.1 M solutions of KNO<sub>3</sub>, NaNO<sub>3</sub>, Mg(NO<sub>3</sub>)<sub>2</sub> · 6H<sub>2</sub>O, Al(NO<sub>3</sub>)<sub>3</sub> · 9H<sub>2</sub>O, by using a Pt wire as CE and SCE as RE. Cycling was run in the -0.6 < E < 0.8

V vs. SCE potential window at  $1 \text{ mV s}^{-1}$ . Further tests have been carried out by modifying the scan rate and the potential window.

After electrodeposition, the so-obtained films of CuHCF (cf. Section 3.3.2) were characterized by means of CV: the functionalized conductive support was immersed in a  $0.1 \text{ M KNO}_3$  solution by adopting the same cell set-up as for the electrodeposition, and 15 cycles were run in the  $-0.2 < E < 1.05 \text{ V}$  vs. SCE potential window at  $20 \text{ mV s}^{-1}$ . These two adopted methods led to reproducible characterization voltammograms, hence electrochemical signatures.

To explore the ion exchange capabilities of the synthesized CuHCF, we varied electrolyte solutions in a systematic way. We conducted cyclic voltammeteries in the  $-0.2 < E < 1.05 \text{ V}$  vs. SCE potential window at  $20 \text{ mV s}^{-1}$ , by adopting the same cell set-up as the one used for both electrosynthesis and electrochemical characterization, and 3-mm glassy carbon functionalized with CuHCF as working electrode. After 15 cycles in  $0.1 \text{ M KNO}_3$  solution, ended at  $-0.2 \text{ V}$  (hence obtaining the ion-intercalated form of the film), the electrolyte solution was changed to  $0.1 \text{ M M}^{n+}(\text{NO}_3)_n$ , where  $\text{M}^{n+}$  is either  $\text{Na}^+$ ,  $\text{Mg}^{2+}$ ,  $\text{Al}^{3+}$ , or  $\text{Cs}^+$ . By starting with a positive polarization and ending at  $-0.2 \text{ V}$ , we were able to see first the extraction of  $\text{K}^+$  ions and the  $\text{M}^{n+}$  insertion in the synthesized film. Finally, we employed again the starting  $0.1 \text{ M KNO}_3$  solution, forcing the de-insertion of  $\text{M}^{n+}$  ions and the insertion of  $\text{K}^+$  ions, observing whether the film was restored to the initial state.

$\text{H}_2\text{O}_2$  determination was carried out by means of chronoamperometry in a stirred  $0.1 \text{ M}$  phosphate buffer solution ( $\text{pH} = 5.5$ ), applying first a potential of  $0.0 \text{ V}$  vs. SCE and waiting for the current to assume a constant value ( $2200 \text{ s}$  for Method A;  $400 \text{ s}$  for Method B). Micromolar aliquots of  $1 \text{ mM}$   $\text{H}_2\text{O}_2$  solution (first five additions:  $50 \mu\text{L}$ ; second five additions:  $100 \mu\text{L}$ ) were added to  $20 \text{ mL}$  of the buffered working solution, while the current increase was recorded.

$\text{K}_3\text{Fe}(\text{CN})_6$ ,  $\text{CuSO}_4 \cdot 5\text{H}_2\text{O}$ , and  $\text{KH}_2\text{PO}_4$  were provided by Riedel-de Haën, while  $\text{KNO}_3$ ,  $\text{NaNO}_3$ ,  $\text{Mg}(\text{NO}_3)_2 \cdot 6\text{H}_2\text{O}$ ,  $\text{Al}(\text{NO}_3)_3 \cdot 9\text{H}_2\text{O}$ ,  $\text{CsNO}_3$ ,  $\text{H}_2\text{O}_2$  ( $30\% \text{ w/w}$  in  $\text{H}_2\text{O}$ ) were purchased by Sigma Aldrich. All chemicals were of analytical grade and were employed without further purification. Phosphate buffer solution was prepared from a  $0.1 \text{ M KH}_2\text{PO}_4$  solution and the pH was adjusted to the value of  $5.5$  by adding concentrated KOH.

## 3.5 OPERANDO CHARACTERIZATION

### 3.5.1 DATA ACQUISITION

XRD and XAFS experiments were performed at Elettra Sincrotrone in Basovizza (Italy), at the MCX [111] and XAFS beam line [1], respectively.

The storage ring operated at 2.0 GeV in top up mode with a typical current of 300 mA.

XRD data were collected using a monochromatic X-ray beam of 1 Å. *Operando* data were collected in reflection mode consecutively from 10° to 30° 2θ range with a 0.01° step and 0.5 s/point acquisition time.

XAFS data were collected at Fe and Co K-edges in transmission mode using ionization chambers filled with a mixture of Ar, N<sub>2</sub>, and He to have 10%, 70%, and 95% of absorption in the I<sub>0</sub>, I<sub>1</sub>, and I<sub>2</sub> chambers. An internal reference of metallic foil corresponding to the absorption species was used for energy calibration in each scan. This allowed a continuous monitoring of the energy during consecutive scans. No energy drifts of the monochromator were observed during the experiments. Spectra at metals K-edge were collected with a constant k-step of 0.03 Å<sup>-1</sup> with 2 s/point acquisition time. Data were collected to include both XANES and EXAFS portions. The energies were calibrated by assigning the first inflection point of the spectra of the metallic species to the reported value found online [here](#). The white beam was monochromatized using a fixed exit monochromator equipped with a pair of Si(111) crystals. Harmonics were rejected by using the cutoff of the reflectivity of the platinum mirror placed at 3 mrad with respect to the beam upstream the monochromator and by detuning the second crystal of the monochromator by 30% of the maximum.

*Operando* Fourier Transform Infrared (FTIR) spectra were recorded on a Nicolet Magna FTIR spectrometer in the Attenuate Total Reflection (ATR) geometry using a specifically built *in situ* cell. The cell was obtained as a modification of the Raman spectroscopy cell used elsewhere [112], by replacing the quartz window with the diamond probe of the ATR module. ATR FT-IR spectra were recorded each 30 minutes from 400 to 4000 cm<sup>-1</sup> under a continuous air flow (0,5 bar/h).

Table 3.5.1 describes the electrochemical conditions of the *operando* measurements.

Material	Potential window (V vs. Li <sup>+</sup> /Li)	Current rate	Notes
FeCo	1.8<E<4.0	C/34	<i>Operando</i> XRD, charge first
FeCo	1.8<E<4.0	C/31	<i>Operando</i> XAFS, charge first
CuFe	2.0<E<4.3	C/31	<i>Operando</i> XAFS, charge first
CuNP	2.0<E<OCP	C/31	<i>Operando</i> XAFS, discharge only
CuNP	1.8<E<3.5	C/22	<i>Operando</i> XRD, discharge first
CuNP	1.5<E<4.2	C/20	<i>Operando</i> IR, discharge first

**Table 3.5.1:** Working parameters for *operando* experiments

### 3.5.2 DATA ANALYSIS

Rietveld refinement was carried out on XRD patterns using FullProf Suite software [113]. A pseudo-Voigt function was adopted for peak shape, while spherical harmonics were included in case of an anisotropic Lorentzian size broadening (cf. Section 4.3). Peaks corresponding to PTFE (contained in the electrode formulation) were not refined, excluding the corresponding regions, *i.e.*, 11.60-11.95° and 16.78-17.31° [114]. Also the 29.31-29.43° region was not considered, due to the presence of the beryllium peak arising from the *in situ* cell window. Graphical representation of structures was exploited by means of VESTA software [115].

XAFS spectra were pre-treated and calibrated using the Athena program [116]. The pre-edge background was removed by subtracting a linear function extrapolated from the pre-edge region, and the XANES spectra were normalized at the unity by extrapolation of the atomic background. The EXAFS analysis was performed using the GNXAS package [117, 118] which is based on the Multiple Scattering (MS) theory. The method uses the decomposition of the EXAFS signals into a sum of several contributions, namely the n-body terms. The theoretical signal is calculated *ab initio* and contains the relevant two-body  $\gamma^{(2)}$ , three-body  $\gamma^{(3)}$ , and four-body  $\gamma^{(4)}$  MS terms [18]. The two-body terms are associated with pairs of atoms, and probe their distances and variances. The three-body terms are associated with triplets of atoms and probe angles, and bond-bond and bond-angle correlations. The four-body terms are associated to chains of four atoms, and probe distances and angles in-between, and bond-bond and bond-angle correlations. However, because of the linearity of the M-NC-B chains constituting PBAs, all the angles were set to be 180°, hence the actual number of parameters used to define the  $\gamma^{(3)}$  and the  $\gamma^{(4)}$  signals was reduced by symmetry. More details on the use of parameters correlation in the four-body term can be found in the references [19, 119]. Data analysis was performed by minimizing a  $\chi^2$ -like residual function that compares the theoretical (model) signal,  $\mu_{mod}(E)$ , to the experimental one,

$\mu_{exp}(E)$ . The phase shifts for the photoabsorber and backscatterer atoms were calculated starting from the structure adopted as model for the studied compound according to the muffin-tin approximation and allowing 10% overlap between the muffin-tin spheres. The Hedin-Lundqvist complex potential [120] was used for the exchange-correlation potential of the excited state. The core-hole lifetime,  $\Gamma_c$ , was fixed to the tabulated value [121] and was included in the phase shift calculation. The experimental resolution used in the fitting analysis was around 1 eV, in agreement with the stated value for the beam line used.

The following structural models have been considered for copper hexacyanoferrate [122], copper nitroprusside [123], and iron hexacyanocobaltate [124].

Data treatment was achieved by means of several softwares, predominantly OriginPro 9 and Matlab R2018a.

### 3.6 DFT CALCULATIONS

Total energy calculations were performed within the DFT framework using the Vienna Ab initio Simulation Package (VASP) [125–128]. The electron wave functions were expanded on a plane-waves basis set with an energy cut-off of 850 eV. Pseudopotentials were used to describe the electron-ion interactions within the projector augmented waves (PAW) approach [129]. The convergence criterion for the electronic self-consistent cycle was fixed at 0.1 meV per cell. The integrations in the Brillouin zone were performed on a grid of  $2 \times 2 \times 2$ . Geometry optimizations were carried out by means of the conjugate gradient technique using the exact Hellman-Feynman forces acting on the ions. The structure was considered as optimized when the forces acting on the atoms were smaller than  $0.03 \text{ eV}\text{\AA}^{-1}$  and the energies variation between successive geometries was below 1 meV.

Lithiated structures during discharge were simulated by inserting consecutive atoms of lithium in the model structure: symmetry calculation was disabled not to take into account the multiplicity of lithium positions. Different calculations have been performed by changing the spin multiplet for the structures containing different number of inserted lithium to probe the electronic structure of the inserted materials. All results are here expressed as number of electrochemically inserted Li per formula unit. Vibrational frequencies are obtained by diagonalization of the dynamical matrix which is obtained by numerical differentiation of the forces acting on the atoms after displacement of  $0.04 \text{ \AA}$  around equilibrium

geometry.

### 3.7 XANES CALCULATIONS

The *ab initio* simulations of the XANES spectra were performed by using the FDMNES software[130] and the MS approximation. Cu and Fe K-edges in copper nitroprusside were calculated in the photoelectron energy range  $-1 < E < 120$  eV with respect to the Fermi energy level. The Hedin-Lundqvist complex potential[34] has been used to calculate the excited states. The absorption cross-section has been calculated within the dipolar approximation. Clusters of 7 Å built around each non-equivalent absorbing atom were considered. Copper nitroprusside space group symmetry ( $I4mm$ ) was disregarded by using the  $P1$  symmetry and inserting as input the positions obtained by the DFT calculations. Optimized convolution parameters were retrieved for the pristine material and kept fixed for all lithiated compounds. Finally, comparison between calculated and convoluted XANES spectra and experimental data was done. FDMNES is *ab initio* in the sense that it generally does not need any auxiliary parameters. Only the atom positions are required (output crystallographic positions computed by DFT) and the code starts from the first-principles equations.

*Io stimo più il trovar un vero, benché di cosa leggiera, che 'l  
disputar lungamente delle massime questioni senza conseguir  
verità nissuna.*

Galileo Galilei

# 4

## Results and Discussion

Hereby we present the results and discussion of the main studied compounds, dedicating a section to each of them. Each section collects the results and discussion of the characterization analyses, the electrochemical tests performed and further data treatment on XAFS and XRD.<sup>1</sup>

The motivation to the work is reported in each section.

---

<sup>1</sup>Sections may contain parts of published works and some of the same used sentences.

## 4.1 POTASSIUM IRON HEXACYANOCOBALTATE<sup>2</sup>

### MOTIVATION

The work based on potassium iron hexacyanocobaltate (FeCo) offers a good starting point to approach the data analyses and data treatment strategies developed by our research group. A blend of different techniques have been employed to investigate the battery system, by exploring the electroactivity, the long-range order, the short-range order, and their evolution upon cycling.

#### 4.1.1 XRD ANALYSIS

The stoichiometry of the resulting FeCo can be written as  $K_{0.44}Fe_{1.56}Co(CN)_6$  after XRF analysis, which provided a K/Fe/Co ratio of 0.44/1.56/1. The obtained pattern for the as-synthesized FeCo, depicted in Figure 4.1.1, well matches with the reported model [124]. The refinement on the powder led to a cubic structure (space group:  $Fm\bar{3}m$ ) characterized by the lattice parameter  $a = 10.224 \text{ \AA}$ . The amounts of interstitial potassium (8c Wyckoff position) and structural iron (4b Wyckoff position) were refined leading to 0.4 K/Co and 1.4 Fe/Co ratios, in agreement with the stoichiometry. The resulting  $[Co(CN)_6]^{2-}$  vacancies can be thus approximated to 29%, which is in line with the experimental value of 36%. During the redox the lattice space group ( $Fm\bar{3}m$ ) did not change, however, the lattice dimension was affected by the process, as displayed in Figure 4.1.1.

Here, the cubic lattice parameter evolution is overlapped with the potential profile during the electrochemical reaction. The lattice parameter value for the pristine electrode ( $a = 10,171 \text{ \AA}$ ) differs from the one derived from the powder, since the electrode was vacuum dried at  $80^\circ\text{C}$  overnight before use, manifesting a negative thermal expansion effect after dehydration [131]. According to the electrochemical curve (Figure 4.1.1), the FeCo-based cathode was able to extract 0.51 K-equivalents in the charge process, while 0.54 Li-equivalents were inserted in the following discharge. However, the calculated amount of  $K^+$  ions exceeds the stoichiometric one, so that we might attribute at least 0.07 ion-equivalents to side reactions in the charge process. Except for the initial part of the cycling, the lattice experienced a slight shrinkage during K-extraction, whereas the Li-insertion provoked a relative expan-

---

<sup>2</sup>Reprinted from *Operando XAFS and XRD of a Prussian Blue Analogue cathode material: Iron Hexacyanocobaltate*, Angelo Mullaliu, Paolo Conti, Giuliana Aquilanti, Jasper Rikkert Plaisier, Lorenzo Stievano, and Marco Giorgetti, *Condensed Matter* 2018, 3, 36

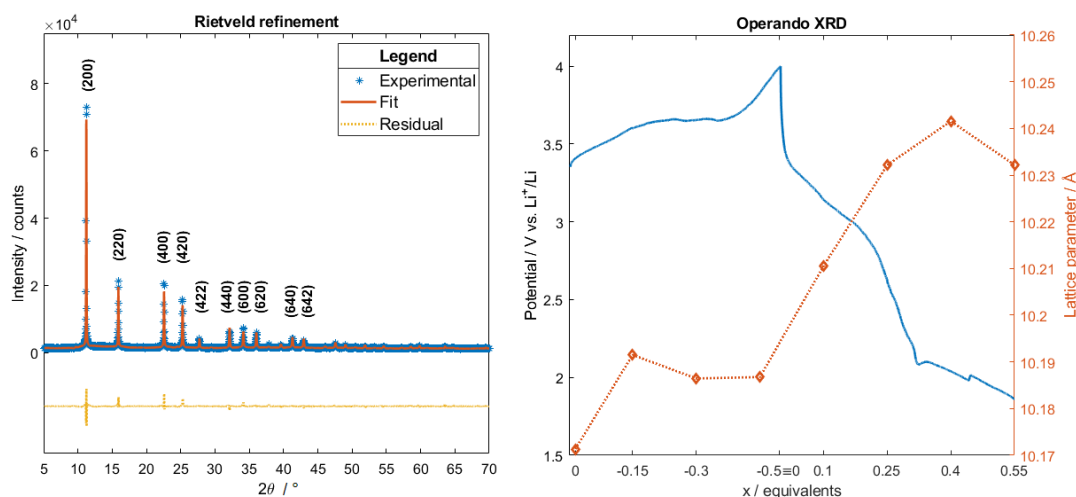


**Figure 4.1.1:** On the left side, the Rietveld refinement on FeCo powder is presented. The most relevant Miller planes are indexed in brackets. On the right side, the *operando* XRD electrochemical profile (blue line) and concomitant lattice parameter evolution (red scatter) are shown

sion, which was however limited to less than 0.6%. The negligible lattice strain exhibited by FeCo is indeed a common characteristic of PBA materials.

Furthermore, the refinement suggests the ion-insertion most likely occurred along the (220) plane. Indeed, as illustrated in Figure 4.1.2, the fit in correspondence of plane (220) improved significantly after refining the 8c occupancy.

#### 4.1.2 XANES ANALYSIS

As previously reported [1, 2], and indicated in Figure 4.1.3, release/insertion reaction induced a deep modification at the Fe K-edge, while the Co K-edge remained mostly unvaried. This highlighted a strong electroactivity of the iron site with consequent electronic and structural adjustments. For instance, the Fe main edge shifted towards higher energies while charging, evidencing an oxidation of the metal, while the opposite trend was observed in the insertion process.

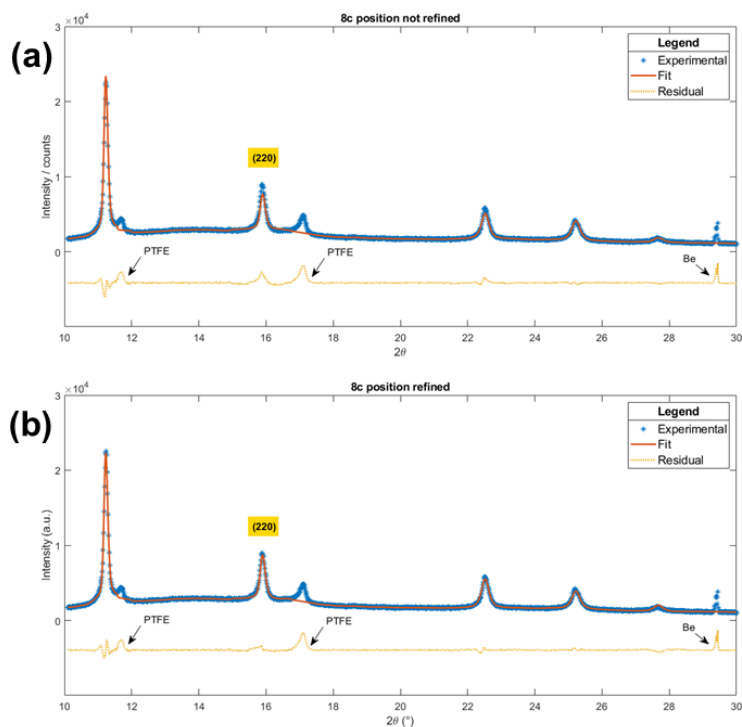


**Figure 4.1.2:** Rietveld refinement on the 60<sup>th</sup> XRD pattern: (a) 8c position not refined and (b) refined. Note the fit improvement at (220) plane

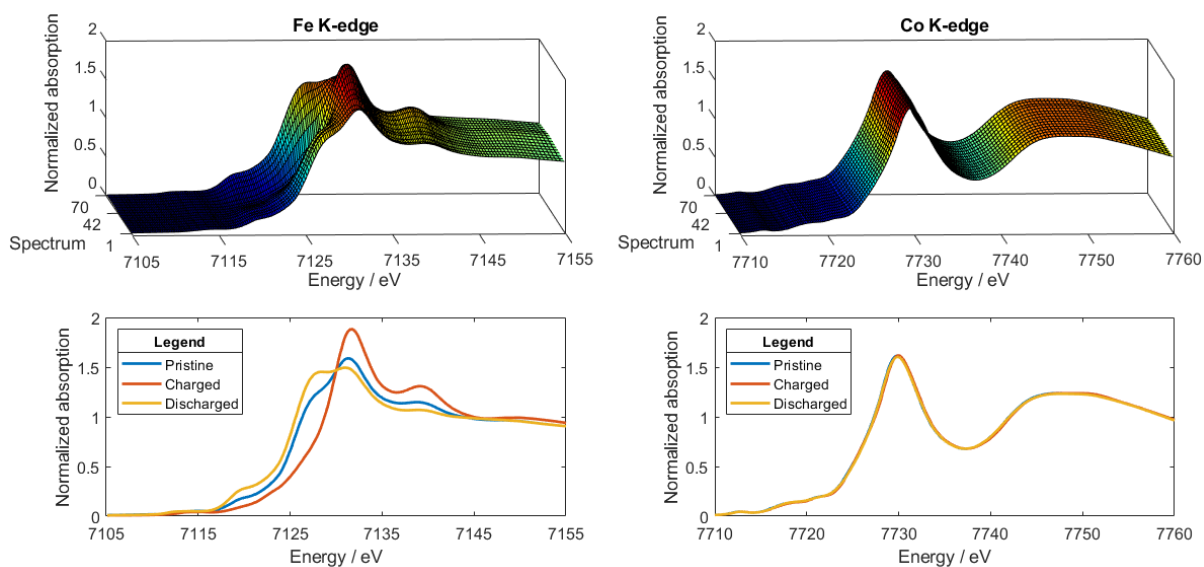


**Figure 4.1.3:** XAFS K-edge evolution for both iron (left) and cobalt (right). In the bottom layer, pristine, charged and discharged states spectra are compared and presented for each metal site. The figure has been adapted from reference [1]

XANES analysis was performed by using MCR-ALS chemometric approach, providing an additive bilinear model of pure contributions without any preexisting model or *a priori* information on the system, decomposing the *operando* data matrix in the product of the pure concentration profiles and the pure

spectral components (cf. Section 2.3). In this case, the MCR-ALS algorithm was applied to the whole series of *operando* Fe K-edge XANES spectra because of the higher variability along the W columns of the experimental  $X_{S,W}$  matrix. In Figure 4.1.4(a,b), the concentration profiles ( $C_{S,F}$ ) and the pure spectral components ( $A_{W,F}$ ) are reported, respectively. The overall results of the chemometric analysis can be sorted as: (i) a transformation during charge that could be approximated to the conversion of species 1 to species 2 took place, while the system evolved to species 3 in the following discharge process [2]; (ii) the concentration profile did not significantly change during the first roughly 0.3 extracted ion-equivalents, after which the redox reaction approached a pseudo-zero order kinetics; (iii) the pristine species does not entirely match with the first pure spectral components, however, they have a likeness equals 74%. As previously discussed [1], the first part of the electrochemical profile (panel c) assumed a curved-shape behavior, which was attributed to an irreversible dehydration process of the pristine electrode. Consequently, the first 0.3 K-equivalents should be considered not extracted from the FeCo material in this initial stage and ascribed to a parasite reaction, explaining also the flat concentration profile. Taking into account this last point, 0.62  $K^+$  were extracted, while 0.62  $Li^+$  inserted. Again, the calculated  $K^+$  ions exceed the stoichiometric value, so that in total at least 0.47 ion-equivalents are attributable to side reactions in the charge process. Moreover, to confirm that the pristine species is in fact a combination of more contributions, we carried out an independent linear combination fitting: panel d illustrates the additive contributions at the Fe K-edge of the fully charged (33%) and discharged states (67%). According to this result, the pristine Fe species might possess an oxidation number close to (+2.3) in a first approximation. FeCo material has to be considered a mixed-valence compound as many other PBAs, therefore the  $(FeCo)^{ox}$  notation adopted by Berrettoni *et al.* [46, 47] to describe the overall oxidation number of the metals appears to be the most appropriate way to refer to this class of material. Therefore, we can write  $(KFeCo)^6$  for the pristine state.

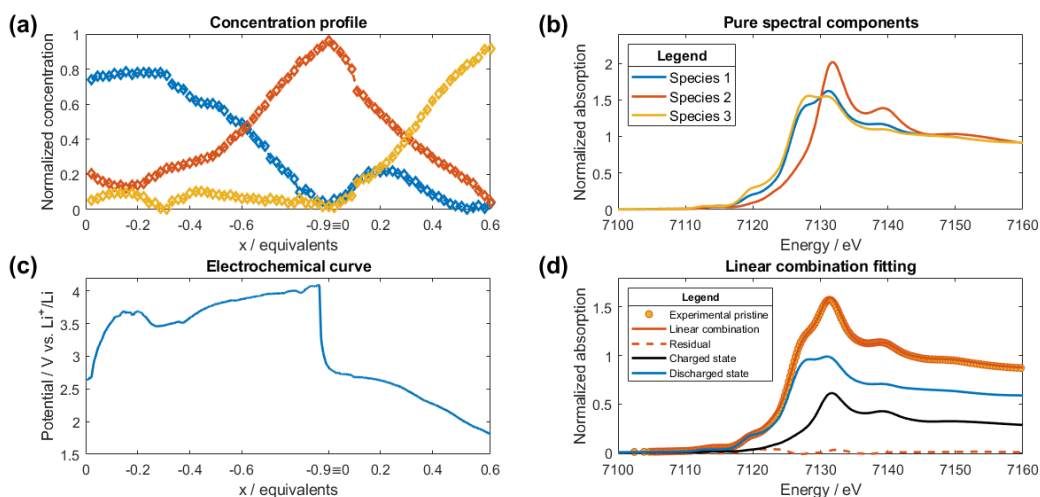


**Figure 4.1.4:** MCR-ALS analysis results: (a) Concentration profile; (b) Pure spectral components. In panel (c), the electrochemical potential profile is reported, while the linear combination fit on the pristine sample is illustrated in panel (d). The MCR-ALS results have been adapted from reference [2]

To complement the analysis on the XANES traces, an independent pre-edge data treatment was performed at the Fe K-edge. The pre-edge region was fitted with a sum of Gaussian functions by first subtracting a spline function background to the normalized spectra, defined by selecting an appropriate number of anchor points in the 7105 – 7125 eV window. Despite the considered approximations, the results are noteworthy. As reported in Figure 4.1.5, the pre-edge displays different features which were separately fitted. The number of Gaussian used to accomplish the fit was kept as low as possible to reduce the amount of refinable parameters, and it varied from two to four to consider all contributions. Interestingly, the peak centred at 7119 eV diminished in intensity during the K-extraction, while it enhanced in intensity during discharge. This pre-peak feature arises from normally forbidden dipole transitions to empty bound states and its evolution might reflect longer-range effects of the shells beyond the cyanides [132–134]. The exact correspondence of the displayed states with the collected spectra can be found in Table 4.1.1.

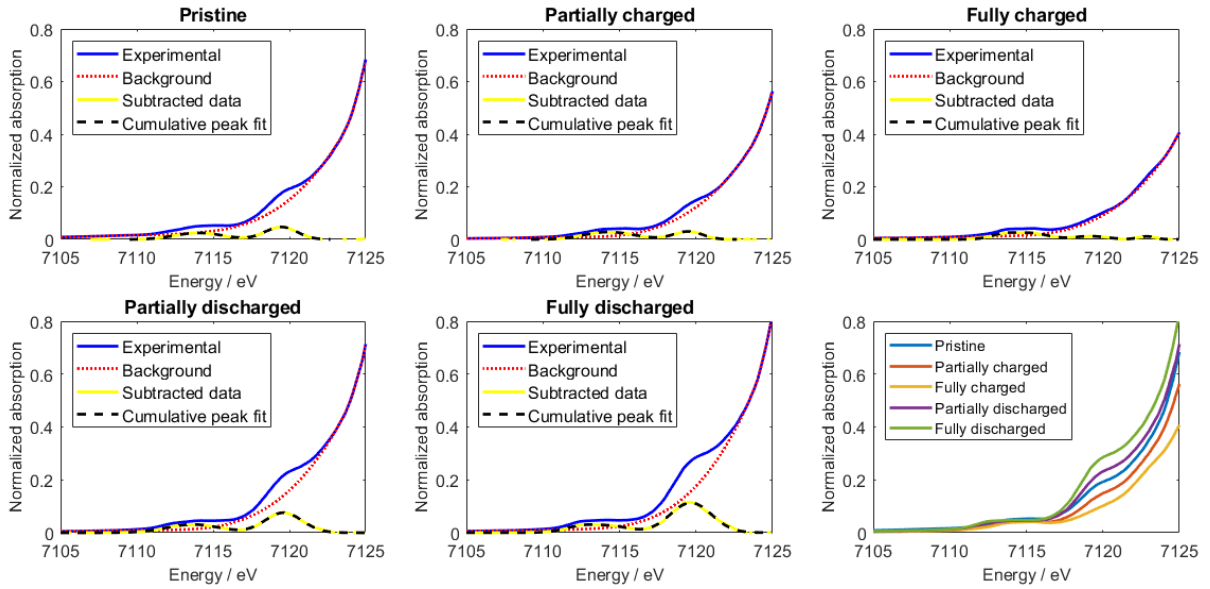


**Figure 4.1.5:** Pre-edge data analysis for the pristine, partially charged, fully charged, partially discharged, fully discharged states, and their comparison

x / equivalents	XAFS spectrum
0	0 (pristine)
-0.22	10
-0.44	20
-0.66	30 (partially charged)
-0.88	40
-0.91	42 (fully charged)
+0.18	50
+0.40	60 (partially discharged)
+0.62	70 (fully discharged)

**Table 4.1.1:** Correspondence between collected spectrum number and extracted/inserted ion equivalents

#### 4.1.3 EXAFS ANALYSIS

Complementary structural information occurring to both Fe and Co sites can be extracted by looking at the EXAFS signals. Analysis of the pristine electrode was first done to check the reliability of the structural model as well as to set the relevant parameters for the minimization. In a second moment, the analysis was extended to the *operando* dataset. For an accurate extraction of the structural information, all the measurements were analyzed by multiple edge approach [19], *i.e.*, a simultaneous fitting procedure at both Fe and Co metal edges. This in turns means that the same structural parameters are probed

using two independent measurements, hence the reliability of the fitting minimization results enhanced. Figure 4.1.6 displays the details of the present EXAFS analysis for the pristine, partially charged, fully charged, partially discharged, fully discharged states at Fe (top layer) and Co (bottom layer) K-edges. Briefly, (i) only few relevant single EXAFS contributions were necessary to simulate the overall EXAFS signal at each edge; (ii) not only the two-body signals, but also the three- and the four-body MS terms are relevant with intensities comparable to the first shell; (iii) the two-body Fe-M<sup>8c</sup> and Co-M<sup>8c</sup> signals depend on the cation occupancy during charge and discharge, explaining the reduced intensities observed for fully charged states; (iv) the multi-edge refinement allows to take into consideration the oscillation of the MS terms at the Fe K-edge that could overlay the Co K-edge.

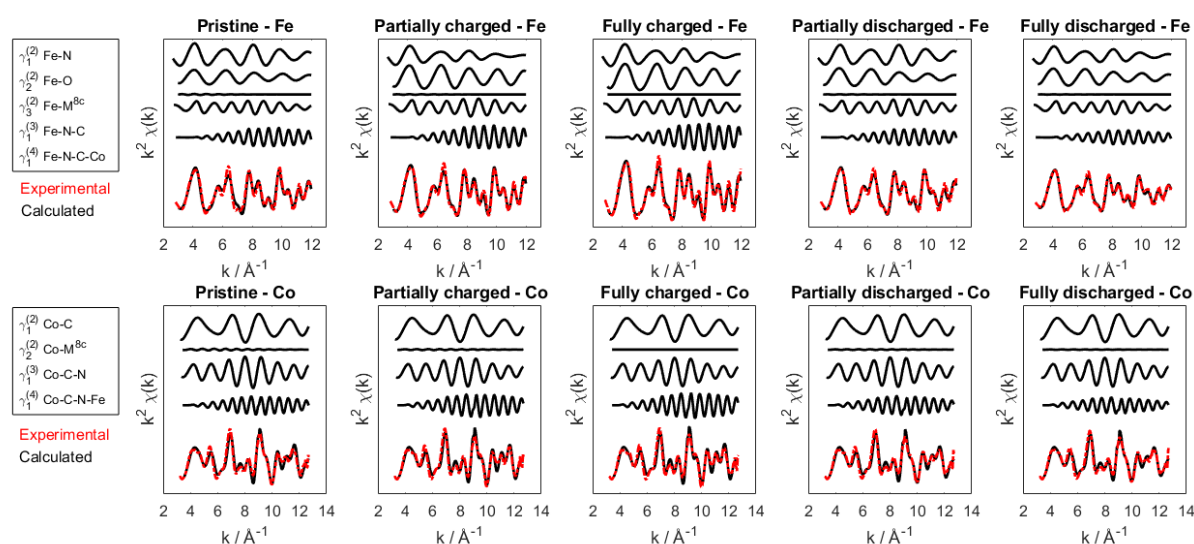


**Figure 4.1.6:** MS contributions and best fit for the pristine, partially charged, fully charged, partially discharged, fully discharged states at Fe (first layer) and Co (second layer) K-edge

The fit was conducted on a selection of spectra, *i.e.*, every three, by taking into account the result of the MCR-ALS analysis. The most relevant fitting results are displayed in Figure 4.1.7. Here, it is noteworthy to point out the differences in the trends displayed in panels a and b. Indeed, even though the bond distances are not significantly altered in the process, the disorder related to the Fe-N bond considerably increases near the fully charged state, *i.e.*, the interstitial ion-depleted state. On the other side, the Co-C fragment is neither electronically (as observed by the XANES of Fig. 4.1.3) nor structurally affected by the electrochemical reaction. Additionally, the number of the linear Fe-NC-Co chains, and labelled as CN<sup>chain</sup>, sets the degeneracy of the Fe-NC-Co fragments and therefore can be considered an indicator of the linearity of the chain (this is due to the strong focusing effect of the linear Co-C-N and of the

additional superfocusing one carried out by the linear Co-C-N-Fe fragment). As seen from panel c, the  $CN^{\text{chain}}$  parameter oscillates around a value of 3.5 during charge, while its centroid slightly decreases in the discharge. Although the large error bars set a limit to further considerations, we might assume that the lithiation could induce a small deviation from the linearity of the orthogonal chains. Finally, the Fe coordination number to the interstitial cation decreases as it is extracted, while it is experiencing a slightly raising trend while discharging (panel d). The number quotation of this parameter can only be considered qualitative. The observed trend is in line with the cation interstitial occupancy in the electrochemical reaction.

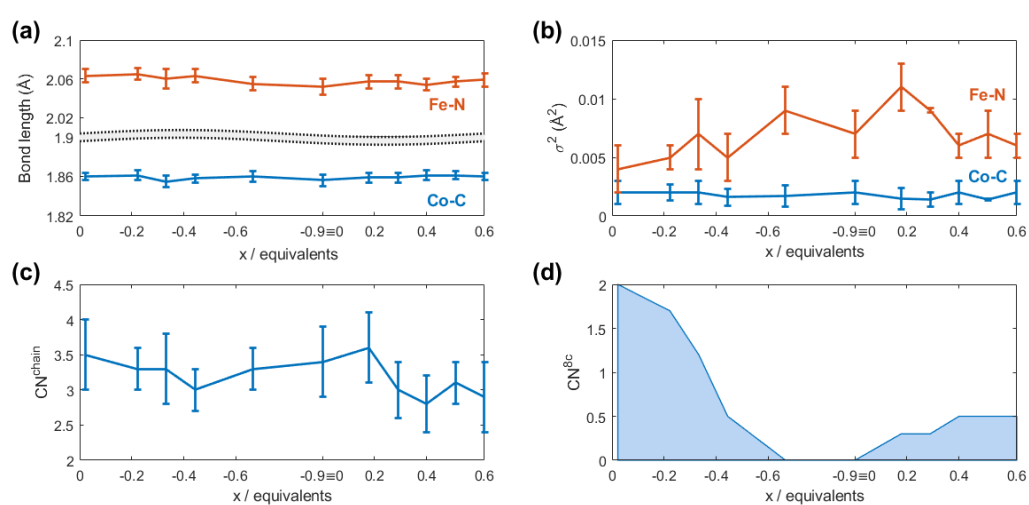
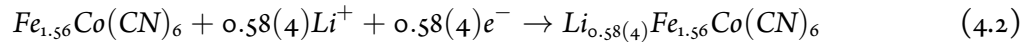
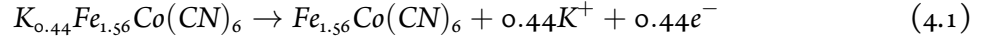


**Figure 4.1.7:** Relevant EXAFS fitting results: (a) First shell distances behavior: Fe-N and Cu-N; (b) EXAFS Debye-Waller factors; (c) Variation in Fe-N-C-Co chains degeneracy during lithiation; (d) Variation in the coordination number of the 8c interstitial cation

The results of the fitting procedure, in terms of relevant bond length distances, corresponding EXAFS Debye Waller factors and coordination numbers are available also in Table 4.5.2 (located at the end of the chapter). In addition, the table indicates the released fitting quotation for  $S_o^2(\text{Fe})$  and  $S_o^2(\text{Co})$  in the pristine sample, which were consequently kept fixed regarding the analysis of the lithiated samples. Moreover, during lithiation process potassium was still considered as 8c metal to obtain a qualitative trend, since  $\text{Li}^+$  ions slightly contribute to the scattering signal. The geometric half-cell parameter ( $a/2$ ) was derived as sum of the Fe-N-C-Co fragment distances.

#### 4.1.4 REACTION MECHANISM

As result of the carried data treatment, we can write in first approximation the following reactions for charge (Equation 4.1) and discharge (Equation 4.2), in the case of a dehydrated structure:



where the number in parentheses indicate the presumable error on lithium equivalents, according to the discussed *operando* measurements.

Due to the importance of deeply understanding the structural and electronic evolution of battery systems, a combined approach adopting independent data treatments able to assess the reliability of the results is a necessity.

#### 4.1.5 CONCLUDING REMARKS

The structural adjustments of the lattice of FeCo were measured via XRD, which probed the material long-range order and retrieved the atomic positions during cycling, confirming an excellent structural retention during the release/insertion processes. Indeed, the *Fm3m* cubic lattice host is preserved through the whole *operando* experiment, with interstitial ions occupying and being extracted from 8c lattice sites. The electronic counterpart was studied via XAFS, which portrayed iron as the main electroactive metal. The MCR-ALS chemometric analysis of the *operando* XANES data was successfully employed to reconstruct the pure spectral components and to follow their respective contribution during cycling, giving further insight into process dynamics. The parasite dehydration process contributes to the irreversible charge capacity, and is not observed in the case of the previously dehydrated *operando* XRD sample. Independent analyses based on linear combination fitting and pre-edge region fitting were carried out to complement and validate the obtained results. Pristine FeCo differs from fully charged and discharged states, but can be described by their linear combination.

The short-range order and structural evolution were investigated by analyzing the EXAFS spectra through a multiple edge refinement approach. While the cobalt centers are not significantly altered by the redox

process, the disorder associated to the Fe-N bond increases remarkably in the oxidized state. Moreover, the linearity of the Fe-NC-Co chains is slightly altered by lithium insertion, while the interstitial cation occupancy is strictly related to the state of charge of the material.

## 4.2 COPPER HEXACYANOFERRATE<sup>3</sup>

### MOTIVATION

Copper hexacyanoferrate (CuHCF) exhibits excellent electrochemical properties as battery electrode [71, 73, 135–141]. In aqueous systems, for instance, it could retain up to 75% of the initial capacity after 40k cycles at a 17C rate [65, 67]. Although the literature reports that both metals in copper hexacyanoferrate can be electroactive [142], the belief that iron is in fact the only active species is widely spread in the battery community [54, 67, 143–145].

In the following extract we demonstrated that also copper is active in copper hexacyanoferrate during the electrochemical reaction with lithium, and that it plays a remarkable role in the redox process. To reach this goal, *operando* XAFS was carried out at both metal centres. The data treatment on the EXAFS was accomplished by using both single edge and multiple edge approaches [19], in the latter case by refining simultaneously the spectral data at two or more edges, which increases the reliability of the structural results. Combined with *operando* XAFS, MCR-ALS was used to recover the spectra of the pure spectral components.

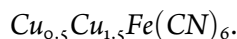
#### 4.2.1 XRD ANALYSIS

The stoichiometry of the resulting CuHCF can be written as  $K_{0.34}Cu_{1.96}Fe(CN)_6$  after XRF analysis, which provided a K/Cu/Fe ratio of 0.34/1.96/1. The Cu/Fe ratio agrees with the weighed ratio of the edge jump values at Cu and Fe K-edge, which resulted 1.9 as well.

The structure of hexacyanoferrates is related to the well-known “soluble” and “insoluble” forms. Both feature a rigid cubic framework of linear –Fe-CN-Cu–NC– chains, where Fe and Cu ions occupy  $4a$  and  $4b$  positions, respectively, and are octahedrally coordinated to –CN and –NC groups, respectively. In case of the “insoluble” form,  $1/3$  of the  $Fe(CN)_6^{4-}$  units is vacant, with the empty nitrogen positions occupied by water molecules to complete the coordination shell of Cu, so that its average coordination would be  $CuN_4O_2$ . Conversely, every  $Fe^{4+}$  atom is octahedrally coordinated by six carbon atoms. Moreover, according to the selected model [122], we considered a fraction of additional Cu atoms occupying interstitial  $8c$  positions, so that the final structure arising from the model can be simplified as

---

<sup>3</sup>Reproduced in part with permission from J. Phys. Chem. C 122, 28, 15868–15877 Copyright 2018 American Chemical Society.



The obtained pattern for copper hexacyanoferrate, depicted in Figure 4.2.1, well matches with the reported model [122], described by a  $\text{Cu}^{\text{II}}/\text{Fe}^{\text{II}}$  ratio of 2. The refinement ( $\chi^2 = 1.45$ ) led to a cubic structure (Space group:  $Fm\bar{3}m$ ) characterized by the lattice parameter  $a = 9.997 \text{ \AA}$ . By refining occupancies of both interstitial and structural copper, and of iron as well, we identified the individual amount of metallic content per site, so that we could write the chemical formula as  $\text{K}_{0.34}\text{Cu}_{0.4}^{\text{8c}}\text{Cu}_{1.6}^{\text{4b}}\text{Fe}(\text{CN})_6$ , where 0.4 is the amount of interstitial copper (8c), the value 1.6 refers to structural copper (4b), while potassium ions were placed in 8c positions. In this case, the refined total amount of ferrocyanide vacancies is about 37%. Although the total amount of copper with respect to iron was not held fixed, the final ratio well agrees with both XRF- and XAFS-derived ratios. This also helps understanding the coordination numbers used for a straightforward EXAFS analysis at the Cu and Fe K-edges.

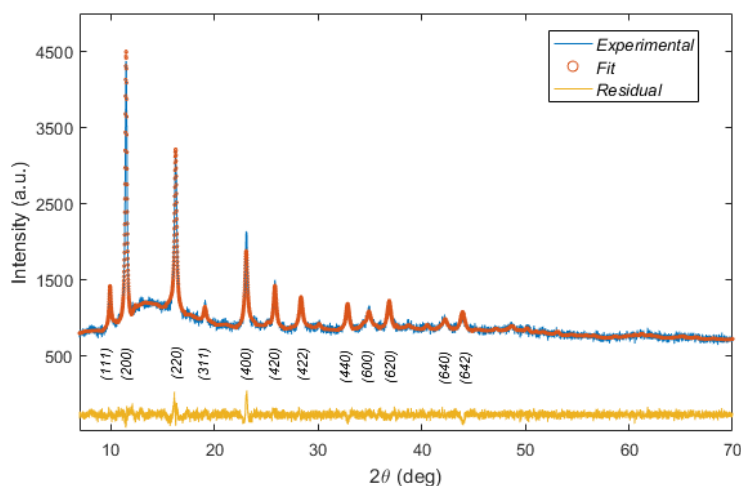


**Figure 4.2.1:** XRD pattern of synthesized CuHCF. In the figure experimental, calculated and residual lines are illustrated. Miller indexes for the main reflections are also shown

#### 4.2.2 XAFS ANALYSIS ON THE PRISTINE MATERIAL

Due to the sensitivity of the XAFS technique for the atomic species, XAFS spectra at both Cu and Fe K-edge of the studied material at the pristine state give information on the charge of the absorbing atom and its coordination geometry. Figure 4.2.2 displays both XANES and EXAFS (experimental best fit) signals as well as the corresponding Fourier Transform curve at the Fe and Cu K-edges. XANES spectra are characterized by pre-edge features due to a transition (labeled as A) to bound states [119], which

becomes an actual pre-edge peak at Cu K-edge. At Cu K-edge this corresponds to the transition  $1s-4p$ , while at Fe K-edge to the dipole forbidden transition  $1s-3d$ . The main peak (labeled as B) called the “edge resonance” is associated to the transition to the continuum. The features of the overall XANES region (labeled as C) arises from multiple scattering resonances of the photoelectrons and from the interatomic distances and coordination geometry [119, 146]. The XANES spectrum of CuHCF at the Fe K-edge is distinctive of Fe in an octahedral environment with the Fe-C-N ligation [134]. The edge position is typical of  $Fe^{II}$  formal oxidation state in the pristine material. For Cu-K-edge XANES spectrum is characterized by the presence of an intense peak before the principal edge which is assigned to the  $1s-4p$  transition [134]. This occurs at about 8984 eV, a value that indicates the presence of a  $Cu^I$  formal oxidation state in the pristine sample, whereas its intensity suggests the 4-fold coordination geometry of the Cu site [147]. This is a reasonable hypothesis based on other evidence available in literature where, for  $Cu^I$ , the transition shows the highest intensity for linear two-coordinated complexes and becomes less intense and broadened as the coordination number increases and/or the symmetry is lowered [148]. Overall this result confirms the local geometry as seen by powder XRD where the absence of 1/3 of the  $[Fe(CN)_6]^{2-}$  ions leads to 4-fold coordination of the Cu site by N ends of the cyanide group. Regarding the associated charge of Cu in the pristine sample the position of the  $1s - 4p$  transition indicates mainly  $Cu^I$ . This result is unexpected, if one considers the precursor salt ( $CuSO_4$ ) used for the synthesis of the material, but is in line to a study of a copper-based PBA [119, 149], suggesting that the formal charge at the copper site for CuHCF is rather close to  $Cu^I$ . Briefly, the driving force of  $Cu^{II}$  to receive electrons in its  $3d$  hole to establish an electron configuration close to  $3d^9$  cooperates with the ability of the CN group to donate electrons from its  $5\sigma$  orbital, resulting in a suppression of the associated positive charge of Cu.

The multiple edge fitting mode has proven to be the most efficient way to analyze the EXAFS spectrum in MHCF [18, 46, 119], since the electron scattering takes place in a strongly correlated system. This allows not only to double up the number of experimental points, while using the same structural parameters which in turn are more constrained by the two absorption channels, but also to check the number of vacancies through the coordination number associated to the Cu-N-C-Fe linear chains. This strategy has already been used by our group and more details about it are available in previous works [19, 119]. Starting from the XRD-derived structural information, the obtained best fit, in terms of  $k^2$ -extracted

EXAFS signal and corresponding Fourier Transforms (FTs), is shown in Figure 4.2.2 for both Fe and Cu K-edges. The good agreement between the experimental curves and the refined ones indicate the reliability of this approach, even though a little discrepancy is observed for the Cu centres (FT above 3 Å). This can be explained by the stoichiometry of the pristine sample, which affects the Cu site exclusively. As shown above by XRD, the chemical formula of CuHCF can be written as  $K_{0.34}Cu_{0.4}^{8c}Cu_{1.6}^{4b}Fe(CN)_6$ , where most of the Cu (*i.e.*, 1.6 Cu per formula unit) occupies the  $4b$  site and is involved in the formation of the CuHCF cubic network, whereas the remaining 0.4 Cu per formula unit occupies the  $8c$  zeolitic site [122]. This has a two-fold effect: i) the Cu K-edge site is characterized by the presence of a secondary site for the Cu and this spoils a little the EXAFS signals as seen before in the FT curve; ii) additional MS signals at both Cu and Fe K-edge due to a Cu-Cu or Fe-Cu interaction at more than 4 Å have been included in the fitting procedure with coordination number of two, which corresponds to the occupation of 1/4 of the  $8c$  structural site. More details about the EXAFS analysis will be presented in the following *operando* XAFS section.

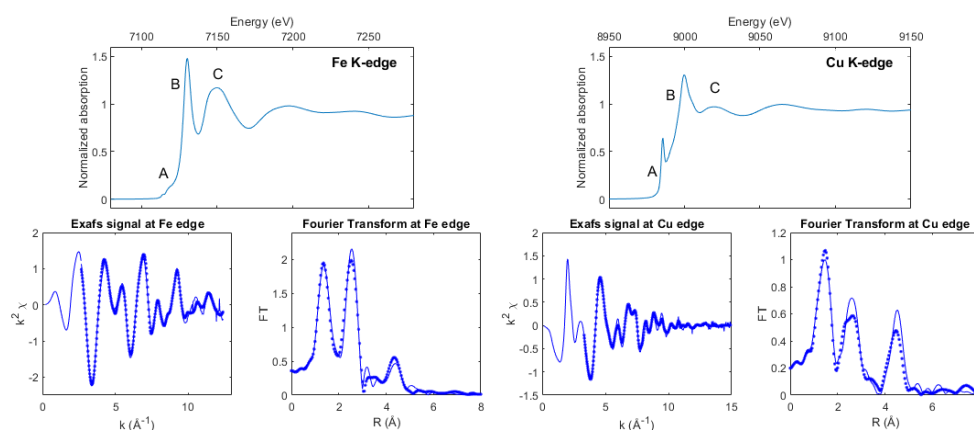


**Figure 4.2.2:** Fe and Cu K-edges. Fit on  $k^2$ -extracted EXAFS signal and corresponding Fourier Transforms (FTs)

A better fit is of course obtained by analyzing the Fe edge in single edge mode. As seen in Figure 4.2.3 the agreement between the experimental and the theoretical curve is excellent. Table 4.5.3<sup>4</sup> (located at the end of the chapter) reports the structural parameters and their corresponding associated errors as obtained by the fitting procedures. The single bond length distances of the Fe-C-N-Cu fragment appear similar in the two-fitting mode, but a quite large uncertainty of 0.03 Å results for the Cu-N distance in the single edge mode. Also, the single edge does not allow the determination of the degree of vacancy in

<sup>4</sup>CN<sup>8c</sup> is a mixed contribution due to potassium and copper during charge (extraction). During lithiation process, the previous metallic species were still considered to obtain a trend, since Li<sup>+</sup> ions slightly contribute to the scattering signal

the structure, which is particularly important during the *operando* scan. Using the multiple-edge fitting, the Fe-C interatomic distance is 1.853(7) Å, a value slightly shorter than those quoted for this class of compounds [18, 119]. The Cu-N bond length results 1.900(15) Å, while the C-N is 1.189(4) Å. Structurally speaking, the occurrence of 1/3 of [Fe(CN)<sub>6</sub>]<sup>2-</sup> ion vacancies reduces the number of Cu-N-C-Fe chains to 4 from the Cu site, unlike the Fe one where the Fe-C-N-Cu fragments is 6. This could be considered only in the multiple edge fitting mode where the best fit is obtained with a value of 4.5(5), in agreement with XRD that returned a 37% of ferrocyanide vacancies. Eventually, these results confirm that the multiple edge fitting is the best choice for this class of compounds.

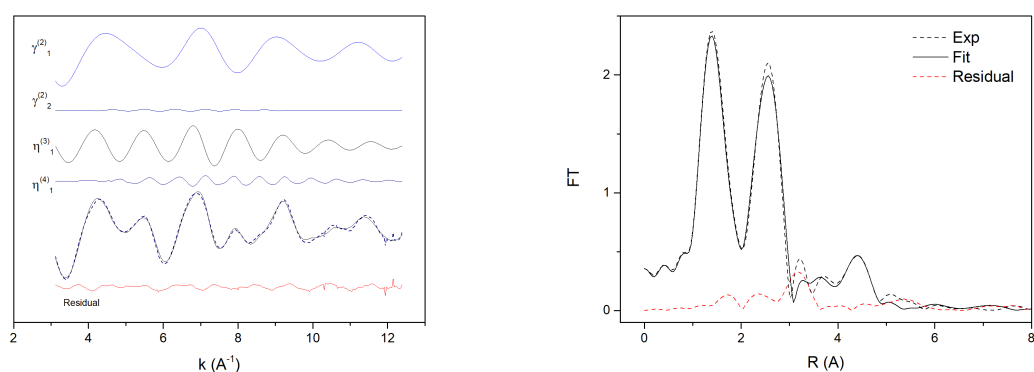


**Figure 4.2.3:** Single edge fitting of the pristine sample (formulated). Fe K-edge

#### 4.2.3 OPERANDO XANES

Figures 4.2.4 and 4.2.11 display the electrochemical signature as obtained during the *operando* XAFS experiment together with the respective XANES curves at both Fe and Cu K-edge. The battery was charged first and then discharged. During the charge, the cations in the 8c position (both potassium and copper ions) are extracted from the hexacyanoferrate structure making feasible the Li<sup>+</sup> insertion in the successive discharge step. We have recorded a total of 64 spectra, 34 during the charge and 30 in the subsequent discharge. The correspondence between ion equivalents and collected spectra is reported in Table 4.2.1.

As shown in Figure 4.2.6, large changes take place in the Cu K-edge spectra, particularly in the pre-edge region. The peak at 8984 eV (1s-4p transition) decreases during charge and is restored during discharge (see Figure 4.2.5). Simultaneously, a new peak grows during charge at slightly higher energy

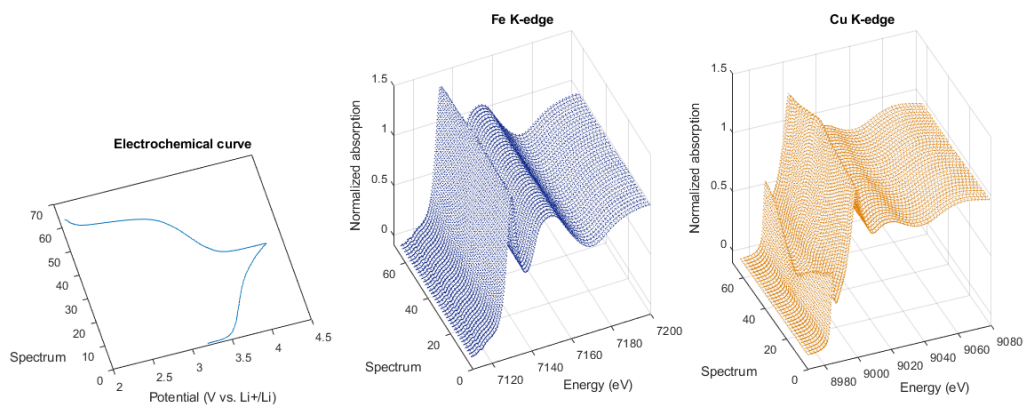


**Figure 4.2.4:** Graphic representation and comparison of iron K-edge and copper K-edge during electrochemical cycling

Charge		Discharge	
x / equivalents	Spectrum	x / equivalents	Spectrum
0.0	1	0.0	34
-0.1	4	0.1	38
-0.2	8	0.2	42
-0.3	11	0.3	45
-0.4	15	0.4	49
-0.5	19	0.5	53
-0.6	23	0.6	57
-0.7	26	0.7	60
-0.8	30	0.8	64
-0.9	34		

**Table 4.2.1:** Correspondence between extracted/ inserted ion equivalents and spectrum number in case of *operando* XAFS

(around 8989 eV) corresponding to the 1s-4p transition in Cu<sup>II</sup>, which disappears during the following discharge. These findings are consistent with the reversible oxidation of Cu<sup>I</sup> to Cu<sup>II</sup> during charge and its subsequent reduction upon discharge.

On the other hand, almost no substantial modification is visible in the XANES spectra at the Fe K-edge, except for a slight shift of the absorption edge to higher energy. A fine structure analysis of the 1s-3d pre-edge peak, however, adds complementary information. As shown in the insert in Figure 4.2.6 and in the are magnification presented in Figure 4.2.7, the peak at 7114 eV shifts towards higher energy at the end of charge, and a new weak peak grows at 7111 eV. These modifications are in line with a different occupancy of the  $t_{2g}$  levels of the 3d orbitals in a low-spin octahedral environment, which is caused by

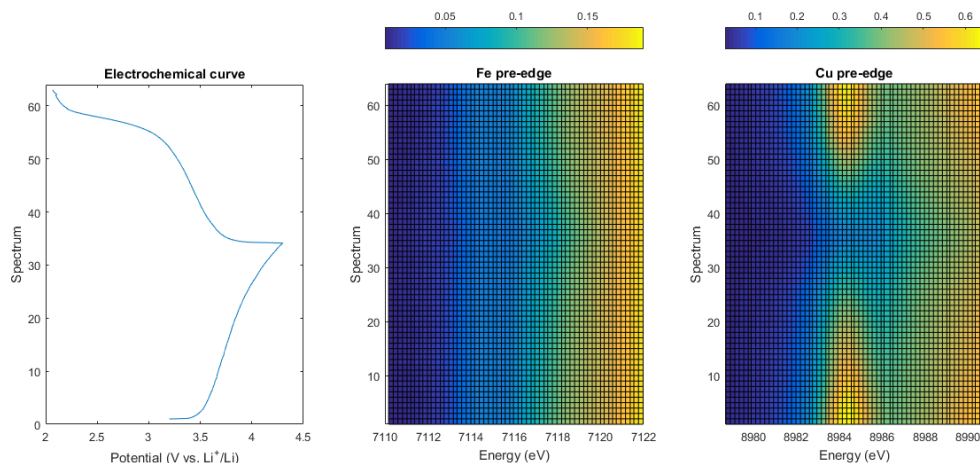


**Figure 4.2.5:** Pre-edge map for both iron and copper metals during cycling

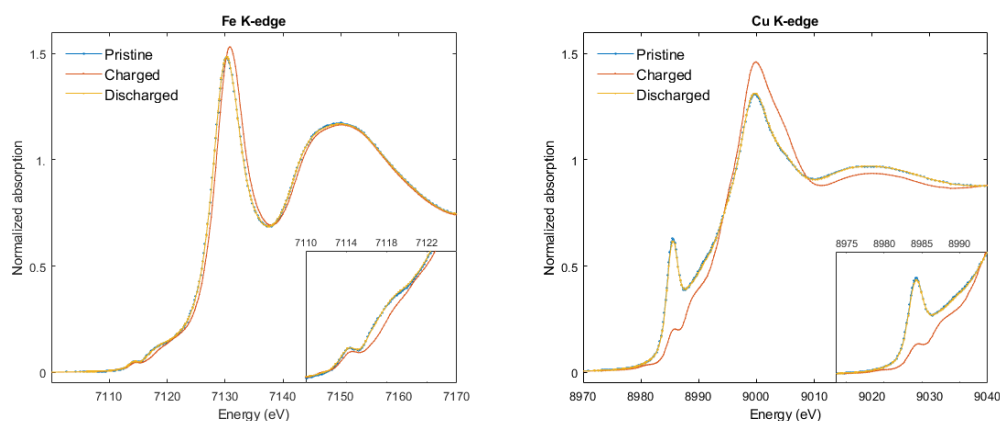


**Figure 4.2.6:** Comparison between pristine, charged, and discharged states at both Fe and Cu K-edge. Insets show the magnification of the pre-edge region

the oxidation of  $Fe^{II}$  to  $Fe^{III}$ .

These results clearly point out that both Fe and Cu are electroactive in this material. This fact represents a new physical insight with respect to the report of Wessells *et al.* [67] on CuHCF material prepared by coprecipitation who only observed  $Fe^{II}/Fe^{III}$  activity, and a confirmation of the mechanism proposed (but not proven) by Okubo *et al.* [150] on the basis of the equivalents of reacted Li. However, Asakura *et al.* [71] previously observed a  $Cu^I/Cu^{II}$  activity by *ex situ* XANES during the lithiation of core@shell CuHCF nanoparticles.

#### 4.2.4 MCR-ALS ANALYSIS

MCR-ALS revealed not only the number of pure spectral components but also their existence range during the whole electrochemical process (see Section 2.3). In this case, the MCR-ALS algorithm was

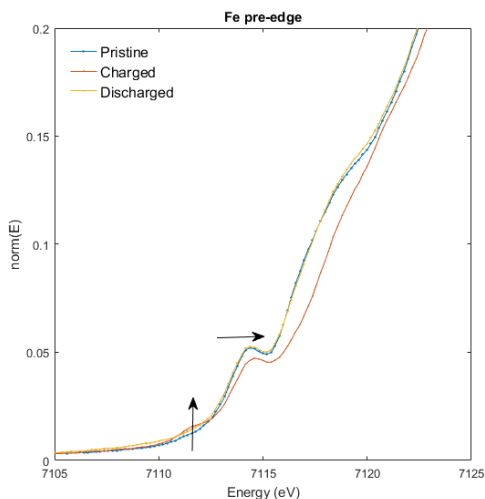


**Figure 4.2.7:** Magnification of Fe pre-edge. Comparison between pristine, charged and discharged states

applied to the whole series of *operando* Cu K-edge XANES spectra. The graphic results of the two matrices, obtained hypothesizing two components for the electrochemical reaction, one the pristine the other the charged sample, are shown in Figure 4.2.8. Further tests considering three species were also computed, but the results of the chemometric procedure sets back to only two components. A complementary analysis was also performed on the Fe XANES spectra, but the dataset was less suitable for MRC-ALS analysis due to the weak dependency of the XANES traces to the intercalation/release reaction. Therefore, it was decided to rely only on the Cu K-edge data.

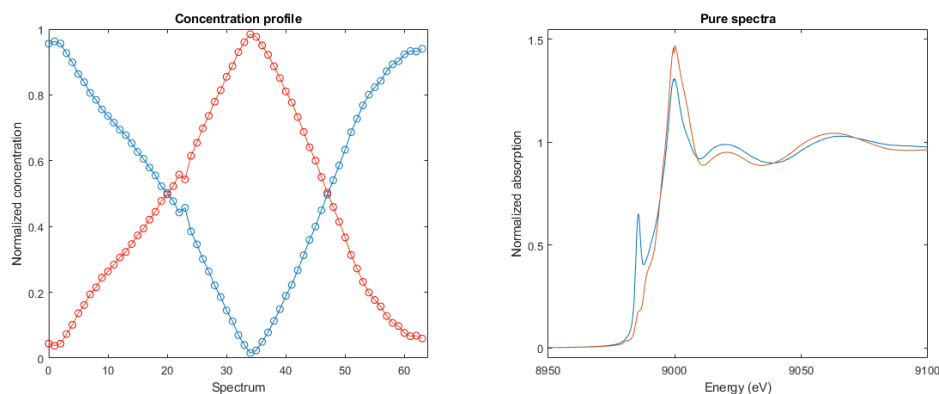


**Figure 4.2.8:** Concentration profile  $C_{S,F}$  and obtained pure spectral components  $A_{W,F}$  of the normalized XANES data taken at the Cu K-edge of CuHCF material

The MRC-ALS analysis indicates that: a) the two components (pristine and charged electrode) progressively transform into each other during the electrochemical reaction; b) by inverting the electrode polarity the initial pristine species is restored; c) the XANES spectra of the pure species computed by

the MRC-ALS analysis are very similar to those measured experimentally (cf. Figure 4.2.6); d) because of the existence of only two spectral components some isosbestic points should be present in the experimental spectra. Finally, the concentration profile described above, where a simple, almost linear and mutual transformation of exclusively two species takes place, demonstrates the weak strain of the material CuHCF, in line with his high cycling stability in the repeated intercalation and release of Li-ions [67].

#### 4.2.5 OPERANDO EXAFS

To investigate the local structure transformation at the two active metallic centers during the *operando* scan, an extensive analysis of the EXAFS data was performed. Since the MRC-ALS analysis presented above for the Cu K-edge XANES spectra indicates that the full charge/discharge cycle can be described as the progressive reversible transformation of only two species, the selection of a limited number of representative spectra for the EXAFS analysis seems largely justified. Therefore, only spectra #1, #10, #18, #27 and the #33 during charge and #40, #54 and #62 in the subsequent discharge were considered. Figure 4.2.9 displays the best-fit plots of the  $k^2$ -extracted EXAFS signals for spectra #1 and #33 at both K-edges, corresponding to the pristine material and to the end of the first charge, respectively. The theoretical curves well match with the experimental ones, demonstrating the reliability of the data analysis. Table 4.5.3 (located at the end of the chapter) reports some relevant structural parameters, such as the interatomic distances and the corresponding Debye-Waller Factors as well as the number of Cu-N-C-Fe fragments, which in turn reveals the degree of vacancies into the open framework structure of CuHCF cathode during the *operando* scan.

Figure 4.2.10 reports the trends of the main calculated EXAFS parameters during charge and discharge. Panels (a) and (b) illustrate the variation in bond lengths and Debye-Waller factors, respectively, of Fe-C and Cu-N. Both Fe-C and Cu-N interatomic distances assume different values in the redox process: in pristine CuHCF (spectrum #1), Fe-C and Cu-N are 1.853(7) and 1.900(15) Å, respectively, whereas in the charged state (spectrum #33) they both stretch to 1.887(7) and 1.954(4) Å. The reverse, instead, is observed at the end of the discharge process (spectrum #62), where these interatomic distances return to 1.856(7) Å and 1.91(1) Å, respectively. Interestingly, Debye-Waller factors give further insight into the redox system. Indeed,  $\sigma^2(\text{Fe-C})$  does not vary almost at all during cycling, assuming a constant value

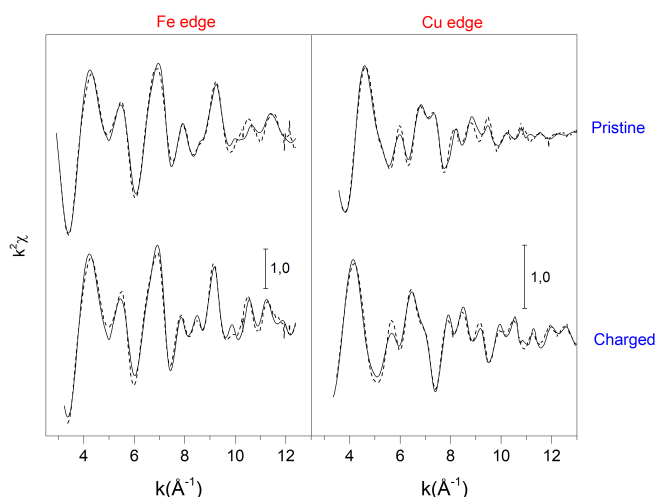


**Figure 4.2.9:** Best fit plots of the  $k^2$ -extracted EXAFS signal of the pristine (spectrum #1) and charged samples (spectrum #33) analyzed at both Fe and Cu K-edges

throughout charge and discharge, and revealing very little modifications of the Fe local environment. On the other side,  $\sigma^2(\text{Cu-N})$  drops during charge, meaning presumably that the ion-extraction process might diminish the copper local asymmetry, whereas it increases during discharge, *i.e.*, ion-insertion, mirroring once again the reversibility of the system. Panel (c) displays the Cu-N coordination number, which is an indicator of the Cu-N-C-Fe linear chains and  $[\text{Fe}(\text{CN})_6]^{2-}$  vacancies. Values oscillate smoothly around the constant value of 4.5, strongly suggesting only a small structural strain in the material during cycling. This result agrees with the long cycle life of copper hexacyanoferrate as cathode material, already reported in the literature [67], since the absence of large distortions during cycling is expected to lead to a better cyclability.

Panel (d), finally, correlates the amount of 8c interstitial cation to the cycling advancement. The trend that we observe, even considering the large associated error, agrees with charge/discharge processes, in other words the system experiences a decrease in cation occupancy (likely due to both potassium and copper extraction) during charge, and the opposite trend is recorded during discharge. This trend has qualitative value, especially for the extraction process, since it derives from a mixed contribution of the interstitial cations.

A last remark on EXAFS fitting parameters concerns the  $a/2$  values, that is the half-cell length (cf. Table 4.5.3). In the pristine sample this results 4.942 Å ( $a = 9.884$  Å), in fair agreement with the value of 4.998 Å obtained by XRD. This small discrepancy is most probably due to the dehydration ( $8\text{o}^{\text{circ}}\text{C}$

overnight) of the electrode before the *operando* XAFS measurement, contrarily to the powder employed for XRD measurement. As a matter of fact, negative thermal expansion is common in PBA materials [131]. Besides, the lattice expands during ion-extraction (charge) and contracts during ion-insertion (discharge), which fully agrees with other works in the literature [96, 97].

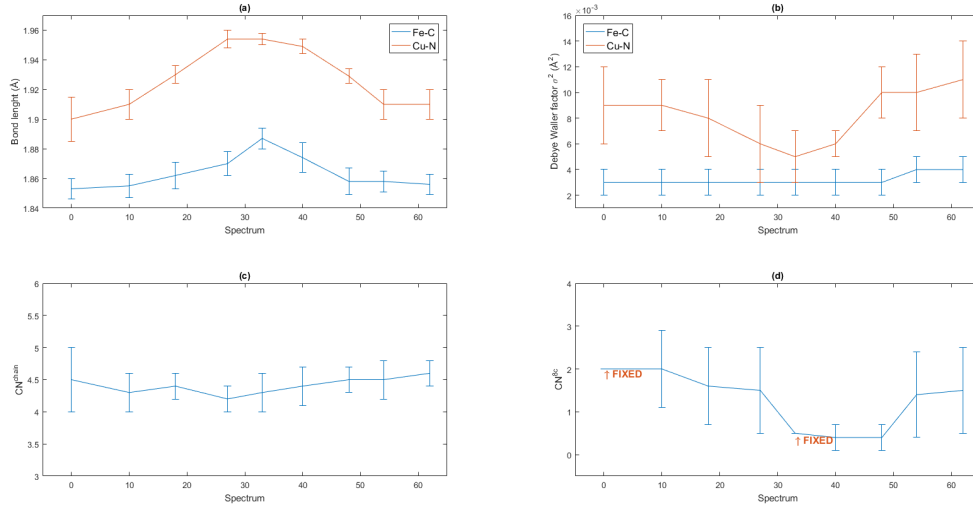
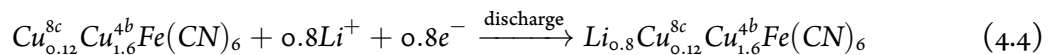
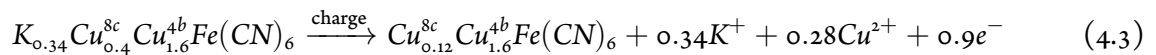


**Figure 4.2.10:** Graphical representation of the main EXAFS parameters trend during cycling. (a) Fe-C and Cu-N bond lengths and (b) Debye Waller factors variation. (c) Copper coordination number to N, or rather number of the Cu-N-C-Fe linear chains. (d) Coordination number to  $8c$  interstitial positions

#### 4.2.6 REACTION MECHANISM

Considering the reported stoichiometry,  $K_{0.34}Cu_{1.96}Fe(CN)_6$ , and that the charge and discharge processes at C/30 current rate last approximately 27 and 24 hours, respectively (cf. electrochemical profile in Figure 4.2.11), we can assume that: 1) during the extraction,  $0.9 e^-$  equivalents flow from the positive electrode, concomitant to the extraction of presumably both  $0.34 K^+$  and  $0.28 Cu^{8c}$ ; 2)  $0.8 Li^+$  equivalents are inserted during the discharge process.

Therefore, we can write in first approximation the charge and discharge processes as follows:



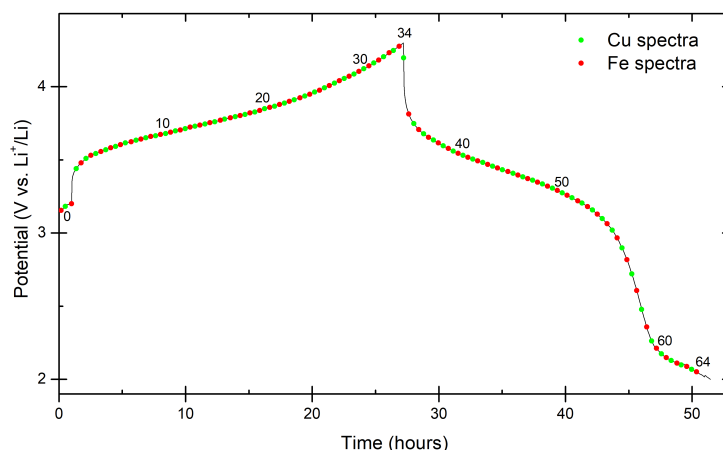


**Figure 4.2.11:** Electrochemical curve recorded during the *operando* XAFS experiment

#### 4.2.7 CONCLUDING REMARKS

Copper hexacyanoferrate was studied for its interesting performance as positive electrode material in alkali-ion batteries. We focused our work on disclosing the participation of the different metal centres during lithiation/de-lithiation electrochemical processes, which is often misinterpreted. The electroactivity of copper and iron centres was proven by means of a joint *operando* XAS/MCR-ALS approach during cycling: *operando* XAS was used to probe simultaneously the chemical environment of both Cu and Fe in CuHCF, while the application of MCR-ALS to the collected data allowed us to discern the presence of two interconvertible spectral components in the charge/discharge processes. The thorough analysis of XANES data confirmed the reversible redox activity of Cu and Fe in CuHCF, the edge and pre-edge signals being strongly influenced by the oxidation state and electron spin configuration. On the other hand, EXAFS fitting underlines the steady multiplicity of Fe-C-N-Cu linear chains, which evidences the structural stability and low strain of CuHCF during cycling, in agreement with the excellent cyclability reported in the literature.

To conclude, it was proven that both metals are electrochemically active during the (de)lithiation process of CuHCF, and that the system relies on a great electronic and structural stability during a full battery cycle.

### 4.3 COPPER NITROPRUSSIDE<sup>5</sup>

#### MOTIVATION

Copper nitroprusside (CuNP) is an analogue compound of CuHCF, where a cyanide in the iron octahedral environment is replaced by a nitrosyl group [123]. Unlike the cyanide ligand, the nitrosyl does not bridge the copper metal, establishing only weak van der Waals interactions with it and enhancing the porosity of the whole structure. Most importantly, the nitrosyl group is a so-called *non innocent* ligand, *i.e.*, it acts as third redox centre, changing meanwhile its coordination to iron and its hybridization. The resulting theoretical capacity is therefore increased compared to CuHCF due to the augmented number of electroactive species and the almost identical formula weight.

The oxidation state and the coordination to iron can be easily asserted by infrared (IR) spectroscopy and DFT-calculated vibrational frequencies, the linear Fe-NO absorbing around 1930-1950  $\text{cm}^{-1}$ , the bent form at 1400-1600  $\text{cm}^{-1}$ .

To the best of our knowledge nothing before us was reported in the literature about the possible use of CuNP as positive electrode material in lithium-ion batteries.

In the following sections, the synthesis, the characterization and the electrochemical properties of CuNP are discussed. Electrochemical tests were first performed, assessing a capacity loss in the first part of the cycling. To deeply investigate the lithiation process and clarify the electrochemical mechanism, *operando* XRD and *operando* XAFS experiments were performed to retrieve structural and electronic information. The dynamic evolution of the system was thoroughly analyzed with the use of MCR-ALS chemometric technique and further compared with *ab initio* simulations. Computational quantum mechanical modelling was accomplished by means of DFT calculations. This combined approach of experimental and theoretical techniques<sup>5</sup> was successfully adopted to untangle the redox mechanism of the electrode material. Differently from other MHCMs that commonly exhibit electroactivity at the metal sites, a ligand was reported for the first time to undergo the redox.

---

<sup>5</sup>Reprinted from 'The electrochemical activity of the nitrosyl ligand in copper nitroprusside: a new possible redox mechanism for lithium battery electrode materials?', Angelo Mullaliu, Moulay-Tahar Sougrati, Nicolas Louvain, Giuliana Aquilanti, Marie-Liesse Doublet, Lorenzo Stievano and Marco Giorgetti, *Electrochimica Acta* 257 (2017) 364–371, Copyright 2017, with permission from Elsevier

#### 4.3.1 SYNTHESIS

The synthesis was repeated three times under exactly the same conditions to evaluate the reproducibility, giving rise to three batches, labeled as AM<sub>1</sub>, AM<sub>2</sub>, AM<sub>3</sub>. The yield was calculated *a posteriori* according to the real composition. As illustrated in Table 4.3.1, the synthesis protocol gave reproducible results in terms of chemical composition and yield.

**Table 4.3.1:** List of samples, Yield, TGA features, and chemical analysis by XRF and CHN

Sample	Cu/Fe	N/C	Fe/NO	Cu/NO	H <sub>2</sub> O/NO	Yield (%)	Inflection point (°C)	Mass loss at inflection point (%)
AM <sub>1</sub>	0.63	1.21	1.20	0.75	0.47	71.4	255.5	22.2
AM <sub>2</sub>	0.63	1.21	1.22	0.77	0.51	71.4	255.7	24.4
AM <sub>3</sub>	0.69	1.20	1.19	0.81	0.56	69.3	255.6	23.9

#### 4.3.2 CHARACTERIZATION

Figure 4.3.1 reports the TGA curves of the three batches, subtracted by the reference (empty holder), and normalized to the initial sample mass. The major weight loss is observed reproducibly for all samples in the range 240°-270°C, with a maximum loss rate at 255°C (Table 4.3.1). This mass loss could be attributed to the decomposition of one cyanide and one nitrosyl ligand. The samples can be considered as non-hydrated, since for hydrated ones the relative mass loss would have exceeded 10% of the initial mass (Figure 4.3.1). Therefore, water is believed to occupy interstitial positions. Only AM<sub>2</sub> and AM<sub>3</sub> display a weak mass loss below 100°C due to their relatively higher water content, in agreement with the hydrogen content revealed by CHN analysis (Table 4.3.1).

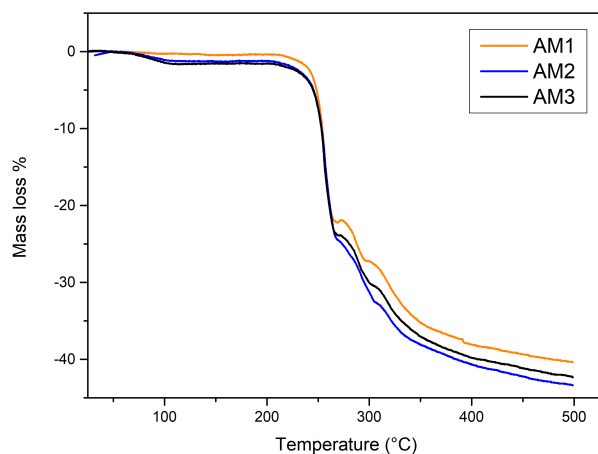


**Figure 4.3.1:** TG Analysis of the synthesized batches

Fe/Cu and C/N ratios were calculated from XRF (Table 4.3.1). Sodium and sulphur, possible contaminants contained in the precursors, were not detected, even though the presence of sodium in interstitial positions is commonly reported in the literature. No clear-cut difference can be appreciated among the three synthesized batches. As a matter of fact, spectra are overlapping. CHN analysis gave information on carbon, hydrogen (*i.e.*, water) and nitrogen content. Table 4.3.1 reports the atomic ratios normalized to the nitrosyl group, giving very reproducible results.

The chemical formula for CuNP can be thus expressed as:  $Cu_{0.8}[Fe_{1.2}(CN)_5(NO)] \cdot 0.5H_2O$ .

Figure 4.3.2 displays the powder XRD profile of the as-synthesized CuNP and the profile matching refinement. The material presents a high degree of crystallinity, while the pattern well matches with the structural model [123]. After profile matching with constant scale factor, the lattice resulted tetragonal (space group  $I4mm$ ), characterized by the cell parameters  $a = 7.12(1) \text{ \AA}$  and  $c = 10.93(1) \text{ \AA}$ .

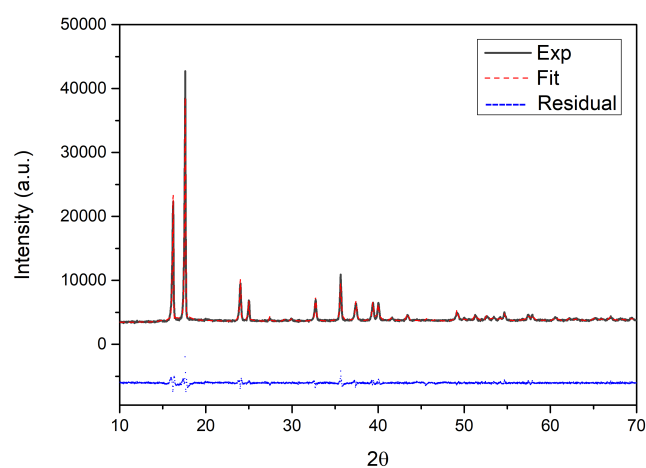


**Figure 4.3.2:** Profile matching refinement of CuNP

The XRD patterns of the three batches are shown in Figure 4.3.3, while the lattice parameters derived from the profile matching analysis are illustrated in Table 4.3.2. Concerning the lattice parameters  $a$  and  $c$ , small differences are appreciated in the second decimal digit which might be correlated to the water content.

The higher the water amount, the smaller the lattice, presumably because of electrostatic attractions. Moreover, the shown patterns display the same array of peaks, apart from the reflection located at  $19.6^\circ$  (Figure 4.3.3). This peak is observed only for AM2 and AM3 and its intensity is proportional to the

**Table 4.3.2:** Results of the profile matching on the synthesized batches. The water content is added as last column

Sample	a (Å)	c (Å)	Water content (mol/formula unit)
AM1	7.1223	10.9421	0.47
AM2	7.1185	10.9327	0.51
AM3	7.1164	10.9289	0.56

water content. The peak situated at  $19.6^\circ$  might therefore be related to the interstitial water. To sustain this hypothesis, the peak under consideration disappears in all samples after vacuum drying at room temperature overnight.

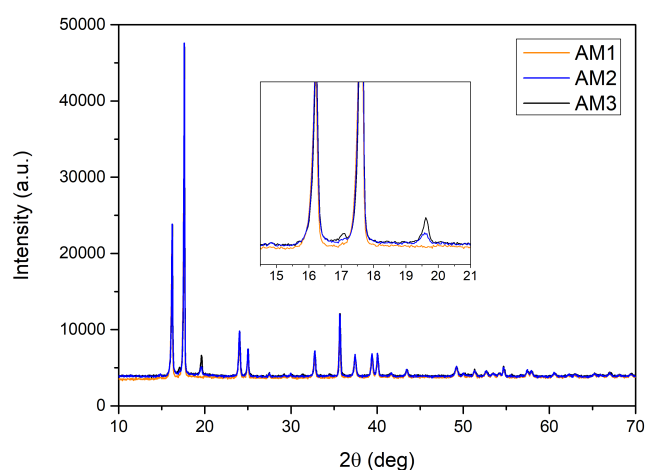


**Figure 4.3.3:** XRD patterns of AM1, AM2, AM3. The inset displays the magnification of the region around  $19.6^\circ$

The cyclic voltammetry curve at low scan rate (starting at OCP value with a negative polarization) shown in Figure 4.3.4 indicates the occurrence of several successive redox processes, labeled with letters a-d. Following the reduction (discharge), the peaks appearing in the 2.0-2.6 V vs.  $\text{Li}^+/\text{Li}$  region may be attributed to redox activity associated to the structural metals constituting the framework, Cu and Fe [142]. Their respective opposite processes are observed during the subsequent anodic scan, which are visible in the following potential ranges: 2.3-2.5, 2.8-3.0 and 3.3-3.5 V vs  $\text{Li}^+/\text{Li}$  (respectively peaks b, c, and d). An additional redox reaction takes place at lower potentials (peak a), *i.e.*, 1.8 V (reduction) – 1.9 V (oxidation) vs.  $\text{Li}^+/\text{Li}$ , an energy at which the reduction of -NO ligand would be possible [151, 152].

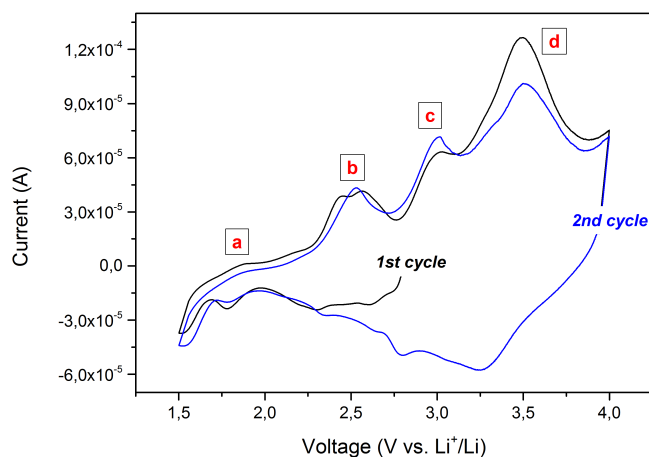


**Figure 4.3.4:** Cyclic voltammetry at  $0.1 \text{ mV s}^{-1}$  scan rate of CuNP in the  $1.5 < E < 4.0 \text{ V}$  vs.  $\text{Li}^+/\text{Li}$  potential window

#### 4.3.3 ELECTROCHEMICAL TESTS

##### LI HALF-CELLS

The trend in capacity upon cycling is shown in Figure 4.3.5 at a moderately fast current rate ( $C/5$ ). The figure displays the evolution of both specific capacity and coulombic efficiency with the number of cycles. The capacity decreases strongly in the first few cycles and remains constant at a relatively low capacity (about  $40 \text{ mAh/g}$ ), whereas the efficiency experiences a remarkable increase within the first 20 cycles.

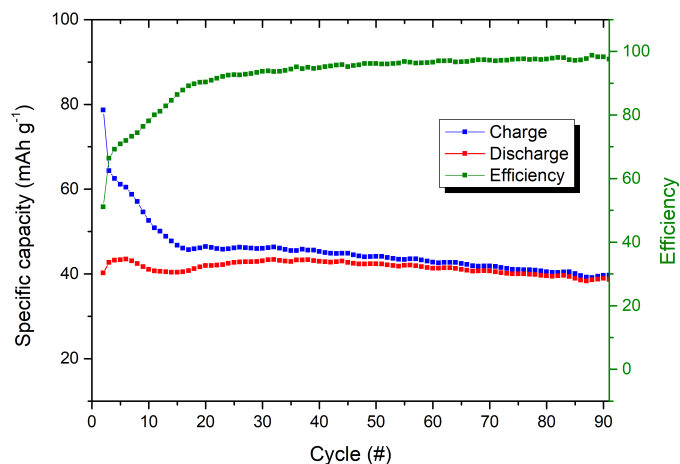


**Figure 4.3.5:** Evolution of specific capacity and coulombic efficiency of CuNP upon cycling by imposing a  $C/5$  rate in the  $1.5 < E < 4.0 \text{ V}$  vs.  $\text{Li}^+/\text{Li}$  potential window

The loss in capacity during the first cycles is accompanied by an important evolution of the electrochemical signature, as shown in Figure 4.3.6. In fact, after a first long charge process associated to a limited discharge, giving as result a poor efficient event (efficiency roughly 50%), the material faces an electrochemical adjustment. Insertion and extraction plateaux raise in potential in the range 3.0-4.0 V. Furthermore, the cycling acquires a more reversible behaviour, and the efficiency increases.

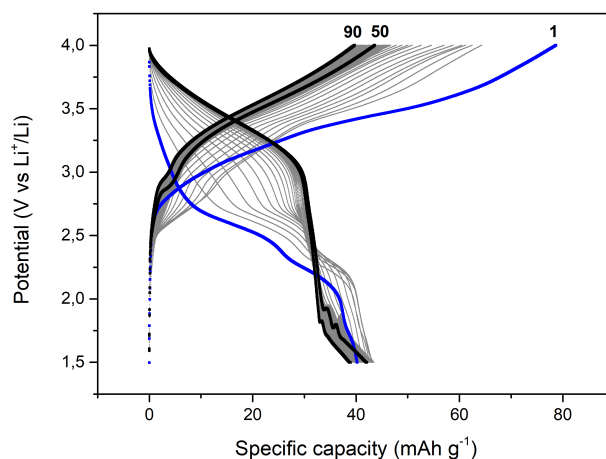


**Figure 4.3.6:** Electrochemical profile upon cycling by imposing a C/5 rate in the  $1.5 < E < 4.0$  V vs.  $\text{Li}^+/\text{Li}$  potential window. The 1<sup>st</sup>, 20<sup>th</sup>, 50<sup>th</sup> and 90<sup>th</sup> cycles are highlighted

*In situ* CV was performed at different cycles to explore the electrochemical signature in distinct cycle moments. Cyclic voltammograms were performed at  $0.1 \text{ mV s}^{-1}$  in the  $1.5 < E < 4.0$  V vs.  $\text{Li}^+/\text{Li}$  potential window. Voltammograms were recorded after the 1<sup>st</sup>, 20<sup>th</sup>, 50<sup>th</sup> and 90<sup>th</sup> galvanostatic cycles and compared in Figure 4.3.7. A deep change in the electrochemical response occurs upon cycling, in agreement with the galvanostatic cycling (Figure 4.3.6). After 20 cycles, the main redox process takes place at 2.7-3.0 V, while reactions of minor entity still occur at 2.3-2.5 and 3.4-3.6 V. After the 50th cycle, the electrochemical response is stable in time, and so do both the redox reactions and the capacity beneath the curve, as already evidenced from galvanostatic cycling.

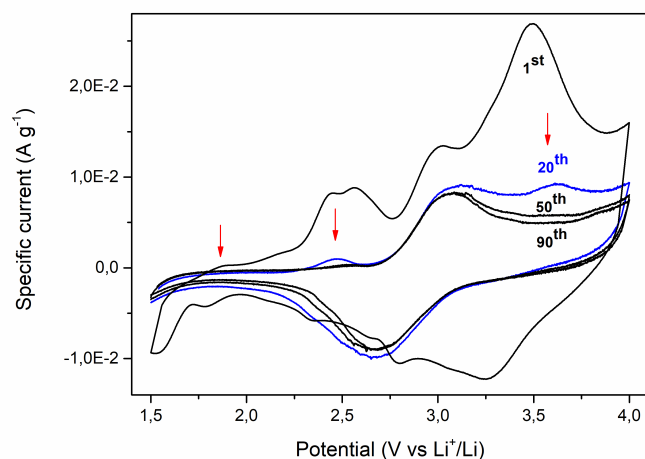


**Figure 4.3.7:** Voltammograms recorded at the 1<sup>st</sup>, 20<sup>th</sup>, 50<sup>th</sup> and 90<sup>th</sup> cycles. CVs have been recorded in the  $1.5 < E < 4.0$  V vs.  $\text{Li}^+/\text{Li}$  potential range at a  $0.1 \text{ mV s}^{-1}$  scan rate

Figure 4.3.8 depicts the trend in specific capacity while varying the current rate (C/40, C/20, C/10, C/5, C/2.5), calculated by considering the theoretical specific capacity equal to 114 mAh/g. Overall, the efficiency is high also at high rates, while the capacity retention is not much affected passing from a C/10 rate to a C/2.5. However, the absolute values remain low.

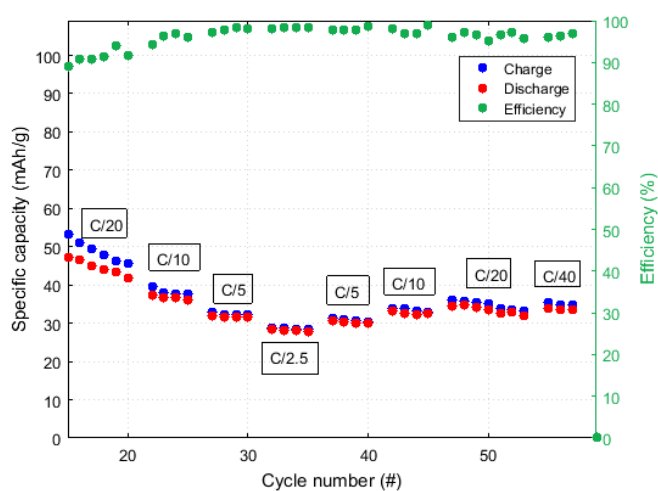


**Figure 4.3.8:** C-rate test in the  $1.5 < E < 4.0$  V vs.  $\text{Li}^+/\text{Li}$  window at C/40, C/20, C/10, C/5 and C/2.5

We have appreciated high specific capacity values only if a low C-rate is applied at the beginning of the cycling. Figure 4.3.9 presents the discharge process on CuNP at C/40 rate after charging at 4.0 V vs.  $\text{Li}^+/\text{Li}$ . The reduction of the active material has been carried out till 1.5 V vs.  $\text{Li}^+/\text{Li}$ , and is responsible

for a specific capacity that exceeds 120 mAh/g. This value is explainable only considering all three redox centres. Nevertheless, the evolution and fading in capacity in the following cycles is coherent with what already shown in Figure 4.3.5.

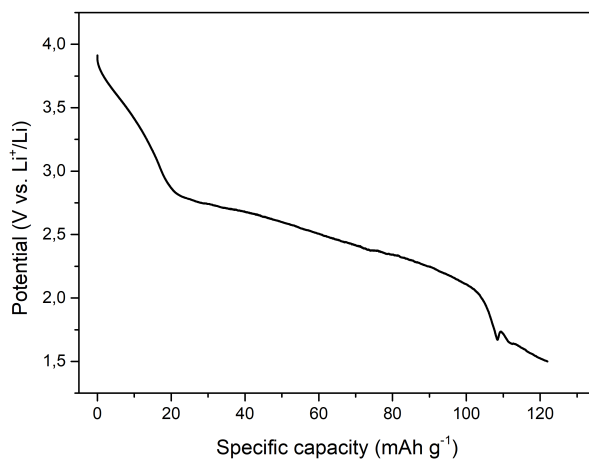


**Figure 4.3.9:** Discharge process at C/40 rate to 1.5 V after charging at 4.0 V vs. Li<sup>+</sup>/Li

#### NA HALF-CELLS

In the perspective of a post-lithium strategy, we have carried out tests in organic Na medium. Figure 4.3.10 displays the evolution in capacity and efficiency while cycling at C/5 rate in a Na half-cell. The observed trend is qualitatively similar to the one obtained in Li half-cells (cf. Figure 4.3.5); despite this, the capacity loss is even greater and the performance stability in time is reached only after 30-40 cycles (capacity  $\approx$  15 mAh/g). An interesting feature concerns the efficiency evolution, whose trend results improved in a Na-ion system. Overall, the implementation in organic Na medium would need further efforts and is at present not competitive with other alternatives.

#### 4.3.4 OPERANDO XRD

The Rietveld refinement on the pristine CuNP electrode is presented in Figure 4.3.11a. Peaks deriving from PTFE and Be are labeled, while Miller planes are indicated in brackets. The resulting structure is tetragonal (space group  $I4mm$ ), characterized by lattice parameters  $a = 7.089 \text{ \AA}$  and  $c = 10,888 \text{ \AA}$ , in agreement with the assumed model [123].

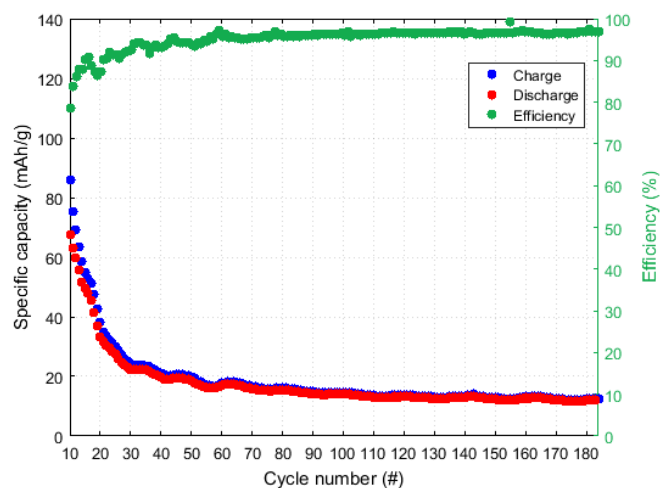


**Figure 4.3.10:** Evolution of specific capacity and coulombic efficiency of CuNP upon cycling by imposing a C/5 rate in the  $1.8 < E < 4.0$  V vs.  $\text{Na}^+/\text{Na}$  potential window

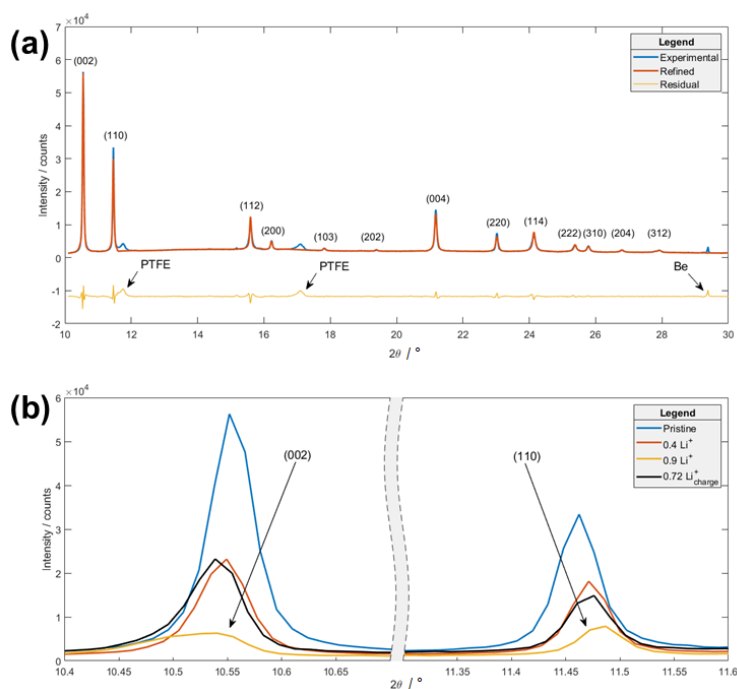


**Figure 4.3.11:** (a) Rietveld refinement of pristine CuNP electrode. (b) (002) and (110) Miller planes at different lithiation steps (pristine, 0.4, 0.9 and 0.72 Li-inserted)

A selection of recorded *operando* XRD patterns is reported in Figure 4.3.11b. Pristine (blue line), partially discharged (incomplete lithiation, *i.e.*, 0.40 Li-equivalents; red line), discharged (complete lithiation, *i.e.*, 0.90 Li-equivalents; yellow line) and partially charged (incomplete de-lithiation, *i.e.*, 0.72 Li-equivalents; black line) states are here compared for the (002) and (110) Miller planes. During discharge (arrows direction), (00x) planes shift towards smaller  $2\theta$  angles, whilst the opposite occurs for

the (yyo) planes. This indicates a gradual and simultaneous (xy) plane contraction and z-axis elongation. This result can be explained as the combination of two main reasons: (i) due to the higher porosity in the z-direction created by the non-bridging nitrosyl ligand and (ii) the elongated structure of CuNP caused by the Jahn-Teller distorted Cu<sup>II</sup> (d<sup>9</sup> configuration), lithium ions are preferentially inserted in the 8c Wyckoff positions (as graphically represented in Figure 4.3.12 and reported in Table 4.3.3), where they interact with the N-terminals of the equatorial cyanides, as suggested by DFT. Moreover, peak intensities decrease during discharge, being the crystallinity reduced in response to lithium insertion, while an inversion of relative peak intensities for the (002) and (110) planes occurs at the end of the discharge. During charge, the opposite trends are observed, being the basal plane, the z-dimension and the peak intensities partially restored. A more quantitative analysis was carried out, further confirming the already observed trends. Figure 4.3.12 illustrates the variation in lattice parameters along the lithiation: the slight peak shifts presented in Figure 4.3.11 correspond to a variation in lattice parameters that never exceeds 0.5%. Such a small lattice strain during the lithiation is typical for so-called zero-strain materials and demonstrates CuNP exhibits a good long-range structural stability during the first cycle.

Atom	Wyckoff position	Site symmetry group	Multiplicity
Fe	2a	4mm	2
Cu	2a	4mm	2
<i>C<sub>equatorial</sub></i>	8c	..m	8
<i>C<sub>axial</sub></i>	2a	4mm	2
<i>N<sub>equatorial</sub></i>	8c	..m	8
<i>N<sub>axial</sub></i>	2a	4mm	2
<i>N<sub>nitrosyl</sub></i>	2a	4mm	2
<i>O<sub>nitrosyl</sub></i>	2a	4mm	2
Li	8c	..m	8

**Table 4.3.3:** Wyckoff positions, site symmetries and multiplicity of atoms in the CuNP unit cell

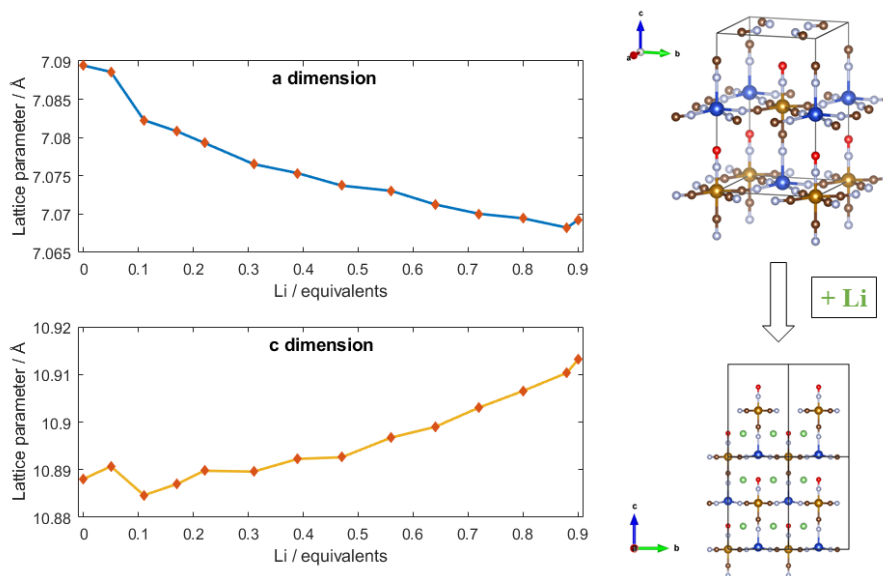


**Figure 4.3.12:** Evolution of the lattice parameters during discharge (left) and graphical representation of the lithiation process (Fe: light- brown; Cu: blue; C: brown; N: light blue; O: red, Li: green)

Further information regarding the fit goodness for the discussed XRD data treatment are available in Table 4.3.4.

Pattern	$xLi^+$	Rwp	$\chi^2$
1 (pristine)	0.00	5.29	7.03
5	0.05	6.43	10.7
10	0.11	6.39	7.31
15	0.17	6.16	5.91
20	0.22	5.45	4.55
25	0.31	6.43	5.15
30 (partially discharged)	0.39	6.72	5.21
35	0.47	6.32	4.33
40	0.56	6.98	4.90
45	0.64	6.95	5.00
50	0.72	6.94	5.10
55	0.80	7.38	5.80
60	0.88	7.39	5.77
65 (fully discharged)	0.90	7.29	6.33
70	0.81	6.06	6.43
75 (partially charged)	0.73	5.18	6.06

**Table 4.3.4:** Fit goodness relative to the XRD data treatment

#### 4.3.5 OPERANDO XAFS

Figure 4.3.13 displays a selection of normalized XANES spectra recorded during the *operando* XAFS experiment at the Fe and Cu K-edge. The formal oxidation state of Fe in the native cathode material could be between (+2) and (+3), in line with a previous soft XAFS study of sodium nitroprusside, where a strong metal-to-ligand charge-transfer from the Fe 3d to NO 2p orbitals was predicted [153]. The initial state of the Fe centres can thus be better described by  $\text{Fe}^{\text{II}+\delta}$ . The  $\text{Fe}^{\text{II}+\delta}/\text{Fe}^{\text{II}}$  reduction is appreciated not only as a slight shift of the white line, but also as a different occupancy of the  $t^{2g}$  levels in the pre-edge region, in line with the reduction of Fe from a partial trivalent to a divalent state in a low-spin octahedral environment. The evolution of Cu K-edge is consistent with the  $\text{Cu}^{\text{II}}/\text{Cu}^{\text{I}}$  reduction: the raise in intensity of the 8981 eV peak (labeled as peak B, cf. Figure 4.3.14) and the decrease of the 8986 eV peak (labeled as peak C, cf. Figure 4.3.14) are attributed to the 1s-4p transition of  $\text{Cu}^{\text{I}}$  and  $\text{Cu}^{\text{II}}$ , respectively [147, 149, 154, 155].

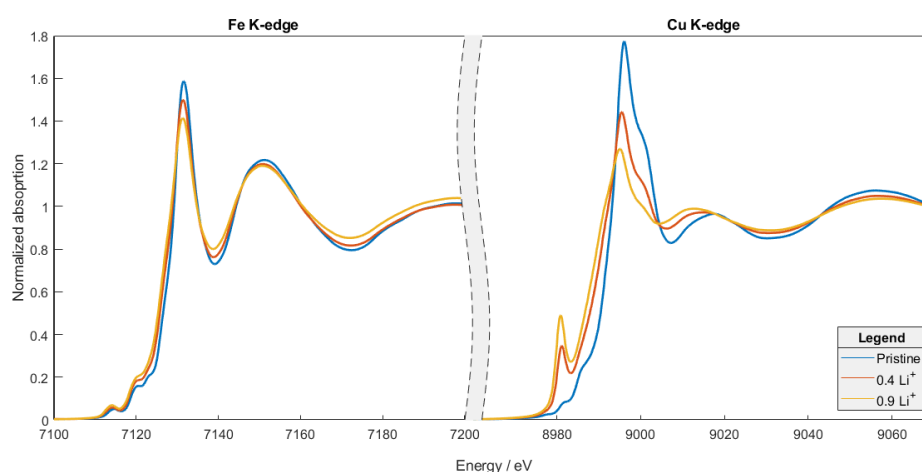


**Figure 4.3.13:** Selected *operando* XAFS spectra at Fe and Cu K-edge during discharge. Pristine and discharged states (0.4 and 0.9 Li-inserted) are shown

A quantitative data treatment was carried out in the Cu pre-edge region and reported in Figure 4.3.14a, b. The pre-edge involves three contributions, labeled as A, B and C (cf. inset of Figure 4.3.14a): the inset of Figure 4.3.14a illustrates a fit example on the pristine sample, where the signal was fitted with three Gaussian functions after background subtraction. Being peak B a signature of  $\text{Cu}^{\text{I}}$  species and already present in the pristine sample, we can deduce that the overall copper has a slight monovalent trait so that we can write  $\text{Cu}^{\text{II}-\epsilon}$ . Panel b correlates the centroid shift relative to peak B to the inserted lithium equivalents. A drastic change in centroid position takes place in the  $0.24 < \text{Li} < 0.60$  range, assuming

instead an almost constant value outside the range. If the slope of this graph could be used as reaction coordinate, we would then suppose that the highest rate for copper reduction occurs around  $0.24 < \text{Li} < 0.60$ .

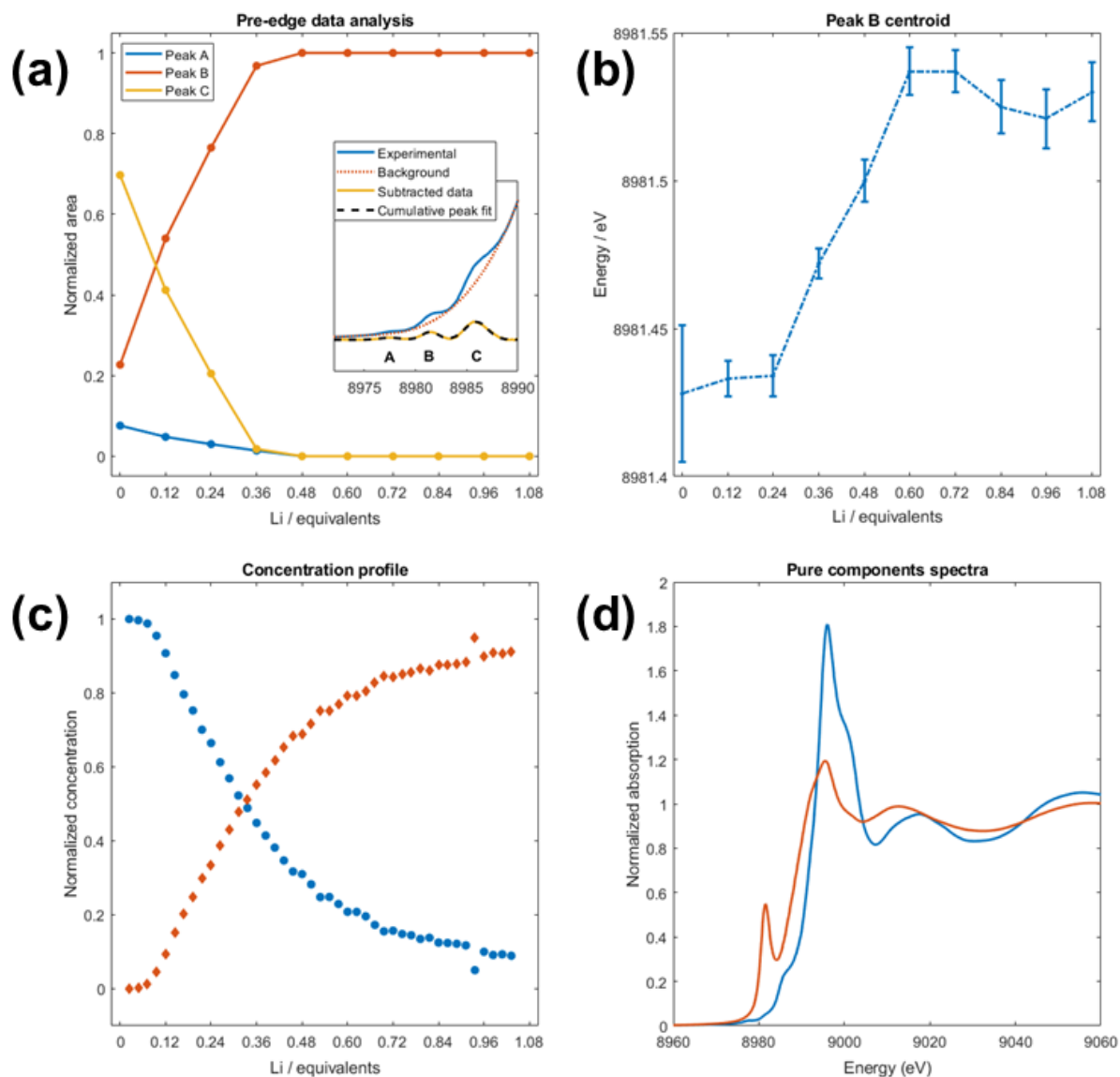


**Figure 4.3.14:** (a) Pre-edge data analysis at the Cu K-edge: evolution of normalized area of three different features (A, B, C) during lithiation. Inset displays the fit performed for the pristine material. (b) Centroid shift for peak B during lithiation. (c) MCR-ALS analysis at the Cu K-edge: concentration profile plot and (d) pure components spectra

An independent analysis was performed by using MCR-ALS chemometric technique. In this case, the MCR-ALS algorithm was applied to the whole series of *operando* Cu K-edge XANES spectra revealing a progressive transformation of the pristine to another species (cf. Figure 4.3.14, panel c), which is most likely the transformation of  $\text{Cu}^{\text{II}}$  containing species to  $\text{Cu}^{\text{I}}$  species. This, in turn, suggests that

two species (represented in Figure 4.3.14, panel d) are exclusively present during the electrochemical reduction. A comparison between the pure spectral components and the pristine and discharged states is reported in Figure 4.3.15.

A similar concentration profile was obtained by looking at the Fe K-edge dataset, while a three-species system was also considered, here not presented, confirming though the occurrence of two species only. Even though the process does not completely end, we can appreciate the concentration profile slope change after 0.60 Li equivalents, suggesting a decreasing rate in the Cu reduction in agreement with the pre-edge data analysis.

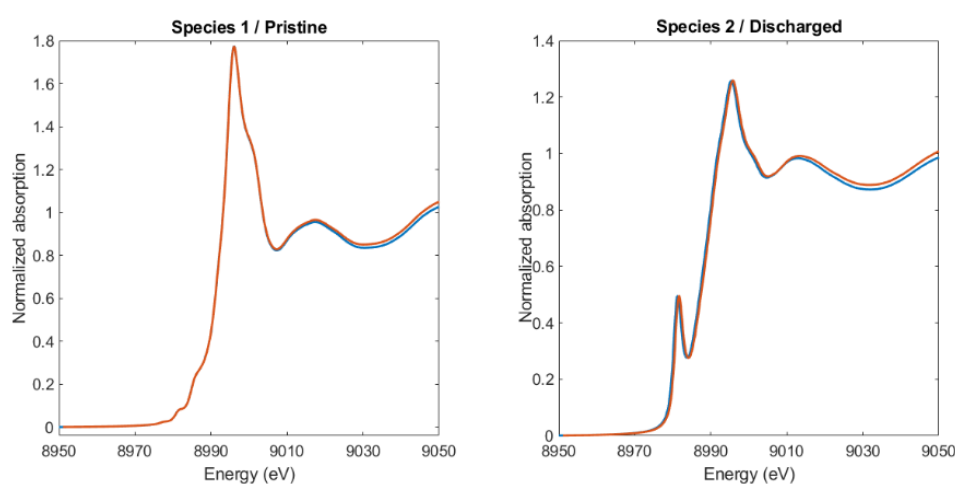


**Figure 4.3.15:** Comparison between pure spectral components and CuNP pristine and discharged states

Complementary structural information occurring to both Cu and Fe site can be gained by looking at the extended portion of their K-edge XAFS spectra. Analysis of the pristine electrode was first done to check the reliability of the structural model as well as to set the relevant parameters for the minimization. For an accurate extraction of the structural information, both Fe and Cu edges were analyzed by multiple edge approach [19], *i.e.*, a simultaneous fitting procedure at both metal edges. This in turn means that the same CuNP structural parameters are probed using two independent measurements, hence the reliability of the fitting minimization results enhanced. Figure 4.3.16 displays the details of the present EXAFS analysis for the pristine electrode at Fe (panel a) and Cu (panel b) K-edges, and respective Fourier transforms (FTs) (panels c and d). Briefly, (i) only few relevant single EXAFS contributions are necessary to simulate the overall EXAFS signal at each edge; (ii) not only the two-body signals, but also the three- and the four- body MS terms are relevant; (iii) the multiple edge refinement

allows to take into consideration the oscillation of the MS contributions at the Fe K-edge that overlay the Cu K-edge.

The results of the fitting procedure, in terms of relevant bond length distances, corresponding EXAFS Debye Waller factors and coordination numbers are available in Table 4.5.4 (located at the end of the chapter). The table also indicates the released fitting quotation for  $S_0^2(\text{Fe})$  and  $S_0^2(\text{Cu})$  in the pristine sample, which were consequently kept fixed regarding the analysis of the lithiated samples.

The fit was conducted on a selection of spectra, *i.e.*, every three, by taking into account the result of the MCR-ALS analysis. Secondly, a more flexible and less rigid structural model was required: as shown by the DFT calculations and XANES traces, the lithiation not only induces local structural arrangements at the Cu site but is also related to the bending of the Fe-N-O angle. The outcome of the fitting procedures for all samples, reported in Table 4.5.4, shows consistent structural modifications upon lithiation. Among the various structural parameters described in the fitting table, the first shell distances and relative Debye-Waller factors deserve a close inspection. Their variation in the electrochemical reaction is plotted in Figure 4.3.16 panels (e) and (f). While bond lengths are almost constant, a dramatic increase of the structural disorder, especially at the Cu site, is demonstrated by the corresponding EXAFS Debye-Waller factors. The C-N bond vibrates similarly around the equilibrium position in all samples. Two more considerations: (i) the number of Cu-NC-Fe linear atomic chains seen from the Cu site, labeled as  $\text{CN}^{\text{chain}}$  in Table 4.5.4, acts as a key parameter, as it sets the degeneracy of the Cu-NC-Fe fragments and therefore can be considered an indicator of the linearity of the chain. The number is fixed to five by the XRD experiment in the pristine sample (also providing the excellent agreement between the theoretical and experimental EXAFS) but decreases upon lithiation, as revealed by Figure 4.3.16, panel g. This in turn reveals that the accommodation of Li-ions induces a distortion of the lattice accompanied by a consistent structural disorder around copper. This agrees with DFT and XANES data. (ii) Even though the Fe-N-O triplet may allow access to the Fe-N-O angle variation, the little degeneracy of this MS path (1 over 6 respects to the Fe center) did not permit to obtain a relevant and statistically significant quotation of this angle while discharging the battery.

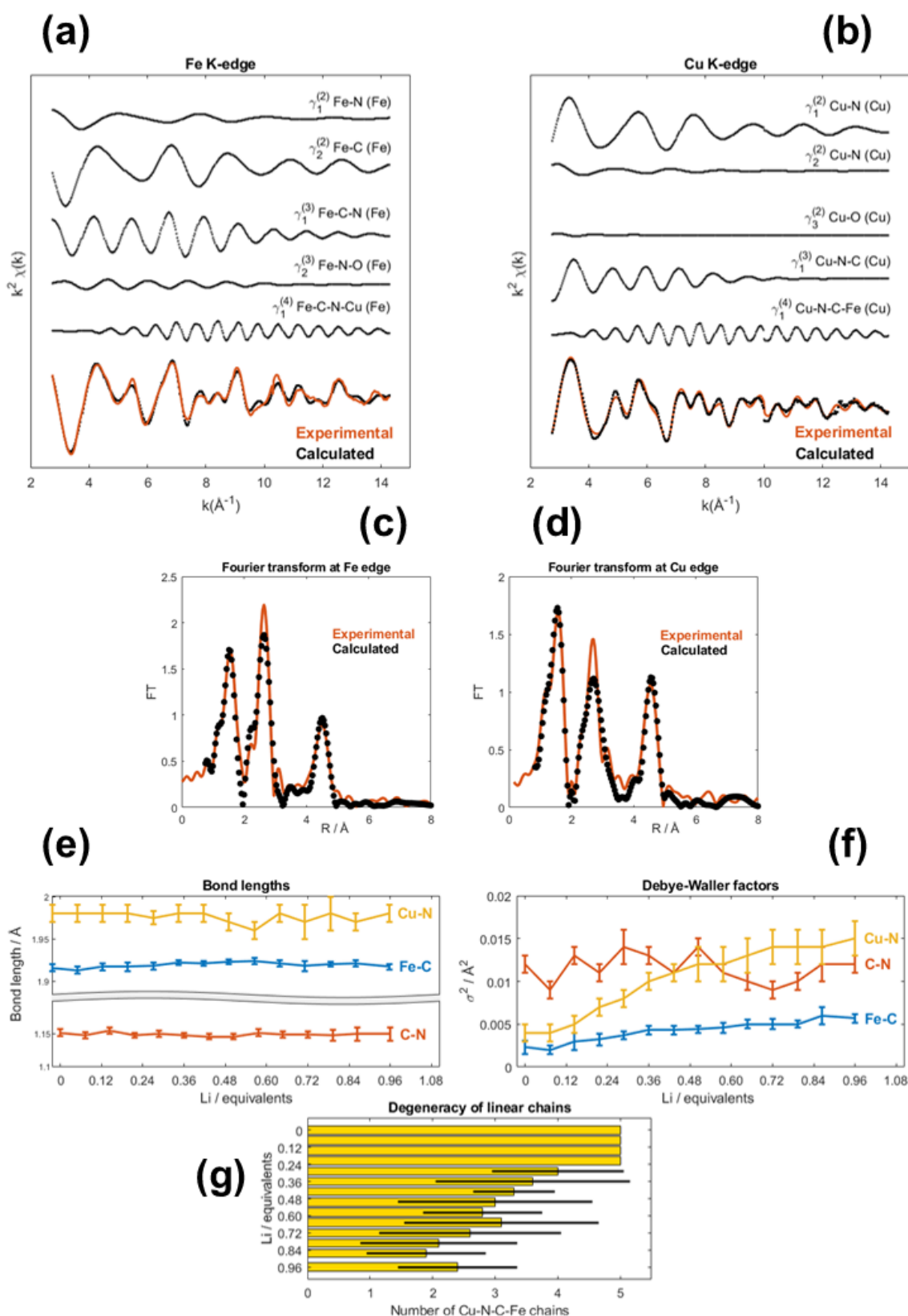


**Figure 4.3.16:** Details of the EXAFS fitting for the pristine electrode: single EXAFS contributions for (a) Fe and (b) Cu K-edge, comparing in the bottom part the theoretical and experimental EXAFS signals; Fourier transforms at (c) Fe and (d) Cu K-edge. Relevant EXAFS fitting results: (e) First shell distances: Fe-C, C-N and Cu-N; (f) Pair EXAFS Debye-Waller factors; (g) Variation in Cu-N-C-Fe chains degeneracy during lithiation

#### 4.3.6 OPERANDO IR

The evolution of the ATR-IR spectra during the first discharge and charge are shown in Figures 4.3.17 and 4.3.18, respectively. Only selected spectra representative of the evolution of the material are reported, and their position in the electrochemical curve is labeled by increasing numbers.

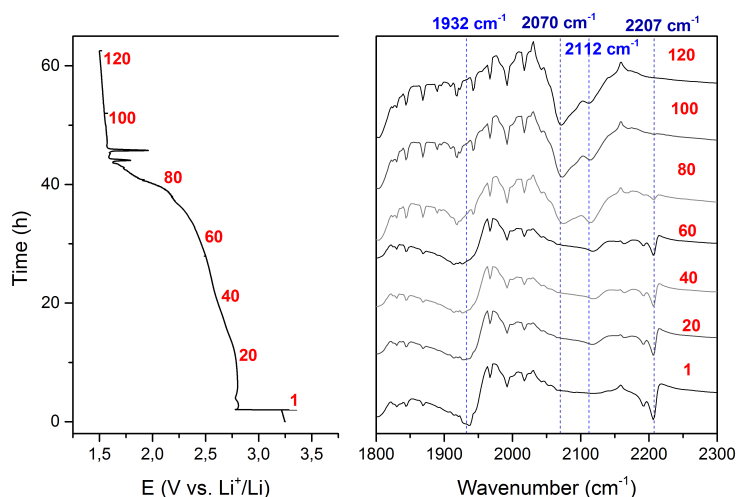


**Figure 4.3.17:** Electrochemical curve during discharge and corresponding IR spectra

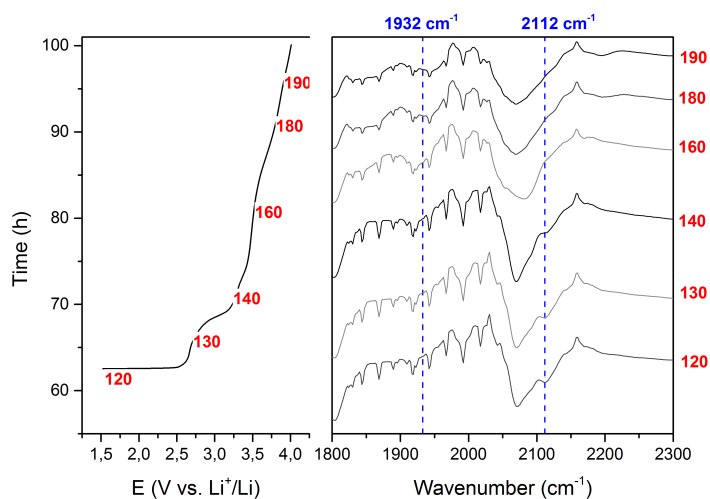


**Figure 4.3.18:** Electrochemical curve during charge and corresponding IR spectra

The electrochemical curve displays different plateaux, in agreement with the results obtained by means of cyclic voltammetry (Figure 4.3.4). In particular, a well-defined plateau is visible in the  $1.5 < E < 1.6$  V vs. Li<sup>+</sup>/Li potential window, where the nitrosyl ligand should be reduced according to the literature [151]. The lithiation process in this potential range appears longer than usual, likely because of side

reactions, corroborated by the fact that spectra 100-120 do not vary significantly, thus, CuNP is not involved in the electrochemical process.

The sharp peak at  $2207\text{ cm}^{-1}$  gradually decreases until 60<sup>th</sup> spectrum where it vanishes, whereas the signal centred at  $2070\text{ cm}^{-1}$  increases in intensity during discharge between spectra 60-80, remaining unchanged during the following charge process and suggesting an irreversible transformation during the first lithiation.

Since the signals in the  $2000\text{-}2200\text{ cm}^{-1}$  range are commonly attributed to cyanide ligands, an irreversible alteration in this spectral region might be attributed to a process involving either the cyanide groups themselves or more probably the bonded metallic centres.

The sharp band at  $1932\text{ cm}^{-1}$  attributed to the linearly coordinated NO vanishes only after 80<sup>th</sup> spectrum, *i.e.*, during the last discharge plateau (cf. Figure (4.3.17)), while it slightly appears back in the first charge plateau (140<sup>th</sup> spectrum, cf. Figure 4.3.18).

However, the observation of some reversible spectral features suggests a reversible character during cycling. The band centred at  $2112\text{ cm}^{-1}$  enhances intensity during lithiation until 80<sup>th</sup> spectrum, remaining unchanged for the rest of the discharge, while it drops intensity during charge, finally disappearing at 140<sup>th</sup> spectrum. This band shows reversibility in the same energy range where copper is electroactive (2.3-3.0 V). This signal, fairly attributed to a cyanide ligand, might be strictly related to the  $\text{Cu}^{2+}/\text{Cu}^{+}$  redox couple.

Similarly, the  $600\text{-}1800\text{ cm}^{-1}$  region shows very good reversibility during cycling, as highlighted by the comparison between pristine, discharged and charged states (4.3.19).

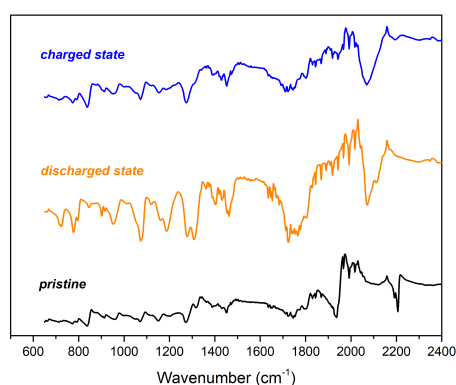


**Figure 4.3.19:** FTIR spectra associated with pristine, discharged, and charged states

This reversible window at low wavenumbers should contain the bent Fe-NO signal. According to Cop-

pens [156], who reported the IR spectra of an electroactive Ni-NO species, the peak attributed to the linear NO gradually and partially decreases during reduction, while the peak attributed to its bent form (at 1392 cm<sup>-1</sup>) appears more sensitive and its intensity varies way more compared to the isonitrosyl signal.

Our results seem to agree well with this study, which could be the key to understand why the peak at 1932 cm<sup>-1</sup> does not recover intensity during charge.

In summary: (i) the region where the bent Fe-NO should give an IR signal is relatively reversible and sensitive during the electrochemical test; (ii) the peak attributed to the linearly coordinated NO disappears during discharge, while it partially rises back during charge; (iii) this could be related to a reduced sensitivity, and not to an irreversible process. To clarify this point, we are running further investigation. Overall, the reduction of the isonitrosyl ligand is responsible for an extra-capacity during discharge, representing a unique case in PBA materials.

#### 4.3.7 DFT CALCULATIONS

Parameters optimization was carried out first on the pristine structure and DFT-optimized geometry was compared to the CuNP structural model [123]. The lowest energy value in the case of the pristine is obtained with two unpaired electrons, while the magnetization value, calculated as the integral over local spin densities in the atomic sphere, indicates these two electrons are mainly located around copper atoms. Taking into consideration the electronic configuration of the atoms in the pristine lattice ( $Z = 2$ ) and approximating the initial oxidation states of copper and iron to (+2), copper possesses a d<sup>9</sup> electronic configuration, thus displaying one unpaired electron per copper, while iron has only paired electrons (d<sup>6</sup> low-spin configuration). Cyanides and nitrosyl ligands in their linear form do not have unpaired electrons either. The obtained result is in line with the CuNP lattice model constituted by two formula units per cell.

Optimized geometries for lithiated structures were obtained by inserting consecutive Li atoms in the lattice, corresponding to 0.5, 1.0 and 1.5 electrochemically inserted Li<sup>+</sup> per formula unit, respectively.

In fact, according to reaction 4.5:



the insertion of one lithium ion can be approximated to the insertion of a lithium atom ( $\text{Li}^+ + \text{e}^- = \text{Li}$ ). Energy minimization for lithiated structures occurred for precise values of spin multiplet. Structures containing 0.5, 1.0 and 1.5 Li experienced a minimum in energy for total spin values equal 1, 0 and 1, respectively (cf. Table 4.3.5). By analyzing the magnetization values, we can assume that the insertion of one Li atom/cell is responsible for the reduction of one Cu atom/cell (Equation 4.5). Indeed, the  $\text{Cu}^{\text{II}}/\text{Cu}^{\text{I}}$  reduction modifies the copper electronic configuration from  $d^9$  to  $d^{10}$  resulting in a reduction of the number of unpaired electrons from 2 to 1 (1 Li/cell) and then to 0 (2 Li/cell). By adding extra Li atom/cell, that is 1.5 Li per formula unit, the structure is further reduced, although the metals are already in their low stable oxidation state. DFT calculations suggested a reduction of the nitrosyl ligand from a  $-\text{NO}^+$  oxidized state to the radical  $-\text{NO}$ , increasing the spin multiplicity due to the presence of one unpaired electron in the  $\pi^*$  orbital.

x Li per unit cell	x Li per unit formula	Unpaired electrons per unit cell
0	0.0	2
1	0.5	1
2	1.0	0
3	1.5	1
4	2.0	2

**Table 4.3.5:** Correspondence between the number of lithium per unit cell ( $Z=2$ ), electrochemically reacted lithium per CuNP formula unit, and number of unpaired electrons per cell

DFT optimized structures highlight a distortion in the lattice during discharge, especially around the copper environment (cf. Figure 4.3.20). Individual nitrogen-copper bond lengths experience a strong variation and the overall coordination number of Cu might be considered diminished.

The relatively high inserted amount of Li and its interaction with the N-terminals of the equatorial cyanides may lead to the observed capacity fading, being the structure not able to entirely extract the initially inserted amount. This may conduct to the loss of capacity experienced in the early stages of the cycling, after which a steady electrochemical performance is obtained, presumably due to the reversible insertion/extraction of a fraction of initially inserted lithium ions.

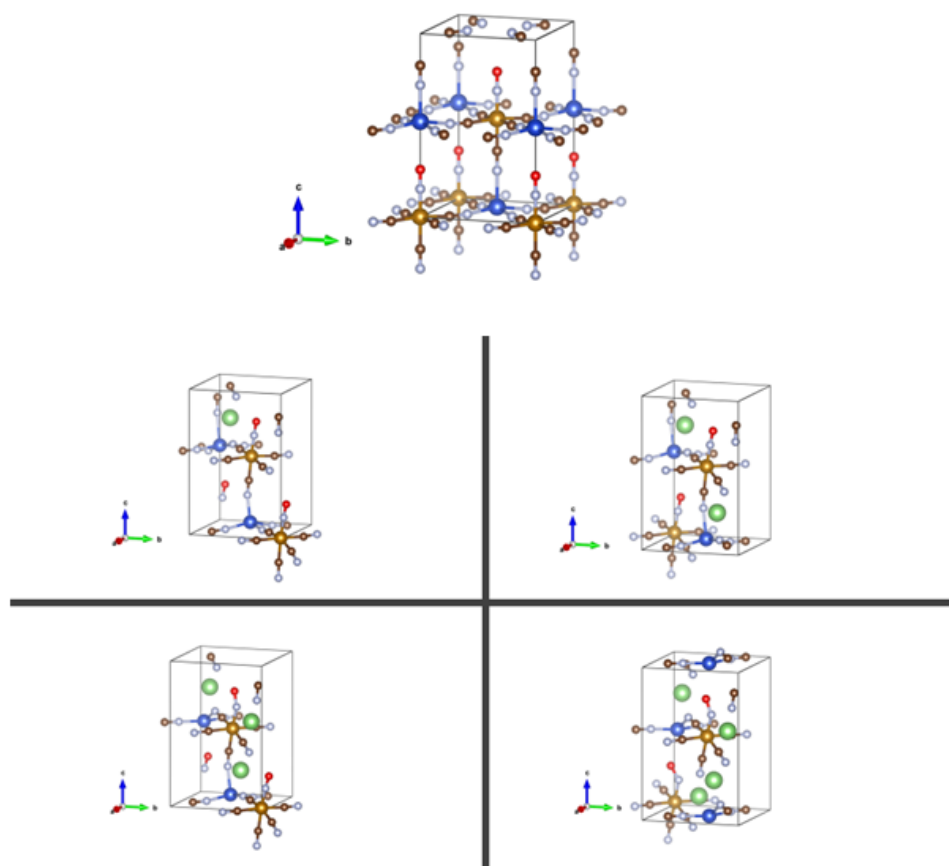


**Figure 4.3.20:** DFT-optimized geometries for pristine and lithiated structures up to 4 Li per unit cell

When reduction of the NO occurs, a change in Fe-N-O bond angle is appreciated, the angle value dropping from  $178^\circ$  to  $142^\circ$ , denoting a partial shift from a  $sp$  to a  $sp^2$  hybridization of the nitrogen atom. Further calculations for higher number of lithium atoms were carried out, even though this condition was not reached in the experiment, featuring a further reduction of the radical NO to the anionic species  $\text{-NO}^-$  and a Fe-N-O bond angle decrease to  $125^\circ$ , corresponding to a planar  $sp^2$  hybridization of the nitrogen atom. The Fe-N-O bending suggested by DFT structure modelling is detectable also by computing vibrational frequencies (see Figure 4.3.21). Indeed, the wavenumber associated to the linearly coordinated NO drops of roughly  $200\text{ cm}^{-1}$  as soon as the NO reduction and respective change in geometry are appreciated. A further decrease is recorded during the hypothetical reduction to anionic

species  $\text{-NO}^-$ . This outcome agrees with and complements the *operando* FT-IR experiment carried out (Section 4.3.6).

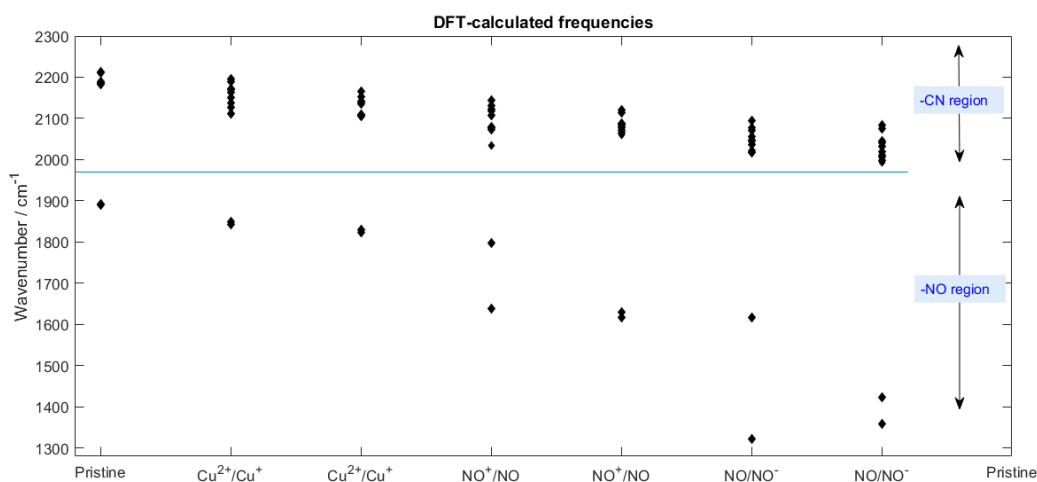


**Figure 4.3.21:** DFT-computed vibrational frequencies and an example of derived geometries. Note that one lattice cell is made of two formula units

#### 4.3.8 XANES CALCULATIONS

The CuNP structural model [123] was first considered to verify its reliability with respect to the experimental CuNP. A comparison between experimental and calculated spectra is reported in Figures 4.3.22 and 4.3.23, evidencing that both calculated edges are representative of the experimental data in terms of main features in the pre-edge, edge, and post-edge regions.

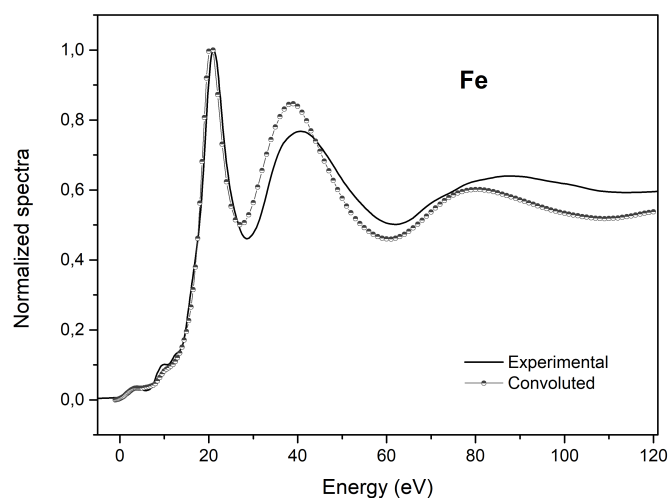


**Figure 4.3.22:** Comparison between experimental XANES and calculated spectra at Fe K-edge

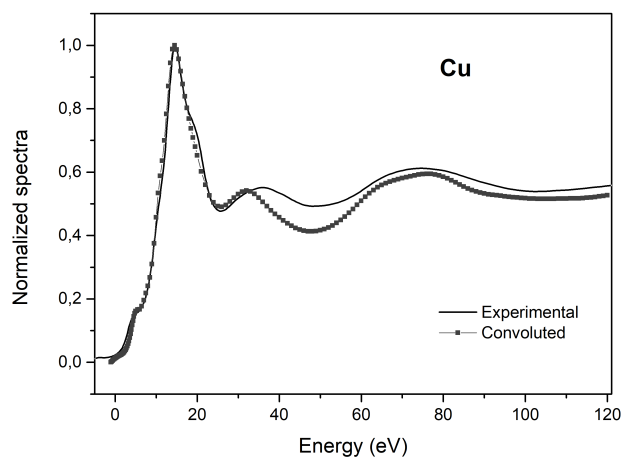


**Figure 4.3.23:** Comparison between experimental XANES and calculated spectra at Cu K-edge

XANES simulations during lithiation are displayed in Figure 4.3.24: XANES spectra of DFT-derived lithiated structures containing 0.5, 1.0, and 1.5 Li are represented for both Fe and Cu K-edge. Both calculated edges present few striking features that fairly match the experimental data. For instance, the 1s-4p transition in the Cu pre-edge enhances intensity while lithium is inserted, lying 10.5 eV before the white line, in accordance with the experimental value (14.2 eV). In addition, the Fe K-edge is not much affected during lithiation and exhibits a decrease in intensity in the white line and following post-edge features, which further points out the agreement between calculated and experimental, thus making the DFT-derived geometries a good approximation of the real system.

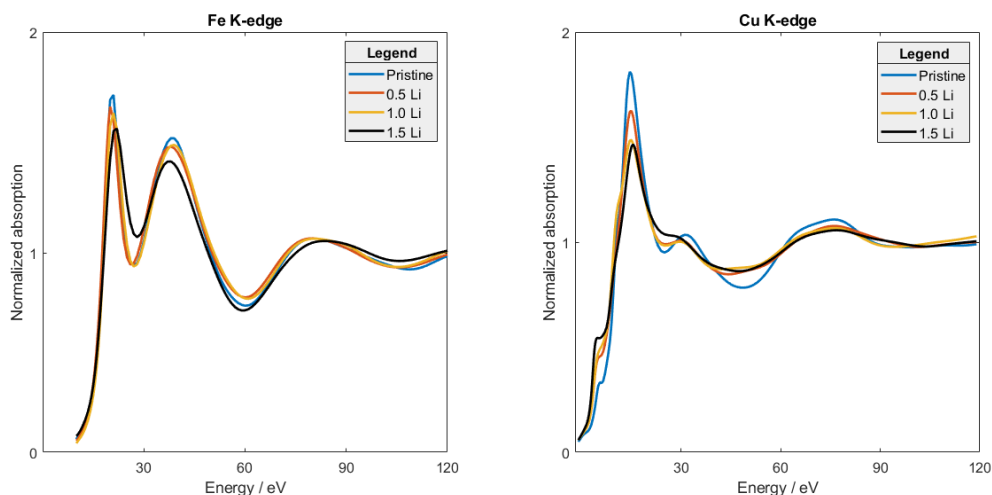


**Figure 4.3.24:** Simulated XANES spectra at Fe K-edge (left) and Cu K-edge (right) during lithiation

#### 4.3.9 CONCLUDING REMARKS

A multi-technique approach was employed to thoroughly investigate the lithiation process of copper nitroprusside, reproducibly synthesized and used as electrode material. We experienced a specific capacity decrease in the first 20 cycles and a reversible electrochemical behavior in the following cycles that was ascribed only to a fraction of available electroactive species. Moreover, we identified the potential range at which the reduction of the nitrosyl might be accessible, opening the path to a new possible redox site for PBAs. Indeed, this compound represents a unique case in PBAs where a ligand is electrochemically active, beyond the metals' redox centres. In this work, *operando* XRD and *operando* XAFS experiments were deeply examined and compared with *ab initio* simulations, whereas computational quantum mechanical modelling was performed to extract additional information on the system.

The reduction of both metals occurs during discharge, simultaneously generating a contraction in the (xy) plane and a z-direction elongation, attributed to the insertion of ions in the lattice. The lithiation induces an increment in the Debye-Waller factors for Cu-N bonds and a decreasing trend for the Cu-NC-Fe linear chains, indicating an augmented disorder in the system and a possible distortion provoked by lithium insertion.

According to DFT calculations, the structure is distorted upon lithiation and copper is reduced. After the Cu<sup>II</sup>/Cu<sup>I</sup> conversion, the nitrosyl is reduced to radical species, while the Fe-N-O angle is bent to 142°.

The lattice deformation induced by the insertion of Li and the interaction with the N-terminals of the equatorial cyanides are thought to be the main cause of the observed capacity fading, while the reversible insertion/extraction of a fraction of initially inserted lithium ions is presumably the reason of the observed steady electrochemical performance after the early stages of cycling.

A very good agreement with experimental data is reached throughout all calculations, making DFT-structures a good approximation of the system under study.

#### 4.4 COPPER HEXACYANOFERRATE - ELECTRODEPOSITION OF THIN LAYER FILMS<sup>6</sup>

##### MOTIVATION

The structure/activity relationship and the capability of tuning physical properties of electroactive material are of great scientific interest. This is generally reached by varying the synthesis in order to confer new properties to the synthesized material, such as the substitution of a ligand to modulate the solubility in metal-ion-selective extractions [157] or to alter the electrostatic fields in metalloproteins by tuning the electronics of the reactive centre [158, 159]. Synthesis of PBAs is commonly based on bulk co-precipitation methods, where  $[\text{Fe}(\text{CN})_6]^{3-}$  and  $\text{M}^{n+}$  salts are simultaneously mixed under constant stirring to yield a precipitate, easily recovered by filtration [24, 54, 79]. An alternative synthetic procedure is based on electrochemical routes, including galvanostatic [26], potentiodynamic [27], and potentiostatic [28–30] methods. The advantage of undertaking an electrochemical-based route is the functionalization of a conductive substrate with a thin film, characterized by an extended active area per surface, while only a potentiostatic method allows the selection and tuning of a proper and fixed energy for the reaction to occur, minimizing the possible formation of undesirable co-products.

The aim of this work was to modulate electrochemical responses and properties by developing different and simple CuHCF electrosynthetic procedures (based on potentiostatic method). In particular, we present the physico-chemical and electrochemical characterization of two different synthesized CuHCF materials and the comparison of the insertion capabilities and electrocatalytic properties, which are of great interest in a wide variety of applications. On one side, ion exchange or (de)insertion capabilities play a major role for instance in battery systems, where the interest towards aqueous media is increasing [61, 96, 144, 145], as well as in the Cs-137 decontamination from soil and waters after the expansion of the nuclear energy utilization and few accidents happened in the past, *e.g.* Chernobyl, Goiana, and Fukushima [35, 160–162]. On the other side, the  $\text{H}_2\text{O}_2$  is the product of various oxidases in several biological reactions [163, 164], hence the importance of the development of biosensors such as PB which has been proven to be an efficient electrocatalyst [41, 165].

---

<sup>6</sup>Reprinted from Thin layer films of copper hexacyanoferrate: Structure identification and analytical applications, Michele Ventura, Angelo Mullaliu, Diana Elena Ciurduc, Sergio Zappoli, Gabriele Giuli, Dino Tonti, Eduardo Enciso, Marco Giorgetti, Journal of Electroanalytical Chemistry 827 (2018) 10–20, Copyright 2018, with permission from Elsevier

#### 4.4.1 XRD, XAFS AND, SEM CHARACTERIZATION

Synthesized CuHCF has been first analyzed by means of X-ray diffraction. Figure 4.4.1 shows the collected patterns for both methods, *i.e.*, A and B. Marked peaks correspond to the reflections of the aluminium sample holder.

Powders are fairly crystalline, taking into account also the fact that the synthesis is carried out via electrochemical route. Patterns correspond to copper hexacyanoferrate (419454-ICSD), [166], as evidenced by the main reflections reported in Figure. If the pattern of Method A – CuHCF is considered, a reflection at roughly 12.5 degrees is also recorded, which cannot be asserted to copper hexacyanoferrate. Even though copper hexacyanoferrate might present a peak at  $2\theta = 12.5$  degrees (corresponding to (110) plane), the intensity cannot surely match. This reflection can be indexed as the (110) plane of PB (*cf.* bottom panel, Figure 4.4.1 [15]). This is not surprising as literature reports the occurrence of PB during the electrosynthesis of CuHCF via potentiodynamic means [119, 167] and also during the copper hexacyanoferrate (CuHCF) film deposition on glassy carbon (GC) electrode from a solution of  $\text{Cu}^{2+}$  and  $[\text{Fe}(\text{CN})_6]^{3-}$  ions in presence of  $\text{HAuCl}_4$ , as suggested by Sharma *et al.* [168]. PB may be formed during the electrosynthetic procedure related to Method A, while Method B does not display this feature. This is a first significant difference in the proposed preparation method. Only method B ensures that the CuHCF material is not contaminated by the presence of a second phase (PB).

XAFS recorded spectra at both Cu and Fe K-edge are presented in Figure 4.4.2, panels (a) and (b), respectively. Regarding Cu K-edge (panel a), CuHCF obtained from the two methods does not report significant differences, except for a slight dissimilarity in intensity in the rising part of the edge and white line features. Therefore, copper site local environment in both compounds is almost identical. On the other side, Fe K-edge (panel b) displays pronounced differences in shape: CuHCF-B is characterized by a broad white line, while in CuHCF-A this is sharper, and resembles qualitatively to the iron K-edge of PB. In this case, similarly to XRD, we denote the potential presence of PB in CuHCF-A. Overall, this different behaviour is most likely due to the longer electrosynthesis time, which can cause a rearrangement of the copper hexacyanoferrate film, triggering the formation of small isles of PB in the electrodeposited film. The size and the percentage of them cannot be accurately determined by refinement in this case; without any doubt, their presence can give specific and peculiar characteristics to the film.

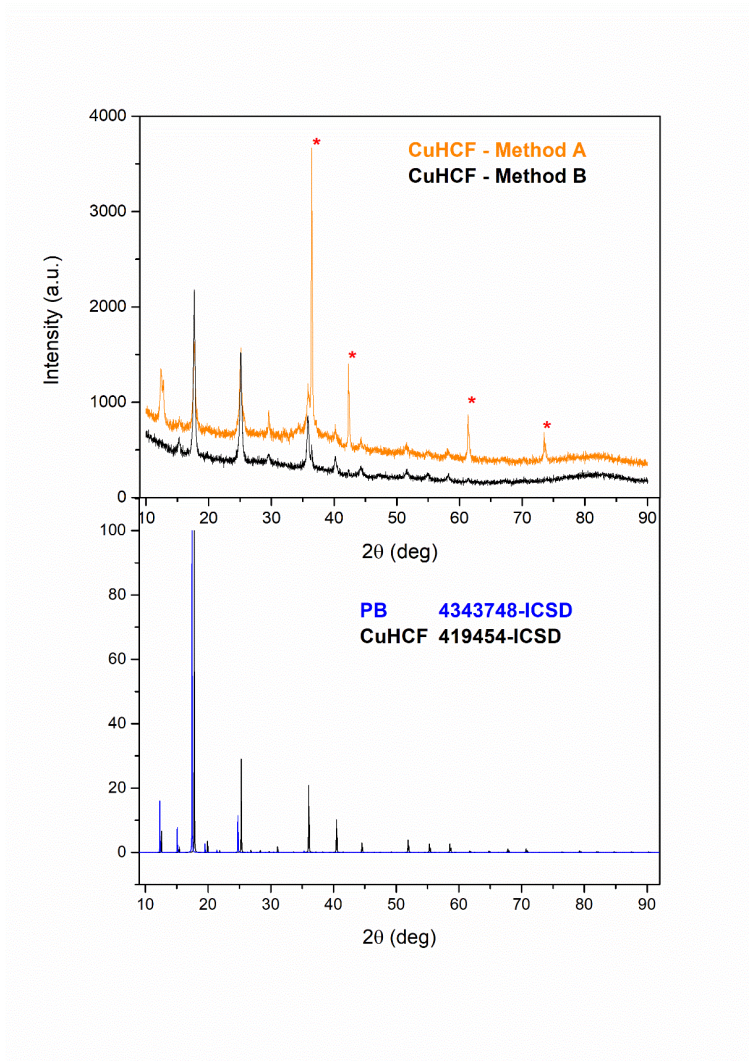


**Figure 4.4.1:** XRD patterns of CuHCF-A and CuHCF-B in the upper panel, compared to PB (4343748-ICSD) and CuHCF's (419454-ICSD) patterns in the bottom panel. Peaks marked with a star match with the aluminium sample holder

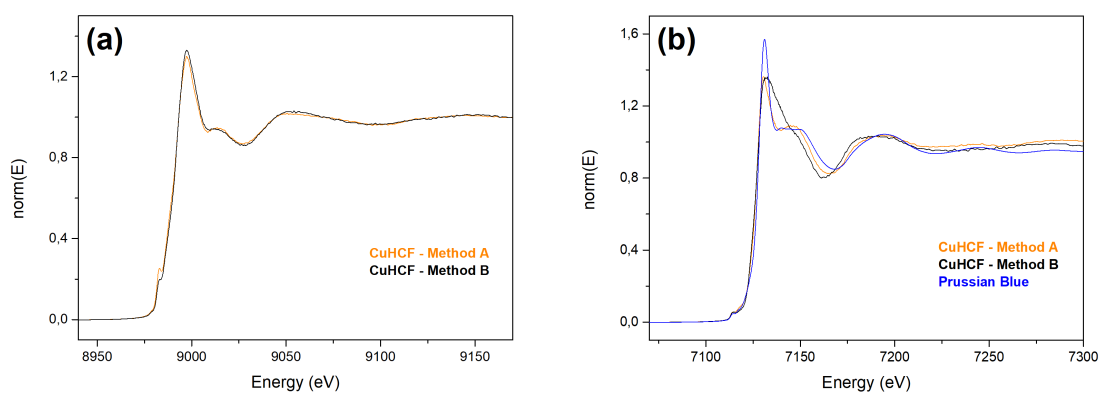


**Figure 4.4.2:** XAFS spectra of CuHCF-A and CuHCF-B. (a) Cu K-edge. (b) Fe K-edge. Here the PB reference at Fe K-edge is also reported

Morphology of electrosynthesized films was checked via scanning electron microscopy. As illustrated in Figure 4.4.3, SEM images were collected for both methods applied on graphite sheet (panels a, b), and carbon cloth (panels c, d). We noticed a substantial difference in the amount of deposited material on the surface and presence of agglomerates. On both substrates the amount of electrodeposited material obtained with Method A (panels a, c) is greater than that obtained with Method B (panels b, d). Moreover, the deposition on carbon tissue (panels c, d) does not occur uniformly and mainly affects the outer part of the support, more precisely the one in direct contact with the solution.

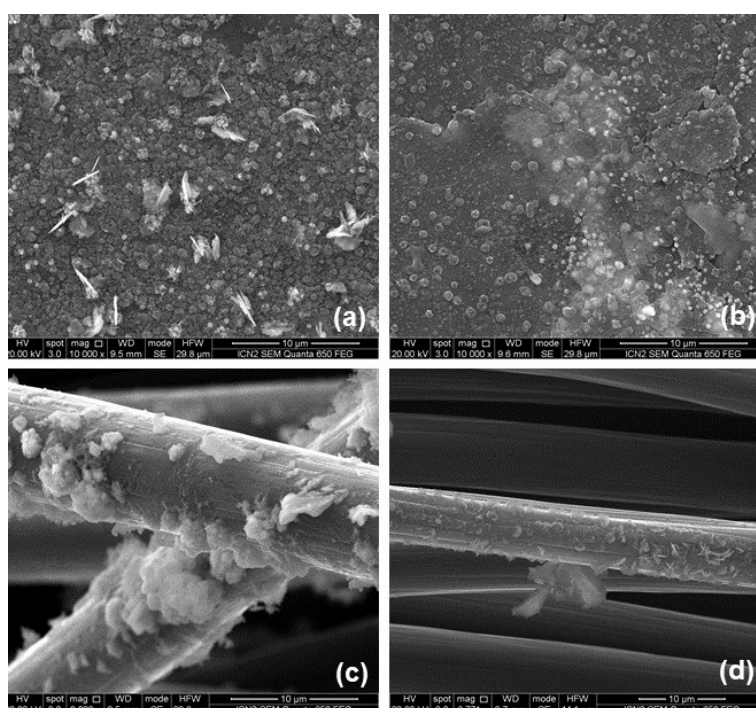


**Figure 4.4.3:** SEM images for electrodeposited CuHCF-A and CuHCF-B on graphite sheet (a), (b), and carbon cloth (c), (d), respectively

EDX analysis revealed in both cases a large amount of copper respects to iron in deposited copper hexacyanoferrate, whose ratios are reported in Table 4.4.1. This ratio is by much higher than expected [166], that is  $\text{Cu}:\text{Fe} = 2:1.8$ .

The acquired trend is reasonable since EDX probes not only the superficial copper hexacyanoferrate, but also the underneath undissolved copper layer derived from the first step of the electrosynthesis procedure. This suggests a two layers structure with the inner layer being electrodeposited Cu, belonging to the first step. In effect, Cu:Fe ratio in CuHCF-A on carbon cloth is significantly higher than the respective in CuHCF-B, since the electrodeposition times considerably change. In the case of graphite

sheet, instead, the relative amount of undissolved Cu-metal and copper hexacyanoferrate are similar for both methods. Under the conditions of Method A, the amount of copper electrodeposited on the carbon cloth substrate is significantly higher compared to the other instances, possibly due to a higher adhesion of copper to carbon cloth.

Overall, EDX cannot be used to semi-quantitatively determine Cu/Fe ratios in the CuHCFs, given that these are overestimated.

Substrate	Method	Cu:Fe ratio
Graphite sheet	A	6:1
	B	7:1
Carbon cloth	A	23:1
	B	5:1

**Table 4.4.1:** EDX Analysis. Cu:Fe ratios for different CuHCF deposited on graphite sheet and carbon cloth

#### 4.4.2 ELECTROCHEMICAL CHARACTERIZATION

Sequential steps are associated to the reported electrosynthesis and modification of the electrode surface (please refer to Section 3.3.2).

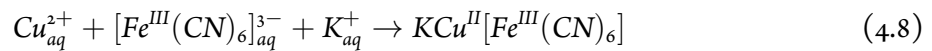
In Figure 4.4.4 we report the CuHCF-A film characterization in 0.1 M KNO<sub>3</sub> solution via 15 cyclic voltammetry curves at 20 mV s<sup>-1</sup>. It can be noted that the first anodic segment, *i.e.*, towards oxidizing potentials, presents a high current intensity centred roughly at +0.85 V, which decreases during cycling and stabilizes after few segments. The same occurs for the first cathodic segment, *i.e.*, towards reductive potentials, where the peak centred at about 0.0 V drops in intensity until reaching a stable value. This peak is attributable to the Cu<sup>II</sup>/Cu<sup>I</sup> reduction process [142]. The reversible peak at 0.65 V is due to the redox couple Cu<sup>II</sup>[Fe<sup>III</sup>(CN)<sub>6</sub>]/Cu<sup>II</sup>[Fe<sup>II</sup>(CN)<sub>6</sub>], as commonly attributed in the literature [51], while the absence of peaks related to the free anions in the 0.25-0.35 V region due to the [Fe<sup>III</sup>(CN)<sub>6</sub>]<sup>3-</sup>/[Fe<sup>II</sup>(CN)<sub>6</sub>]<sup>4-</sup> couple denotes a fast pseudo first-order kinetics between Cu<sup>II</sup> and [Fe<sup>III</sup>(CN)<sub>6</sub>]<sup>3-</sup>.

To summarize, we could write the reactions occurring during the two-steps electrosynthesis and the related characterization in potassium nitrate solution:

(1) First step – copper deposition on the electrode surface by applying a potential of -0.8 V vs. SCE for



(2) Second step – copper anodization by applying a potential of +0.6 V vs. SCE for 300 s and precipitation of copper hexacyanoferrate on the electrode surface



(3) Characterization of the modified electrode via cyclic voltammetry in 0.1 M  $\text{KNO}_3$  solution

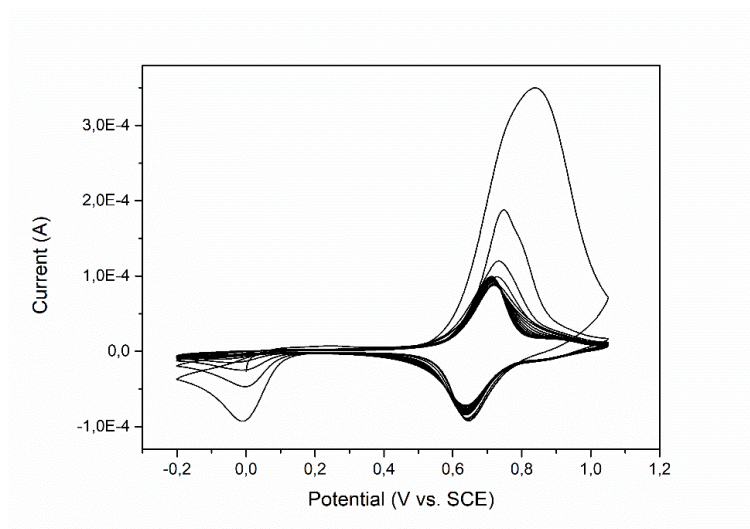
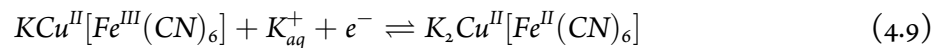


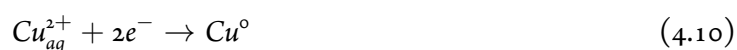
**Figure 4.4.4:** CuHCF – Method A. Characterization via cyclic voltammetry of the as-synthesized copper hexacyanoferrate.  $-0.2 < E < 1.05$  V vs. SCE potential window,  $20 \text{ mVs}^{-1}$  scan rate, 0.1M  $\text{KNO}_3$  aqueous solution

In Figure 4.4.5 we report the analogous characterization for Method B. The considerations made about the absence of the free anions  $[\text{Fe}^{\text{III}}(\text{CN})_6]^{3-} / [\text{Fe}^{\text{II}}(\text{CN})_6]^{4-}$  redox couple and the presence of the  $\text{Cu}^{\text{II}}[\text{Fe}^{\text{III}}(\text{CN})_6] / \text{Cu}^{\text{II}}[\text{Fe}^{\text{II}}(\text{CN})_6]$  corresponding peak at 0.65 V vs. SCE are still valid.

Three main features about Method B are: (i) the amount of deposit on the electrode, hence the current

intensity during the redox processes, is smaller compared to Method A, for the deposition times are lower, even though potential conditions are more severe. If we consider the electrode geometric area being constant, the current intensity is proportional to the deposit thickness, for current is dependent on the amount of electrosynthesized CuHCF. Therefore, Method B generates thinner films. (ii) Voltammetric curves appear quite stable since the beginning of the cycling, differently from what reported for Method A. (iii) An additional anodic peak at 0.4 V vs. SCE is visible and related to the cathodic one appearing at 0.0 V vs. SCE. This is attributed to the Cu<sup>II</sup>/Cu<sup>I</sup> couple in copper hexacyanoferrate, and the difference in potential between the oxidation and the reduction (>300 mV) is ascribed to the irreversible nature of this process, and likely a structural reorganization, as reported in the literature [169]. Briefly, the reactions involved in the illustrated Figure 4.4.5 can be written as below:

(1) First step – copper deposition on the electrode surface by applying a potential of -1.0 V vs. SCE for 4 s



(2) Second step – copper anodization by applying a potential of +1.0 V vs. SCE for 15 s and precipitation of copper hexacyanoferrate on the electrode surface



(3) Characterization of the modified electrode via cyclic voltammetry in 0.1 M KNO<sub>3</sub> solution



+0.5 < E < +0.8 V vs. SCE



-0.1 < E < +0.5 V vs. SCE

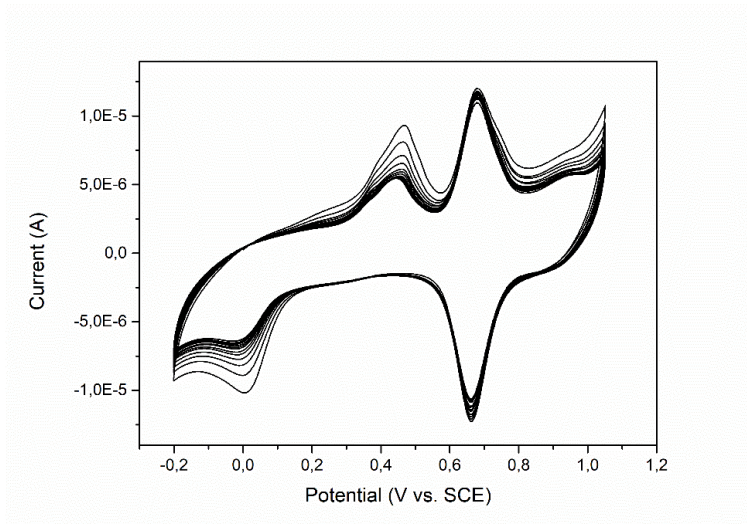


**Figure 4.4.5:** CuHCF – Method B. Characterization via cyclic voltammetry of the as-synthesized copper hexacyanoferrate.  $-0.2 < E < 1.05$  V vs. SCE potential window,  $20 \text{ mVs}^{-1}$  scan rate,  $0.1\text{M KNO}_3$  aqueous solution

By taking into consideration the area beneath the anodic and cathodic sweeps of the voltammetric curves, we can approximate the mass of copper hexacyanoferrate obtained in the electrochemical syntheses as it follows:

$$\text{Mass}(\text{CuHCF}) = \frac{\text{Area} \cdot \text{FW}(\text{CuHCF})}{\text{Scan rate} \cdot F \cdot n(\text{CuHCF})} \quad (4.15)$$

where the area is expressed in  $[\text{A V}]$ , the scan rate is expressed in  $[\text{V s}^{-1}]$ ,  $F$  is the Faraday constant,  $n$  is the moles of electrons exchanged per mole of CuHCF, giving as result a mass with an order of magnitude of roughly  $10^1 \mu\text{g}$  for Method A and  $10^0 \mu\text{g}$  for Method B.

By further approximation, we could even consider a general density ( $\rho$ ) for metal hexacyanoferrates equal to  $1.8 \text{ g/cm}^3$ , and reminding that the exposed electrode area was  $(0.5 \times 0.5) \text{ cm}^2$ :

$$\text{Thickness} = \frac{\text{mass}(\text{CuHCF})}{\rho \cdot \text{Exposed Area}} \quad (4.16)$$

where the thickness is expressed in  $[\text{cm}]$ . The application of equation 4.16 leads to estimated thicknesses of  $0.1 \mu\text{m}$  and  $0.01 \mu\text{m}$  for Method A and B, respectively.

Please note that Equations 4.15 and 4.16 consist of large approximations, for instance the exposed area is not the actual electrode area.

We further verified that these two methods can be transferred to other carbon-based substrates, since

the substrate effect is minimal and leads to the same electrochemical signature. In Figure 4.4.6, the characterization voltammograms performed on different functionalized conductive substrates are reported.

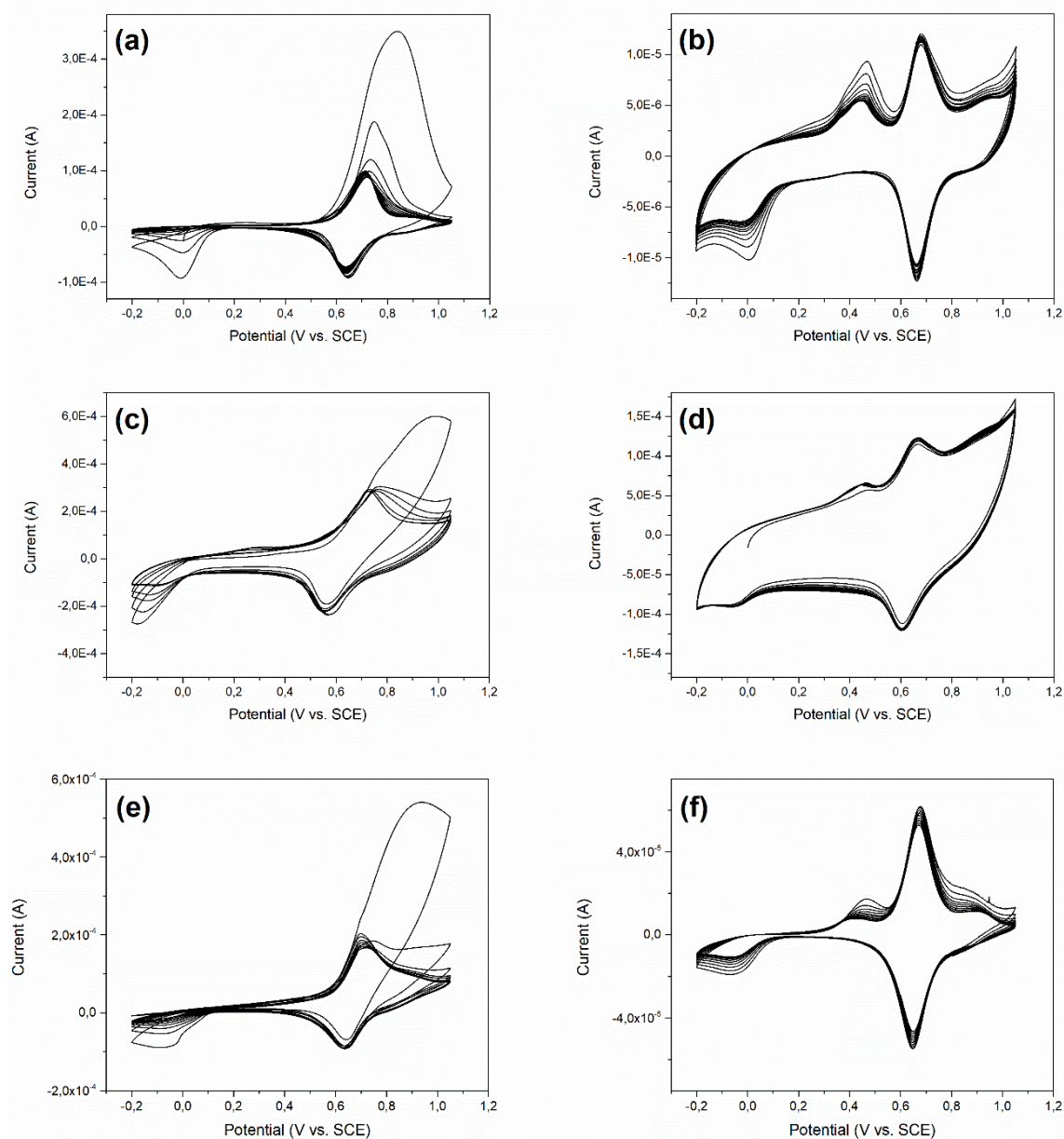


**Figure 4.4.6:** Cyclic voltammograms of electrosynthesized copper hexacyanoferrate in 0.1 M  $\text{KNO}_3$  aqueous solution at  $20 \text{ mV s}^{-1}$  scan rate. Method A on glassy carbon (a), graphite sheet (c), and carbon cloth (e). Method B on glassy carbon (b), graphite sheet (d), and carbon cloth (f).

The syntheses have been carried out by using both described methods, *i.e.*, Method A and B, on glassy carbon, graphite sheet, and carbon cloth. In particular, panels (a), (c), and (e) display the voltammetric curves of the synthesis according to Method A on glassy carbon, graphite sheet and carbon cloth, respec-

tively, while panels (b), (d), and (f) regard Method B on the same substrates. CuHCF-A always presents the above-mentioned peak at +0.85 V, which decreases after few anodic sweeps to a stable value; all other aspects, such as the copper ferrocyanide/ copper ferricyanide redox couple, are qualitatively maintained regardless the employed conductive substrate, even though differences can be appreciated due to dissimilarities attributable to the exposed surface and nature of the conductive substrate. However, considering the same electrode substrate, syntheses are reproducible. CuHCF-B consistently exhibits two redox couples, as previously discussed, which can be asserted to  $\text{Cu}^{\text{II}}/\text{Cu}^{\text{I}}$  and  $\text{Fe}^{\text{III}}/\text{Fe}^{\text{II}}$  couples. As for Method A, distinct substrates give different quantitative signals, although the basic aspects related to this method are maintained. Moreover, also in this case syntheses are completely reproducible, if the same substrate is considered.

In Figure 4.4.7 we report a study made on different concentrations and scan rates. Considering a  $\text{KNO}_3$  solution, we varied its concentration by choosing 0.01 M, 0.1 M, and 1 M concentrations, while keeping constant the other operating conditions, *i.e.*,  $50 \text{ mV s}^{-1}$  scan rate,  $-0.2 < E < 1.05 \text{ V}$  vs. SCE potential window, and experimental set-up. Performances of both methods are shown in panels (a) and (b), displaying Method A and B, respectively. Moreover, insets correlate insertion potential (roughly at 0.6 V) to the concentration of  $\text{K}^+$ -ion. A linear correlation between insertion potential (that is the potential corresponding to the cathodic peak) and the logarithm of  $\text{K}^+$  molar concentration is verified for both methods, which is consistent with the Nernst equation for the case under study:

$$E = k + 0.059 \cdot \text{Log}[\text{K}^+] \quad (4.17)$$

where a monoelectronic process is involved, and ion concentration is assimilated to ion activity.

Concerning Method A (Figure 4.4.7a), the higher the concentration of the electrolyte solution, the sharper the peaks, in other words the redox processes occur at a narrower potential range. On the other side, Method B (Figure 4.4.7b) shows a peculiar behaviour: if 0.1 M electrolyte concentration is employed, the redox couple at 0.0/0.4 V is enhanced, contrary to what is obtained for the other two concentrations. Interestingly, both CuHCF-A and CuHCF-B have a similar electrochemical curve, when  $10^{-2} \text{ M KNO}_3$  is adopted.

In panels (c) and (d) we report the study on scan rates performed on CuHCF-A and CuHCF-B, respectively. Cyclic voltammeteries in aqueous 0.1 M  $\text{KNO}_3$  solution at different scan rates, precisely at 500,

200, 50, 20, 5  $\text{mV s}^{-1}$ , in the -0.2-1.05 V potential range are presented. Insets display a magnification of the 5  $\text{mV s}^{-1}$  cyclic voltammetry and the calibration curves that correlate cathodic/anodic peak intensity to the square root of scan rate. By considering the peak due to the  $\text{Cu}^{\text{II}}[\text{Fe}^{\text{III}}(\text{CN})_6]/\text{Cu}^{\text{II}}[\text{Fe}^{\text{II}}(\text{CN})_6]$  couple at about 0.65 V, we can express the peak current intensity,  $I_p$ , as a function of scan rate according to the Randles-Sevcik equation:

$$I_p = 2.686 \cdot 10^5 \cdot n^{3/2} \cdot A \cdot D^{1/2} \cdot C \cdot v^{1/2} \quad (4.18)$$

where  $C$  is the analyte concentration [ $\text{mol}/\text{cm}^3$ ];  $v$  is the scan rate [ $\text{V s}^{-1}$ ];  $D$  is the analyte diffusion coefficient [ $\text{cm}^2 \text{s}^{-1}$ ];  $A$  is the electrode area [ $\text{cm}^2$ ];  $n$  is the number of exchanged electrons;  $I_p$  is the peak current intensity [A].

Thus, we can assert that the insertion/extraction process is diffusion-controlled, given that  $I_p \propto v^{1/2}$ .

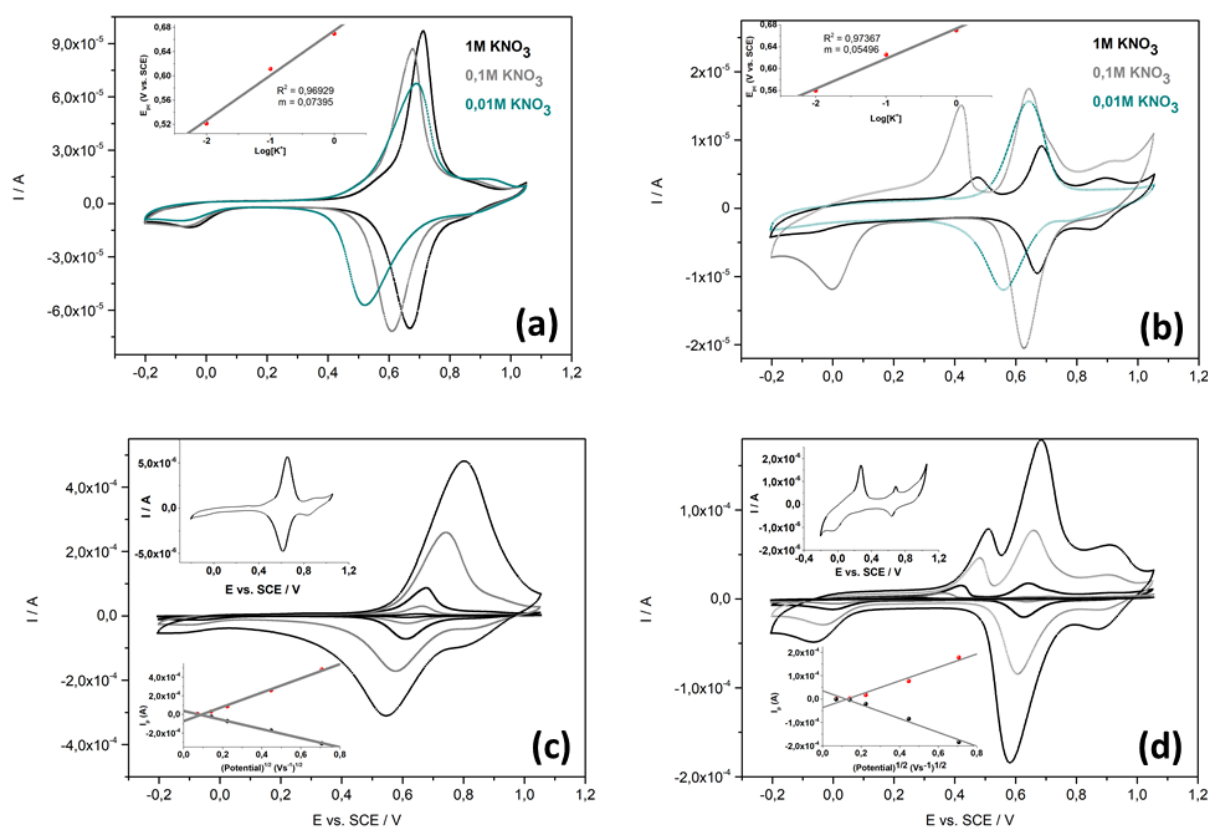


**Figure 4.4.7:** Cyclic voltammeteries in aqueous 0.1  $\text{KNO}_3$  solution at different concentrations (0.01, 0.1, 1 M) at  $50 \text{ mVs}^{-1}$  of electrosynthesized copper hexacyanoferrate: Method A (a), Method B (b). Cyclic voltammeteries in aqueous 0.1  $\text{KNO}_3$  solution at different scan rates (500, 200, 50, 20, 5  $\text{mV s}^{-1}$ ) of electrosynthesized copper hexacyanoferrate: Method A (c), Method B (d). Insets show curves recorded at a 5  $\text{mV s}^{-1}$  scan rate

A striking feature is visible in the case of CuHCF-B: by lowering the scan rate, the peak related to the  $\text{Cu}^{\text{II}}[\text{Fe}^{\text{II}}(\text{CN})_6]/\text{Cu}^{\text{I}}[\text{Fe}^{\text{II}}(\text{CN})_6]$  couple at 0.0/0.4 V vs. SCE is enhanced compared to the redox couple associated to  $\text{Fe}^{\text{III}}/\text{Fe}^{\text{II}}$ . We already suggested that the large difference in potential between the oxidation and the reduction for the copper site is ascribed to a likely structural reorganization, and this can be supported to the study on scan rates as well: as a matter of fact, by scanning the potential slowly, the system under study is able to re-equilibrate more efficiently to the new voltage, thus making feasible a lattice re-organization and the copper site redox possible.

#### 4.4.3 ION EXCHANGE CAPABILITIES

To explore the ion exchange capabilities of the synthesized copper hexacyanoferrate, we performed sequential ion-(de)insertion by adopting different cations and by means of cyclic voltammetry. After 15 cycles in 0.1 M  $\text{KNO}_3$  solution ended at -0.2 V to give the  $\text{K}^+$ -rich CuHCF, the electrolyte solution has been changed to 0.1 M  $\text{M}^{\text{n+}}(\text{NO}_3)_n$ , where  $\text{M}^{\text{n+}}$  is either  $\text{Na}^+$ ,  $\text{Mg}^{2+}$ ,  $\text{Al}^{3+}$ , or  $\text{Cs}^+$ . By starting with a positive polarization and ending at -0.2 V, we first force the extraction of  $\text{K}^+$  ions, then the  $\text{M}^{\text{n+}}$  insertion in the synthesized film. Finally, by switching to the initial 0.1 M  $\text{KNO}_3$  solution, the deinsertion of  $\text{M}^{\text{n+}}$  ions and the insertion of  $\text{K}^+$  ions take place.

In Figure 4.4.8 we report the results of this study. Panels (a) and (b), (c) and (d), (e) and (f), (g) and (h) refer to  $\text{NaNO}_3$ ,  $\text{Mg}(\text{NO}_3)_2$ ,  $\text{Al}(\text{NO}_3)_3$ ,  $\text{CsNO}_3$ , respectively; panels on the left side (a, c, e, g) regard CuHCF-A, while panels on the right side (b, d, f, h) regard CuHCF-B. Both CuHCF-A and CuHCF-B can exchange all tested ions. Electrochemical signatures via CVs present different features that are here discussed. The difference in cathodic and anodic peaks current prior and after the insertion of  $\text{M}^{\text{n+}}$  ion for both methods can be found in Table 4.4.2. CuHCF-A can reversibly exchange  $\text{Na}^+$  ions and restore its initial state prior to sodium insertion (Figure 4.4.8a): actually, CVs recorded in 0.1 M  $\text{KNO}_3$  before and after exchanging sodium-ion show almost no difference, asserted to the high reversible character of the film. CuHCF-B shows an enhancement of the redox couple located at 0.0/0.4 V vs. SCE, attributed to the  $\text{Cu}^{\text{II}}/\text{Cu}^{\text{I}}$  process, when potassium-ion is replaced by sodium, which probably interacts to a large extent with copper sites.

On the other side, the peak intensity due to the  $\text{Fe}^{\text{III}}/\text{Fe}^{\text{II}}$  couple is lowered, while different redox processes occur, to whom it is not obvious to assign a define chemical reaction, likely due to different elec-

trochemical sites. After sodium removal, we observe in 0.1 M  $\text{KNO}_3$  a decrease in current intensity for both anodic and cathodic peaks, which is higher compared to Method A case (cf. Table 4.4.2). The same pattern appears in the case of  $\text{Mg}^{2+}$  ions: CuHCF-A and CuHCF-B (panels c, d) can both host  $\text{Mg}^{2+}$  ions, although Method A seems to confer a higher stability to the film than Method B. Regarding the (de)insertion of aluminium ion, it is discernible how this affects the deposited film, by comparing the peaks intensity in  $\text{KNO}_3$  prior to and after  $\text{Al}^{\text{III}}$  (de)insertion. The lowering of peaks intensity suggests an irreversible damage to the film, probably due to the size of the hydrated aluminium ion and the relative steric hindrance and coulombic effects. As reported in the literature [35, 161, 170, 171], CuHCF confirms a high affinity towards cesium, given the fast substitution of potassium and the slow replacement of  $\text{Cs}^+$  by  $\text{K}^+$ , reported in Figure 4.4.8 and Figure 4.4.9. Indeed, the  $\text{K}^+$  ion replacement (see Figure 4.4.9 panels a, c) is almost instantaneous, while the re-insertion (panels b, d) occurs throughout some voltammetric cycles, CuHCF-A and B displaying comparable performance. Hence, the possible decontamination of cesium ions via a typical electrochemically switched ion exchange (ESIX) would be feasible for both CuHCFs.

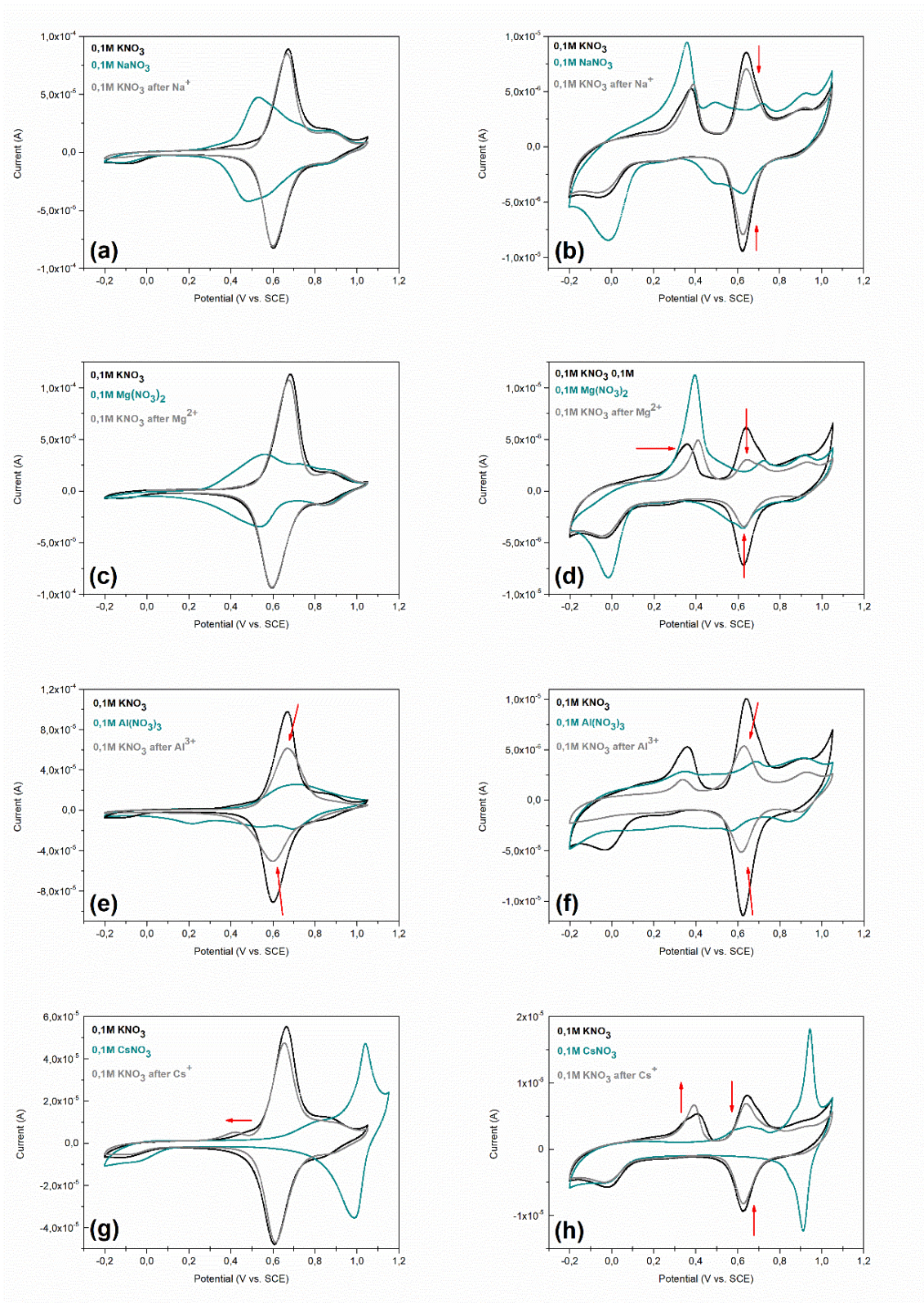


**Figure 4.4.8:** Cyclic voltammeteries of the electrosynthesized CuHCF in the  $-0.2 < E < 1.05$  V vs. SCE potential range at a  $20 \text{ mVs}^{-1}$  scan rate. Electrochemical signatures in 0.1 M  $\text{KNO}_3$  solution, 0.1 M  $\text{M}^{n+}(\text{NO}_3)_n$  solution, and again 0.1 M  $\text{KNO}_3$  solution after the insertion of  $\text{M}^{n+}$ . (a), (b): 0.1 M  $\text{NaNO}_3(\text{aq})$ ; (c), (d): 0.1 M  $\text{Mg}(\text{NO}_3)_2(\text{aq})$ ; (e), (f): 0.1 M  $\text{Al}(\text{NO}_3)_3(\text{aq})$ ; (g), (f): 0.1 M  $\text{CsNO}_3(\text{aq})$ . Panels (a), (c), (e), (g) refer to CuHCF-A, while panels (b), (d), (f), (h) refer to CuHCF-B

Method A		
$M^{n+}$	$\frac{\Delta I_a(\text{after } M^{n+} \text{ extraction})}{\Delta I_a(\text{prior to } M^{n+} \text{ insertion})}$	$\frac{\Delta I_c(\text{after } M^{n+} \text{ extraction})}{\Delta I_c(\text{prior to } M^{n+} \text{ insertion})}$
NaNO <sub>3</sub>	-4%	-2%
Mg(NO <sub>3</sub> ) <sub>2</sub>	-5%	-1%
Al(NO <sub>3</sub> ) <sub>3</sub>	-37%	-45%
CsNO <sub>3</sub>	-14%	-2%

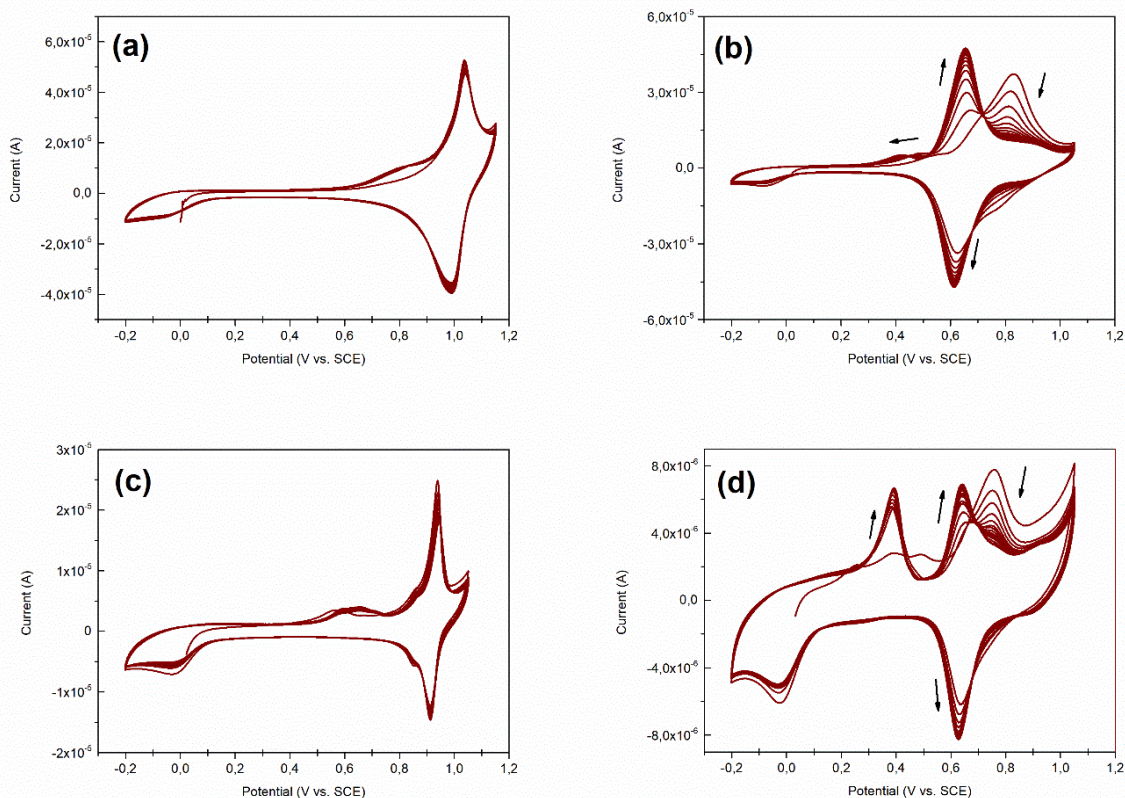
  

Method B		
$M^{n+}$	$\frac{\Delta I_a(\text{after } M^{n+} \text{ extraction})}{\Delta I_a(\text{prior to } M^{n+} \text{ insertion})}$	$\frac{\Delta I_c(\text{after } M^{n+} \text{ extraction})}{\Delta I_c(\text{prior to } M^{n+} \text{ insertion})}$
NaNO <sub>3</sub>	-17%	-16%
Mg(NO <sub>3</sub> ) <sub>2</sub>	-51%	-52%
Al(NO <sub>3</sub> ) <sub>3</sub>	-47%	-55%
CsNO <sub>3</sub>	-15%	-12%

**Table 4.4.2:** CuHCF. Methods A, B. Differences in anodic ( $\Delta I_a$ ) and cathodic ( $\Delta I_c$ ) peak intensity in 0.1 M KNO<sub>3</sub> solution between prior and after insertion of  $M^{n+}$  salt

Based on effective hydrated ionic radii, the tested ions sizes order is Cs<sup>+</sup> (3.29 Å) > K<sup>+</sup> (3.31 Å) > Na<sup>+</sup> (3.58 Å) > Mg<sup>2+</sup> (4.28 Å) > Al<sup>3+</sup> (4.75 Å) [172]. Given the tunnels size, only cesium, potassium and sodium would be able to enter the structure without any damage to the film. However, CuHCF-A shows good exchange properties and film stability also with Mg<sup>2+</sup>, while only Al<sup>3+</sup> does not seem to adequately fit in the lattice. This electrochemical behaviour might be attributed to the presence of a greater amount of vacancies in the CuHCF-A than in CuHCF-B, which seems to accommodate well only monovalent ions.

Overall, CuHCF-A seems more suitable for ion exchange applications, due to the large versatility towards different cations, characterized both by different sizes and positive charge. The exchange results feasible and non-destructive, since the film does not seem to suffer from structural damage and the response to KNO<sub>3</sub> looks almost invariant. However, CuHCF-B displays good stability and high affinity towards cesium as well, therefore both CuHCFs result suitable in cleaning waters that have been contaminated by radioactive Cs-137.



**Figure 4.4.9:** Cs-insertion (a) and de-insertion (b) in CuHCF-A and CuHCF-B (c,d)

#### 4.4.4 $\text{H}_2\text{O}_2$ DETERMINATION

The response to  $\text{H}_2\text{O}_2$  has been evaluated in chronoamperometry, by working at a reduction potential of 0.0 V vs. SCE. The response to hydrogen peroxide is likely due to the presence of PB impurities [119], or thanks to the participation of the  $\text{Cu}^{\text{II}}/\text{Cu}^{\text{I}}$  redox couple. In Figure 4.4.10 the comparison in electrocatalytic response between CuHCF-A and CuHCF-B is reported: panel (a) shows the chronoamperometric curve for several additions of hydrogen peroxide, as described in the Methodology section, while calibration curves for the two methods are illustrated in panel (b). Even though the calculated sensitivity to  $\text{H}_2\text{O}_2$  (reported in Table 4.4.3) is dependent on deposit amount, there is a significant dissimilarity in trend for hydrogen peroxide detection. Indeed, CuHCF-A displays a sensitivity that is six times higher than CuHCF-B, which might be asserted to the presence and active participation of PB in CuHCF-A, in accordance with XRD and XAFS measurements. To further corroborate this hypothesis, it has already been observed as PB activity towards hydrogen peroxide reduction is orders of magnitude larger than other non-iron hexacyanoferrates, and that PB impurities can affect and enhance the  $\text{H}_2\text{O}_2$

sensing [173].

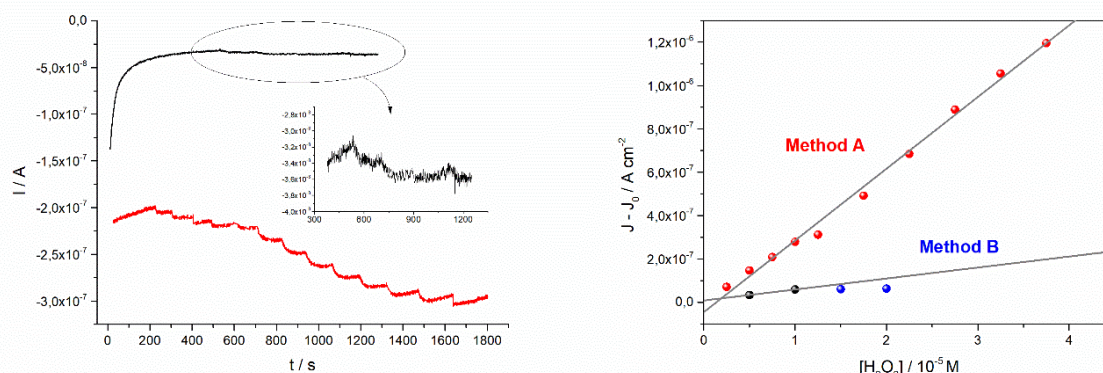


**Figure 4.4.10:** (a) Chronoamperometry on synthesized CuHCF-A (red line) and CuHCF-B (black line). (b) Calibration curve for both methods

Active material	Sensitivity / mA (mol / L) <sup>-1</sup> cm <sup>-2</sup>	Linearity Range (L.O.D.-L.O.L.) / (mol / L)
CuHCF-A	33.1	$1.7 \cdot 10^{-6}$ - $5.25 \cdot 10^{-5}$
CuHCF-B	5.07	$N/A$ - $1.0 \cdot 10^{-5}$

**Table 4.4.3:** Sensitivity and linearity range for hydrogen peroxide detection. L.O.D. stands for limit of detection, while L.O.L. stands for limit of linearity

#### 4.4.5 CONCLUDING REMARKS

Copper hexacyanoferrate has been reproducibly electrodeposited on different conductive substrates by following two different methods, A and B. Both methods consist in two consecutive steps, where the electrodeposition of a thin Cu layer is followed by its partial dissolution and formation of CuHCF in presence of a solution of hexacyanoferrate anion, giving as result a two-layers film. By tuning both potentials and application times, we were able to confer to the films different features, which is reflected both in terms of structure and physico-chemical properties.

Structural information has been acquired by means of XRD and XAFS measurements: CuHCF-A includes a likely two-phase solid solution, copper hexacyanoferrate co-existing with PB impurities, as revealed by both extra peaks in the XRD pattern and edge shape at the Fe K-edge, while Method B leads to a pure CuHCF phase.

Two analytical applications have been considered to investigate the physico-chemical characteristics of the synthesized films, *i.e.*, ion exchange and H<sub>2</sub>O<sub>2</sub> sensing. Different salt solutions containing various

cations have been interchanged to verify the ability of the films to accommodate and reversibly exchange ions. Both CuHCFs can reversibly insert/extract monovalent as well as multivalent ions. Although CuHCF-A shows a higher stability towards multivalent cations, possibly due to extended vacancies, the ion exchange properties towards monovalent ions are similar. Furthermore, we concluded that CuHCF-A is more suitable towards  $H_2O_2$  electrocatalysis for its higher sensibility due to the PB impurities.

## 4.5 TITANIUM HEXACYANOFERRATE

### MOTIVATION

Research based on secondary cells is constantly developing due to its importance in technological applications. Cells with an excellent cyclability are sought out, and performance can be improved by changing operative conditions as well as the materials: new electrodic materials are tested, such as those characterized by an open-framework structure, which allows for rapid insertion and extraction with little lattice strain. Different electrolytes and solvents are used in order to achieve desirable ion-mobility and stability within a given the potential window. The goal of this work was to investigate a porous electrodic material, titanium hexacyanoferrate (TiHCF), and characterize it through a variety of analytical techniques. Synthesis was carried out by dropwise precipitation method, and characterization employed the use of techniques such as TGA, XRD, and ICP-OES. Electrochemical tests were performed both in glass cells. Cyclic voltammetry was used in order to explore the electrochemical properties of titanium hexacyanoferrate in aqueous solutions, all while selecting for optimal conditions. With the use of  $K^+$  and  $Na^+$  salts, the studied material exhibited reversible processes and relatively high capacities.

### 4.5.1 XRD, TGA, ICP-OES CHARACTERIZATION

Figure 4.5.1 displays the powder XRD profile of the synthesized TiHCF and its profile matching refinement. The residual curve is plotted to provide a quality check of the fitting performance. The material presents a high degree of crystallinity. After profile matching with constant scale factor, a space group of  $Pm\bar{3}m$  resulted, hence a cubic structure characterized by the average cell parameter  $a = 10.190 \text{ \AA}$ . As host materials are able to insert ions in their channels and cavities, a peak shift in XRD diffractograms would be expected while cycling. The intercalation of ions generally results in an increase in the interplanar distance, resulting in a gradual peak shift towards smaller  $2\theta$  angles. Nevertheless, if attractive forces prevail over steric hindrance, the opposite is observed. XRD profiles have been recorded on both pristine and cycled materials in an attempt to observe differences in patterns. More precisely, the PFTE-based TiHCF electrodes have been polarized in  $KNO_3$  solution to induce the oxidation/ reduction of the active species, as reported in Table 4.5.1.

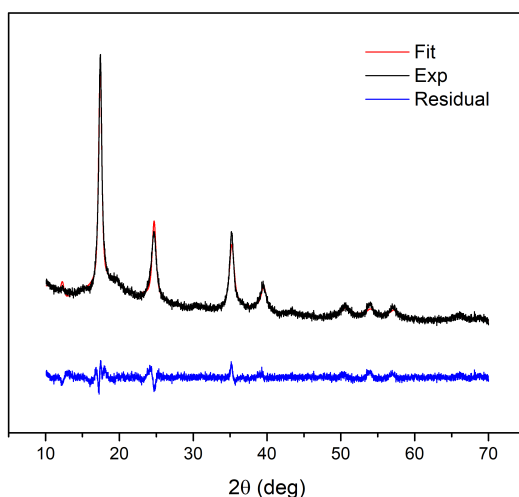


**Figure 4.5.1:** XRD pattern of TiHCF and its profile matching refinement

Electrode	Applied Potential (V vs. SCE)	Time span (min)	Peak Centroid ( $2\theta$ )
Pristine	-	-	17.49
Oxidized	0.7	25	17.46
Reduced	-0.6	25	17.51

**Table 4.5.1:** Conditions pertaining to the pristine, oxidized, and reduced states of the XRD analyte. Potentials were selected with help from completed cyclic voltammograms in  $\text{KNO}_3$

Referring to Figure 4.5.2, where a zoomed area of the patterns is pictured, the centroid of the main peak positioned at 17.5 degrees varies according to the state of charge of the electrode (cf. Table 4.5.1). This fact is related to interplanar distance, and even though we are not able to quantitatively assign cell parameters for formulated electrodes (profile matching refinement is not as straightforward, since the patterns appear much noisier than those recorded on powders), we are still able to deduce a general trend. In fact, if we consider an ion intercalation process that takes place during reduction, it can be said that the presence of K-ions in the cavities results in a contraction of the lattice, according to the shift of the main peak towards greater values of  $2\theta$ . Conversely, the extraction of K-ions during oxidation produces an expansion and a shift towards smaller  $2\theta$ . In essence, the slight lattice strain is said to be caused by the insertion/ extraction of potassium ions in the host material.

According to TG analysis reported in Figure 4.5.3, two main mass losses occur. The first mass loss step is located between 50 and 170 °C and is entirely due to the loss of water molecules. The remaining losses above 250 °C correspond to the decomposition of the material. The information derived from TGA dictates that the water content is 16% in weight, which can be used to extrapolate the formula

unit combining it with the metals ratio derived from ICP-OES. This stated that Ti/ Fe are in 1.3/ 1.0 stoichiometric ratio, hence we can write for the present material the following formula:  $Ti_{1.3}Fe(CN)_6 \cdot 2.4H_2O$ .

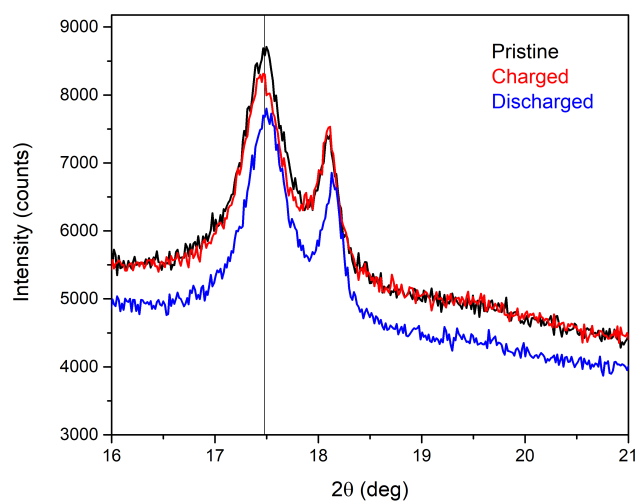


**Figure 4.5.2:** A section of the XRD profile for pristine TiHCF, as well as the cycled electrodes in the reduced and oxidized states

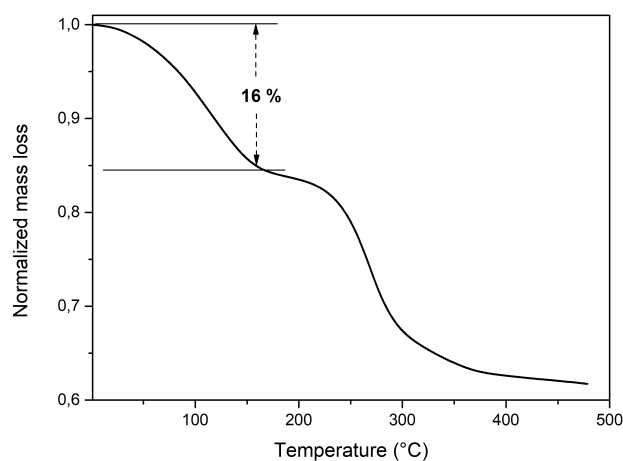


**Figure 4.5.3:** TG analysis on TiHCF

#### 4.5.2 ELECTROCHEMICAL CHARACTERIZATION

Figure 4.5.4 demonstrates the effect of changing the cation in solution while scan rate, concentration, voltage window, and counter anion remain constant. It can be seen that TiHCF is versatile and is able to

accommodate a variety of ions, ranging from the monovalent  $K^+$  and  $Na^+$ , divalent  $Zn^{2+}$ , and trivalent  $Al^{3+}$ .

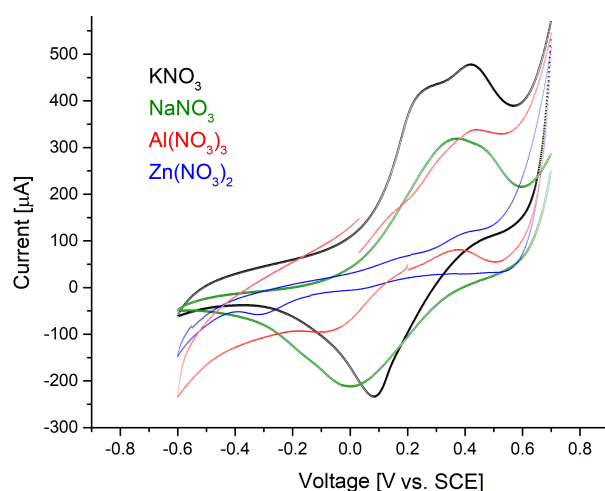


**Figure 4.5.4:** Cyclic voltammograms comparing different electrolyte solutions at a constant scan rate of  $1 \text{ mV s}^{-1}$  and at a concentration of  $0.1\text{M}$

Ions are able to be reversibly inserted and extracted, and they are done so through a single or multi-step process. In the case of potassium, the extraction takes place at two different potentials, which is demonstrated by the presence of two peaks in the oxidation. However, if the concentration of potassium is increased, the process seems to occur at a single potential (c.f. Figure 4.5.5, left panel). In the case of sodium, the peaks are quite broad regardless of change in concentration (c.f. Figure 4.5.5, right panel). This may be due to the presence of a multi-step extraction occurring at different sites. For aluminum and zinc, there are many distinguishable extraction and insertion processes occurring at different potentials (cf. Figure 4.5.4). The insertion and extraction processes may demonstrate a larger variation as they may be dependent on ion size as well as ion charge. The cyclic voltammograms demonstrate that both  $KNO_3$  and  $NaNO_3$  are likely more promising than the alternative electrolytes. Not only do they possess quality life cycle, but they also show to be relatively reversible and show high capacities (proportional to the area beneath the voltammogram).

For hexacyanoferrates in this potential window, it is commonly reported that the active metal is iron. Potassium and sodium have shown to be the most appealing cations and an optimal concentration has been selected. In order to further explore the electrochemical properties of the material, it is necessary to explore variations in the voltage range. Figure 4.5.6 (left panel) shows a cyclic voltammogram rang-

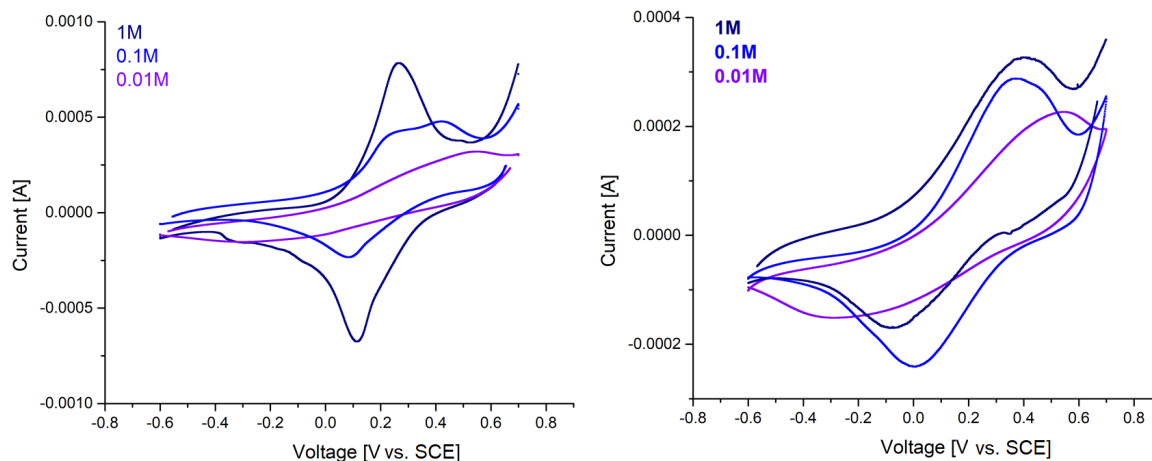


**Figure 4.5.5:** Voltammograms taken at varying electrolyte concentration for KNO<sub>3</sub> (left) and NaNO<sub>3</sub> (right)

ing from -1.3 V to +1.3 V vs. SCE with potassium and sodium nitrate. As we have seen, there is the reversible process taking place from 0 V to 0.5 V, as well there is what seems to be a reversible process occurring at the higher end of the potential range. What is peculiar in this process is the presence of an irreversible redox pair at lower potentials. A reduction occurs at a potential of -1.3 V, however there is no associated oxidation upon charge. In order to maximize efficiency, a lower limit will need to be applied to the cycle, selected at -0.7 V. Figure 4.5.6 (right panel) depicts the associated cyclic voltammogram in the optimized conditions, conducted at a slow scan rate of 5 mV/s in an attempt to acquire high resolved peaks associated to the redox processes under investigation. Under these operating conditions, the recorded reversible specific capacities are 55 mAh/g and 27 mAh/g for potassium and sodium, respectively. Moreover, given that we observe two distinct redox couples centred at 0.2 V and 0.9 V vs. SCE, we cannot exclude the Ti-species participation to the overall process. To assess this hypothesis, further tests should be performed, for instance by carrying out a *post mortem* XAFS experiment on the cycled electrodes equilibrated at different potentials.

#### 4.5.3 CONCLUDING REMARKS

Titanium hexacyanoferrate was studied to provide electrochemical information on the material in aqueous electrolytes in a post-lithium strategy. Synthesis was carried out via precipitation method. Characterization revealed the crystallinity of the compound and cubic symmetric structure. The combination

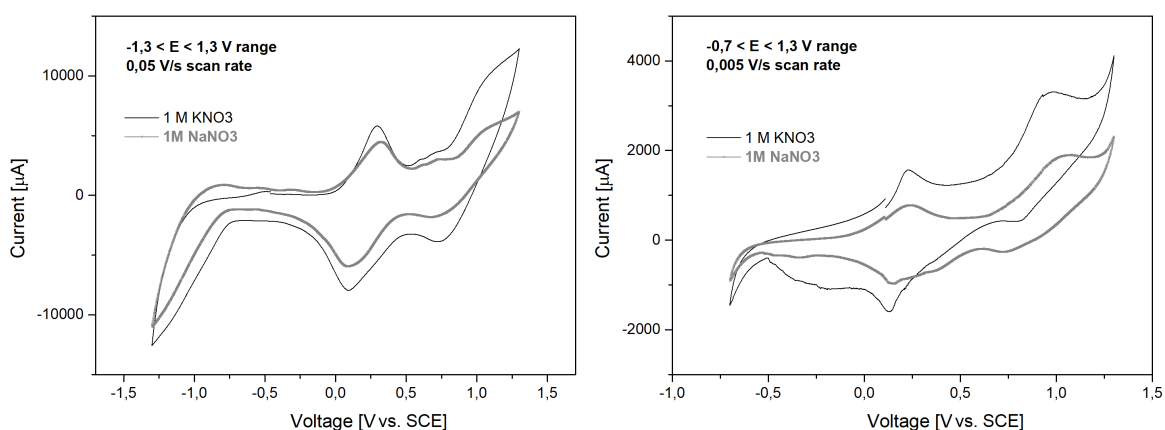


**Figure 4.5.6:** Voltammograms taken at varying potential window for  $\text{KNO}_3$  (left) and  $\text{NaNO}_3$  (right)

of TGA and ICP-OES provided useful in assigning the chemical formula to the synthesized material:  $\text{Ti}_{1.3}\text{Fe}(\text{CN})_6 \cdot 2.4\text{H}_2\text{O}$ . Cyclic voltammetry has been used to study the electrochemical behavior of the PTFE-formulated electrodes in aqueous solutions. A deep and systematic study on the material has been done, by varying operating potential window, salt composition, and salt concentration. As a result of the carried optimization, higher capacities were obtained, demonstrating good performance in aqueous medium, delivering reversible specific capacities of 55 mAh/g and 27 mA/h in potassium and sodium nitrates, respectively. Finally, further experiments should be performed to assess the metals electroactivity after observation of two distinct and well-separated redox couples in different potential ranges, centred at 0.2 V and 0.9 V, respectively.

		Spectrum number											
		Powder											
		0	10	15	20	30	42	50	55	60	65	70	
Co-C (N) / Å	1.862(3)	1.860(4)	1.861(5)	1.855(6)	1.858(4)	1.860(5)	1.856(6)	1.859(5)	1.859(5)	1.861(5)	1.861(4)	1.860(4)	
$\sigma^2$ Co-C / Å <sup>2</sup>	0.0016(5)	0.002(1)	0.0020(7)	0.002(1)	0.0016(7)	0.0017(9)	0.002(1)	0.002(1)	0.0015(9)	0.0014(6)	0.002(1)	0.0014(7)	
CN / Å	1.187(5)	1.185(5)	1.187(7)	1.18(1)	1.18(1)	1.182(7)	1.184(7)	1.183(6)	1.182(6)	1.184(6)	1.184(7)	1.186(6)	
$\sigma^2$ CN / Å <sup>2</sup>	0.007(2)	0.005(2)	0.0013(6)	0.005(2)	0.003(1)	0.002(1)	0.002(1)	0.006(2)	0.005(2)	0.0012(4)	0.004(2)	0.004(1)	
Fe-N / Å	2.077(8)	2.063(7)	2.065(6)	2.06(1)	2.063(7)	2.055(7)	2.052(8)	2.057(7)	2.057(7)	2.054(6)	2.057(5)	2.059(7)	
$\sigma^2$ Fe-N / Å <sup>2</sup>	0.007(2)	0.004(2)	0.005(1)	0.007(3)	0.005(2)	0.009(2)	0.007(2)	0.011(2)	0.009(2)	0.006(1)	0.007(2)	0.006(1)	
Fe-O / Å	2.09(2)	2.02(1)	2.02(2)	2.03(1)	2.036(8)	2.015(9)	2.00(1)	2.008(8)	2.009(9)	2.02(1)	2.02(2)	2.02(1)	
$\sigma^2$ Fe-O / Å <sup>2</sup>	0.006(3)	0.005(3)	0.004(2)	0.004(2)	0.002(1)	0.003(2)	0.003(2)	0.002(1)	0.003(1)	0.006(2)	0.004(1)	0.005(2)	
$\sigma^2$ Co-C-N / deg <sup>2</sup>	4(3)	4(3)	4(2)	4(3)	4(3)	4(3)	4(3)	4(3)	5(4)	4(3)	4(3)	5(4)	
$\sigma^2$ Fe-N-C / deg <sup>2</sup>	9(6)	10(8)	10(8)	3(2)	10(9)	10(8)	9(8)	9(8)	9(8)	9(8)	9(8)	9(8)	
$E_0$ (Fe)	7121.4(6)	7123.4	7123.2	7123.7	7124.2	7124.3	7124.9	7124.3	7123.7	7123.5	7122.9	7122.4	
$E_0$ (Co)	7717.8(6)	7717.5	7718.4	7717.2	7717.3	7717.4	7717.2	7717.3	7717.3	7717.4	7717.4	7717.4	
CN <sup>chain</sup>	3.5(3)	3.5(5)	3.3(3)	3.3(5)	3.0(3)	3.3(3)	3.4(5)	3.6(5)	3.0(4)	2.8(4)	3.1(3)	2.9(5)	
CN <sub>3</sub> (Fe-O)	1.8(5)	1.9(3)	2.0(4)	2.2(3)	2.2(3)	2.7(3)	2.9(4)	2.6(3)	2.6(3)	2.4(3)	2.0(3)	2.3(4)	
CN <sup>8c</sup> (M <sup>8c</sup> = K)	1	Fixed 2	Fixed 2	1.7	1.2	0.5	0.0	0.0	0.3	0.3	0.5	0.5	
S <sub>0</sub> <sup>2</sup> (Fe)	0.66(4)	0.65(4)	0.66(3)	0.66(4)	0.66(3)	0.65(3)	0.66(3)	0.65(3)	0.66(3)	0.66(3)	0.69(6)	0.65(3)	
S <sub>0</sub> <sup>2</sup> (Co)	0.71(3)	0.76(4)	0.77(4)	0.73(3)	0.72(3)	0.74(3)	0.73(4)	0.78(4)	0.72(4)	0.72(3)	0.73(3)	0.72(3)	
a/2 / Å	5.12	5.10	5.11	5.10	5.10	5.09	5.09	5.10	5.10	5.10	5.10	5.10	
$\chi^2$ -like residual (10 <sup>6</sup> )	3.63	5.83	5.91	5.80	5.72	6.50	7.22	6.02	5.34	4.95	4.98	4.44	

**Table 4.5.2:** Results of the EXAFS fitting procedure on FeCo

		Spectrum number									
		Charge					Discharge				
Pristine (Fe K-edge only)	Pristine	10	18	27	33	40	48	54	62		
Fe-C / Å	1.857(5)	1.853(7)	1.855(8)	1.862(9)	1.870(8)	1.887(7)	1.874(10)	1.858(9)	1.858(7)	1.856(7)	
$\sigma^2$ Fe-C / Å <sup>2</sup>	0.0010(4)	0.003(1)	0.003(1)	0.003(1)	0.003(1)	0.003(1)	0.003(1)	0.003(1)	0.004(1)	0.004(1)	
CN / Å	1.19(1)	1.189(4)	1.189(6)	1.186(4)	1.182(7)	1.17(1)	1.178(8)	1.189(5)	1.189(4)	1.189(4)	
$\sigma^2$ CN / Å <sup>2</sup>	0.008(2)	0.011(2)	0.011(2)	0.009(3)	0.011(2)	0.012(3)	0.011(5)	0.012(4)	0.008(3)	0.011(3)	
Cu-N / Å	1.91(3)	1.900(15)	1.91(1)	1.930(6)	1.954(6)	1.954(4)	1.949(5)	1.929(5)	1.91(1)	1.91(1)	
$\sigma^2$ Cu-N / Å <sup>2</sup>	0.019(4)	0.009(3)	0.009(2)	0.008(3)	0.006(3)	0.005(2)	0.006(1)	0.010(2)	0.010(3)	0.011(3)	
Cu-O / Å		2.25(5)	2.37(8)	2.25(6)	2.25(6)	2.35(5)	2.25(6)	2.26(8)	2.25(7)	2.25(6)	
$\sigma^2$ Cu-O / Å <sup>2</sup>		0.029(8)	0.03(1)	0.03(1)	0.03(1)	0.03(1)	0.03(1)	0.03(1)	0.03(1)	0.03(1)	
$\sigma^2$ (Fe-C-N) / deg <sup>2</sup>	3(1)	3(1)	3(1)	3(1)	3(1)	3(1)	3(1)	3(1)	3(1)	3(1)	
$\sigma^2$ (C-N-Cu) / deg <sup>2</sup>	36(10)	40(10)	26(10)	53(30)	65(20)	74(30)	48(25)	74(24)	35(20)	74(20)	
CN <sup>8c</sup> (M <sup>8c</sup> =K/Cu)	2 Fixed	2 Fixed	2.0(9)	1.6(9)	1.5(10)	0.5 Fixed	0.4(3)	0.4(3)	1.4(10)	1.5(10)	
$E_0$ Fe	7116.5(4)	7116.0(5)	7116(1)	7117(1)	7117(1)	7117(1)	7117(1)	7117(1)	7117(1)	7117(1)	
$E_0$ Cu		8991(1)	8990(1)	8992(1)	8992(1)	8991(1)	8991(1)	8991(1)	8991(1)	8991(1)	
CN <sup>chain</sup>		4.5(5)	4.3(3)	4.4(2)	4.2(2)	4.3(3)	4.4(3)	4.5(2)	4.5(3)	4.6(2)	
S <sub>o</sub> (Fe)	0.76(6)	0.84(4)	0.84 Fixed								
S <sub>o</sub> (Cu)		0.75(7)	0.75 Fixed								
a/2 / Å		4.942	4.954	4.978	5.006	5.011	5.001	4.976	4.957	4.955	

**Table 4.5.3:** Results of the EXAFS fitting procedure on CuHCF

Inserted Li equivalents															
Powder	Pristine (0 Li)	0.07 Li	0.14 Li	0.22 Li	0.29 Li	0.36 Li	0.43 Li	0.50 Li	0.58 Li	0.65 Li	0.72 Li	0.79 Li	0.86 Li	0.94 Li	1.01 Li
Fe-C (N) / Å	1.916(4)	1.913(4)	1.917(4)	1.918(4)	1.919(4)	1.922(3)	1.922(4)	1.921(3)	1.923(3)	1.924(4)	1.921(4)	1.918(6)	1.920(3)	1.921(4)	1.917(3)
$\sigma^2(\text{Fe-C}) / \text{Å}^2$	0.0023(8)	0.0020(5)	0.003(1)	0.0032(7)	0.0037(5)	0.0043(5)	0.0040(5)	0.0043(5)	0.0044(4)	0.0046(6)	0.0050(5)	0.0050(6)	0.0050(4)	0.006(1)	0.0057(5)
CN / Å	1.152(5)	1.148(5)	1.155(5)	1.148(4)	1.150(5)	1.148(4)	1.150(5)	1.146(4)	1.146(4)	1.152(5)	1.149(5)	1.149(5)	1.148(8)	1.15(1)	1.15(1)
$\sigma^2(\text{CN}) / \text{Å}^2$	0.012(1)	0.009(1)	0.013(1)	0.011(1)	0.012(1)	0.013(1)	0.013(1)	0.011(1)	0.014(1)	0.011(1)	0.010(1)	0.009(1)	0.010(1)	0.012(2)	0.012(1)
Cu-N (C) / Å	1.98(1)	1.98(1)	1.98(1)	1.975(8)	1.973(9)	1.98(1)	1.97(1)	1.98(1)	1.97(1)	1.96(1)	1.98(1)	1.97(2)	1.98(2)	1.97(1)	1.98(1)
$\sigma^2(\text{Cu-N}) / \text{Å}^2$	0.004(1)	0.004(1)	0.005(1)	0.007(1)	0.008(1)	0.010(1)	0.009(2)	0.011(1)	0.012(2)	0.012(2)	0.013(2)	0.014(2)	0.014(2)	0.014(2)	0.015(2)
Cu-N (C) / Å	2.123	2.119	2.149	2.149	2.149	2.149	2.149	2.149	2.149	2.149	2.148	2.149	2.148	2.149	2.149
$\sigma^2(\text{Cu-N}) / \text{Å}^2$	0.018	0.029	0.022	0.028	0.024	0.029	0.023	0.024	0.024	0.024	0.024	0.024	0.024	0.023	0.024
Fe-N (O) / Å	1.693	1.670	1.691	1.670	1.672	1.673	1.672	1.686	1.666	1.665	1.656	1.652	1.655	1.657	1.649
$\sigma^2(\text{Fe-N}) / \text{Å}^2$	0.006	0.0038	0.009	0.0047	0.0045	0.0035	0.0035	0.0045	0.0036	0.0047	0.0045	0.004	0.0044	0.0064	0.0046
N-O / Å	1.118	1.124	1.125	1.136	1.134	1.136	1.138	1.140	1.140	1.148	1.148	1.144	1.145	1.147	1.15(1)
$\sigma^2(\text{N-O}) / \text{Å}^2$	0.001	0.001	0.0018	0.0010	0.001	0.001	0.0010	0.0013	0.0010	0.0010	0.0010	0.001	0.0010	0.0010	0.0010
Cu-O / Å	2.98	2.97	2.95	2.98	2.97	2.979	2.40	2.40	2.40	2.495	2.40	2.425	2.40	2.400	2.40
$\sigma^2(\text{Cu-O}) / \text{Å}^2$	0.034	0.034	0.034	0.034	0.033	0.034	0.022	0.011	0.013	0.019	0.012	0.012	0.011	0.014	0.010
$\sigma^2(\text{Fe-C-N}) / \text{deg}^2$	15(10)	23(10)	30(15)	38(15)	32(12)	50(12)	4(3)	43(11)	31(15)	4(3)	6(4)	4(3)	13(10)	10(8)	15(8)
$\sigma^2(\text{Cu-N-C}) / \text{deg}^2$	9(6)	9(5)	9(6)	9(6)	9(6)	10(7)	26(9)	38(15)	36(10)	18(8)	37(15)	30(20)	43(13)	26(9)	38(10)
$\sigma^2(\text{Fe-N-O}) / \text{deg}^2$	63(40)	54(25)	42(30)	48(20)	34(25)	26(20)	50(20)	45(20)	47(25)	53(20)	36(20)	70(30)	10(8)	41(15)	39(20)
$\theta$ Fe-N-O / deg	180 Fixed	180 Fixed	180 Fixed	180 Fixed	180 Fixed	180 Fixed	177	144	140	140	143	179(15)	142	179(30)	166(20)
$E_0(\text{Fe})$	7119.6(5)	7119.1(4)	7119.9(6)	7119.4(5)	7119.6(4)	7119.7(3)	7119.6(3)	7119.5(3)	7119.6(3)	7119.7(3)	7119.2(3)	7118.9(3)	7119.0(4)	7119.2(4)	7119(1)
$E_0(\text{Cu})$	8992.0(6)	8992(1)	8992(1)	8992(1)	8991.7(8)	8991.6(8)	8992.2(8)	8993(1)	8993(1)	8992(1)	8993(1)	8993(1)	8993(1)	8992(1)	8993(1)
CN1 ( $\gamma^{(3)}\text{Cu}$ )	Fixed 4	Fixed 4	Fixed 4	Fixed 4	Fixed 4	Fixed 4	Fixed 4	3.9(6)	3.9(6)	4.0(3)	3.9(6)	4.0(4)	3.4(5)	3.5(5)	3.8(5)
CN2 ( $\gamma^{(4)}\text{Fe}$ )	Fixed 5	Fixed 5	Fixed 5	Fixed 5	Fixed 5	Fixed 5	4(1)	4.5(6)	4.3(9)	2.8(8)	3.8(9)	3.2(6)	3.4(7)	2.7(9)	4.4(8)
CN <sup>thinn</sup>	Fixed 5	Fixed 5	Fixed 5	Fixed 5	Fixed 5	Fixed 5	3.6(15)	3.3(6)	3.0(15)	2.8(9)	3.1(15)	2.6(14)	2.1(12)	1.9(9)	2.4(9)
$S_0^{\text{Fe}}$	0.77	Fixed Fixed	Fixed	Fixed	Fixed	Fixed	Fixed	Fixed	Fixed	Fixed	Fixed	Fixed	Fixed	Fixed	Fixed
$S_0^{\text{Cu}}$	0.89	Fixed Fixed	Fixed	Fixed	Fixed	Fixed	Fixed	Fixed	Fixed	Fixed	Fixed	Fixed	Fixed	Fixed	Fixed
$\chi^2$ -like residual ( $\cdot 10^6$ )	2.18	2.15	1.82	1.74	1.77	2.03	1.68	1.93	1.96	1.49	1.75	1.74	1.66	1.74	1.72

Table 4.5.4: Results of the EXAFS fitting procedure on CuNP

*Sometimes in the morning, when it's a good surf, I go out there,  
and I don't feel like it's a bad world.*

Kary Mullis

# 5

## Finals remarks and perspectives

The complexity of a battery, which consists of different components and various contributions to the overall redox process, can be untangled by using a combined complementary multi-technique approach. XRD is commonly used to identify crystalline phases, and to follow their modification during cycling. XAFS is the technique of choice for retrieving electronic and short-range structural information in transition-metal based systems, by analyzing both XANES and EXAFS portions. Moreover, *operando* measurements allow for a continuous monitoring of the system dynamics; however, the acquired large datasets make necessary an advanced data treatment, often supported by chemometric techniques, such as multivariate curve resolution refined by alternating least squares (MCR-ALS). The complementary assistance of MCR-ALS might reveal the occurrence of complex multicomponent reactions, making the EXAFS interpretation more reliable. This joint approach has been demonstrated to have a wide potentiality in retrieving the local structural dynamics of selected absorbing species, allowing a quick

and efficient data interpretation which would be otherwise time consuming. In addition, the support of theoretical studies permitted the validation of our hypotheses and gave further insight into reaction mechanisms.

PBAs are characterized by porous open 3D-frameworks which allow for a facile insertion/ extraction of ions with negligible lattice strain. The electroactivity of the metals constituting the lattice forms the basis for a series of properties, which have been studying in several fields. Due to their high electrochemical efficiency, low-cost, affordable price, and versatility towards a wide selection of ions, they have been investigating as electrode materials in Li-ion batteries, as well as Na-ion batteries and aqueous systems in the perspective of a post-lithium strategy, intended to provide for alternatives to the use of lithium in current technologies. We have studied a series of PBAs and assessed their electrochemical behavior in organic and aqueous media. We have tested copper hexacyanoferrate and titanium hexacyanoferrate in aqueous solutions and studied the (de)intercalation of monovalent and multivalent ions in the structure. This led to the conclusion that a H<sub>2</sub>O-based system would be feasible for the studied materials, and more in general for this class of compounds.

Despite the overall high efficiency, they usually suffer from poor specific capacities. For this reason, starting from a well-known highly performant copper hexacyanoferrate, we have successfully accomplished to increase the capacity per formula unit by replacing a cyanide ligand in the iron octahedral environment with an extra redox centre, *i.e.*, a *non-innocent* ligand, the nitrosyl. Moreover, the assembly in Na-ion battery was aimed to evaluate the electrochemical behavior in case of replacement of Li. Although we observed and theoretically predicted the reduction of the ligand, the increase in specific capacity was limited to the beginning of the cycling, causing a local distortion around the copper site. Nevertheless, the introduction of a third redox site might be a good strategy to increase the capacity.

By carefully choosing the metals constituting the lattice, it is possible to tune structural and electrochemical properties. Therefore, we replaced the Jahn-Teller distorted copper in copper nitroprusside with cobalt, and investigated the activity of the resulting cobalt nitroprusside (CoNP). Figure 5.0.1 shows some interesting electrochemical features of this newly synthesized material. The cyclic voltammetry (left panel) suggests an irreversible reaction in the first discharge process corresponding to the recorded peak at 1.2 V vs. Li<sup>+</sup>/Li, followed by a reproducible electrochemical behavior after it. Surprisingly, the

redox activity is located at relatively low potentials, differently from other metal hexacyanoferrates-like materials, making CoNP a potential anode material (redox reactions are situated below 2 V vs.  $\text{Li}^+/\text{Li}$ ). The right panel highlights the extraordinary performance at high C-rate values: while maintaining a high coulombic efficiency throughout the testing, CoNP is able to tolerate high current rates maintaining extremely high specific capacities, far above other PBAs.

The *operando* investigation is currently running, however, we have already assessed the electrochemical activity of both cobalt and iron.

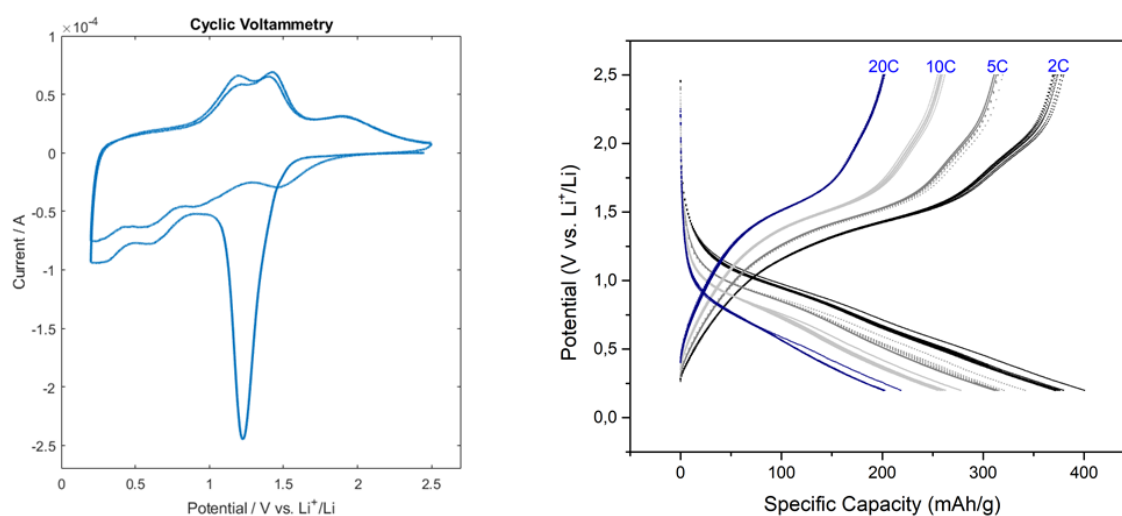


**Figure 5.0.1:** Electrochemical tests on CoNP. CV (left) recorded in the  $0.2 < E < 2.5$  V vs.  $\text{Li}^+/\text{Li}$  at  $0.1$  mV/s scan rate; and GCPL (right) recorded in the same potential window at different current rates (2C, 5C, 10C, 20C)

Another interesting PBA is represented by sodium-rich manganese hexacyanoferrate. By optimizing the synthesis, we were able to produce  $\text{Na}_{1.9}\text{Mn}_{1.1}\text{Fe}(\text{CN})_6$  (MnHCF). The already reported GCPL (cf. Figure 2.1.3) is presented again in Figure 5.0.2 together with the evolution of Mn K-edge during the first charge. The electrochemical behavior of such compound in an organic Na system is promising, showing good cycling stability and a reversible redox in a very narrow window at high potentials ( $E_{\text{ox}} = 3.53$  V;  $E_{\text{red}} = 3.45$  V). Furthermore, the reversible delivered specific capacity is roughly 130 mAh/g. The Mn-site has been demonstrated to be active during the electrochemical charge/ discharge, being for instance oxidized during the charge process (K-edge shifts towards higher energies, cf. Figure 5.0.2). We are currently carrying on other tests to elucidate the electrochemical activity and performance.

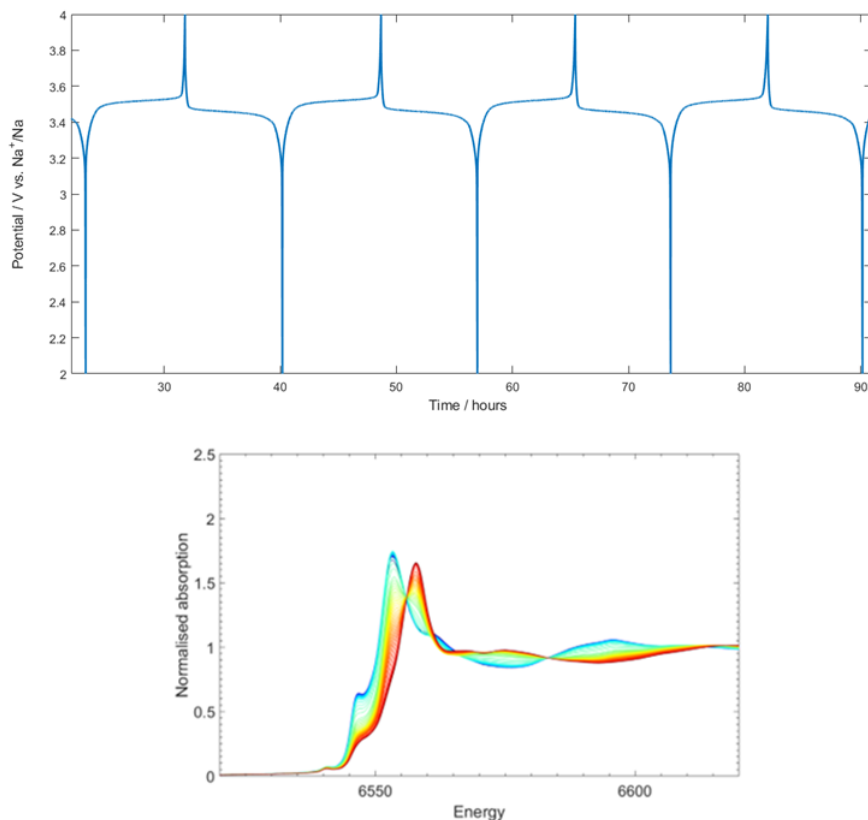


**Figure 5.0.2:** GCPL on MnHCF at C/10 rate in the  $2.0 < E < 4.0$  V vs. Na<sup>+</sup>/Na potential window (top panel), and Mn K-edge evolution during the first charge (bottom panel)

The feasibility to use Prussian blue analogues in Li-ion and post-Li batteries has been proven and anticipated. High coulombic efficiency and affordable price could be coupled to competitive specific capacities and/ or to alternative solutions to Li-based systems, for instance Na-ion and aqueous batteries.

## References

- [1] Giuliana Aquilanti, Marco Giorgetti, Robert Dominko, Lorenzo Stievano, Iztok Arčon, Nicola Novello, and Luca Olivi. Operando characterization of batteries using x-ray absorption spectroscopy: Advances at the beamline XAFS at synchrotron Elettra. *Journal of Physics D: Applied Physics*, 50:074001, 2017. doi: 10.1088/1361-6463/aa519a.
- [2] Marco Giorgetti, Adriana Mignani, Giuliana Aquilanti, Paolo Conti, Marcus Fehse, and Lorenzo Stievano. Structural and electronic studies of metal hexacyanoferrates based cathodes for Li rechargeable batteries. *Journal of Physics: Conference Series*, 712:012127, 2016. doi: 10.1088/1742-6596/712/1/012127.
- [3] Christophe Pillot. Battery Market Development for Consumer Electronics , Automotive , and Industrial : Materials Requirements and Trends. Technical report, 2015.
- [4] O. Schmidt, A. Hawkes, A. Gambhir, and I. Staffell. The future cost of electrical energy storage based on experience rates. *Nature Energy*, 6:17110, 2017. doi: 10.1038/nenergy.2017.110.
- [5] European Commission. Study on the review of the list of critical raw materials. Non-critical raw materials factsheets. Technical report, 2017.
- [6] Cui Rongguo, Guo Juan, Yin Liwen, Dieter Huy, and Maren Liedtke. Supply and Demand of Lithium and Gallium. Technical report, 2016.
- [7] Steven Chu and Arun Majumdar. Opportunities and challenges for a sustainable energy future. *Nature*, 488:294–303, 2012. doi: 10.1038/nature11475.
- [8] Steven Chu, Yi Cui, and Nian Liu. The path towards sustainable energy. *Nature Materials*, 16:16–22, 2016. doi: 10.1038/nmat4834.

- [9] U.S. Department of Energy (DOE). EV Everywhere Grand Challenge Blueprint. 2013. URL [https://www.energy.gov/sites/prod/files/2014/02/f8/eveverywhere\\_blueprint.pdf](https://www.energy.gov/sites/prod/files/2014/02/f8/eveverywhere_blueprint.pdf).
- [10] Energy International, IEA Agency. 2017 Global Outlook EV Electric Vehicles. 2017.
- [11] U.S. Department of Energy (DOE). 80 Million Investment in Advanced Vehicle Technologies Research. URL <https://www.energy.gov/articles/>.
- [12] Mike Ware. Prussian Blue: Artists' Pigment and Chemists' Sponge. *Journal of Chemical Education*, 85: 612–621, 2008. doi: 10.1021/ed085p612.
- [13] Hugh Davies. Prussian blue: From the Great Wave to Starry Night , how a pigment changed the world, 2017. URL <https://www.abc.net.au/news/2017-07-21/prussian-blue-hokusai-great-wave-how-a-pigment-changed-the-world/8731732>.
- [14] J. F. Keggin and F. D. Miles. Structures and formulæ of the prussian blues and related compounds. *Nature*, 137:577–578, 1936. doi: 10.1038/137577a0.
- [15] H. J. Buser, A. Ludi, D. Schwarzenbach, and W. Petter. The Crystal Structure of Prussian Blue:  $\text{Fe}_4[\text{Fe}(\text{CN})_6]_3 \cdot x\text{H}_2\text{O}$ . *Inorganic Chemistry*, 16:2704–2710, 1977. doi: 10.1021/ic50177a008.
- [16] A. Harrison and S. J. Clarke. 23. Magnetism. *Annual Reports Section "a" (Inorganic Chemistry)*, 89:425–452, 1992. doi: 10.1039/IC9928900425.
- [17] F. Herren, A. Ludi, P. Fischer, and W. Halg. Neutron Diffraction Study of Prussian Blue,  $\text{Fe}_4[\text{Fe}(\text{CN})_6]_3 \cdot x\text{H}_2\text{O}$ . Location of Water Molecules and Long-Range Magnetic Order. *Inorganic Chemistry*, 19:956–959, 1980. doi: 10.1021/ic50206a032.
- [18] Marco Giorgetti, Mario Berrettoni, Adriano Filipponi, Pawel J. Kulesza, and Roberto Marassi. Evidence of four-body contributions in the EXAFS spectrum of  $\text{Na}_2\text{Co}[\text{Fe}(\text{CN})_6]$ . *Chemical Physics Letters*, 275: 108–112, 1997. doi: 10.1016/S0009-2614(97)00724-0.
- [19] Marco Giorgetti and Mario Berrettoni. Structure of Fe/Co/Ni hexacyanoferrate as probed by multiple edge X-ray absorption spectroscopy. *Inorganic Chemistry*, 47:6001–6008, 2008. doi: 10.1021/ic800289c.
- [20] J. Rodríguez-Hernández, E. Reguera, E. Lima, J. Balmaseda, R. Martínez-García, and H. Yee-Madeira. An atypical coordination in hexacyanometallates: Structure and properties of hexagonal zinc phases. *Journal of Physics and Chemistry of Solids*, 68:1630–1642, 2007. doi: 10.1016/j.jpcs.2007.03.054.

- [21] Christopher M. Kareis, Saul H. Lapidus, Jae Hyuk Her, Peter W. Stephens, and Joel S. Miller. Non-Prussian blue structures and magnetic ordering of  $\text{Na}_2\text{Mn}[\text{Mn}(\text{CN})_6]$  and  $\text{Na}_2\text{Mn}[\text{Mn}(\text{CN})_6]\cdot 2\text{H}_2\text{O}$ . *Journal of the American Chemical Society*, 134:2246–2254, 2012. doi: 10.1021/ja209799y.
- [22] R. Martínez-García, M. Knobel, J. Balmaseda, H. Yee-Madeira, and E. Reguera. Mixed valence states in cobalt iron cyanide. *Journal of Physics and Chemistry of Solids*, 68:290–298, 2007. doi: 10.1016/j.jpcs.2006.11.008.
- [23] Long Wang, Yuhao Lu, Jue Liu, Maowen Xu, Jinguang Cheng, Dawei Zhang, and John B. Goodenough. A superior low-cost cathode for a Na-Ion battery. *Angewandte Chemie - International Edition*, 52:1964–1967, 2013. doi: 10.1002/anie.201206854.
- [24] Marzhana Omarova, Aibolat Koishybay, Nulati Yesibolati, Almagul Mentbayeva, Nurzhan Umirov, Kairat Ismailov, Desmond Adair, Moulay Rachid Babaa, Indira Kurmanbayeva, and Zhumabay Bakenov. Nickel Hexacyanoferrate Nanoparticles as a Low Cost Cathode Material for Lithium-Ion Batteries. *Electrochimica Acta*, 184:58–63, 2015. doi: 10.1016/j.electacta.2015.10.031.
- [25] Colin D. Wessells, Matthew T. McDowell, Sandeep V. Peddada, Mauro Pasta, Robert A. Huggins, and Yi Cui. Tunable reaction potentials in open framework nanoparticle battery electrodes for grid-scale energy storage. *ACS Nano*, 6:1688–1694, 2012. doi: 10.1021/nn204666v.
- [26] Roger J. Mortimer and David R. Rosseinsky. Electrochemical polychromicity in iron hexacyanoferrate films, and a new film form of ferric ferricyanide. *Journal of Electroanalytical Chemistry*, 151:133–147, 1983. doi: 10.1016/S0022-0728(83)80429-X.
- [27] Lorella Guadagnini, Artjom Maljusch, Xingxing Chen, Sebastian Neugebauer, Domenica Tonelli, and Wolfgang Schuhmann. Visualization of electrocatalytic activity of microstructured metal hexacyanoferrates by means of redox competition mode of scanning electrochemical microscopy (RC-SECM). *Electrochimica Acta*, 54:3753–3758, 2009. doi: 10.1016/j.electacta.2009.01.076.
- [28] Yuping Shan, Guocheng Yang, Jian Gong, Xiaoli Zhang, Liande Zhu, and Lunyu Qu. Prussian blue nanoparticles potentiostatically electrodeposited on indium tin oxide/chitosan nanofibers electrode and their electrocatalysis towards hydrogen peroxide. *Electrochimica Acta*, 53:7751–7755, 2008. doi: 10.1016/j.electacta.2008.05.035.

- [29] Roger J. Mortimer, David R. Rosseinsky, and Andrew Glidle. Polyelectrochromic Prussian blue: a chronoamperometric study of the electrodeposition. *Solar Energy Materials and Solar Cells*, 25:211–223, 1992. doi: 10.1016/0927-0248(92)90069-2.
- [30] Marcin Zadroncki. Study of Growth and the Electrochemical Behavior of Prussian Blue Films Using Electrochemical Quartz Crystal Microbalance. *Journal of The Electrochemical Society*, 146:620, 1999. doi: 10.1149/1.1391653.
- [31] M. Giorgetti, E. Scavetta, M. Berrettoni, and D. Tonelli. Nickel hexacyanoferrate membrane as a coated wire cation-selective electrode. *Analyst*, 126:2168–2171, 2001. doi: 10.1039/b107034g.
- [32] O. Sato, T. Iyoda, A. Fujishima, and K. Hashimoto. Photoinduced magnetization of a cobalt-iron cyanide. *Science*, 272:704–705, 1996. doi: 10.1126/science.272.5262.704.
- [33] Paulo Roberto Bueno, David Giménez-Romero, Fabio Fburlan Ferreira, Grazielle Oliveira Setti, José Juan Garcia-Jareño, Jerónimo Agrisuelas, and Francisco Vicente. Electrochromic switching mechanism of iron hexacyanoferrates molecular compounds: the role of Fe(CN)<sub>6</sub> vacancies. *Journal of Physical Chemistry C*, 113:9916–9920, 2009. doi: 10.1021/jp901146w.
- [34] Vernon D. Neff. Some Performance Characteristics of a Prussian Blue Battery. *Journal of The Electrochemical Society*, 132:1382–1385, 1985. doi: 10.1149/1.2114121.
- [35] Rongzhi Chen, Hisashi Tanaka, Tohru Kawamoto, Miyuki Asai, Chikako Fukushima, Masato Kurihara, Masayuki Watanabe, Makoto Arisaka, and Takuya Nankawa. Preparation of a film of copper hexacyanoferrate nanoparticles for electrochemical removal of cesium from radioactive wastewater. *Electrochemistry Communications*, 25:23–25, 2012. doi: 10.1016/j.elecom.2012.09.012.
- [36] Michela Ciabocco, Patrizia Cancemi, Maria Luisa Saladino, Eugenio Caponetti, Rosa Alduina, and Mario Berrettoni. Synthesis and antibacterial activity of iron-hexacyanocobaltate nanoparticles. *Journal of Biological Inorganic Chemistry*, 23:385–398, 2018. doi: 10.1007/s00775-018-1544-x.
- [37] D. Ravi Shankaran and S. Sriman Narayanan. Characterization and application of an electrode modified by mechanically immobilized copper hexacyanoferrate. *Fresenius' Journal of Analytical Chemistry*, 364: 686–689, 1999. doi: 10.1007/s002160051414.

- [38] Shen Ming Chen and Chia Ming Chan. Preparation, characterization, and electrocatalytic properties of copper hexacyanoferrate film and bilayer film modified electrodes. *Journal of Electroanalytical Chemistry*, 543:161–173, 2003. doi: 10.1016/S0022-0728(03)00017-2.
- [39] Dong Mei Zhou, Huang Xian Ju, and Hong Yuan Chen. Catalytic oxidation of dopamine at a microdisk platinum electrode modified by electrodeposition of nickel hexacyanoferrate and Nafion®. *Journal of Electroanalytical Chemistry*, 408:219–223, 1996. doi: 10.1016/0022-0728(95)04522-8.
- [40] Gabriela López de Lara González, Heike Kahlert, and Fritz Scholz. Catalytic reduction of hydrogen peroxide at metal hexacyanoferrate composite electrodes and applications in enzymatic analysis. *Electrochimica Acta*, 52:1968–1974, 2007. doi: 10.1016/j.electacta.2006.08.006.
- [41] Arkady A. Karyakin. Prussian blue and its analogues: Electrochemistry and analytical applications. *Electroanalysis*, 13:813–819, 2001. doi: 10.1002/1521-4109(200106)13:10<813::AID-ELAN813>3.0.CO;2-Z.
- [42] F. Ricci and G. Palleschi. Sensor and biosensor preparation, optimisation and applications of Prussian Blue modified electrodes. *Biosensors and Bioelectronics*, 21:389–407, 2005. doi: 10.1016/j.bios.2004.12.001.
- [43] Ivanildo Luiz De Mattos, Lo Gorton, Thomas Laurell, A. Malinauskas, and Arkady A. Karyakin. Development of biosensors based on hexacyanoferrates. *Talanta*, 52:791–799, 2000. doi: 10.1016/S0039-9140(00)00409-4.
- [44] Ana Paula Baioni, Marcio Vidotti, Pablo A. Fiorito, E. A. Ponzio, and Susana I Córdoba De Torresi. Synthesis and characterization of copper hexacyanoferrate nanoparticles for building up long-term stability electrochromic electrodes. *Langmuir*, 23:6796–6800, 2007. doi: 10.1021/la070161h.
- [45] Rasa Pauliukaite, Monica Florescu, and Christopher M.A. Brett. Characterization of cobalt- and copper hexacyanoferrate-modified carbon film electrodes for redox-mediated biosensors. *Journal of Solid State Electrochemistry*, 9:354–362, 2005. doi: 10.1007/s10008-004-0632-8.
- [46] Marco Giorgetti, Giuliana Aquilanti, Michela Ciabocco, and Mario Berrettoni. Anatase-driven charge transfer involving a spin transition in cobalt iron cyanide nanostructures. *Physical Chemistry Chemical Physics*, 17:22519–22522, 2015. doi: 10.1039/c5cp03580e.
- [47] Mario Berrettoni, Marco Giorgetti, Silvia Zamponi, Paolo Conti, David Ranganathan, Antonio Zanotto, Maria Luisa Saladino, and Eugenio Caponetti. Synthesis and characterization of nanostructured cobalt hexacyanoferrate. *Journal of Physical Chemistry C*, 114:6401–6407, 2010. doi: 10.1021/jp100367p.

- [48] D. Ellis, M. Eckhoff, and V. D. Neff. Electrochromism in the mixed-valence hexacyanides. 1. Voltammetric and spectral studies of the oxidation and reduction of thin films of Prussian blue. *Journal of Physical Chemistry*, 85:1225–1231, 1981. doi: 10.1021/j150609a026.
- [49] Kalnila P. Rajan and Vernon D. Neff. Electrochromism in the mixed-valence hexacyanides. 2. Kinetics of the reduction of ruthenium purple and Prussian blue. *Journal of Physical Chemistry*, 86:4361–4368, 1982. doi: 10.1021/j100219a017.
- [50] Michael K. Carpenter, Robert S. Conell, and Steven J. Simko. Electrochemistry and Electrochromism of Vanadium Hexacyanoferrate. *Inorganic Chemistry*, 29:845–850, 1990. doi: 10.1021/ic00329a054.
- [51] Lorraine M. Siperko. Electrochemical and Spectroscopic Studies of Metal Hexacyanometalate Films. *Journal of The Electrochemical Society*, 130:396–402, 1983. doi: 10.1149/1.2119718.
- [52] Mian Jiang and Zaofan Zhao. A novel stable electrochromic thin film: a Prussian Blue analogue based on palladium hexacyanoferrate. *Journal of Electroanalytical Chemistry*, 292:281–287, 1990. doi: 10.1016/0022-0728(90)87343-I.
- [53] Richard Y. Wang, Badri Shyam, Kevin H. Stone, Johanna Nelson Weker, Mauro Pasta, Hyun Wook Lee, Michael F. Toney, and Yi Cui. Reversible Multivalent (Monovalent, Divalent, Trivalent) Ion Insertion in Open Framework Materials. *Advanced Energy Materials*, 5:1401869, 2015. doi: 10.1002/aenm.201401869.
- [54] Colin D. Wessells, Sandeep V. Peddada, Matthew T. McDowell, Robert A. Huggins, and Yi Cui. The Effect of Insertion Species on Nanostructured Open Framework Hexacyanoferrate Battery Electrodes. *Journal of The Electrochemical Society*, 159:A98, 2012. doi: 10.1149/2.060202jes.
- [55] Yutaka Moritomo, Shota Urase, and Takayuki Shibata. Enhanced battery performance in manganese hexacyanoferrate by partial substitution. *Electrochimica Acta*, 210:963–969, 2016. doi: 10.1016/j.electacta.2016.05.205.
- [56] Jie Song, Long Wang, Yuhao Lu, Jue Liu, Bingkun Guo, Penghao Xiao, Jong Jan Lee, Xiao Qing Yang, Graeme Henkelman, and John B. Goodenough. Removal of interstitial H<sub>2</sub>O in hexacyanometalates for a superior cathode of a sodium-ion battery. *Journal of the American Chemical Society*, 137:2658–2664, 2015. doi: 10.1021/ja512383b.

- [57] Colin D. Wessells, Sandeep V. Peddada, Robert A. Huggins, and Yi Cui. Nickel hexacyanoferrate nanoparticle electrodes for aqueous sodium and potassium ion batteries. *Nano Letters*, 11:5421–5425, 2011. doi: 10.1021/nl203193q.
- [58] Ali Eftekhari. Potassium secondary cell based on Prussian blue cathode. *Journal of Power Sources*, 126: 221–228, 2004. doi: 10.1016/j.jpowsour.2003.08.007.
- [59] Tohru Shiga, Hiroki Kondo, Yuichi Kato, and Masae Inoue. Insertion of Calcium Ion into Prussian Blue Analogue in Nonaqueous Solutions and Its Application to a Rechargeable Battery with Dual Carriers. *Journal of Physical Chemistry C*, 119:27946–27953, 2015. doi: 10.1021/acs.jpcc.5b10245.
- [60] Munseok S. Chae, Joeeun Hyoung, Minchul Jang, Hochun Lee, and Seung Tae Hong. Potassium nickel hexacyanoferrate as a high-voltage cathode material for nonaqueous magnesium-ion batteries. *Journal of Power Sources*, 363:269–276, 2017. doi: 10.1016/j.jpowsour.2017.07.094.
- [61] S. Liu, G. L. Pan, G. R. Li, and X. P. Gao. Copper hexacyanoferrate nanoparticles as cathode material for aqueous Al-ion batteries. *Journal of Materials Chemistry A*, 3:959–962, 2015. doi: 10.1039/c4ta04644g.
- [62] Liumin Suo, Oleg Borodin, Tao Gao, Marco Olguin, Janet Ho, Xiulin Fan, Chao Luo, Chunsheng Wang, and Kang Xu. "Water-in-salt" electrolyte enables high-voltage aqueous lithium-ion chemistries. *Science*, 350:938–943, 2015. doi: 10.1126/science.aab1595.
- [63] Kosuke NAKAMOTO, Ryo SAKAMOTO, Masato ITO, Ayuko KITAJOU, and Shigeto OKADA. Effect of Concentrated Electrolyte on Aqueous Sodium-ion Battery with Sodium Manganese Hexacyanoferrate Cathode. *Electrochemistry*, 85:179–185, 2017. doi: 10.5796/electrochemistry.85.179.
- [64] Xianyong Wu, Yang Luo, Mengying Sun, Jiangfeng Qian, Yuliang Cao, Xinping Ai, and Hanxi Yang. Low-defect Prussian blue nanocubes as high capacity and long life cathodes for aqueous Na-ion batteries. *Nano Energy*, 13:117–123, 2015. doi: 10.1016/j.nanoen.2015.02.006.
- [65] Mauro Pasta, Colin D. Wessells, Nian Liu, Johanna Nelson, Matthew T. McDowell, Robert A. Huggins, Michael F. Toney, and Yi Cui. Full open-framework batteries for stationary energy storage. *Nature Communications*, 5:3007, 2014. doi: 10.1038/ncomms4007.
- [66] Hyun Wook Lee, Richard Y. Wang, Mauro Pasta, Seok Woo Lee, Nian Liu, and Yi Cui. Manganese hexacyanomanganate open framework as a high-capacity positive electrode material for sodium-ion batteries. *Nature Communications*, 5:5280, 2014. doi: 10.1038/ncomms6280.

- [67] Colin D. Wessells, Robert A. Huggins, and Yi Cui. Copper hexacyanoferrate battery electrodes with long cycle life and high power. *Nature Communications*, 2:550, 2011. doi: 10.1038/ncomms1563.
- [68] Zhijun Jia, Jun Wang, and Yi Wang. Electrochemical sodium storage of copper hexacyanoferrate with a well-defined open framework for sodium ion batteries. *RSC Advances*, 4:22768–22774, 2014. doi: 10.1039/c4ra02559h.
- [69] Zhijun Jia, Baoguo Wang, and Yi Wang. Copper hexacyanoferrate with a well-defined open framework as a positive electrode for aqueous zinc ion batteries. *Materials Chemistry and Physics*, 149:601–606, 2015. doi: 10.1016/j.matchemphys.2014.11.014.
- [70] Rafael Trócoli and Fabio La Mantia. An aqueous zinc-ion battery based on copper hexacyanoferrate. *ChemSusChem*, 8:481–485, 2015. doi: 10.1002/cssc.201403143.
- [71] Daisuke Asakura, Carissa H. Li, Yoshifumi Mizuno, Masashi Okubo, Haoshen Zhou, and Daniel R. Talham. Bimetallic cyanide-bridged coordination polymers as lithium ion cathode materials: Core@Shell nanoparticles with enhanced cyclability. *Journal of the American Chemical Society*, 135:2793–2799, 2013. doi: 10.1021/ja312160v.
- [72] Carissa H. Li, Marcus K. Peprah, Daisuke Asakura, Mark W. Meisel, Masashi Okubo, and Daniel R. Talham. Stepwise reduction of electrochemically lithiated core-shell heterostructures based on the Prussian blue analogue coordination polymers  $\text{K}_{0.1}\text{Cu}[\text{Fe}(\text{CN})_6]_{0.7} \cdot 3.5\text{H}_2\text{O}$  and  $\text{K}_{0.1}\text{Ni}[\text{Fe}(\text{CN})_6]_{0.7} \cdot 4.4\text{H}_2\text{O}$ . *Chemistry of Materials*, 27:1524–1530, 2015. doi: 10.1021/cm503639a.
- [73] Yuhao Lu, Long Wang, Jinguang Cheng, and John B. Goodenough. Prussian blue: A new framework of electrode materials for sodium batteries. *Chemical Communications*, 48:6544–6546, 2012. doi: 10.1039/c2cc3177j.
- [74] Masashi Okubo, Carissa H. Li, and Daniel R. Talham. High rate sodium ion insertion into core-shell nanoparticles of Prussian blue analogues. *Chemical Communications*, 50:1353–1355, 2014. doi: 10.1039/c3cc47607c.
- [75] Albert L. Lipson, Baofei Pan, Saul H. Lapidus, Chen Liao, John T. Vaughey, and Brian J. Ingram. Rechargeable Ca-Ion Batteries: A New Energy Storage System. *Chemistry of Materials*, 27:8442–8447, 2015. doi: 10.1021/acs.chemmater.5b04027.

- [76] Yoshifumi Mizuno, Masashi Okubo, Eiji Hosono, Tetsuichi Kudo, Katsuyoshi Oh-Ishi, Atsushi Okazawa, Norimichi Kojima, Ryosuke Kurono, Shin Ichi Nishimura, and Atsuo Yamada. Electrochemical Mg(II) intercalation into a bimetallic CuFe Prussian blue analog in aqueous electrolytes. *Journal of Materials Chemistry A*, 1:13055–13059, 2013. doi: 10.1039/c3ta13205f.
- [77] Ke Lu, Bin Song, Jintao Zhang, and Houyi Ma. A rechargeable Na-Zn hybrid aqueous battery fabricated with nickel hexacyanoferrate and nanostructured zinc. *Journal of Power Sources*, 321:257–263, 2016. doi: 10.1016/j.jpowsour.2016.05.003.
- [78] Yanfeng Yue, Andrew J. Binder, Bingkun Guo, Zhiyong Zhang, Zhen An Qiao, Chengcheng Tian, and Sheng Dai. Mesoporous prussian blue analogues: Template-free synthesis and sodium-ion battery applications. *Angewandte Chemie - International Edition*, 53:3134–3137, 2014. doi: 10.1002/anie.201310679.
- [79] Richard Y. Wang, Colin D. Wessells, Robert A. Huggins, and Yi Cui. Highly reversible open framework nanoscale electrodes for divalent ion batteries. *Nano Letters*, 13:5748–5752, 2013. doi: 10.1021/nl403669a.
- [80] Albert L. Lipson, Sang-Don Han, Soojeong Kim, Baofei Pan, Niya Sa, Chen Liao, Timothy T. Fister, Anthony K. Burrell, John T. Vaughey, and Brian J. Ingram. Nickel hexacyanoferrate, a versatile intercalation host for divalent ions from nonaqueous electrolytes. *Journal of Power Sources*, 325:646–652, 2016. doi: 10.1016/j.jpowsour.2016.06.019.
- [81] Tomoyuki Matsuda, Masamitsu Takachi, and Yutaka Moritomo. A sodium manganese ferrocyanide thin film for Na-ion batteries. *Chemical Communications*, 49:2750–2752, 2013. doi: 10.1039/c3cc38839e.
- [82] Yutaro Kurihara, Tomoyuki Matsuda, and Yutaka Moritomo. Structural properties of manganese hexacyanoferrates against Li concentration. *Japanese Journal of Applied Physics*, 52, 2013. doi: 10.7567/JJAP.52.017301.
- [83] Leyuan Zhang, Liang Chen, Xufeng Zhou, and Zhaoping Liu. Towards high-voltage aqueous metal-ion batteries beyond 1.5 V: The zinc/zinc hexacyanoferrate system. *Advanced Energy Materials*, 5:1400930, 2015. doi: 10.1002/aenm.201400930.
- [84] Hongkyung Lee, Yong Il Kim, Jung Ki Park, and Jang Wook Choi. Sodium zinc hexacyanoferrate with a well-defined open framework as a positive electrode for sodium ion batteries. *Chemical Communications*, 48:8416–8418, 2012. doi: 10.1039/c2cc33771a.

- [85] M Jayalakshmi and F Scholz. Performance characteristics of zinc hexacyanoferrate r Prussian blue and copper hexacyanoferrate r Prussian blue solid state secondary cells. *Journal of Power Sources*, 91:217–223, 2000. doi: 10.1016/S0378-7753(00)00475-4.
- [86] M. Oliver-Tolentino, G. Ramos-Sánchez, G. Guzmán, M. Avila, I. González, and Edilso Reguera. Water effect on sodium mobility in zinc hexacyanoferrate during charge/discharge processes in sodium ion-based battery. *Solid State Ionics*, 312:67–72, 2017. doi: 10.1016/j.ssi.2017.10.013.
- [87] Masamitsu Takachi, Tomoyuki Matsuda, and Yutaka Moritomo. Cobalt hexacyanoferrate as cathode material for Na secondary battery. *Applied Physics Express*, 6:025802, 2013. doi: 10.7567/APEX.6.025802.
- [88] Masamitsu Takachi, Tomoyuki Matsuda, and Yutaka Moritomo. Structural, Electronic, and Electrochemical Properties of  $\text{Li}_x\text{Co}[\text{Fe}(\text{CN})_6]_{0.90} \cdot 2.9\text{H}_2\text{O}$ . *Japanese Journal of Applied Physics*, 52:044301, 2013. doi: 10.7567/JJAP.52.044301.
- [89] Yutaro Kurihara and Yutaka Moritomo. Electrochemical, structural, and electronic properties of Mn–Co hexacyanoferrates against Li concentration. *Japanese Journal of Applied Physics*, 53:067101, 2014. doi: 10.7567/JJAP.53.067101.
- [90] Man Xie, Yongxin Huang, Menghao Xu, Renjie Chen, Xiaoxiao Zhang, Li Li, and Feng Wu. Sodium titanium hexacyanoferrate as an environmentally friendly and low-cost cathode material for sodium-ion batteries. *Journal of Power Sources*, 302:7–12, 2016. doi: 10.1016/j.jpowsour.2015.10.042.
- [91] Xin Sun, Xiao Yang Ji, Yu Ting Zhou, Yu Shao, Yong Zang, Zhao Yin Wen, and Chun Hua Chen. A new gridding cyanoferrate anode material for lithium and sodium ion batteries:  $\text{Ti}_{0.75}\text{Fe}_{0.25}[\text{Fe}(\text{CN})_6]_{0.96} \cdot 1.9\text{H}_2\text{O}$  with excellent electrochemical properties. *Journal of Power Sources*, 314:35–38, 2016. doi: 10.1016/j.jpowsour.2016.03.011.
- [92] Yushan Luo, Bolei Shen, Bingshu Guo, Linyu Hu, Qiuju Xu, Renming Zhan, Youquan Zhang, Shujuan Bao, and Maowen Xu. Potassium titanium hexacyanoferrate as a cathode material for potassium-ion batteries. *Journal of Physics and Chemistry of Solids*, 122:31–35, 2018. ISSN 00223697. doi: 10.1016/j.jpcs.2018.06.014.
- [93] John B. Goodenough and Arumugam Manthiram. A perspective on electrical energy storage. *MRS Communications*, 4:135–142, 2014. doi: 10.1557/mrc.2014.36.

- [94] Yoon Sung Lee, Won Kyung Shin, Aravindaraj G. Kannan, Sang Man Koo, and Dong Won Kim. Improvement of the Cycling Performance and Thermal Stability of Lithium-Ion Cells by Double-Layer Coating of Cathode Materials with Al<sub>2</sub>O<sub>3</sub> Nanoparticles and Conductive Polymer. *ACS Applied Materials and Interfaces*, 7:13944–13951, 2015. doi: 10.1021/acsami.5b02690.
- [95] D. R. Allan, S. P. Collins, G. Evans, D. Hall, K. McAuley, R. L. Owen, T. Sorensen, C. C. Tang, F. von Delft, A. Wagner, and H. Wilhelm. Status of the crystallography beamlines at Diamond Light Source. *European Physical Journal Plus*, 130:1–20, 2015. doi: 10.1140/epjp/i2015-15056-x.
- [96] Viktor Renman, Dickson O. Ojwang, Mario Valvo, Cesar Pay Gómez, Torbjörn Gustafsson, and Gunnar Svensson. Structural-electrochemical relations in the aqueous copper hexacyanoferrate-zinc system examined by synchrotron X-ray diffraction. *Journal of Power Sources*, 369:146–153, 2017. doi: 10.1016/j.jpowsour.2017.09.079.
- [97] Dickson O. Ojwang, Jekabs Grins, Dariusz Wardecki, Mario Valvo, Viktor Renman, Lennart Häggström, Tore Ericsson, Torbjörn Gustafsson, Abdelfattah Mahmoud, Raphaël P. Hermann, and Gunnar Svensson. Structure Characterization and Properties of K-Containing Copper Hexacyanoferrate. *Inorganic Chemistry*, 55:5924–5934, 2016. doi: 10.1021/acs.inorgchem.6b00227.
- [98] Marco Giorgetti. A Review on the Structural Studies of Batteries and Host Materials by X-Ray Absorption Spectroscopy. *ISRN Materials Science*, 2013:1–22, 2013. doi: 10.1155/2013/938625.
- [99] Daniel Buchholz, Jie Li, Stefano Passerini, Giuliana Aquilanti, Diandian Wang, and Marco Giorgetti. X-ray Absorption Spectroscopy Investigation of Lithium-Rich, Cobalt-Poor Layered-Oxide Cathode Material with High Capacity. *ChemElectroChem*, 2:85–97, 2015. doi: 10.1002/celec.201402324.
- [100] Marco Giorgetti and Lorenzo Stievano. *X-Ray Absorption Spectroscopy Study of Battery Materials*. InTech, Rijeka, 1 edition, 2017. doi: 10.5772/66868.
- [101] Paolo Conti, Silvia Zamponi, Marco Giorgetti, Mario Berrettoni, and William H. Smyrl. Multivariate Curve Resolution Analysis for Interpretation of Dynamic Cu K-Edge X-ray Absorption Spectroscopy Spectra for a Cu Doped V<sub>2</sub>O<sub>5</sub> Lithium Battery. *Analytical Chemistry*, 82:3629–3635, 2010. doi: 10.1021/ac902865h.
- [102] K. Mizushima, P. C. Jones, P. J. Wiseman, and J. B. Goodenough. Li<sub>x</sub>CoO<sub>2</sub> (0 < x ≤ 1): A new cathode ma-

- terial for batteries of high energy density. *Solid State Ionics*, 3-4:171–174, 1981. doi: 10.1016/0167-2738(81)90077-1.
- [103] Grant Bunker. *Introduction to XAFS: A Practical Guide to X-ray Absorption Fine Structure Spectroscopy*. Cambridge University Press, 2010. doi: 10.1017/CBO9780511809194.
- [104] Carlo Meneghini Settimio Mobilio, Federico Boscherini. *Synchrotron Radiation. Basics, Methods and Applications*. Springer-Verlag Berlin Heidelberg, 2015. doi: 10.1007/978-3-642-55315-8.
- [105] Vitalij K. Pecharsky and Peter Y. Zavalij. Fundamentals of Diffraction. In *Fundamentals of Powder Diffraction and Structural Characterization of Materials*, pages 133–149. Springer US, Boston, MA, 2003. doi: 10.1007/978-0-387-09579-0\_7.
- [106] F. De Groot and J. Vogel. Fundamentals of X-ray absorption and dichroism: The multiplet approach. In *Neutron and X-ray Spectroscopy*, pages 3–66. Springer Netherlands, Dordrecht, 2006. doi: 10.1007/1-4020-3337-0\_1.
- [107] B. Lengeler. Extended X-ray absorption fine structure. In *Neutron and X-ray Spectroscopy*, pages 131–168. Springer-Verlag, Berlin/Heidelberg, 2006. doi: 10.1007/1-4020-3337-0\_4.
- [108] NASA. Messier 1 (The Crab Nebula). URL <https://www.nasa.gov/feature/goddard/2017/messier-1-the-crab-nebula>.
- [109] Michael L. Baker, Michael W. Mara, James J. Yan, Keith O. Hodgson, Britt Hedman, and Edward I. Solomon. K- and L-edge X-ray absorption spectroscopy (XAS) and resonant inelastic X-ray scattering (RIXS) determination of differential orbital covalency (DOC) of transition metal sites. *Coordination Chemistry Reviews*, 345:182–208, 2017. doi: 10.1016/j.ccr.2017.02.004.
- [110] Anna De Juan, Joaquim Jaumot, and Romà Tauler. Multivariate Curve Resolution (MCR). Solving the mixture analysis problem. *Analytical Methods*, 6:4964–4976, 2014. doi: 10.1039/c4ay00571f.
- [111] Luca Rebuffi, Jasper R. Plaisier, Mahmoud Abdellatif, Andrea Lausi, Scardi, and Paolo. MCX: A synchrotron radiation beamline for X-ray diffraction line profile analysis. *Zeitschrift für Anorganische und Allgemeine Chemie*, 640:3100–3106, 2014. doi: 10.1002/zaac.201400163.
- [112] Julien Hannauer, Johan Scheers, Julien Fullenwarth, Bernard Fraise, Lorenzo Stievano, and Patrik Johansson. The Quest for Polysulfides in Lithium-Sulfur Battery Electrolytes: An Operando Confocal Raman Spectroscopy Study. *ChemPhysChem*, 16:2755–2759, 2015. doi: 10.1002/cphc.201500448.

- [113] J Rodriguez-Carvajal. Recent advances in magnetic structure determination by neutron powder diffraction. *Physica B: Physics of Condensed Matter*, 192:55–69, 1993. doi: 10.1016/0921-4526(93)90108-I.
- [114] Masaru Yao, Kentaro Kuratani, Toshikatsu Kojima, Nobuhiko Takeichi, Hiroshi Senoh, and Tetsu Kiyobayashi. Indigo carmine: An organic crystal as a positive-electrode material for rechargeable sodium batteries. *Scientific Reports*, 4:3650, 2014. doi: 10.1038/srep03650.
- [115] Koichi Momma and Fujio Izumi. VESTA 3 for three-dimensional visualization of crystal, volumetric and morphology data. *Journal of Applied Crystallography*, 44:1272–1276, 2011. doi: 10.1107/S0021889811038970.
- [116] B. Ravel and M. Newville. ATHENA, ARTEMIS, HEPHAESTUS: Data analysis for X-ray absorption spectroscopy using IFEFFIT. *Journal of Synchrotron Radiation*, 12:537–541, 2005. doi: 10.1107/S0909049505012719.
- [117] Adriano Filipponi, Andrea Di Cicco, and Calogero Renzo Natoli. X-ray-absorption spectroscopy and n-body distribution functions in condensed matter. I. Theory. *Physical Review B*, 52:15122–15134, 1995. doi: 10.1103/PhysRevB.52.15122.
- [118] Adriano Filipponi and Andrea Di Cicco. X-ray-absorption spectroscopy and n-body distribution functions in condensed matter. II. Data analysis and applications. *Physical Review B*, 52:15135–15149, 1995. doi: 10.1103/PhysRevB.52.15135.
- [119] Marco Giorgetti, Lorella Guadagnini, Domenica Tonelli, Marco Minicucci, and Giuliana Aquilanti. Structural characterization of electrodeposited copper hexacyanoferrate films by using a spectroscopic multi-technique approach. *Physical Chemistry Chemical Physics*, 14:5527–5537, 2012. doi: 10.1039/c2cp24109a.
- [120] Lars Hedin, Bengt I. Lundqvist, and Stig Lundqvist. Local exchange-correlation potentials. *Solid State Communications*, 9:537–541, 1971. doi: 10.1016/0038-1098(71)90141-4.
- [121] M. O. Krause and J. H. Oliver. Natural widths of atomic K and L levels, K-alpha X-ray lines and several KLL Auger lines. *Journal of Physical and Chemical Reference Data*, 8:329–338, 1979. doi: 10.1063/1.555595.
- [122] S Ayrault, B Jimenez, E Garnier, M Fedoroff, D J Jones, and C Loos-Neskovic. Sorption Mechanisms of Cesium on  $\text{Cu}_2\text{Fe}(\text{CN})_6$  and  $\text{Cu}_3[\text{Fe}(\text{CN})_6]_2$  Hexacyanoferrates and Their Relation to the Crystalline Structure. *Journal of Solid State Chemistry*, 141:475–485, 1998. doi: <http://dx.doi.org/10.1006/jssc.1998.7997>.

- [123] A. Gómez, J. Rodríguez-Hernández, and E. Reguera. Unique coordination in metal nitroprussides: The structure of  $\text{Cu}[\text{Fe}(\text{CN})_5\text{NO}] \cdot 2\text{H}_2\text{O}$  and  $\text{Cu}[\text{Fe}(\text{CN})_5\text{NO}]$ . *Journal of Chemical Crystallography*, 34: 893–903, 2004. doi: 10.1007/s10870-004-7724-2.
- [124] D. F. Mullica, J. D. Oliver, W. O. Milligan, and F. W. Hills. Ferrous hexacyanocobaltate dodecahydrate. *Inorganic and Nuclear Chemistry Letters*, 15:361–365, 1979. doi: 10.1016/0020-1650(79)80111-7.
- [125] G. Kresse and J. Hafner. Ab initio molecular dynamics for liquid metals. *Physical Review B*, 47:558–561, 1993. doi: 10.1103/PhysRevB.47.558.
- [126] G. Kresse and J. Hafner. Ab initio molecular-dynamics simulation of the liquid-metalamorphous- semiconductor transition in germanium. *Physical Review B*, 49:14251–14269, 1994. doi: 10.1103/PhysRevB.49.14251.
- [127] G. Kresse and J. Furthmüller. Efficiency of ab-initio total energy calculations for metals and semiconductors using a plane-wave basis set. *Computational Materials Science*, 6:15–50, 1996. doi: 10.1016/0927-0256(96)00008-0.
- [128] G. Kresse and J. Furthmüller. Efficient iterative schemes for ab initio total-energy calculations using a plane-wave basis set. *Physical Review B - Condensed Matter and Materials Physics*, 54:11169–11186, 1996. doi: 10.1103/PhysRevB.54.11169.
- [129] D. Joubert. From ultrasoft pseudopotentials to the projector augmented-wave method. *Physical Review B - Condensed Matter and Materials Physics*, 59:1758–1775, 1999. doi: 10.1103/PhysRevB.59.1758.
- [130] Y. Joly. X-ray absorption near-edge structure calculations beyond the muffin-tin approximation. *Physical Review B - Condensed Matter and Materials Physics*, 63:125120, 2001. doi: 10.1103/PhysRevB.63.125120.
- [131] Sourav Adak, Luke L. Daemen, Monika Hartl, Darrick Williams, Jennifer Summerhill, and Heinz Nakotte. Thermal expansion in 3d-metal Prussian Blue Analogs - A survey study. *Journal of Solid State Chemistry*, 184:2854–2861, 2011. doi: 10.1016/j.jssc.2011.08.030.
- [132] A. Bianconi, M. Dell’Ariccia, P. J. Durham, and J. B. Pendry. Multiple-scattering resonances and structural effects in the x-ray-absorption near-edge spectra of Fe(II) and Fe(III) hexacyanide complexes. *Physical Review B*, 26:6502–6508, 1982. doi: 10.1103/PhysRevB.26.6502.

- [133] Nobuhiro Kosugi, Toshihiko Yokoyama, and Haruo Kuroda. Polarization dependence of XANES of square-planar  $\text{Ni}(\text{CN})_4(2-)$  ion. A comparison with octahedral  $\text{Fe}(\text{CN})_6(4-)$  and  $\text{Fe}(\text{CN})_6(3-)$  ions. *Chemical Physics*, 104:449–453, 1986. doi: 10.1016/0301-0104(86)85034-0.
- [134] Kuniko Hayakawa, Keisuke Hatada, Paola D'Angelo, Stefano Della Longa, Calogero R. Natoli, and Maurizio Benfatto. Full quantitative multiple-scattering analysis of X-ray absorption spectra: Application to potassium hexacyanoferrate(II) and -(III) complexes. *Journal of the American Chemical Society*, 126: 15618–15623, 2004. doi: 10.1021/ja045561v.
- [135] Penghao Xiao, Jie Song, Long Wang, John B. Goodenough, and Graeme Henkelman. Theoretical study of the structural evolution of a  $\text{Na}_2\text{FeMn}(\text{CN})_6$  cathode upon Na intercalation. *Chemistry of Materials*, 27: 3763–3768, 2015. doi: 10.1021/acs.chemmater.5b01132.
- [136] Renjie Chen, Yongxin Huang, Man Xie, Ziheng Wang, Yusheng Ye, Li Li, and Feng Wu. Chemical inhibition method to synthesize highly crystalline prussian blue analogs for sodium-ion battery cathodes. *ACS Applied Materials and Interfaces*, 8:31669–31676, 2016. doi: 10.1021/acsami.6b10884.
- [137] Dong-Min Kim, Youngjin Kim, Durairaj Arumugam, Sang Won Woo, Yong Nam Jo, Min-Sik Park, Young-Jun Kim, Nam-Soon Choi, and Kyu Tae Lee. Co-intercalation of Mg(II) and Na(I) in  $\text{Na}_{0.69}\text{Fe}_2(\text{CN})_6$  as a High-Voltage Cathode for Magnesium Batteries. *ACS Applied Materials and Interfaces*, 8:8554–8560, 2016. doi: 10.1021/acsami.6b01352.
- [138] Hee Man Yang, Sung Chan Jang, Sang Bum Hong, Kune Woo Lee, Changhyun Roh, Yun Suk Huh, and Bum Kyoung Seo. Prussian blue-functionalized magnetic nanoclusters for the removal of radioactive cesium from water. *Journal of Alloys and Compounds*, 657:387–393, 2016. doi: 10.1016/j.jallcom.2015.10.068.
- [139] Feipeng Zhao, Yeyun Wang, Xiaona Xu, Yiling Liu, Rui Song, Guang Lu, and Yanguang Li. Cobalt hexacyanoferrate nanoparticles as a high-rate and ultra-stable supercapacitor electrode material. *ACS Applied Materials and Interfaces*, 6:11007–11012, 2014. doi: 10.1021/am503375h.
- [140] Xiao Jun Wang, Frank Krumeich, and Reinhard Nesper. Nanocomposite of manganese ferrocyanide and graphene: A promising cathode material for rechargeable lithium ion batteries. *Electrochemistry Communications*, 34:246–249, 2013. doi: 10.1016/j.elecom.2013.06.019.
- [141] Ya You, Xing Long Wu, Ya Xia Yin, and Yu Guo Guo. High-quality Prussian blue crystals as superior

- cathode materials for room-temperature sodium-ion batteries. *Energy and Environmental Science*, 7:1643–1647, 2014. doi: 10.1039/c3ee44004d.
- [142] Oktawian Makowski, Jadwiga Stroka, Pawel J. Kulesza, Marcin A. Malik, and Zbigniew Galus. Electrochemical identity of copper hexacyanoferrate in the solid-state: Evidence for the presence and redox activity of both iron and copper ionic sites. *Journal of Electroanalytical Chemistry*, 532:157–164, 2002. doi: 10.1016/S0022-0728(02)00965-8.
- [143] Robert A. Huggins. Review—A New Class of High Rate, Long Cycle Life, Aqueous Electrolyte Battery Electrodes. *Journal of The Electrochemical Society*, 164:A5031–A5036, 2017. doi: 10.1149/2.0571701jes.
- [144] Ping Jiang, Hezhu Shao, Liang Chen, Jiwen Feng, and Zhaoping Liu. Ion-selective copper hexacyanoferrate with an open-framework structure enables high-voltage aqueous mixed-ion batteries. *Journal of Materials Chemistry A*, 5:16740–16747, 2017. doi: 10.1039/c7ta04172a.
- [145] Mauro Pasta, Colin D. Wessells, Robert A. Huggins, and Yi Cui. A high-rate and long cycle life aqueous electrolyte battery for grid-scale energy storage. *Nature Communications*, 3:1149, 2012. doi: 10.1038/ncomms2139.
- [146] Tami E. Westre, Pierre Kennepohl, Jane G. DeWitt, Britt Hedman, Keith O. Hodgson, and Edward I. Solomon. A multiplet analysis of Fe K-edge  $1s \rightarrow 3d$  pre-Edge features of iron complexes. *Journal of the American Chemical Society*, 119:6297–6314, 1997. doi: 10.1021/ja964352a.
- [147] Francesco Tisato, Cristina Marzano, Valentina Peruzzo, Matteo Tegoni, Marco Giorgetti, Marko Damjanovic, Angela Trapananti, Alessandro Bagno, Carlo Santini, Maura Pellei, Marina Porchia, and Valentina Gandin. Insights into the cytotoxic activity of the phosphane copper(I) complex  $[\text{Cu}(\text{thp})_4][\text{PF}_6]$ . *Journal of Inorganic Biochemistry*, 165:80–91, 2016. doi: 10.1016/j.jinorgbio.2016.07.007.
- [148] Ingrid J. Pickering, Graham N. George, Charles T. Dameron, Boris Kurz, Dennis R. Winge, and Ian G. Dance. X-ray Absorption Spectroscopy of Cuprous-Thiolate Clusters in Proteins and Model Systems. *Journal of the American Chemical Society*, 115:9498–9505, 1993. doi: 10.1021/ja00074a014.
- [149] Jesús Chaboy, Adela Muñoz-Páez, Flora Carrera, Patrick Merkling, and Enrique Sánchez Marcos. Ab initio x-ray absorption study of copper K-edge XANES spectra in Cu(II) compounds. *Physical Review B - Condensed Matter and Materials Physics*, 71:134208, 2005. doi: 10.1103/PhysRevB.71.134208.

- [150] Masashi Okubo, Daisuke Asakura, Yoshifumi Mizuno, Tetsuichi Kudo, Haoshen Zhou, Atsushi Okazawa, Norimichi Kojima, Kazumichi Ikedo, Takashi Mizokawa, and Itaru Honma. Ion-induced transformation of magnetism in a bimetallic CuFe Prussian blue analogue. *Angewandte Chemie - International Edition*, 50: 6269–6273, 2011. doi: 10.1002/anie.201102048.
- [151] M. D. Bartberger, W. Liu, E. Ford, K. M. Miranda, C. Switzer, J. M. Fukuto, P. J. Farmer, D. A. Wink, and K. N. Houk. The reduction potential of nitric oxide (NO) and its importance to NO biochemistry. *Proceedings of the National Academy of Sciences*, 99:10958–10963, 2002. doi: 10.1073/pnas.162095599.
- [152] Chung Hung Hsieh, Shengda Ding, Özlen F. Erdem, Danielle J. Crouthers, Tianbiao Liu, Charles C.L. McCrory, Wolfgang Lubitz, Codrina V. Popescu, Joseph H. Reibenspies, Michael B. Hall, and Marcetta Y. Darensbourg. Redox active iron nitrosyl units in proton reduction electrocatalysis. *Nature Communications*, 5:3684, 2014. doi: 10.1038/ncomms4684.
- [153] Y. A.L. Nanba, Daisuke Asakura, Masashi Okubo, Haoshen Zhou, Kenta Amemiya, Kozo Okada, Per Anders Glans, Catherine A. Jenkins, Elke Arenholz, and Jinghua Guo. Anisotropic charge-transfer effects in the asymmetric Fe(CN)<sub>5</sub>NO octahedron of sodium nitroprusside: A soft X-ray absorption spectroscopy study. *Physical Chemistry Chemical Physics*, 16:7031–7036, 2014. doi: 10.1039/c3cp55471f.
- [154] Angelo Mullaliu, Moulay Tahar Sougrati, Nicolas Louvain, Giuliana Aquilanti, Marie Liesse Doublet, Lorenzo Stievano, and Marco Giorgetti. The electrochemical activity of the nitrosyl ligand in copper nitroprusside: a new possible redox mechanism for lithium battery electrode materials? *Electrochimica Acta*, 257:364–371, 2017. doi: 10.1016/j.electacta.2017.10.107.
- [155] Angelo Mullaliu, Giuliana Aquilanti, Paolo Conti, Jasper R. Plaisier, Marcus Fehse, Lorenzo Stievano, and Marco Giorgetti. Copper Electroactivity in Prussian Blue-Based Cathode Disclosed by Operando XAS. *Journal of Physical Chemistry C*, 122:15868–15877, 2018. doi: 10.1021/acs.jpcc.8b03429.
- [156] Philip Coppens, Irina Novozhilova, and Andrey Kovalevsky. Photoinduced linkage isomers of transition-metal nitrosyl compounds and related complexes. *Chemical Reviews*, 102:861–883, 2002. doi: 10.1021/cr000031c.
- [157] F. Kubota, K. Shinohara, K. Shimojo, T. Oshima, M. Goto, S. Furusaki, and T. Hano. Extraction of rare earth metals by calix[4]arene solubilized in AOT reversed micellar solution. *Separation and Purification Technology*, 24:93–100, 2001. doi: 10.1016/S1383-5866(00)00215-X.

- [158] Nydia D. Villanueva, Michael Y. Chiang, and Jeffrey R. Bocarsly. Copper Complexes Bearing Pendant, Protonatable Noncoordinating Groups: Synthesis, Characterization, and Protonation Chemistry. *Inorganic Chemistry*, 37:685–692, 1998. doi: 10.1021/ic9703843.
- [159] Peter Comba and Marion Kerscher. Computation of structures and properties of transition metal compounds. *Coordination Chemistry Reviews*, 253:564–574, 2009. doi: 10.1016/j.ccr.2008.05.019.
- [160] International Atomic Energy Agency. The radiological accident in Goiânia. Volume 815 de Proceedings series. Technical report, Vienna, 1988.
- [161] Rongzhi Chen, Hisashi Tanaka, Tohru Kawamoto, Miyuki Asai, Chikako Fukushima, Masato Kurihara, Manabu Ishizaki, Masayuki Watanabe, Makoto Arisaka, and Takuya Nankawa. Thermodynamics and mechanism studies on electrochemical removal of cesium ions from aqueous solution using a nanoparticle film of copper hexacyanoferrate. *ACS Applied Materials and Interfaces*, 5:12984–12990, 2013. doi: 10.1021/am403748b.
- [162] Michael A. Lilga, Rick J. Orth, Johannes P.H. Sukamto, Scot D. Rassat, J. David Genders, and Ram Gopal. Cesium separation using electrically switched ion exchange. *Separation and Purification Technology*, 24:451–466, 2001. doi: 10.1016/S1383-5866(01)00145-9.
- [163] K. Wu, X. Zhao, M. Chen, H. Zhang, Z. Liu, X. Zhang, X. Zhu, and Q. Liu. Synthesis of well-dispersed  $\text{Fe}_3\text{O}_4$  nanoparticles loaded on montmorillonite and sensitive colorimetric detection of  $\text{H}_2\text{O}_2$ -based on its peroxidase-like activity. *New Journal of Chemistry*, 42:23–25, 2018. doi: 10.1039/c8nj01190g.
- [164] Hao Liu, Yanan Ding, Baochan Yang, Zhenxue Liu, Qingyun Liu, and Xiao Zhang. Colorimetric and ultrasensitive detection of  $\text{H}_2\text{O}_2$  based on  $\text{Au}/\text{Co}_3\text{O}_4\text{-CeO}_x$  nanocomposites with enhanced peroxidase-like performance. *Sensors and Actuators, B: Chemical*, 271:336–345, 2018. doi: 10.1016/j.snb.2018.05.108.
- [165] Arkady A. Karyakin, Elena E. Karyakina, and Lo Gorton. On the mechanism of  $\text{H}_2\text{O}_2$  reduction at Prussian Blue modified electrodes. *Electrochemistry Communications*, 1:78–82, 1999. doi: 10.1016/S1388-2481(99)00010-7.
- [166] M. Avila, L. Reguera, J. Rodríguez-Hernández, J. Balmaseda, and E. Reguera. Porous framework of  $\text{T}_2[\text{Fe}(\text{CN})_6] \cdot x\text{H}_2\text{O}$  with  $\text{T}=\text{Co}, \text{Ni}, \text{Cu}, \text{Zn}$ , and  $\text{H}_2$  storage. *Journal of Solid State Chemistry*, 181:2899–2907, 2008. doi: 10.1016/j.jssc.2008.07.030.

- [167] M. Giorgetti, G. Aquilanti, and M. Minicucci. Structural study of the  $\text{Cu}^{2+}$ -loaded copper hexacyanoferrate electrode deposited on indium tin oxide substrate. *Journal of Physics: Conference Series*, 430:012049, 2013. doi: 10.1088/1742-6596/430/1/012049.
- [168] Manoj K. Sharma and Suresh K. Aggarwal. Simultaneous formation of Prussian Blue and copper hexacyanoferrate from a solution of  $\text{Cu(II)}$  and  $\text{K}_3[\text{Fe(CN)}_6]$  in presence of  $\text{HAuCl}_4$ . *Journal of Electroanalytical Chemistry*, 705:64–67, 2013. doi: 10.1016/j.jelechem.2013.07.023.
- [169] Lorella Guadagnini, Domenica Tonelli, and Marco Giorgetti. Improved performances of electrodes based on  $\text{Cu(II)}$ -loaded copper hexacyanoferrate for hydrogen peroxide detection. *Electrochimica Acta*, 55:5036–5039, 2010. doi: 10.1016/j.electacta.2010.04.019.
- [170] Rongzhi Chen, Miyuki Asai, Chikako Fukushima, Manabu Ishizaki, Masato Kurihara, Makoto Arisaka, Takuya Nankawa, Masayuki Watanabe, Tohru Kawamoto, and Hisashi Tanaka. Column study on electrochemical separation of cesium ions from wastewater using copper hexacyanoferrate film. *Journal of Radioanalytical and Nuclear Chemistry*, 303:1491–1495, 2015. doi: 10.1007/s10967-014-3588-x.
- [171] C. Loos-Neskovic, S. Ayrault, V. Badillo, B. Jimenez, E. Garnier, M. Fedoroff, D. J. Jones, and B. Merinov. Structure of copper-potassium hexacyanoferrate (II) and sorption mechanisms of cesium. *Journal of Solid State Chemistry*, 177:1817–1828, 2004. doi: 10.1016/j.jssc.2004.01.018.
- [172] E. R. Nightingale. Phenomenological theory of ion solvation. Effective radii of hydrated ions. *Journal of Physical Chemistry*, 63:1381–1387, 1959. doi: 10.1021/j150579a011.
- [173] Natalya A. Sitnikova, Maria A. Komkova, Irina V. Khomyakova, Elena E. Karyakina, and Arkady A. Karyakin. Transition metal hexacyanoferrates in electrocatalysis of  $\text{H}_2\text{O}_2$  reduction: An exclusive property of prussian blue. *Analytical Chemistry*, 86:4131–4134, 2014. doi: 10.1021/ac500595v.

# Colophon

**T**HIS THESIS WAS TYPESET using  $\LaTeX$ , originally developed by Leslie Lamport and based on Donald Knuth's  $\TeX$ . The original body text is set in 11 point Arno Pro, designed by Robert Slimbach in the style of book types from the Aldine Press in Venice, and issued by Adobe in 2007. A template, which can be used to format a PhD thesis with this look and feel, has been released under the permissive MIT (X11) license, and can be found online at [github.com/suchow/](https://github.com/suchow/) or from the author at [suchow@post.harvard.edu](mailto:suchow@post.harvard.edu).